



University of Pennsylvania
ScholarlyCommons

Departmental Papers (ESE)

Department of Electrical & Systems Engineering

11-3-2017

Modular Hopping and Running via Parallel Composition

Avik De
avik@seas.upenn.edu

Follow this and additional works at: http://repository.upenn.edu/ese_papers

 Part of the [Electrical and Computer Engineering Commons](#), and the [Systems Engineering Commons](#)

Recommended Citation

Avik De, "Modular Hopping and Running via Parallel Composition", . November 2017.

This paper is posted at ScholarlyCommons. http://repository.upenn.edu/ese_papers/794
For more information, please contact repository@pobox.upenn.edu.

Modular Hopping and Running via Parallel Composition

Abstract

Though multi-functional robot hardware has been created, the complexity in its functionality has been constrained by a lack of algorithms that appropriately manage flexible and autonomous reconfiguration of interconnections to physical and behavioral components.

Raibert pioneered a paradigm for the synthesis of planar hopping using a composition of ``parts": controlled vertical hopping, controlled forward speed, and controlled body attitude. Such reduced degree-of-freedom compositions also seem to appear in running animals across several orders of magnitude of scale. Dynamical systems theory can offer a formal representation of such reductions in terms of ``anchored templates," respecting which Raibert's empirical synthesis (and the animals' empirical performance) can be posed as a parallel composition. However, the orthodox notion (attracting invariant submanifold with restriction dynamics conjugate to a template system) has only been formally synthesized in a few isolated instances in engineering (juggling, brachiating, hexapedal running robots, etc.) and formally observed in biology only in similarly limited contexts.

In order to bring Raibert's 1980's work into the 21st century and out of the laboratory, we design a new family of one-, two-, and four-legged robots with high power density, transparency, and control bandwidth. On these platforms, we demonstrate a growing collection of $\{\text{body, behavior}\}$ pairs that successfully embody dynamical running / hopping ``gaits" specified using compositions of a few templates, with few parameters and a great deal of empirical robustness. We aim for and report substantial advances toward a formal notion of parallel composition--embodied behaviors that are correct by design even in the presence of nefarious coupling and perturbation--using a new analytical tool (hybrid dynamical averaging).

With ideas of verifiable behavioral modularity and a firm understanding of the hardware tools required to implement them, we are closer to identifying the components required to flexibly program the exchange of work between machines and their environment. Knowing how to combine and sequence stable basins to solve arbitrarily complex tasks will result in improved foundations for robotics as it goes from ad-hoc practice to science (with predictive theories) in the next few decades.

Keywords

modularity, legged robots, composition, dynamics, locomotion

Disciplines

Electrical and Computer Engineering | Engineering | Systems Engineering

MODULAR HOPPING AND RUNNING VIA PARALLEL COMPOSITION

Avik De

A DISSERTATION

in

Electrical and Systems Engineering

Presented to the Faculties of the University of Pennsylvania

in

Partial Fulfillment of the Requirements for the

Degree of Doctor of Philosophy

2017

Supervisor of Dissertation

Daniel E. Koditschek, Alfred Fitler Moore Professor

Graduate Group Chairperson

Alejandro Ribeiro, Rosenbluth Associate Professor

Dissertation Committee

George Pappas, Department of ESE

Daniel Koditschek, Department of ESE

Cynthia Sung, Department of MEAM

Jessy Grizzle, Department of EECS, UMich

MODULAR HOPPING AND RUNNING VIA PARALLEL COMPOSITION

© COPYRIGHT

2017

Avik De

This work is licensed under the

Creative Commons Attribution

NonCommercial-ShareAlike 3.0

License

To view a copy of this license, visit

<http://creativecommons.org/licenses/by-nc-sa/3.0/>

ACKNOWLEDGEMENTS

This material is based upon work supported in part by the U. S. Army Research Laboratory and the U. S. Army Research Office under contract/grant number W911NF-16-1-0158, in part by NSF grant #1028237, and in part by ONR grant #N00014-16-1-2817, a Vannevar Bush Fellowship held by Daniel E. Koditschek, sponsored by the Basic Research Office of the Assistant Secretary of Defense for Research and Engineering.

This work would not have been possible without the vision of my advisor, who amazes me with his deep high-level insight into the successful operation of physical machines in the real world. My experience of going from complete cluelessness about mechatronics to (very slowly) building robots from scratch was invaluable; in this regard I must thank all my labmates, and particularly Aaron Johnson, Deniz Ilhan, and Gavin Kenneally, for helping fill in the gaps and encouraging (not discouraging) this protracted endeavor.

Finally, I thank my partner, Sarah Costrell, for her unwavering support despite the stresses of graduate school, and possessing a rare, deep-seated, selflessness that has been a true inspiration. I thank my family for unconditionally believing in me, and my cats for frequently reminding me that, sometimes, life need not be complicated after all.

ABSTRACT

MODULAR HOPPING AND RUNNING VIA PARALLEL COMPOSITION

Avik De

Daniel E. Koditschek

Though multi-functional robot hardware has been created, the complexity in its functionality has been constrained by a lack of algorithms that appropriately manage flexible and autonomous reconfiguration of interconnections to physical and behavioral components.

Raibert pioneered a paradigm for the synthesis of planar hopping using a composition of “parts”: controlled vertical hopping, controlled forward speed, and controlled body attitude. Such reduced degree-of-freedom compositions also seem to appear in running animals across several orders of magnitude of scale. Dynamical systems theory can offer a formal representation of such reductions in terms of “anchored templates,” respecting which Raibert’s empirical synthesis (and the animals’ empirical performance) can be posed as a parallel composition. However, the orthodox notion (attracting invariant submanifold with restriction dynamics conjugate to a template system) has only been formally synthesized in a few isolated instances in engineering (juggling, brachiating, hexapedal running robots, etc.) and formally observed in biology only in similarly limited contexts.

In order to bring Raibert’s 1980’s work into the 21st century and out of the laboratory, we design a new family of one-, two-, and four-legged robots with high power density, transparency, and control bandwidth. On these platforms, we demonstrate a growing collection of {body, behavior} pairs that successfully embody dynamical running / hopping “gaits” specified using compositions of a few templates, with few parameters and a great deal of empirical robustness. We aim for and report substantial advances toward a formal notion of parallel composition—embodied behaviors that are correct by design even in the presence of nefarious coupling and perturbation—using a new analytical tool (hybrid dynamical averaging).

With ideas of verifiable behavioral modularity and a firm understanding of the hardware tools required to implement them, we are closer to identifying the components required to flexibly program the exchange of work between machines and their environment. Knowing how to combine and sequence stable basins to solve arbitrarily complex tasks will result in improved foundations for robotics as it goes from ad-hoc practice to science (with predictive theories) in the next few decades.¹

¹[Video of thesis defense on Sep 20, 2017 \[YouTube\]](#)

ACKNOWLEDGEMENTS	iii
ABSTRACT	iv
LIST OF TABLES	vi
LIST OF ILLUSTRATIONS	viii
CHAPTER 1 : Introduction	1
1.1 Motivation	1
1.2 Contributions and Organization	6
1.3 Related Work	10
CHAPTER 2 : Design of High-Bandwidth Legged Robots	20
2.1 Motor Selection and Design	21
2.2 Drivetrain Design: Transparency and Gearbox Selection	28
2.3 Actuator Recruitment via Leg Design	39
2.4 Platform Design	42
CHAPTER 3 : Toward Correct-by-Design Compositions	52
3.1 Templates for Hopping and Running	55
3.2 Averaging Theory and its Application to Locomotion	62
3.3 Symmetry-Factored Hybrid Averaging	74
3.4 Application: Coordination of Independent Vertical Hoppers (2DOF)	77
3.5 Application: Coordination of Coupled Vertical Hoppers (2DOF)	90
3.6 Time-Reversal Symmetry and its Relation to Averaging	118
3.7 Applications of HSAS	131
3.8 Discussion	138
CHAPTER 4 : Empirical Compositions	140
4.1 Tailed Planar Hopping (4 DOF)	140
4.2 3D Virtual Bipedal Running (6 DOF)	150
CHAPTER 5 : Conclusion	167
5.1 Hardware: Actuator Design using Dynamic Models	167
5.2 Hybrid Averaging	168
5.3 Design Paradigm	171
BIBLIOGRAPHY	172

List of Tables

TABLE 1 :	Comparison of specific conventional and DD actuators.	30
TABLE 2 :	Physical properties of the machines of interest (2.4.1).	43
TABLE 3 :	Performance measures of the machines of interest (2.4.1)	43
TABLE 4 :	Jerboa Physical Parameter values	48
TABLE 5 :	Assumptions made to facilitate slot hopper analytical results	81
TABLE 6 :	Slot hopper behavioral regimes and analytical results	98
TABLE 7 :	Slot hopper empirical extensions via template composition	98
TABLE 8 :	Jerboa control parameters (all scalars unless noted)	144
TABLE 9 :	Comparison to prior virtual leg management for quadruped gaits	152

List of Figures

FIGURE 1 :	An overview of some of the results presented in this thesis	7
FIGURE 2 :	Hypotheses about neuromechanical control architectures	12
FIGURE 3 :	Block-diagram architecture of a feedback-driven biped	14
FIGURE 4 :	A family of DD robots built at Penn between 2014–2016	21
FIGURE 5 :	Stator and rotor of a motor showing the critical geometric constants	24
FIGURE 6 :	Peak specific torque	26
FIGURE 7 :	Thermal specific torque	27
FIGURE 8 :	Bode plot of amplitude response of the motor output	30
FIGURE 9 :	Average climbing speed under periodic intermittent operation	36
FIGURE 10 :	A comparison of the best vertical climbing performance possible	37
FIGURE 11 :	Optimal gear ratios for a subset of the motors	38
FIGURE 12 :	Leg designs	39
FIGURE 13 :	Metrics for leg kinematics	41
FIGURE 14 :	Self-manipulability as a design principle	45
FIGURE 15 :	48cm vertical jump of the Minitaur robot.	46
FIGURE 16 :	The Jerboa	47
FIGURE 17 :	The Jerboa tail	48
FIGURE 18 :	Jerboa leg designs	49
FIGURE 19 :	Jerboa motor	50
FIGURE 20 :	Jerboa motor controller	50
FIGURE 21 :	Visual depiction of the limit cycle	54
FIGURE 22 :	Plant models for the templates	56
FIGURE 23 :	A hybrid 2 DOF inertial reorientation template	60
FIGURE 24 :	A class of hybrid averageable systems	70
FIGURE 25 :	Two decoupled unit mass vertical hoppers, shown here in a single stance mode.	73
FIGURE 26 :	A depiction of the two kinds of hybrid dynamical limit cycles	74
FIGURE 27 :	Virtual biped models of increasing complexity	78
FIGURE 28 :	Vertical hopper averaging simulation	88
FIGURE 29 :	Comparison of coordination through pure “abstract” phase vs. its perceptually direct surrogate	89
FIGURE 30 :	Phase locking at non-extreme κ	91
FIGURE 31 :	Center of percussion	95
FIGURE 32 :	Projecting Minitaur and sagittal plane biped trajectories onto the slot hopper DOF	110
FIGURE 33 :	2DOF slot-hopper as a template anchored by the Sagittal Plane biped . .	111
FIGURE 34 :	Comparison of slot hopper simulation to SC-Minitaur	113
FIGURE 35 :	Qualitative effect of active toe extension for simultaneous transitions . .	114
FIGURE 36 :	Robustness to parametric inaccuracy	115

FIGURE 37 : Strongly coupled in-phase stability vs. κ	116
FIGURE 38 : A spring-loaded inverted pendulum (SLIP).	119
FIGURE 39 : Asymmetric monoped trajectories	125
FIGURE 40 : A computational recipe for stability analysis	130
FIGURE 41 : Averaging “neutral point” approximation	137
 FIGURE 42 : Control of a tail-energized hopping behavior expressed as a hierarchical composition of closed-loop templates	142
FIGURE 43 : Simulation traces of tail-energized and hip-energized hopping on the Jerboa	143
FIGURE 44 : Snapshots from apex to apex of tail-energized planar hopping	144
FIGURE 45 : Effect of changing tail mass	148
FIGURE 46 : Testing our decoupling change of coordinates to “shape coordinates”	149
FIGURE 47 : Trading off speed for height in tail-energized hopping	150
FIGURE 48 : Plots of a single stride of tail-energized hopping	151
FIGURE 49 : State machines utilized to implement the various gaits	153
FIGURE 50 : Virtual bipedal gaits on a quadruped	154
FIGURE 51 : SC-Minitaur preflexive pronking	155
FIGURE 52 : SC-Minitaur feedback-stabilized bounding	156
FIGURE 53 : Minitaur feedback-stabilized pronking	159
FIGURE 54 : Minitaur preflexive bounding	160
FIGURE 55 : Minitaur bounding leap	162
FIGURE 56 : Minitaur pronking leap	162
FIGURE 57 : Minitaur preflexive and feedback-stabilized pacing	163
FIGURE 58 : Minitaur pacing in place	163
FIGURE 59 : Minitaur feedback-stabilized trotting	165
FIGURE 60 : Snapshots of trotting	165

CHAPTER 1 : Introduction

1.1 Motivation

More than three decades after “sense/think/act” was accepted as a roadmap for robotics research and practice [Asada and Slotine \(1986\)](#), the robotics community has made large demonstrable advances¹ in isolated “thinking,” with clearly defined inputs (e.g., Go board state) and outputs (e.g., allowed Go moves). However, at the dawn of commercially-viable robotics, the “users” of new robotics technology need further assurances that the machines will be prepared for interactions (both of sensors and actuators) with an unstructured and unmodeled world.

The work in this thesis was inspired to a great degree by the success of Raibert’s MIT Leg Lab in the 1980’s—demonstrating simple machines that blindly hopped, ran, and performed acrobatic maneuvers [Raibert \(1986\)](#). Over three decades later, the performance of state-of-the-art machines in the face of physical interaction is underwhelming to the public². The DRC challenges were more complex than those solved by Raibert’s robots, but it should give us (robotics scientists) pause that years of preparation were insufficient to generate successful control strategies for a predefined set of tasks. One of the fundamental reasons our robots are “stuck” is the lack of principled methodologies for re-using and re-combining motor control algorithms such as the ones Raibert’s machines used—why must we re-invent how to walk and run again and again?

There is no doubting the difficulty of the challenges: these robots are all complex, highly non-linear and hybrid (smooth flows punctuated by discontinuous changes in the states—some selectable by the controller; some imposed by the physics) dynamical systems, they all have > 20 -dimensional state spaces (most much larger), and dynamic legged locomotion systems are all statically unstable.³ An additional symptom of the complexity is the lack of breadth in robotics research (with many efforts focusing only on mathematics, software/algorithms, or design/hardware⁴); an unfortunate disconnection from the strongly interdependent nature of the challenge.

1.1.1 Compositions: a Scheme for Taming and Using Complexity in Autonomous Robotics

The research described in this thesis involves the programming of autonomous dynamic behaviors on physical robotic systems. The usage of “programming” naturally draws comparisons to computer science, the parallels to which are on one hand fraught—the physics of energy-exchange precludes success factors such as “re-use of library elements” [Whitney \(1996\)](#) from computer engineering, and the physical world that the machines interact with is unpredictable and imprecise in a way that electrical signals on PCB’s are not, necessitating structural stability against perturbations in states and parameters. On the other hand, the analogy is enticing: steps toward mirroring the ability in computer science of re-using primitives (“modules” or “functions”) between robots, or having re-combinations in the same robot, would lead to rapid improvements in the capabilities of our machines.

¹Google’s AlphaGo Defeats Chinese Go Master in Win for A.I. [\[NYTimes\]](#)

²The Hard Lessons of DARPA’s Robotics Challenge [\[IEEE\]](#), The DARPA Robotics Challenge Was A Bust [\[PopSci\]](#)

³Even though quasi-static stability can be attained by keeping the center of gravity within the base of support (e.g. foot), this limits the machine to low speeds and renders it incapable of navigating rougher terrain where footholds cannot be chosen precisely.

⁴Surprisingly, including in the afore-mentioned DRC, where many teams participated on a “simulation track.”

The work contained in this thesis has emphasized a strong integration of three efforts: mathematical foundations of compositions in legged robotics, design of a new generation of robotic systems, and fielding abstract principles on systems in the real world. The specific task emphasized is the synthesis of steady-state locomotion in the horizontal plane using a method that generalizes across different morphologies (such as a hopping monoped, tailed biped, and a quadruped), at varying speeds of up to 5 body lengths/second, while maintaining formally-verified (“correct by design”) stability properties.

Desired programming paradigm

We pursue a paradigm of behavior programming that involves the following sequential steps:

Modular task specification Tasks are specified as a parallel composition of target dynamics; e.g., a bounding quadruped should control the horizontal components of its center-of-mass velocity to a desired setpoint, while ensuring its body roll angle is stabilized to zero, and its body pitch angle oscillates in synchrony with front and hind steps. This thesis makes no contributions to this step (which may be performed by a human operator, or perhaps by a high-level autonomy program).

Composition of dynamic primitives Controllers on the coupled high-dimensional body attempt to simultaneously instantiate the template behaviors while ignoring coupling interactions, thus still having only sparse dependence on states and parameters.

In order to implement this paradigm, two logical components are required:

First, we need an expressive library of primitives⁵ that can be used as a “basis” for task specification. In the context of legged locomotion, these primitives are 1 or 2 degree of freedom (DOF) mechanical systems exhibiting a desired limiting behavior, e.g., a vertically-constrained mass on a springy, actuated, massless leg stably hopping to a desired height. These primitives include as sub-components: (a) isolated template plants (usually 2-dimensional); (b) control strategies that need few parameters and up to two states as input; and (c) a coordinate change from physical states to model coordinates that we use for analysis (to be described in Chapter 3). We include a small library of templates in Sec. 3.1.

Second, from a systems perspective, a tool for verification of correctness or a “correct by design” formal synthesis tool (such as type theoretic guarantees in functional programming) is required for the viability of this approach. The popular template/anchor framework [Full and Koditschek \(1999\)](#) posits a formal relation (invariant attracting submanifolds with conjugate flows) which has only been established/instantiated in limited instances in the literature. In our work, we find that mechanical coupling interactions don’t allow for a classical anchoring relation for systems composed from templates, motivating the use of a less rigid equivalence such as a closed-loop-vector-field analogue of approximate bisimulation [Haghverdi et al. \(2005\)](#), [Tabuada et al. \(2008\)](#). In Chapter 3 we formalize for the first time the ingredients and algorithms required to automate the “composition” step above in the context of a steady locomotion task.

In other words, we aim to create modules (templates) that are externally robust, with carefully-defined interfaces built upon formal guarantees [De et al. \(2016\)](#) to address fragility to interconnection errors. This notion of “modularity” is related to complexity theory literature [Csete and Doyle](#)

⁵Or “templates,” in the language of [Full and Koditschek \(1999\)](#).

(2004), popularized by Doyle’s “bow-tie” metaphor.⁶

Desired outcomes

From the perspective of the behavior programmer, the resulting compositions must have the following properties (we list our formal claims in the next section):

Guarantees of stability In consequence of (the long-known Holmes (2005)) non-integrability of most two (and higher) DoF mechanical systems no procedural strategy has been developed for analyzing hybrid dynamical systems with greater than 2 degrees of freedom (DOF) representative of locomotion (LLS Schmitt and Holmes (2000), SLIP with torso, etc.). By providing a principled means of approximating these generically non-integrable systems with “nearby” integrable stand-ins, we believe our averaging approach (Sec. 3.2) may offer a route toward such a procedural analysis of much higher dimensional locomotion systems than has heretofore been possible, allowing us to reap the aforementioned benefits.

Efficient synthesis Depending on the approach, the complexity of traditional control synthesis (as distinct from the problem of analytical guarantees) can grow unmanageably with system size (the “curse of dimensionality”). Some approaches to mitigate this have included the template-anchor framework Full and Koditschek (1999), (hybrid) zero dynamics Grizzle et al. (2014), but there has been no prescription for successfully using low-dimensional controllers (that don’t require knowledge of all states and/or parameters). In contrast, in our various demonstrations (e.g. Sec. 3.4, 3.5, 3.7) the synthesis problem reduces to an assignment of a few template controllers (Sec. 3.1) with few tuning parameters.

Behavioral complexity Since target behaviors are generated through arbitrary (verifiable) compositions of a known library of templates, there is a *combinatorially growing expressible behavioral complexity* (while still maintaining low synthesis complexity). In consequent exploitation of this new expressive capability, the empirical work related to this thesis spanned the creation of three entirely new robot platforms (more on design below), and the synthesis of eight gaits on them (Chapter 4).

Robustness Due largely to the diversity (and immaturity) of these platforms, we prioritize *generalizability, transferability, and robustness to plant modeling errors* (since in real world applications, the robots’ dynamical and kinematic parameters will be changing dramatically from task to task and it is impractical to imagine fielding precisely calibrated controllers). We provide detailed numerical characterization of this kind of robustness in the context of a vertically hopping biped in Sec. 3.5.6.

Granularity As we come to rely more heavily on robotic machines, it is concerning that the failure modes of monolithic optimal or learned controllers offer few clues to the designer about how to repair or reuse them. Conversely, the “behaviorally granular” composition construction we suggest reveals *debuggable and potentially swappable modules*; we provide a suggestion of an environment-dependent swap in Sec. 4.1.

⁶As articulated in other work by the author Carlson and Doyle (2002), a complex system will generically be robust to large perturbations in its components or modules (the wide ends of the bow-tie), but highly sensitive to perturbations at their interface (the neck of the bow-tie). This motivates a formal study of these interfaces and a scientific process for defining and manipulating them, which we have pursued in the context of legged locomotion in this thesis.

1.1.2 The Need for High-Bandwidth Electromechanical Systems

Why are robots so much worse than animals?

Encouraged though we are with our progress on dynamic locomotion so far, we are constantly aware of how far the robots lag the animals that helped inspire their designs. At interdisciplinary meetings, engineers will often express our puzzlement about this topic: our actuators have higher power and force density (when appropriately geared) than muscle does (modulo scaling and packaging), we can make materials that are lighter and stronger, our robots don't need to perform nearly as many functions, but they still lag in sheer performance (jumping height, running speed, etc.). Even more shockingly, our robots can poll sensors and change actuator signals several thousand times per second, whereas animals typically face delays in the order of tens to hundreds of milliseconds in their sensorimotor loops.

In this thesis, we hypothesize that the animals' success is in part due to *their large libraries of known primitives* (manifesting perhaps as synergies [Bernstein \(1967\)](#)), together with the ability to re-use and re-combine them. In Sec. 1.1.1 we introduced a programming paradigm that emphasizes the same requirement for our robots. Our hope is that a compositional view of control design as outlined above will kick off a structured and profitable exploration of useful primitives.

However, there is an additional requirement for robot hardware components that allow for on-the-fly embedding of these primitives. Perhaps counter-intuitively, this a strong departure from biomimetic design: over time, animals have fine-tuned their control strategies, and indeed successfully distributed the control effort over their hardware (muscles, tendons, ligaments, ...) as well as their software (reflexes, neural feedback pathways, ...). In fact, in many of the configurations we study, the animals' robust gait stability can be formally attributed largely (and sometimes entirely) to natural stabilizing forces arising from intrinsic body morphology that have been termed *preflexes*⁷ in the biomechanics literature to distinguish them from feedback (*reflex*) endowed stability.

In contrast, even just in the context of robotic actuators, our creations cannot exhibit a continuum of variable and active-tuned impedance profiles as animals can. The only remaining option is for robot designers to instead pursue a systems-level design that enables accurate programming of feedback control laws into digital computers contained on the robots. This includes *sensory, computing, communications, actuation, and transmission design for high bandwidth* sensorimotor loops, for which we scrutinized the designs of robot components (Chapter 2), though much work remains to be done:

Sensing [Kenneally and Koditschek \(2017\)](#) are presently working on fundamental limits on the energy/information tradeoff in proprioception, so that we may have a good understanding of rate limitations in one of the “fastest” sensing modalities our robots have.

Computation, communication, and drive electronics In the process of selecting new electronics for our robots, we designed an entirely custom new system since commercial off-the-shelf motor controllers with sufficient power, force-control bandwidth, and ease-of-adoption were not available. Additionally, usable models for these components do not exist, and much work must be done in this space to understand fundamental tradeoffs in terms of their contribution to system bandwidth. However, for the most part, electrical subsystems generally have

⁷Stabilizing forces generated through the interaction of the body mechanics with contact forces without any non-zero work output from actuators [Brown and Loeb \(2000\)](#).

time constants that are at least an order of magnitude faster than mechanical signals,⁸ and we are justified in deferring further study of these components for the moment.

Actuation and transmission The electromagnetic motors and the transmission at their outputs can very easily hamper system bandwidth in significant ways, as we described in Kenneally et al. (2016)—motors from “reputable” motor manufacturers such as Maxon are not, in fact, the best ones available based on physically fundamental limits, conventional geared series-elastic transmissions needlessly sacrifice control bandwidth, etc. More work is needed to develop useful models of motors, fundamental rate/energy limits in controlling their torque output, and how their performance scales with various geometric parameters (some of which we begin to describe in Chapter 2), so that we optimally select motors for tasks.

Based on improvements in these and several other areas (including custom design of every component except the motors), we implemented a revised design paradigm following which a family of direct-drive robots was created at UPenn Kenneally et al. (2016), the first of which was the tailed bipedal Jerboa De and Koditschek (2015c), and the second of which was the quadruped Minitaur.

In this thesis, we place emphasis on developing (a) *better models* for these components, incorporating energetic flows and dynamics, but remaining analytical / numerically tractable, to accurately incorporate design constraints such as mass, power, bandwidth, etc.; (b) *better metrics* to allow for guided selection in a high-dimensional design parameter space.

Programmability

The X-RHex platform Galloway et al. (2010b), a descendant of the first outdoor running robot, RHex Saranli et al. (2001), possesses “mechanical intelligence” that hides many of locomotion’s challenges from the user: it is quite capable of running over moderately rough terrain, but neither affords the designer high-fidelity control of the forces it exerts on the world, nor is it able to report back the forces the world exerts on it. It was designed to be driven “open-loop” Saranli et al. (2001), and despite its running prowess, it has been historically difficult to program new behaviors for it Johnson and Koditschek (2013a,b).

In contrast, the robots mentioned in the previous segment proved to be particularly easy to design dynamical gaits for (“program”), beginning from the abstract synthetic principles outlined in the previous section: the first Minitaur prototype Kenneally et al. (2016), Minitaur (2016) went from construction to bounding at 3 body-lengths / second in about one month. While we don’t yet have a formal language for describing why some robots are easier to program than others, we suspect that faithful embedding of template dynamics (as described above) plays an important role.

1.1.3 Commercially Viable Robots Must Be Work-Programmable

As commercial robots begin to proliferate into every aspect of our daily lives, the seemingly short-sighted focus of this thesis on developing algorithms for steady-state locomotion in the plane begs the question: *isn’t locomotion a solved problem?*

The celebrated success stories of robotics to date include (among others) (a) factory floor robots, usually feedforward-programmed to stiffly (ignoring the possibility of unexpected contact forces) and accurately track desired trajectories; (b) the Roomba, a vacuuming robot whose environment is a

⁸For example, even in “slow” electrical systems such as electric motors Maxon Motors (2010).

flat indoor floor; (c) AI systems such as AlphaGo, operating as a disembodied “brain” fed structured input and producing structured outputs; (d) photography drones typically operating in wind-free conditions devoid of unexpected perturbations, etc. A common thread shared by the systems listed above is that they operate in very structured environments, and they perform very specific tasks, somewhat blurring the line between what constitutes a *robot* and a *machine* (a philosophical question we will sidestep in this thesis). A notable exception includes the general-purpose legged machines produced by Boston Dynamics, whose inner workings have now been hidden from the academic community for almost three decades. We observe that their primary focus remains (after three decades) robust locomotion over challenging terrain.

Desired: structural stability, generalizable solutions

We argue that in order to fulfill the promises of robots truly assisting and relieving humans of tasks that are mundane or dangerous, they must be capable of interacting with far less structured working environments. For instance, we are motivated to build agriculture robots that can traverse through miles and miles of crop rows and monitor their health (a mundane task), or exploration robots that search in collapsed mines and disaster areas (a dangerous task). No robots commercially available today can confidently navigate these unstructured areas. We hypothesize that placing emphasis on structurally stable behaviors for robotic systems that reject perturbations from the messy and unknown environment is a fundamental requirement for robots of tomorrow.

Additionally, due in part to the ever-changing environment, and in part to the unforeseen demands of the robot’s user or operator, it is important that we have generalizable solutions. Our robots must be programmed so that they can (perhaps autonomously) generalize what they know to changing environmental, payload, and operating conditions.

1.2 Contributions and Organization

1.2.1 High-Level View of Contributions

Organized by order of impact that we believe the work has to the robotics community, our contributions in this thesis include the following:

- 1) We have developed a family of machines (Chapter 2) and behaviors (Chapter 3) exhibiting dynamic steady-state locomotion that is
 - a) formally shown to be model-insensitive, in the sense that only a crude model of the robot body is required for controller synthesis (Sec. 3.1);
 - b) numerically demonstrated to be robust to parameter perturbations, in the sense that stability survives large variations in design parameters (e.g. Sec. 3.5.6);
 - c) empirically demonstrated to be robust to state perturbations, in the sense that stability survives persistent coupling disturbances introduced due to composition (e.g. Sec. 4.2.4); and
 - d) formally, numerically, and empirically demonstrated to be generalizable, in the sense that component controllers can be re-used across different bodies (Sec. 4.1, 4.2), or across different compositions on the same body (Sec. 4.1.1)

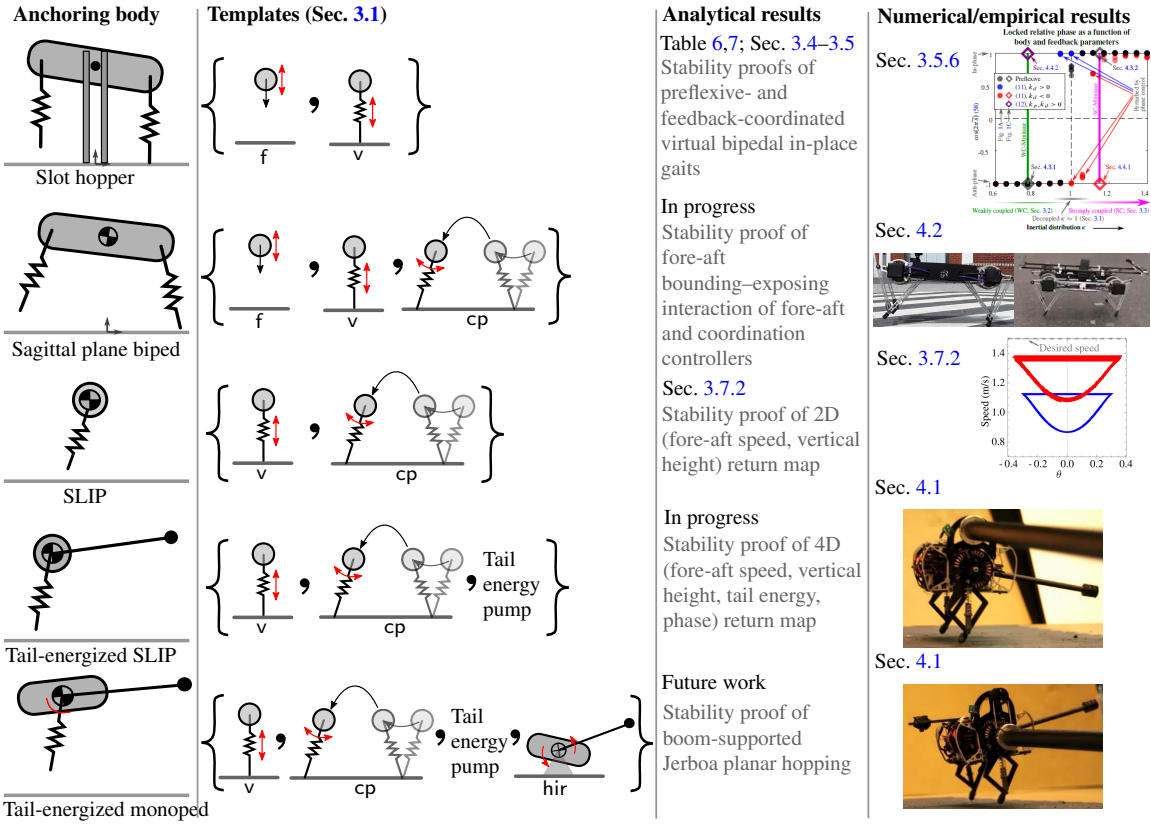


Figure 1: An overview of some of the results presented in this thesis displaying a diversity of anchoring compared to the component templates (Sec. 3.1) utilized for control synthesis. We also list the analytical results as well as the empirical results that either demonstrate the analytical results, or are suggested by them. In addition, in Sec. 4.1.1 we describe an alternate anchoring of the same composition as in the tail-energized monoped. Our quadrupedal physical platform is the [Minitaur \(2016\)](#), and our tailed monoped is the [Penn Jerboa \(Sec. 2.4.3\)](#).

- 2) Keeping in focus the goal of autonomous correct-by-design behavior synthesis from task specification (Sec. 1.1.1), we contribute in this thesis an initial version of a conceptual synthesis procedure using closed-loop components (Chapter 3).⁹ To this end, we have developed a new mode of analysis for 4+ dimensional nonlinear hybrid dynamical systems representative of legged locomotion, which
 - a) enables for the first time¹⁰ (via an “averaged approximation”) a route for closed-form solutions for fixed points, return map stability (Thm. 4), and return map approximation (enabling deadbeat control strategies e.g. Sec. 3.7.2) for a class of coupled non-integrable dynamical systems; and
 - b) is a crucial component for the correct-by-design synthesis procedure (Fig. 40).

⁹The procedure also lays a foundation for autonomous behavior synthesis by suggesting two complementary avenues of future research: composability-constrained controller synthesis (Sec. 5.2.2) and morphological reduction / computation (Sec. 5.2.3).

¹⁰See, for instance, [Holmes \(2005\)](#), for a survey of the challenges of analysis of non-integrable 4+ dimensional systems.

- 3) The combination of abstract and empirical results shown in Fig. 1 illustrates a conceptual advance of the field, by
- suggesting a new¹¹ approximate relation between composed mechanical systems and their dynamical components (Sec. 5.2.5);
 - suggesting a general method of introducing template control strategies for anchor (body) stabilization via principled approximation / simplification (e.g. vertical hopper control for bounding and pronking Sec. 3.4–3.5); and
 - suggesting a prospective means for selection of control *and* design parameters (e.g. analysis-guided mass / inertia restriction in assumption 10), leveraging closed-form stability expressions.

1.2.2 Claims Mapped to Organization

Next we map the high-level claims above into the contents of this document, which are organized in order of logical dependency (hardware design → formal behavior design → empirical extensions).

Design of high-bandwidth legged robot systems (Chapter 2)

Our contributions toward addressing the desiderata in Sec. 1.1.2 include new custom hardware that resulted in dramatically improved specific power¹² in a family of new robots built at Penn, as well as

- simple models for electromagnetic rotary actuators that expose their relevant energetic and thermal properties as a function of their construction parameters, as well as metrics for motor selection (Sec. 2.1);
- gearbox modeling criteria and selection based on a dynamic task specification exposing the dynamic nature of the thermal dissipation problem (Sec. 2.2);
- manipulator design criteria and selection based on traditional manipulability measures as well as some new introductions (Sec. 2.3);
- criteria and metrics for platform design, and application to the design of a 4-actuator tailed bipedal robot (Sec. 2.4).

Correct-by-design compositions (Chapter 3)

In order to implement the synthesis paradigm described in Sec. 1.1.1, we have made the following novel scientific contributions:

- In Sec. 3.2–3.6, we first show how classical averaging (Thm. 1) can be applied to problems of robotics, and also develop novel theoretical results (Thm. 2–4) on the averageability of a large class of coupled mechanical systems arising in legged locomotion.

¹¹Specifically, as a more widely-applicable version of the template/anchor relation Full and Koditschek (1999).

¹²The direct-drive 6 kg Minitaur has a power density of 377 W/kg, and a planned (single-stage geared) 16 kg Minitaur will reach 620 W/kg, compared to 228 W/kg in the 28:1 geared X-RHex Galloway et al. (2010b). DD Minitaur has a continuous force density of 46 N/kg, single-stage 16 kg Minitaur will reach 117 N/kg, compared to 123 N/kg in the 28:1 X-RHex. Bandwidth and transparency, which are both expected to be far superior in the Minitaur robots is more difficult to quantify, but is the topic of work in progress Kenneally and Koditschek (2017).

- Leveraging classical averaging, we propose a new approximate hierarchical relation between composed systems and their constituent templates (linearization of *averaged* return map) as a means of formal design and verification.¹³
- An algorithmic procedure for synthesis (Fig. 40) that provides sufficiency conditions for correctness.¹⁴

We first discuss template dynamical systems, controllers, and appropriate coordinate mappings to “oscillator coordinates” in Sec. 3.1. Then we develop our first single-mode hybrid averaging results for switching and event-selected systems in Sec. 3.2. In Sec. 3.3 we show how to apply our single-mode result to a hybrid system with two modes using a symmetry factoring of the return map.

In Sec. 3.4–3.5 we present an application of hybrid averaging to the hopping and phase regulation of a 2DOF vertically-constrained virtual biped, with or without mechanical coupling between them.

In Sec. 3.6, we leverage time-reversal symmetry (first formally introduced in the legged locomotion setting by [Schwind and Koditschek \(1997\)](#)) to greatly simplify the procedure by which averageable coordinates can be automatically found for a large class of hybrid dynamical systems. In so doing, we show how symmetry properties greatly simplify the averaged dynamics, prominently exposing how “odd” and “even” components affect energy dissipation and phase relations. We use non-conservative 2DOF SLIP (a simple, but non-integrable system which precludes analytical solutions) as an example for our presentation in this section.

Robust empirical robotics (Chapter 4)

As a consequence of the desiderata in Sec. 1.1.3, we have developed control strategies that have successfully been deployed on (among others¹⁵)

- a 2.5 kg planarized tailed biped that hops on the plane using only two actuators (Sec. 4.1) and leaps to heights of 15 cm while hopping;
- a 6 kg quadruped that bounds at 2 m/s (5 body lengths/s), leaps across gaps that are 1.5 body lengths while running, and also pronks, trots, and paces (Sec. 4.2).

The gaits respect our task specification (Sec. 1.1.1) in the sense that appropriate projections of the robot’s hopping trajectories match closely those of the templates, and they are robust (Sec. 1.1.3) in the sense that they persist in the face of mechanical cross-talk arising from adjoining compartments in the physical machine.

In both settings, we explicate, generalize, and extend Raibert’s pioneering work [Raibert et al. \(1989\)](#): in the context of the tailed hopper, we show that compositional control techniques can be applied to a distinctly different morphology than Raibert’s robots, and in the context of the quadruped, we clearly articulate our empirical advances in Table 9.

¹³Some approximation seems imperative since the traditional notion of invariance and dynamical conjugacy [Full and Koditschek \(1999\)](#) seems to fail even for a 2DOF SLIP composition (see our discussion in Sec. 3.8).

¹⁴At present, it is possible for the algorithm to “fail” (with an inconclusive result) before a stability test can be evaluated. If, on the other hand, the stability test is evaluated, instability results can be obtained as well as stability results.

¹⁵We have also successfully deployed identical control strategies for planar hopping on a planarized monopod using 3 actuators (Delta hopper), and used similar techniques to design a feedback-driven walking gait for the quadruped. These results will be reported in future publications and are not in the scope of this thesis.

The empirical work in this chapter is motivated and guided by our analytical results of Chapter 3, even though the resulting deployments are in systems with far higher number of DOFs than the analytical models.

1.3 Related Work

We logically organize this review based on the areas in which our contributions lie:

Design of high-bandwidth legged robot systems

Bandwidth and proprioception It is well known that the introduction of a feedback delay can cause instabilities even in smooth linear systems [Richard \(2003\)](#). A possible alternative to using digital computers to reproduce control signals is to use analog computers in the form of mechanical springs, dampers, and variable impedance [Pratt and Williamson \(1995\)](#) into which our desired impedance controllers are programmed at design-time. However, this approach leads to a lack of run-time versatility. Animals can stiffen their leg springs when they run faster [Arampatzis et al. \(1999\)](#); using fixed mechanical compliance hampers our robots' ability to do the same.

In Chapter 2, we also pay particular attention to proprioception as a sensing modality. There are several advantages to relying on proprioception: it is *free* in the sense that no additional hardware components are required, it is *fast* in the sense that the signal processing is all analog and performed within the mechanical transmission and motor control hardware already present on the system—no additional digital processing of the signal is required.¹⁶ We find that improving bandwidth simultaneously improves the quality of proprioceptive sensing, for reasons that are still being uncovered by ongoing research [Kenneally and Koditschek \(2017\)](#).

The presence of accurate high-bandwidth signal flows and “clean” proprioceptive signals together encourage the implementation of feedback controllers on our hardware. As discussed in [Kuo \(2002\)](#), the potential applicability of feedback (vs. feedforward) is enhanced by an improvement in the quality of the sensory signals, and consequently, the application of feedback (as described in the Introduction) enables better rejection of external disturbances.

Component selection Choosing the appropriate motors for an autonomous legged robot (Sec. 2.1) poses challenges not typically faced by designers in other domains of mechatronics and electromechanical automation. The highly varied and fundamentally intermittent nature of a running, climbing, or crawling machine’s interactions with its environment combined with the severe limitations of contemporary actuator power density present a narrowly constrained set of design choices, whose constraints are at the same time very hard to characterize. Currently, many designers rely heavily on empirical trial and error; many versions of a robot are built with iteratively better motor/gearbox choices.¹⁷ Another method is to pick a single speed/torque operating point and find a motor that

¹⁶We contrast this with (for instance) computer vision, which may require a large amount of digital processing, inducing its own inherent delays and uncertainties.

¹⁷This design procedure was required for all the usefully working machines whose development we are familiar with—EduBot, RiSE, DynoClimber [Clark et al. \(2007\)](#), and most recently X-RHex [Galloway et al. \(2010b\)](#)—and we strongly suspect, most of the legged robots that have demonstrated capable locomotion in unstructured, outdoor environments

can achieve this at continuous steady-state operation [Kafader \(2006\)](#). Other, more considered approaches to motor sizing employ dynamical simulations of the robot in question [Clark et al. \(2007\)](#), [Gregorio et al. \(1997\)](#), [Poulakakis et al. \(2004\)](#), whereby a significant component of the empirical “generate and test” cycle can be iterated in software. In this work we are motivated to develop a still-more rational approach to motor sizing, attempting to develop mathematically generated (hence, *a priori* formally guaranteed) guidelines while enforcing constraints that arise from the interaction of motor dynamics and thermal behavior with the task assigned to the robot.

Rational selection of robot motors and gearboxes has traditionally been driven by industrial applications, in which a task typically consists of a known target trajectory [Potkonjak \(1989\)](#) (eg. a robotic arm in an assembly line lifts and precisely maneuvers a specified part) accomplished by an amply-sized actuator. However, in the realm of mobile, legged robots, motor capabilities (and damage/failure conditions) and robot behavior (leg trajectories) can not be so neatly divorced. Hence, we address two coupled problems: the representation of a motor operating regime, and a model of the thermal consequences of that operational mode.

The motor selection methodology explored in Sec. 2.2 is motivated by the experience of iterative motor selection for X-RHex [Galloway et al. \(2010b\)](#) and operating-point-based selection for its predecessors. Specifically, coupling the electromechanical to the thermal models, we outline a design methodology that selects the best performance from our actuator while avoiding thermal damage (including selection of the optimal gear ratio). We run numerical simulations over the space of commercially available motors and demonstrate how our algorithm produces results notably different from conventional motor sizing methods that typically either ignore thermal considerations entirely or impose overly conservative current limits based upon the permissible ceiling associated with continuous steady state operation.

Platform design Our family of direct-drive robots (Sec. 2.4), and indeed our ideas and contributions on design were inspired by work that spans several decades, and we list them in roughly chronological order:

Raibert’s Leg Lab machines: dynamic legged locomotion Dynamic legged robots first came into being in Raibert’s Leg Lab. He used a very specialized hardware setup including (a) an offboard power source giving his machines essentially unlimited power density¹⁸, and (b) custom high-speed hydraulic valves unavailable to other practitioners, which both contributed to his Leg Lab robots not transitioning “outside.” [Koditschek and Buehler \(1991\)](#) took the analytical route to understand what Raibert was doing empirically, but also realized that a bouncing pogo stick has deep connections to a bouncing ball [Buehler et al. \(1989\)](#), [Rizzi and Koditschek \(1994\)](#).

Buehler’s machines: the importance of specific power Martin Buehler is attributed with the realization that *specific power* is indeed a scarce resource [Gregorio et al. \(1997\)](#), and he subsequently went on to design SCOUT [Buehler et al. \(1998\)](#) a severely underactuated 3D quadruped with just a single joint per leg. Despite difficulties in control and lack of versatility, SCOUT demonstrated dynamic locomotion while being completely power-autonomous. Based on similar principles (single joint per leg), and incorporation of a “sprawled posture,” RHex was born in 1998 and went on to become the first legged robot to run at high speeds

¹⁸Necessary for the implementation of the discontinuous “thrust at bottom” hopping energization strategy ([Raibert, 1986](#), Chapter 2).

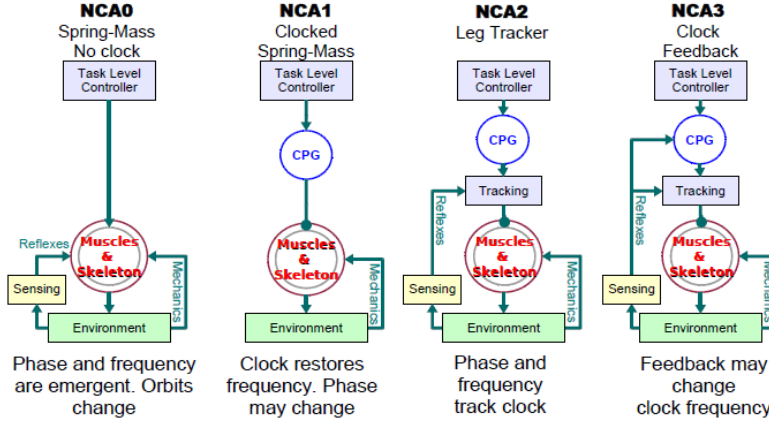


Figure 2: Hypotheses about neuromechanical control architectures from (Revzen et al., 2009, Fig. 3). The work presented in this thesis falls on the far left NCA0 category, and in some respects is even further simplified (more reactive) than NCA0 (see the “control modules in biology” paragraph below).

outdoors. Unfortunately, while RHex Galloway et al. (2010a) is very good at exerting forces on the world, it is not good perceiving forces. Secondly, the compliant legs (essential for running with RHex) also drastically reduce the available control bandwidth.

Asada’s direct-drive manipulators Asada and Youcef-Toumi (1987) lays out a number of reasons that direct-drive is beneficial in the context of a direct-drive manipulator, though we must add many constraints related to the mass, force and power limits of the mobile base in our application domain.

Haptic devices Transparency (ability to perceive end-effector forces at the base of the robot) is fundamentally important in haptics for user engagement; we are inspired by work on haptic devices such as the Salisbury hand Salisbury and Roth (1983), and consider its relevance to the legged application domain. Cable drive systems, a popular choice in haptic systems, have the drawback of needing precise and frequent calibration Park et al. (2011).

MIT Cheetah: “proprioceptive” actuator design The design principles of the MIT Cheetah Seok et al. (2012) influence many aspects of our own designs. The authors emphasize the need for good actuator transparency, and also develop useful models to predict how to get it. In addition, Wensing et al. (2017) characterize proprioception and bandwidth based on new models in the context of legged locomotion and show that the low-reduction drivetrain has superior performance on both counts.

Correct-by-design compositions

Raibert’s empirical compositions Raibert (1986) first demonstrated dynamic legged locomotion using systematic compositions of simple one degree of freedom (DOF) feedback controllers (and no feedforward signals). He further generalized the same technique to work on a planar monoped, spatial monoped, spatial biped, and a spatial quadruped Raibert et al. (1989). From the perspective of control architecture and experimental practice, our work is arguably most inspired by Raibert, and we have included a careful comparison of specific aspects of our control strategies to

Raibert's where applicable in the following chapters (e.g. Table 9 for our quadruped work).

However, Raibert's robots were plugged into the wall and had unlimited available power (untenable for aspiring mobile robots), very specific (advantageous) morphologies, and his work left open a number of intriguing research questions were inspired by Raibert's work, some of which we attempt to answer in this research. We provide a few examples below:

- *Can we use these control strategies on other morphologies?* We demonstrate tailed planar hopping with an extension of Raibert's planar hopper controllers in Sec. 4.1.
- *Can we compose other component controllers?* We demonstrate the application of new coordination controllers to Raibert's quadruped control ideas in Sec. 4.2.
- *What is the relative importance of various design parameters¹⁹ in the stability of the composition?* We have shown formally for the first time why Raibert's quadruped coordinated its legs to bound without any coordination control, as well as the relation of morphology to this coordination (Sec. 3.5).
- *Can we predict how close the composed limit cycle will be to the product of the commanded limit sets in each of the components?*²⁰ Our analytical results show formally why the composed limit cycle is not coincident with the templates' (Sec. 3.2), as well as show how to develop a far superior approximation for it (Sec. 3.7.2),

Control architectures in biology While we don't make any contributions to biology in this thesis, we take inspiration from research in this area about how locomotion is synthesized in animals. Biology points out that animals of even low levels of complexity such as invertebrate swimmers [Gazzola et al. \(2015\)](#) exhibit very low-level rhythmic locomotor behaviors. In animals, these cyclic motions have variously been attributed to central pattern generator (CPG) circuits, or to distal coupled oscillator circuits. In this thesis, we explore how these cyclic patterns may be generated by distal circuits (in the form of template dynamical systems), using feedback instead of feedforward control (e.g. for quadruped gait control in Sec. 4.2).

We find it effective to contextualize our outlook on control architecture in the terms of some prior work:

Fig. 2 from [Revzen et al. \(2009\)](#) describes a few model “control architectures” with successively greater “neural” involvement. The algorithms developed in this thesis fall to the extreme left (NCA0) of this diagram, with no clock signal. In some instances, our algorithms pare down this architecture further and forgo the need for sensing and reflexes—closed loops are instantiated with our control strategies completely reactively, with no additionally introduced states.²¹

Fig. 3 from [Klavins et al. \(2002\)](#) pictorially depicts an example structure of an oscillator-driven legged system: notice that there is no external clock signal input to the structure. Legs one and two generate their own oscillatory limit cycle (we design our own hopping controllers in a similar fash-

¹⁹Together with Ben Brown, Raibert designed his early robots very carefully. As we progress with our work, we find that their specific morphology made a large contribution in the closed-loop system behavior. For instance, the presence of a “balance beam” on the planar hopper [Raibert \(1986\)](#) ensured that the leg inertia was negligible compared to the body's, resulting in minimal perturbation to the body attitude when the leg was swung in aerial phase.

²⁰[Raibert \(1986\)](#) noted that the attained fore-aft speed and height in his planar hopper did not quite match their commanded setpoints, though the resulting behavior was stable.

²¹This is in contrast to additional states being introduced that live on the various green arrows in the NCA0; for instance additional memory for storing computational results about the sensed environment, before generating motion plans in the form of actuator outputs.

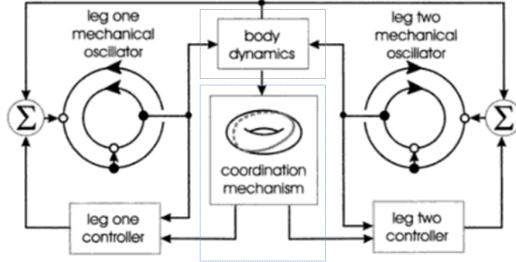


Figure 3: Block-diagram architecture of a feedback-driven biped from the BBR model in [Klavins et al. \(2002\)](#). Our work in this thesis uses similar CPG-less strategies for generating periodic gaits, relying on analytically understood body dynamics (preflexes) or feedback coordination strategies as required to couple various oscillators.

ion in Sec. 3.1), and these oscillators interact with the physical embodiment on one hand (“body dynamics”), and the neural controllers on the other (“coordination mechanism”). We show in Sec. 3.5 how coordination may arise without a coordination mechanism block, and only from the body mechanics. [Klavins et al. \(2002\)](#) numerically studied the coordination of two separate “bipedal” models using both feedforward (“central pattern generator, or CPG”) and feedback schemes, finding that the feedback-generated oscillators were more robust to environmental uncertainty. Motivated by these results, we pursue feedback-only coordination here, and show analytically the stability of the resulting limit cycles with desired phase relations. As articulated by [Kuo \(2002\)](#), the quality of sensory signals on one hand, and the presence of external disturbances on the other, affect if the robot should rely on feedforward or feedback control strategies. Anecdotally, we have found our feedback-controlled gaits to be quite robust to perturbations of various forms²² (Chapter 4) using body designs that provide adequate bandwidth and transparency (Chapter 2).

In many biological creatures, studies have identified the presence of synergies [Bernstein \(1967\)](#), or patterns of muscle co-activation which serve a dimension-reduction-like function in the coordination of our complex bodies. We are motivated to consider these synergies the biological equivalents of our templates; stabilized (in biology) using neural activation patterns working together with a complex musculoskeletal system, or (in our robots) using feedback control laws. This connection provides us with a biological inspiration for new templates to embed in our robots (extending our current list in Sec. 3.1), and also suggests future exploration of the biological processes underlying the composition of synergies.

Our quadrupedal control strategies are also inspired by biology: almost all biological quadrupeds exhibit one or more effectively bipedal gaits wherein the legs are coordinated into two pairs that seem to operate in synchrony [Biewener \(2003\)](#). Inspired by this phenomenon, engineers have formulated the concept of a *virtual leg* [Raibert \(1986\)](#), [Sutherland and Carlson \(1983\)](#), whereby groups of legs are “coordinated” such that the forces they exert on the body are equivalent to those that would have been exerted by a single virtual leg. The details of this coordination vary by implementation (ours is detailed in Chapter 4), but the goal is that the dynamical behavior of the physical legs collapse down from their full state to a lower dimensional subspace well-represented by a single-leg system, i.e. that the physical legs *anchor* a monoped *template* in the terminology of [Full and](#)

²²in the form of coupling forces from composition, model parameter variation, large external forces, etc.

Koditschek (1999).

Multilegged coordination in legged systems Coordination of multiple limbs in legged systems is one of our most important application areas for compositional ideas. As discussed in the preceding “biology” section, it is appealing to pursue the implications of control “modules”²³ being located at the limb-level, in which case the limb coordination problem is related problem of composition of limb control modules (the topic of our Sec. 3.4–3.5).

Past work in this area has modeled the legs as abstract oscillators. This point-of-view permits ready formulation of gait coordination in terms of the oscillators’ relative phases, as in Golubitsky et al. (1998). The work of Klavins et al. (2000) additionally shows how to construct these phase dynamics from some simple Hamiltonian mechanical systems, but that approach is more difficult to extend to non-Hamiltonian coupled dynamics required for implementation on the physical mechanisms that we consider here. Proctor et al. (2010) shows how to use dynamical averaging to simplify the analysis of a network of coupled (identical) neurons, and we propose a generalization to non-identical oscillators (necessary for our application domain) in Sec. 3.6.

Researchers in robotics have numerically studied coordination on simplified models of quadrupedal behavior: the pair of papers Poulakakis (2005) and Poulakakis (2006) study bounding on Scout II: an underactuated quadruped with fixed shank compliance and a single rotary actuator at each hip. Shahbazi and Lopes (2016) introduced a “Dual-SLIP” model of informationally-coupled, mechanically-decoupled hoppers, and showed numerically that it was possible to coordinate them into pronking and bounding limit cycles by directly specifying the desired touchdown and liftoff times for each hip using a once-per-stride optimized controller. Our modeling paradigm is similar; the analysis in Sec. 3.4 provably attains similar coordination between two (now vertically restricted) hoppers with simple feedback laws. Gan et al. (2016) found periodic orbits in a planar quadrupedal Hamiltonian model by optimizing body parameters, and relying on preflexive coordination.

Prior analytical work Our work is also related to analytical attempts at understanding the behavior of hybrid nonlinear systems pertaining to locomotion. Unfortunately, there seems in applied dynamical systems no procedural way to analyze many 2DOF, and almost any useful 3DOF hybrid dynamical systems representative of locomotion. The work in this thesis is therefore related to previous stability analyses of hybrid oscillators appearing in locomotion (e.g. for a single vertical hopper Koditschek and Buehler (1991)), informationally-coupled, physically-decoupled vertical hoppers Klavins and Koditschek (2002), Klavins et al. (2000), a 2DOF spring-loaded inverted pendulum Ghigliazza et al. (2005), a horizontal-plane 3DOF running model (LLS) Schmitt and Holmes (2000). In each of these cases, only with special “tricks” has it been possible to garner analytical insight into 2DOF coupled mechanical systems (e.g. SLIP Geyer et al. (2005), Schwind and Koditschek (1995), LLS with decoupled heading dynamics Schmitt and Holmes (2000)), and not at all for any systems with ≥ 3 DOF (e.g. LLS with coupled heading dynamics Schmitt and Holmes (2000), bounding model in Berkemeier (1998)).

Application of our hybrid averaging result (Chapter 3) in these “benchmark problems” in some

²³We use this term informally and without definition; intuitively we relate it to the centralization / distributedness of the control strategy, e.g. the vertical energization controller for preflexive bounding in Sec. 4.2 may be located at the hip (i.e. it is distributed rather than centralized).

cases yields a greater analytical simplification than has been possible before²⁴, and in other cases, makes analytical headway possible when it was not before. For these reasons, our hybrid averaging result makes a contribution to the field of applied dynamical systems as well as to robotics. For classes of non-integrable, coupled, 4+ dimensional vector fields, our perturbation analysis yields a closed-form solution for fixed points, return map stability, as well as return map approximation.

These analytical insights give us useful understanding about the (a) conditions under which our proposed control strategies succeed, (b) indications about conditions under which they will fail to work, and lastly, (c) information about the relation of the control strategy to the morphological parameters of the robot body. In this thesis, we have provided several detailed examples of the benefits of analytical insight.

For instance, [Murphy and Raibert \(1985\)](#) and [Raibert et al. \(1989\)](#) observed preflexive bounding stability in their simulation and physical models; later [Berkemeier \(1998\)](#) provided a restricted explanation of this stability.²⁵ In Sec. 3.5 we are able to (using formal analysis) for the first time (a) explain the mechanism of this preflexive bounding stability, (b) explain a second mechanism for preflexive pronking stability, (c) explain analytically and not anecdotally the relation of the morphological “non-dimensional inertia” parameter to both preflexes, and (d) use our analytical insight to not just exploit but also countermand the preflexive tendencies on our quadrupedal robot to achieve a highly robust gait stabilization feedback paradigm requiring very few tuning parameters (see Sec. 3.5 for details).

Modularity in robotics The long-standing field of modular robots has made great strides in the design and construction of robot hardware that can act as component modules [Davey et al. \(2012\)](#), as well as in the development of algorithms that can enable efficient task assignment, reconfiguration, and planning [Sung et al. \(2015\)](#), [Tosun et al. \(2015\)](#). Our contributions in this thesis are focused on *behavioral modularity* (as distinct from hardware modularity), and specifically we list the following distinctions in our motivations and approach:

Heterogeneity of modules Many modular robot algorithms typically assume that the components are interchangeable (e.g. [Sung et al. \(2015\)](#)), while in our area of interest these behavioral components are usually²⁶ distinct (e.g. control of hopping in three parts [Raibert \(1986\)](#)).

Complexity of interfaces In the context of hardware; connection interfaces can be carefully controlled at design-time. E.g. popular communication interfaces such as USB, Ethernet can be designed into device firmware, forward-compatible for future interconnections with other

²⁴For instance, we show in our analysis that the nonlinear stance dynamics in our vertical hopper (Example 3) can be reduced to an “averaged” continuous dynamics that appears as a phase-independent proportional controller on the energy (3.47). While single-vertical-hopper stability results have been obtained before without averaging (e.g. [Koditschek and Buehler \(1991\)](#)), the more complex latter instance (informationally-coupled vertical hoppers) has heretofore only been analyzed in the context of a simplified integrable stance model ([Klavins and Koditschek, 2002](#), eqn. (20)). Integrable stance dynamics allowed for a discrete return map control strategy ([Klavins and Koditschek, 2002](#), eqn. (26)), but cannot be extended to more general non-integrable dynamical templates such as the so-called Spring-Loaded Inverted Pendulum (SLIP) [Saranguly et al. \(1998\)](#). Hybrid averaging allows us to analyze with relative ease this plant model obviating the need to integrate the time-varying flow and, rather, requiring only examination of its reduced-dimensional, simplified, averaged approximant.

²⁵[Berkemeier \(1998\)](#) computes approximate return maps of in-place bounding and pronking using Raibert’s (piecewise-Hamiltonian) shank energization controller, and an ε -perturbation analysis. However, a full stability analysis for $\varepsilon \neq 0$ was not possible due to analytical intractability.

²⁶Identical modules appear in the relatively limited context of coupled oscillators in locomotion [Golubitsky et al. \(1998\)](#).

devices. However, the same is not true in the context of energy-exchange interfaces [Whitney \(1996\)](#); e.g. adding a mass on top of an actively stabilized acrobot model system [Tedrake \(2009\)](#) would likely cause its control system to fail.

Anchoring In our behavioral context, to ultimately implement our solution, the templates must be embedded²⁷ on a body. While there is much literature on algorithms for synthesizing compositions from a task specification [Tosun et al. \(2015\)](#), there is no common analogue of the embedding constraints imposed by an “anchoring body” in the context of hardware modularity. The synthesis algorithms we develop must therefore consider not just the template libraries and the task, but in addition the body on which the composition is implemented.

Our work is also related to literature on modularity at a systems level. The work of [Slotine \(2003\)](#) proposes contractiveness as a useful property invariant to several composition operations. However, we find that naive contractiveness is too rigid and are unable to demonstrate this property on most of our compositions. A deeper study of contraction in the context of averaged orbits is a topic of future work. Even closer to our application area, [Seyfarth et al. \(2015\)](#) proposes the concept of “locomotor subfunctions” as a behavioral decomposition of human running. The author states “*In order to resolve this issue, it would be extremely helpful if the tangential leg function could be accessed independently from the radial leg function;*” our agenda includes solutions that possess properties exactly such as this (e.g. we demonstrate in Sec. 4.1 independent control of vertical and fore-aft behavior, and in Sec. 4.2 independent control of leg coordination and horizontal plane locomotion in a quadruped).

Robust empirical robotics

Despite our insistence on compositionality and modularity, we must acknowledge recent progress on other approaches to dynamic legged locomotion. Both of the contrasting feedforward / feedback approaches mentioned above in the “control modules” segment appear in empirical quadrupedal demonstrations in the literature. [Righetti and Ijspeert \(2008\)](#) optimize parameters for a CPG whose outputs are used to set the motor control signals. This technique is able to propel some quadrupeds at speeds of 5–7 body lengths/second (see [Fukuoka and Kimura \(2009\)](#) and [Sprowitz et al. \(2013a\)](#), though the latter results are from a 1 kg prototype without onboard power). However, purely open-loop control signals are particularly sensitive to perturbations from the environment [Klavins et al. \(2002\)](#), and also do not provide any analytical affordance since the body dynamics are invisible in the gait design space.

Some researchers eschew the CPG and directly optimize some parameterization of the motor signals: [Shkolnik et al. \(2011\)](#) use pre-planned position trajectories using an offline planning phase for a specific terrain which is assumed known a-priori. [Pusey et al. \(2013\)](#) use timing parameters which are optimized by hand to demonstrate feedforward bounding at a given speed. [Culha and Saranli \(2011\)](#) use an open-loop hip retraction scheme and passive shank to reduce the number of control parameters, add a spine joint for thrust, and numerically optimize gait parameters using a Nelder-Mead optimization step. However, in these purely open-loop implementations, the parameters are sensitive to desired speed, and the stability basin (in the presence of perturbations from external forces or rough terrain) is small.

²⁷“anchored”, in the terminology of [Full and Koditschek \(1999\)](#)

Model-based and optimization methods On the other hand, the noticeable trend in the literature is to utilize so-called “model-based” methods to synthesize controllers. As the name suggests, these methods rely (to varying degrees) on an accurate model of the robot plant (necessitating its precise calibration). A simple family of strategies used frequently in industrial settings is “computed torque” or “inverse dynamics” [Murray et al. \(1994\)](#); however, they are unsuitable for our mobile robots since (a) the robots are underactuated (and thus unable to cancel each component of the natural dynamics); (b) cancellation involves terms that are squared in the joint velocities / body orientation, and thus susceptible to noise in velocity estimates from encoders and IMUs; and (c) cancellation is often energetically wasteful. Other model-based techniques leverage various heuristics to stabilize desirable subsets of the states, e.g. “operational space control” introduced in [Hutter et al. \(2014\)](#).

Significant advances in optimization tools have provided researchers with numerical methods to find control strategies if the task can be formulated as an optimization (see [Wieber et al. \(2016\)](#) for a summary). Optimization has recently surged in popularity in the literature—with the advent of new tools [Tedrake \(2009\)](#) and the simultaneous boom in computing power—resulting in almost-universal preference among competitors in the recent DRC (e.g. [Kuindersma et al. \(2016\)](#)). Either the states and control inputs can be co-optimized, or only the control inputs can be optimized while “simulating” the states forward in time. Unfortunately, solutions from optimization algorithms are difficult to generalize and also tend to be fragile to modeling errors (e.g. [Topping et al. \(2016\)](#)). Explicitly encoding robustness in the problem formulation often makes has large drawbacks in optimality [Bertsimas and Sim \(2004\)](#) as well as solubility. Additionally, very little is known about composing the solutions of optimization problems in order to re-use prior libraries of solutions [Todorov \(2009\)](#). Nonetheless, currently available computing hardware puts us on the verge of real-time model-predictive control (MPC) running on-line on a mobile legged robot. The recent preprint from [Neunert et al. \(2016\)](#) brings MPC to bear on a physical quadruped. These papers are representative of a trend of growing decision-space (and complexity) of optimization methods being applied to gait generation. MPC-like methods alleviate some of the fragility problems of the previously-discussed open-loop strategies as well as some of the infinite horizon optimization strategies, by optimizing online over short horizons.

Why not use deep learning? The success stories of deep learning are pouring in, and so are the commercial and industrial dollars to further its proliferation in our lives. However, learning is notoriously bad at addressing both the desiderata from the end of Sec. 1.1.3: structural stability and generalizable solutions: learned solutions typically cannot be reused if the conditions are different from the training conditions, and robustness must typically be learned by (resource-intensive) training on perturbed / noisy trials.

Additionally, deep learning is generally only effective when the representation is well understood; however there is no consensus on the correct internal structure. Some researchers have considered the control module an isolated brain deciding what actuator signals to apply in direct response to visual inputs [Levine et al. \(2016\)](#). Other attempts have been made instead at hierarchical learning (including intermediate representations between sensors and actuator signals), with the hope that generalizable primitives may be learned at a lower level than end-to-end solutions for more complex tasks, e.g. [Heess et al. \(2016\)](#).

In contrast, the methods we develop in this thesis explicitly prioritize generalizability of solutions.

However, there is also a large opportunity for leveraging some of these very powerful tools once the ideal internal structure (like modules and their interfaces, as described in Sec. 1.1.1) are better understood. For instance, learning, characterizing, and optimizing the primitives seems like a viable step *in conjunction with* using our formal methods to ensure correct composition; we anticipate that such a workflow could result in a far richer array of addressable tasks than we presently can with our hand-crafted templates.

CHAPTER 2 : Design of High-Bandwidth Legged Robots

In the Introduction, we justified our reasoning for the pursuit of high-bandwidth electromechanical hardware, and in this Chapter we detail the progress we have made.

Some hardware features proved to be necessary to the process of synthesizing these behavioral compositions. As shall be demonstrated later, high-bandwidth control of the forces between the robot and the environment are important.

The Direct-Drive (DD) Extremum

Our interest in DD (direct-drive) architecture is motivated by a number of specific benefits first understood in the context of manipulation [Asada and Youcef-Toumi \(1987\)](#). We review how the DD paradigm presents advantages (and disadvantages) in the context of legged locomotion.

- a) **Transparency.** DD actuation benefits robotics applications by avoiding backlash, achieving high mechanical stiffness, and mitigating reflected inertia of the motor and coulomb and viscous friction in the gearbox so that motor dynamics can be more quickly and easily influenced by external forces acting on the leg [Asada and Youcef-Toumi \(1987\)](#).
- b) **Mechanical performance.** Eliminating the gearbox results in improvements in: **mechanical robustness**, since there are no gears to protect from impulses [Hurst \(2008\)](#), [Pratt and Williamson \(1995\)](#); **dynamic isolation of the body**, since it is only coupled to the legs through the motor's air gap and inertially through the motor's bearing; **mechanical efficiency**, since DD machines experience no mechanical losses due to gear reduction whereas standard planetary gearboxes have a maximum efficiency of 60–90%[Maxon Motors \(2010\)](#), and exhibit directional dependency [Wang and Kim \(2015\)](#); and **control methodology** since decreased mechanical complexity exposes Lagrangian dynamics, promoting behavioral strategies relying on torque [Asada and Youcef-Toumi \(1987\)](#), [Seok et al. \(2012\)](#), impedance [Hogan \(1985\)](#), [Raibert \(1986\)](#), and other “natural” (physically robust and mathematically well-founded) control methods [Koditschek and Buehler \(1991\)](#).
- c) **High-bandwidth signal flow.** Removing the gearbox enables advantages in: **sensing**, mitigating low-pass spring dynamics arising in SEA [Pratt and Williamson \(1995\)](#), as well as filter dynamics in feeding back distal force/torque readings [Loughlin et al. \(2007\)](#) (slowing a 3kHz control loop down to 600Hz in the latter case); **actuation**, since avoiding SEA also removes the low-pass filtering of actuation signals [Pratt and Williamson \(1995\)](#); hence **tunable compliance** can be implemented at kHz timescales, the sort of reactivity known to play an important role in animal negotiation of complex terrain [Spence et al. \(2010\)](#).
- d) **Specific power.** Since a gearbox both increases mass and decreases power (because of its associated losses), the peak specific power of DD actuators will be significantly higher than their geared counterparts.

However, this paradigm comes with the following (interrelated) drawbacks as well:

- a) **Efficiency / thermal losses.** Without a gearbox to amplify the output torque and decrease the output speed, DD motors must operate in high-torque, low-speed regimes where Joule heating is significant. Since winding temperature is the most apparent failure mode of a conventional motor, this design constraint is important in ensuring continued operation of the robot. Additionally, the actuators must mostly operate far from both their peak power and peak efficiency, which both occur much closer to no-load speed [Maxon Motors \(2010\)](#). While

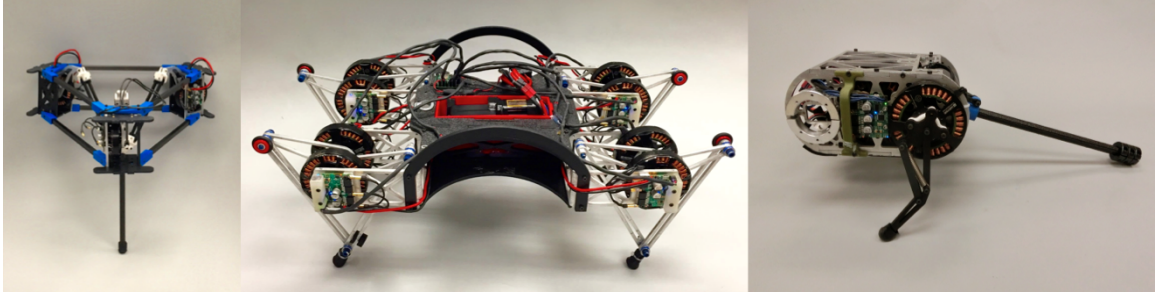


Figure 4: A family of DD robots built at Penn between 2014–2016: Delta Hopper (**left**), Minitaur (**center**), and Jerboa (**right**).

solutions such as active cooling may potentially aid the thermal problem, they fundamentally cannot improve efficiency.

- b) Specific force.* Gear ratios in legged robots are typically in the range of 20:1 to 300:1 [Galloway et al. \(2010b\)](#), [Grimes and Hurst \(2012\)](#), [Hutter et al. \(2013\)](#), [Sprowitz et al. \(2013b\)](#), so by removing the gearbox, mass-specific torque (not power) becomes the first limiting resource in electromagnetically actuated robots [Asada and Youcef-Toumi \(1987\)](#), [Seok et al. \(2012\)](#). Adopting the perspective of locomotion as self-manipulation [Johnson and Koditschek \(2013a\)](#), the force/torque resource becomes even more scarce as the machine’s payload must now include the robot mass itself.

The design problems associated with actuator selection, configuration, recruitment, and leg kinematics must therefore address one central theme, namely how to mitigate the specific force scarcity.

Claims and Organization

In this chapter, we discuss

Better models Analytically / numerically tractable models enable predictive design for motor selection (Sec. 2.1.1), gearbox selection (Sec. 2.2)

Better metrics Leveraging these predictive models, we propose new selection criteria for motors (Sec. 2.1.2), reinterpret metrics for leg design (Sec. 2.3), and develop new insights for platform design (Sec. 2.4.1–2.4.1)

Resulting platforms Putting these ideas together, we describe the new platforms Minitaur [Minitaur \(2016\)](#) and Jerboa (Sec. 2.4.3).

2.1 Motor Selection and Design

2.1.1 Motor Modeling and Fundamentals

In this section, we present simple models that aid in motor selection for legged applications. We first discuss traditionally known motor models, and then present some recent progress made in more helpful models of motors based on their geometry.

Traditional Motor Models

The salient characteristics of a particular motor used in a robot are heavily dependent on the gearbox placed at its output. In this work we want to focus on the intrinsic properties of a motor which affect its performance across operational regimes, so our approach will be to normalize the effect by choosing the best possible gearbox for the motor to perform the task. The author of [Potkonjak \(1989\)](#) investigated the gearbox-independent capabilities of motors for a known output trajectory; we address a similar question for a specific motor and a known dynamical (“task”) model.

A typical motor operating at its nominal voltage operates along a speed-torque curve determined fully by the stall torque τ_s and no-load speed ω_{nl} [Gregorio et al. \(1997\)](#), [Maxon Motors \(2010\)](#). Whereas the corresponding stall torque and no load speed after gearing are both affected by the reduction ratio G , the peak mechanical power,

$$P = \frac{\tau_s \omega_{\text{nl}}}{4}, \quad (2.1)$$

is not.

We now assume that the angular displacement of the output shaft is proportional to vertical displacement of the mass. This is equivalent to the introduction of a rack-and-pinion transmission with selected pinion radius R_p . Our *actuator*, consisting of the motor and two-stage transmission, has a no-load *speed* and stall *force* given by

$$v_{\text{nl}} = \frac{R_p \omega_{\text{nl}}}{G} \quad \text{and} \quad F_s = \frac{4P}{v_{\text{nl}}} \quad (2.2)$$

These parameters define an output speed-force curve, along which the actuator operates.

We will choose (P, v_{nl}) as our motor operating parameterization. Note that the effect of varying the reduction ratio is completely captured in the scalar parameter v_{nl} , and we optimize over all possible values it can take in Section 2.2.2.

Actuator Dynamics Our task involves lifting a mass m (includes motor and payload) vertically. If v is the vertical speed of the mass m , the relationship between vertical speed and upward force on the mass can be written as

$$\frac{v}{v_{\text{nl}}} = 1 - \frac{F}{F_s}, \quad (2.3)$$

since any achievable pair (F, v) lies on the output speed-force line with intercepts at $(F_s, 0)$ and $(0, v_{\text{nl}})$.

Accounting for gravity, the system dynamics are given by $F = m(g + \dot{v})$. Specifically, for the initial condition $v(0) = 0$, we abbreviate the dependence upon the motor parameters by defining $a_1(v_{\text{nl}}) = \frac{4P}{mv_{\text{nl}}} - g$ and $a_2(v_{\text{nl}}) = \frac{4P}{mv_{\text{nl}}^2}$. Using these substitutions, the system’s explicit solution can be written concisely:

$$v(t, v_{\text{nl}}) = \frac{a_1}{a_2} (1 - e^{-a_2 t}), \quad (2.4)$$

Taking the time derivative, $\dot{v}(t, v_{\text{nl}}) = a_1 e^{-a_2 t}$.

Thermal Model For thermal behavior, we use a second order dissipative thermal model excited by the coil current [DeWitt and Incropera \(1996\)](#), [Galloway et al. \(2010b\)](#), [Kafader \(2006\)](#). We are interested in the “thermal current” (which is the heat source as described in [Galloway et al. \(2010b\)](#)),

$$\iota(t, v_{\text{nl}}) = i_m^2 R_{\text{coil}} = \frac{R_{\text{coil}} v_{\text{nl}}^2 F(t, v_{\text{nl}})^2}{K_T^2 \omega_{\text{nl}}^2}, \quad (2.5)$$

where K_T is the torque constant of the motor, $i_m(t)$ is the coil current, and $F(t, v_{\text{nl}})$ is the force applied to the mass. Note that R_P , as defined above, cancels out and does not appear in this equation.

Full Thermal Model The full thermal model can be written in state space as

$$\dot{\rho}(t) = A\rho(t) + B\iota(t) + B_0, \quad (2.6)$$

where $\rho = (\rho_{\text{core}}, \rho_{\text{case}})^T$ are the core and case temperatures,

$$A = \begin{bmatrix} -\frac{1}{R_1 C_1} & \frac{1}{R_1 C_1} \\ \frac{1}{R_1 C_2} & -\frac{1}{C_2} \left(\frac{1}{R_1} + \frac{1}{R_2} \right) \end{bmatrix},$$

$$B = \begin{bmatrix} \frac{1}{C_1} \\ 0 \end{bmatrix}, \quad \text{and} \quad B_0 = \begin{bmatrix} 0 \\ \frac{\rho_{\text{ambient}}}{R_2 C_2} \end{bmatrix},$$

where $R_1 C_1$ and $R_2 C_2$ are the motor’s specified thermal time constants for core and case, respectively.

Considered as linear time invariant control system with input ι and output ρ , system (2.6) admits exact closed form solutions involving a convolution integral that depends upon the specific thermal input profile, $\iota(t)$. We next provide a simplification which allows a qualitative understanding of system behavior without explicit evaluation of this convolution integral for each specific thermal profile $\iota(t)$.

RMS Method For typical motors, (2.6) acts as a low pass filter, attenuating frequencies greater than that specified by the lower system time constant (in this case, the smaller of the two real eigenvalues of A that evaluates to approximately 10^{-2} rad/s for the typical range of motors found in the Maxon catalog [Maxon Motors \(2010\)](#)). For an intermittent input which is periodic in nature the thermal excitation can be re-expressed as a Fourier series, respecting which an aggressive simplification (motivated by this characterization of the thermal plant as a low-pass filter) suggests an approximation based solely upon the DC term,

$$\bar{\iota} = \frac{R_{\text{coil}} \int_0^T (i_m(t))^2 dt}{T}, \quad (2.7)$$

where T is the time period. Note that this is the square of the RMS current, scaled by a constant.

Under these assumptions the equation (2.6) has a constant input, and we can calculate steady state

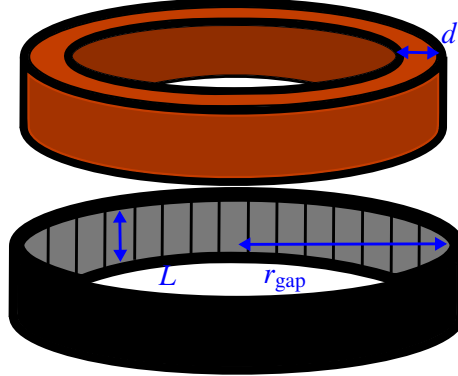


Figure 5: Stator and rotor of a motor showing the critical geometric constants which are related to its performance (shown using our models below).

values by setting $\dot{\rho} = 0$ to obtain the steady-state temperature

$$\Delta \bar{\rho}_{\text{core}}(v_{\text{nl}}) = (R_1 + R_2)\bar{t}, \quad (2.8)$$

where the bar denotes that it is the RMS solution, and the Δ denotes that it is the difference between the core and ambient temperatures.

New Motor Models

In selecting motors for near-DD operation, we are operating close to the edge of physically feasible performance of motors. We rely on the well-known motor constant (torque production per unit heat), which is invariant to details of winding (Prop. 1). However, we can go further and predict limitations on the motor constant arising from the design parameters of the motor (Prop. 2).

Fundamental limits on the motor constant Additionally, we make the following assumption about ideal motor construction

Assumption 1 (Motor construction). *The motor is constructed such that*

- a) *wire volume is a fixed percent of stator volume (aspect ratio of stator teeth is not varied as the motor is scaled)*
- b) *the stator is densely packed*
- c) *motor mass is proportional to stator mass*

We will pay attention to motor construction parameters (shown in Fig. 5), and

L Length of magnets

d Stator thickness

r_{gap} The radius of the air gap (interface between rotor and stator)

B Field strength of permanent magnets; assumed constant¹

n Number of loops of wire in all stator teeth

¹Increasing *B* is indeed beneficial to torque density, but due to physical limitations, increasing *B* by choosing a different magnet grade invariably results in worse temperature-related performance [Temperature and Neodymium Magnets].

R Phase-phase resistance

l Length of wire

ρ Radius of wire

m Motor mass

Proposition 1. *The motor constant Asada and Youcef-Toumi (1987) only depends on the motor dimensions,*

$$K_m^2 \propto r_{\text{gap}} dL. \quad (2.9)$$

Proof. From Asada and Youcef-Toumi (1987), the motor constant is defined as $K_m^2 = K_t^2 / R$. Simple electromagnetic model

$$K_t = n B L r_{\text{gap}} \implies K_m^2 \propto n^2 L^2 r_{\text{gap}}^2 \quad (2.10)$$

We know that the stator volume is $V = 2\pi r_{\text{gap}} dL \propto r_{\text{gap}} dL$. From our assumption about stator aspect ratio, the total wire volume is also $\propto r_{\text{gap}} dL = \pi \rho^2 l$. Thus, the resistance of the wire is $R \propto l / \rho^2 \propto r_{\text{gap}} dL / \rho^4$.

Substituting this into (2.10), we get

$$K_m^2 \propto \frac{n^2 L^2 r_{\text{gap}}^2 \rho^4}{r_{\text{gap}} dL} = \frac{n^2 L r_{\text{gap}} \rho^4}{d}$$

Now, the number of turns of wire can also be estimated from the available wire volume (based on our assumption of dense packing). Thinking about a radial cross-section, $n \propto d / \rho^2$. Substituting above, we get (2.9). \square

Note that (2.9) above captures a very important fact: with the assumptions of ideal motor construction (Assumption 1), the motor constant is only a function of the motor dimensions; specifically, it is invariant to the winding parameters (wire gauge).

Note however, that the torque constant does depend on the winding parameters, and can be used to optimize the distribution of thermal energy between the motors and motor controllers optimally (as we discuss in Sec. 2.1.2).

Proposition 2 (Specific force limitations). *Specific K_m follows the following scale relationships: (a) with fixed length scale, deteriorates with mass scale: $K_m / m \propto m^{-1/2}$, and (b) with fixed mass scale, deteriorates with length scale: $K_m / m \propto l^{-1}$.*

Proof. As shown in the proof of Prop. 1, the volume of wire in the stator is $V \propto r_{\text{gap}} dL$. Since the density of copper wire is constant as the motor is scaled, and by our assumption of motor mass being proportional to stator mass, we get $m \propto r_{\text{gap}} dL$. Together with (2.9), we get

$$K_m^2 \propto m \implies K_m \propto m^{1/2} \implies K_m / m \propto m^{-1/2}. \quad (2.11)$$

Additionally, if the mass is fixed and a lever arm of length l is attached, the specific force is simply the specific torque divided by l , and so we get the second result. \square

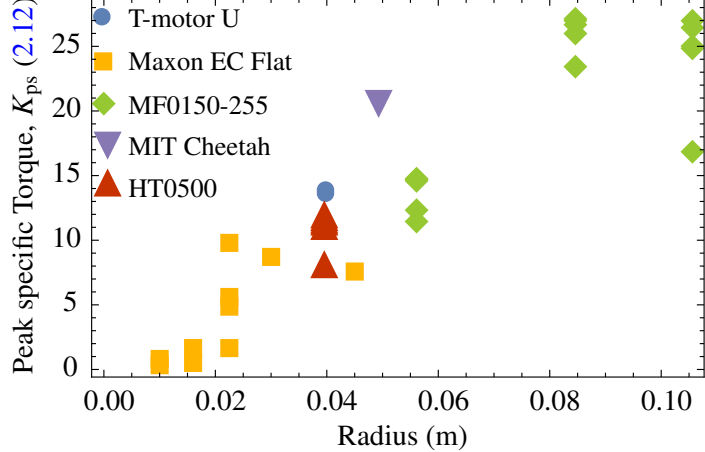


Figure 6: Peak specific torque (limited by flux saturation; affects instantaneous performance) against gap radius for a selection of legged robot actuators.

In the future we will incorporate a model for thermal dissipation based on different sources of cooling (radiation, convection, conduction), which depend on the construction geometry in different ways.

Relation to Drive Electronics We have not yet considered the interaction of the motor with the drive electronics. Let us define the steady-state current capability i_e and voltage V_e of the drive electronics. Our intuitive steady-state goal is to balance the current/voltage passing through the system such that both the motor and the motor controller are operating at their thermal limits (since, if not, there is “room” for additional useful output power to be produced). Work currently in progress is formalizing this intuitive principle.

2.1.2 Quantifying Motor Selection

We first present older results [Kenneally et al. \(2016\)](#) for isolated motor selection (not benefiting from the new modeling results above). At the end we present some newer results on coupled selection of motor parameters with the drive electronics for optimal robot performance.

Motor Selection in Isolation

In the DD family, motors are selected to maximize specific torque at two time scales: **instantaneous performance** (peak specific torque) limited by flux saturation of the motor’s core, and **steady performance** (thermal specific torque) limited by the winding enamel’s maximum temperature.

One of the key motor characteristics that is not easily modeled (Sec. 2.1.1) is the peak specific torque [Seok et al. \(2012\)](#),

$$K_{ps} := \frac{K_t i_p}{m} \quad (\text{in units of } \frac{\text{Nm}}{\text{kg}}), \quad (2.12)$$

where K_t is the motor’s torque constant (Nm/A), i_p the peak current (A) before the core is flux saturated, and m the motor’s mass (kg). The flux saturation effect is highly nonlinear, phase dependent,

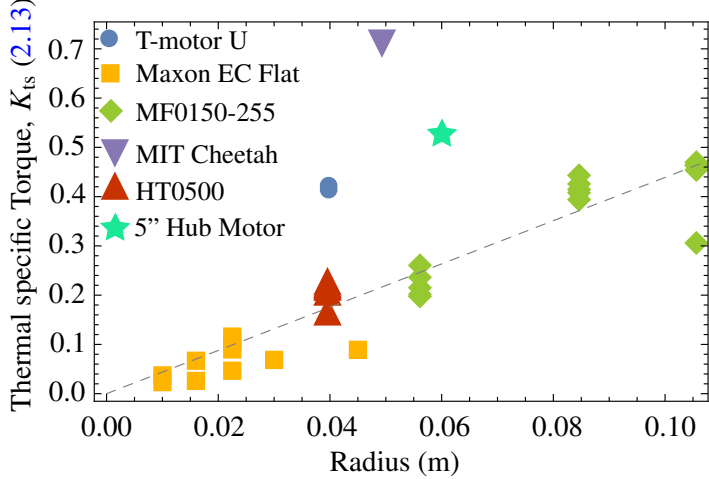


Figure 7: Thermal specific torque (limited by winding temperature; affects steady-state performance) against gap radius for a selection of legged robot actuators. The dashed line indicates the mean of the “inliers.”

and there are not many useful analytically tractable models for it. Our new metric, thermal specific torque,

$$K_{ts} := \frac{K_t}{m} \sqrt{\frac{1}{R_{th}R}}, \quad \text{(in units of } \frac{\text{Nm}}{\text{kg}\sqrt{\text{C}}}\text{)}, \quad (2.13)$$

where R_{th} is the motor’s thermal resistance (in units of $^{\circ}\text{C}/\text{W}$), and R is its electrical resistance (in Ohms), conveys a motor’s desirable ability to produce torque at stall in contrast with its production and dissipation of waste thermal energy caused by Joule heating. Thermal specific torque is similar to the dimensionless motor constant K_m (in units of $\text{N m}/\sqrt{\text{W}}$) [Asada and Youcef-Toumi \(1987\)](#) and is also winding invariant but takes mass and thermal dissipation into account. The incorporation of dissipation makes this metric analytically intractable (beyond Sec. 2.1.1), but heating and cooling curves are relatively simple to determine empirically. As we see in Fig. 7, this measure is generally tied favorably to the motor’s gap radius [Seok et al. \(2012\)](#) resulting in better performance for outrunners (rotor on the outside) compared to inrunners (rotor on the inside), and motors with a large radius to depth ratio [Asada and Youcef-Toumi \(1987\)](#).

Figs. 6 and 7 show plots of K_{ps} and K_{ts} (respectively) against gap radius for a variety of motors, many of which are used in the state of the art machines listed in Table 2, whose motors are specified in footnote 16.

The plot of peak specific force against gap radius, r , in Fig. 6 demonstrates a very strong linear trend (up to differences in framing mass and magnetic permeability of the core). Thermal specific force (Fig. 7) is also quite linear in gap radius, but three important outliers become apparent: the 5" hub motor, T-Motor U series (used in this family of machines) and the custom motors made for the MIT Cheetah [Seok et al. \(2013\)](#).

The new K_{ts} metric (2.13) reveals that electromechanical DD design for legged locomotion entails a degree of “inverse motor sizing,” whereby the robot’s length scale is constrained by the availability of COTS motors with adequately good K_{ts} (such as the outliers noted in Fig. 7) at that scale. That is to say that this is a technological, as opposed to fundamental limitation. Here, the

term ‘adequately good’ is governed by the effect of K_{ts} on the continuous thermally sustainable torque in the a_{mcv} measure detailed in (2.39), which must be positive for the machine to stand indefinitely in the least favorable posture that keeps the toes directly below the hips. Ignoring the three outliers in the K_{ts} plot, a linear fit over the rest of the data gives $K_{ts} = 4.39r$, with a coefficient of determination of 0.895. Using the standard thermal model [Maxon Motors \(2010\)](#), [Rad et al. \(1993\)](#), actuators can incur a core rise of $100^\circ C$ ², and the robot’s design is assumed to achieve an optimistic (Table 2) actuator mass fraction of 40%. Measuring the length of the first link in units of r (gap radius) to cancel the r in the K_{ts} plot, results in $\min(\Gamma_v) = \frac{1}{r}$ (2.35). For the linear fit of most of the motors, $a_{mcv} \geq 0$ implies the first link must be $\leq 1.79r$, whereas the 5” hub motor can be $\leq 3.60r$, for the U8 $\leq 4.34r$ is possible, and for the MIT Cheetah motors, $\leq 6.02r$ can be achieved. In other words, for all these ‘inliers’ (the actuators with aggregate 4.39 slope in Fig. 7), a DD legged platform would be uselessly ‘stubby’ as the majority of the first link length would be consumed by the motor’s radius, resulting in minimal usable toe workspace (see Section 2.3 for more detailed explanation of the workspace of these mechanisms). The MIT Cheetah motors would be very suitable for DD use, but the length scale of the machine would have to decrease significantly compared to the existing Cheetah robot.

2.2 Drivetrain Design: Transparency and Gearbox Selection

From our Prop. 2, we see that scaling up direct-drive is physically impossible. This motivates a study of gearbox selection, which is influenced by several factors:

- a) **Dynamic performance when paired with the motor.** Dynamic task specifications (for hopping, running, etc.) provide crucial information about gearbox sizing beyond steady-state criteria which are common practice in industry. For instance, in Sec. 2.2.2 we show how a very simple repetitive ‘climbing’ task results in a unique optimum (for climbing speed) for gear ratio based on thermal limits [De et al. \(2011\)](#) (see Fig. 9). We have recently begun to use similar task specifications to estimate energetics of quadrupedal gaits, which again seem to point toward an unique optimum (for battery life) for gear ratio.
- b) **Efficiency and friction.** Gearboxes have input/output efficiencies that are difficult to model, and even different properties depending on whether they are doing positive or negative work [Wang and Kim \(2015\)](#). Their geometric properties (tradeoff between friction and backlash) affect robot performance in important ways that we do not (at present) have tractable models for.
- c) **Information rate.** [Kenneally and Koditschek \(2017\)](#) shows that the proprioception capabilities of an actuator (in terms of amount of energy required to get a single bit of information) is highly correlated with the number of gearbox stages, and in order to maximize the signal/noise ratio of proprioceptive sensing, we must carefully consider the gearbox design.

In this section, we first go over some of the considerations that motivate a low gear ratio (Sec. 2.2.1), and then present a numerical study of (ideal) gearbox selection using a dynamic task specification (Sec. 2.2.2).

²This somewhat arbitrary criterion reflects our working practice safety margin with our lab’s various electromagnetic actuators since the windings typically melt around $140^\circ C$

2.2.1 Drivetrain Modeling

A simple linear dynamical model (consisting of static, kinetic, and viscous friction, and the actuator’s reflected inertia), that is invariant to gear ratio, permits a quantitative comparison between DD and conventional geared design. We thus characterize actuation bandwidth, for just as transparency improves proprioception, high bandwidth is necessary for fast closed-loop response. Finally, these relative advantages in our design are contextualized with respect to the family of machines presented in this work.

Transparency measures The reflected inertia of the Maxon EC-45 is reported in [Maxon Motors \(2010\)](#) and then scaled by the gear ratio (23:1 in this case) squared. The T-Motor U8’s rotor inertia is over-estimated by assuming that the full mass of the rotor is located in an annular ring bound by the outer and gap radii. The static friction (“stiction”) of the two actuators is found by attaching 25mm radius pulleys onto the output shafts, and adding mass until there is movement. Using the same pulleys, varying masses are attached and allowed to fall for 2m, accelerating the motors. This time series data is fit to a first-order system and the steady speed is extracted in each trial. This experiment is performed at five different steady speeds for each motor (10-200 rad/s for the U8 and 5-20 rad/s for the EC45) resulting in a strong affine fit (coefficient of determination > 0.995), where the vertical axis intercept and slope are the kinetic (“Coulomb” or “dry”) and viscous (“Rayleigh” or “damping”) friction coefficients, respectively.

In each of the three measures shown in Table 1, the DD actuator (U8) fared significantly better than the conventional geared alternative (EC-45, 23:1), representing a 96x decrease in reflected inertia, 3.89x decrease in static friction, 3.83x decrease in kinetic friction, and 54.6x decrease in viscous drag. This comes at the price of a 2.5x decrease in continuous and a 5.39x decrease in peak specific torque. We leave the larger issues of this tradeoff to the existing analysis in the prior DD robotics literature [Asada and Youcef-Toumi \(1987\)](#) because we believe the cost/benefit relationships are general to the field whereas we are specifically focused here, simply on the achievability of DD design for legged locomotion.

Reflected Inertia Invariance If motors are scaled by varying gap radius, r , then torque $\propto r^2$ and inertia $\propto r^3$, and so torque/inertia $\propto \frac{1}{r}$. If the motors are scaled isometrically, inertia goes $\propto r^4$, and torque $\propto r^3$, so once again torque/inertia is $\propto \frac{1}{r}$. Considering a gearbox with gear ratio G , torque goes $\propto G$, reflected inertia $\propto G^2$, and so torque/inertia $\propto \frac{1}{G}$. In both cases, to increase torque (either by choosing a motor with a larger gap radius, or by increasing the gear ratio) the price in terms of increased reflected inertia is the same, giving no advantage to minimal gear ratio or even DD.

Actuation Bandwidth Actuation bandwidth between the two motors of interest (EC45 23:1, and U8) was explored by connecting the motors to a power supply at 12V, and limited to their thermally sustainable currents representing a 100°C rise in steady state (3.25A and 9A respectively). The motors were then commanded open-loop sinusoidal voltages at various frequencies, and the amplitude of the output shaft of the motor (in revolutions) was recorded. The U8s performed significantly better at this bandwidth measure, rotating on average 17.4x more than the geared EC45’s, as shown in Fig. 8.

Table 1: Comparison of specific conventional and DD actuators.

	EC45-70W, 23:1	U8
Mass (kg)	0.35	0.25
K_v ($\frac{\text{rev}}{\text{V sec}}$)	0.188	1.67
Continuous Torque (Nm)	2.95	0.855
Peak Torque (Nm)	18.86	3.5
Max Continuous Power @ 15V (W)	12.18	35.63
Reflected Inertia ($\text{kg}\cdot\text{m}^2$)	0.0096	0.0001
Static Friction (Nm)	0.218	0.056
Kinetic Friction (Nm)	0.088	0.023
Viscous Friction ($\frac{\text{Nm}}{\text{rad/s}}$)	0.0071	0.00013
Backlash (deg)	0.8	0

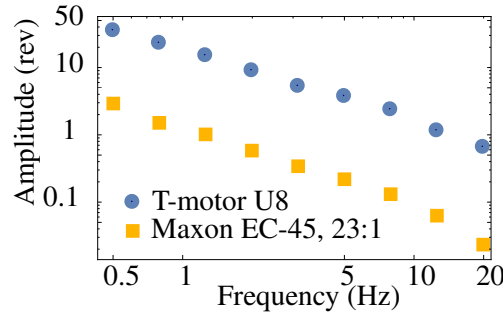


Figure 8: Bode plot of amplitude response of the motor output (in revolutions) to sinusoidal voltage input at various frequencies.

Relevance to Behaviors For the 2–5 kg machines in this family, the duration of stance phase is on the order of 0.1 seconds, corresponding (roughly) to a spring-mass time constant of > 5 Hz for each stance leg. This illustrates the importance of having good actuation performance at the time scales depicted in Figure 8.

2.2.2 Gearbox Selection using a Numerical Dynamic Thermal Model

Problem Statement We apply our thermal-mechanical coupled motor models to a climbing problem by positing a scenario in which the actuator must lift a constant mass vertically against gravity, absent any friction.

We characterize the operating regime by substituting for the traditional library of typical task trajectories a single dynamical model that generates—at least in caricature—the entire family of speed-torque challenges likely to be encountered over the task domain. In this preliminary work we commit to the very specific task domain described above, and limit the design choices to varied control policies in the following manner: the motor can either be running *continuously*, in which mode a constant voltage is applied to the motor terminals, or *intermittently*, wherein the motor switches between operation at a constant voltage and being disconnected from the system (applies no force). The continuous operation mode can be thought of as representing a robot with wheels

rolling up a pole, while the intermittent operation mode corresponds to a legged robot that bounds or leaps upward. Within this very specific task domain, we formally characterize the manner in which legged robots (morphologically constrained to intermittent loading) pose a fundamentally different set of requirements for motor selection than do wheeled robots (in which continuous power delivery is acceptable).

We use a motor thermal model [Galloway et al. \(2010b\)](#), [Kafader \(2006\)](#), [Zocholl \(2007\)](#) to characterize the thermal penalties of task achievement. By seeking optimal performance while satisfying thermal constraints, we can evaluate motors based both on their ability to accomplish a given task while incorporating some view of the performance quality they afford.

Analytical Results

Intermittent Operation Incurs a Thermal Penalty We consider, analytically, the simple, constrained scenario arising from expending a fixed amount of mechanical energy in the shortest possible amount of time. We will prove that a motor operating at a constant velocity introduces less (wasteful) thermal energy than does a motor operating intermittently (with such operations' requisite variation in velocity). Furthermore, this result is true irrespective of the gearbox used with the intermittent motor, as long as the reduction ratio is chosen optimally in the continuous case.

Smoothing actuator power output is intuitively beneficial: thermal energy emitted by the motor coil is proportional to the square of motor torque, while at a given speed, motor power output is linearly dependent on output torque. Intermittent operation requires a motor to operate at slower speeds and higher torques for part of each stride; these higher torques incur a large thermal cost which, as we demonstrate, can not be outweighed by a refractory period.

On the other hand, we approach intermittent operation here with no assumption other than that the motor is disconnected from the mass at some point during task execution. It is not immediately obvious that every possible intermittent control strategy of engagement/disengagement will be thermally inferior to continuous steady-state operation, but we show that this is indeed the case.

We assume that, as is the case for a legged robot, intermittent operation is constrained morphologically (eg. ground contact occurs only periodically), yet, as would be the typical case for a well designed control policy,³ within any given “on” period, we wish to maximize output power and therefore apply constant (maximal) voltage to the motor terminals.

Comparing Cost of Mechanical Work Whereas in Section 2.2.2 we compare the performance (vertical climbing speed) of different motors, in this section (for analytical simplicity) we are comparing the *thermal cost* of equal mechanical work in continuous and intermittent modes of operation for the *same motor*. We will formally show that intermittent operation must result in a higher thermal cost in this setting. As a corollary, if we lift the “equal work” restriction and instead restrict both continuous and intermittent systems to the same peak temperature, the intermittent system must, necessarily, do less work.

³ We are not presuming that all actuation effort is aimed at producing the maximal positive work. For example, animal locomotion typically does not support this presumption since muscles are as often used as “brakes” or “struts” as they are as “motors” [Dickinson et al. \(2000\)](#). We merely presuppose that effort to either oppose or advance the direction of mass motion, once recruited, will typically be as great as possible for its entire duration.

We denote the force exerted on the mass as $F_c(t)$ and its velocity as $v_c(t)$ for the continuous case, and $(F_i(t), v_i(t))$ denote the analogous quantities in intermittent operation.

We assume that $F_c(t) > 0$ for $t \in T$, and the range of T is the maximum time interval of the experiment. We also assume that $F_i(t) > 0$ for $t \in A$ (“active” time interval), where $A \subset T$ strictly. This means that for the time in $T \setminus A$ the motor is switched off (hence intermittent).

Average Thermal Power Output The average thermal power output for continuous operation (for example) is, from (2.7) and (2.3),

$$\frac{R_{\text{coil}} \int_T i_c^2 dt}{|T|} \propto \int_T \tau_c^2 dt \propto \int_T \left(1 - \frac{v_c}{v_{\text{nl},c}}\right)^2 dt$$

where the constants of proportionality are the same in both intermittent and continuous modes, so it suffices to compare them with respect to the rightmost quantity. We are interested in the difference in the average thermal power output between continuous and intermittent operation,

$$D = \int_A \left(1 - \frac{v_i}{v_{\text{nl},i}}\right)^2 dt - \int_T \left(1 - \frac{v_c}{v_{\text{nl},c}}\right)^2 dt \quad (2.14)$$

To compare the thermal effects, we will enforce the condition that the mechanical power output is the same in both modes of operation,

$$\int_A F_i v_i dt = \int_T F_c v_c dt. \quad (2.15)$$

We can write the mass’s dynamics in the intermittent case as

$$\int_T m \dot{v}_i dt = \int_A F_i dt - \int_T mg dt. \quad (2.16)$$

Lemma 1 (Thermal power relation to applied force). *The difference in the average thermal power output between continuous and intermittent operation, D , follows*

$$D = mg|T| \left(\frac{1}{F_{s,i}} - \frac{1}{F_{s,c}} \right). \quad (2.17)$$

Proof. Equal average mechanical power output implies (from 2.15)

$$\int_A F_i v_i dt = \int_T F_c v_c dt. \quad (2.18)$$

For steady state rolling, $F_c = mg$. Suppose the height gained in continual operation is h . Then the right hand side of (2.15) is equal to mgh .

Combining these with the motor kinematics (2.3), we get

$$F_{s,i} \int_A v_i \left(1 - \frac{v_i}{v_{\text{nl},i}}\right) dt = mgh,$$

or

$$\int_A \left(-\frac{v_i}{v_{nl,i}} + \frac{v_i^2}{v_{nl,i}^2} \right) dt = -\frac{mgh}{4P}, \quad (2.19)$$

remembering from (2.1) that $F_{s,i} v_{nl,i} = 4P$ where P is the constant peak motor power (irrespective of gearbox).

The discrepancy in average thermal power output is,

$$\begin{aligned} D &= \int_A \left(1 - \frac{v_i}{v_{nl,i}} \right)^2 dt - \int_T \left(1 - \frac{v_c}{v_{nl,c}} \right)^2 dt \\ &= \int_A \left(1 - \frac{2v_i}{v_{nl,i}} + \frac{v_i^2}{v_{nl,i}^2} \right) dt - \frac{mg}{F_{s,c}} \left(1 - \frac{v_c}{v_{nl,c}} \right) \int_T dt. \end{aligned} \quad (2.20)$$

In the mass dynamics from (2.16),

$$\begin{aligned} \int_T m\dot{v}_i dt &= \int_A F_i dt - \int_T mg dt \\ \implies \int_A F_i dt &= mg|T|. \end{aligned} \quad (2.21)$$

We assumed here that the net change in momentum of the mass over the interval is zero. This will obviously happen if the intermittent motion is periodic and the time interval covers a whole number of periods.

Using this in (2.14),

$$\begin{aligned} D &= \int_A \left(1 - \frac{v_i}{v_{nl,i}} \right) dt - \frac{mgh}{4P} - \left(\frac{mg|T|}{F_{s,c}} - \frac{mg(|T|v_c)}{F_{s,c}v_{nl,c}} \right) \\ &= \int_A \frac{F_i}{F_{s,i}} dt - \frac{mg|T|}{F_{s,c}}, \end{aligned} \quad (2.22)$$

where we used the notation $|T| = \int_T dt$, noted that $|T|v_c = h$, $F_{s,c}v_{nl,c} = 4P$, and used (2.19) above. Now using (2.21), we get (2.17). \square

Lemma 2 (Comparing $F_{s,i}$ and $F_{s,c}$). *The solution of (2.4) is increasing in a first-order manner without overshoot, and is asymptotic to the constant $v_{max}(v_{nl}) = a_1/a_2$. We argue that it must be the case that*

$$\frac{dv_{max}}{dv_{nl}} > 0. \quad (2.23)$$

Proof. The reasoning is that, for continual operation, it must be true that we were thermally limited.⁴ Recall from (2.5) that the RMS thermal constraint gives an *upper bound* on v_{nl} . If (2.23) were not

⁴If continual operation were not thermally limited, we could set our reduction ratio so as to harvest the peak motor power for the whole interval T . In this case, it would be impossible for intermittent operation to match it.

true, in the continual operation case we could get better performance by reducing v_{nl} , which is a contradiction because we assume we are already operating at the optimal v_{nl} . \square

Proposition 3 (Intermittent operation is thermally worse). *With our dynamic task specification, the average power consumed in intermittent operation is higher.*

Proof. Using the Lemmas above, note that one of the following must be true:

- a) If $v_{nl,i} = v_{nl,c}$, \forall finite $t \in T$, $v_i(t) < v_{\max}(v_{nl,i}) = v_{\max}(v_{nl,c}) = v_c(t)$.
- b) If $v_{nl,i} < v_{nl,c}$, using (2.23) we get $v_{\max}(v_{nl,i}) < v_{\max}(v_{nl,c})$. So \forall finite $t \in T$, $v_i(t) < v_{\max}(v_{nl,i}) < v_{\max}(v_{nl,c}) = v_c(t)$.
- c) If $v_{nl,i} > v_{nl,c}$, $v_{\max}(v_{nl,i}) > v_{\max}(v_{nl,c})$, and it is possible that $\exists t \in T$ s.t. $v_i(t) > v_c(t)$.

In situations 1 and 2, it is not possible that $\int_T v_i dt = \int_T v_c dt$, and intermittent performance is worse than continuous performance. Situation 3 is the only feasible one, i.e., the gear ratio must be lower in intermittent operation for the same mechanical power output in both cases.

Intuitively, for both systems to have the same average speed, the intermittent system must travel sometimes faster, and sometimes slower than the continuous system. Its v_{\max} , and thus v_{nl} , must be larger than that of the continuous system.

This means that

$$\frac{F_{s,i}}{F_{s,c}} = \frac{v_{nl,c}}{v_{nl,i}} < 1.$$

We can put this in (2.17) and see that $D > 0$. Intermittent operation necessarily produces more thermal energy. \square

This result represents a *fundamental property* of motors that cannot be affected by changing the reduction ratio or control scheme.⁵ A number of designers have implemented passive energy storage mechanisms [Clark et al. \(2007\)](#), [Clark and Koditschek \(2006\)](#) to allow for higher average motor power output and this analytical result further corroborates that such mechanisms are well motivated from a motor-thermal perspective.

Exposing Innate Motor Properties

Instead of tackling the coupled problems of motor and gearbox selection, the parameterization in 2.1.1 allows us to assess and select a motor independent of choice of gear ratio by determining the optimal reduction for each given motor.

Optimization Without Thermal Constraints The motion equations (2.4) are parameterized by v_{nl} . In order to compare the motors independent of this reduction, we perform a one-dimensional optimization over this parameter.

We will ignore the thermal constraints for this subsection only, and focus on relating our performance metric to fundamental motor parameters.

In continuous operation and in steady state ($F = mg$), (2.4) has the simple solution

$$v_c(v_{nl}) = v_{nl} \left(1 - \frac{mg v_{nl}}{4P} \right), \quad (2.24)$$

⁵“Control scheme” here refers to the policy or rule that controls the on/off switching schedule in intermittent operation.

which is quadratic in v_{nl} and is maximized when $v_{\text{nl}} = \frac{2P}{mg}$.

For intermittent operation we assume periodic operation (motivated by animals), and fix a “stride length” appropriate in dimension to the pinion gear and mass being lifted by the robot, x_r . The task is to achieve the maximum average vertical climbing speed in intermittent operation (see Section 2.2.2 for definition). Note that the scalar parameter v_{nl} can be arbitrarily chosen for any motor by varying the reduction G , and we will refer interchangeably to “varying v_{nl} ” and “varying G ”.

Let us denote the vertical position of the robot, i.e. time integral of the velocity v in (2.4), as $x = s(t, v_{\text{nl}})$, where $s : \mathbb{R}^+ \times \mathbb{R}^+ \rightarrow \mathbb{R}$ is obtained by direct integration as

$$s(t, v_{\text{nl}}) = \frac{a_1}{a_2} \left(t + \frac{1}{a_2} (e^{-a_2 t} - 1) \right).$$

Note that the release time at which the motor temporarily ceases operation, $t_r = \sigma(v_{\text{nl}})$ is defined implicitly by $x_r = s(\sigma(v_{\text{nl}}), v_{\text{nl}})$. It is easy to show via the implicit function theorem that $\sigma(v_{\text{nl}})$ is indeed a function. We numerically find an explicit form of t_r by solving $s(t, v_{\text{nl}}) = x_r$. Let us also define $v_r(v_{\text{nl}}) := v(t_r, v_{\text{nl}})$.

We seek to maximize the average intermittent velocity,

$$v_i(v_{\text{nl}}) = \frac{x_r + \frac{v_r^2}{2g}}{t_r + \frac{v_r}{g}}, \quad (2.25)$$

but unlike before, there is no easy calculus solution. This function is not explicit, but we can numerically find an optimal solution (using eg. interior point methods).

With Thermal Consequences In 2.2.2 we found equations which generate our motor speed-torque trajectories, parameterized by gear ratio G . By using a thermal model for our motor and leveraging our freedom in G , we can dynamically generate trajectories of operation—ensuring thermal constraints are satisfied—based on a more abstract task specification, using our thermal model in the analysis itself.

We use the thermal model formulation of 2.1.1, where $F(t, v_{\text{nl}}) = m\dot{v}(t, v_{\text{nl}})$ in (2.5) is given by the equations of motion in 2.1.1. For continuous operation in steady state, (2.5) and (2.7) give

$$\bar{t}_c(t, v_{\text{nl}}) = \frac{R_{\text{coil}}v_{\text{nl}}^2(mg)^2}{K_T^2\omega_{\text{nl}}^2}, \quad (2.26)$$

while for intermittent operation with stride length x_r as defined above, we get

$$\bar{t}_i = \frac{R_{\text{coil}}v_{\text{nl}}^2m^2}{K_T^2\omega_{\text{nl}}^2(t_r + v_r/g)} \int_0^{t_r} (g + a_1 e^{-a_2 t})^2 dt. \quad (2.27)$$

Using (2.26) or (2.27) in (2.8) we can compute the temperature rise and limit our optimization in Section 2.2.2 to gear ratios that keep the core temperature under acceptable limits.⁶

⁶Note that, intuitively, an arbitrarily large gear ratio will allow any force to be generated with very small motor currents. Thus, there always exists a “feasible” gear ratio.

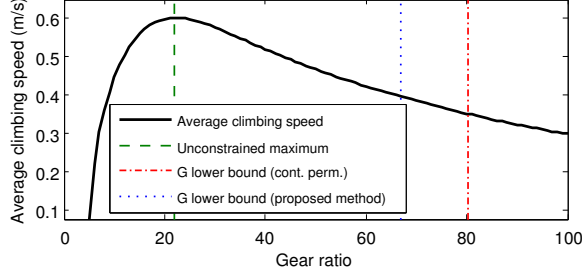


Figure 9: Average climbing speed under periodic intermittent operation as a function of G for Maxon EC45 Flatmotor 251601 [Maxon Motors \(2010\)](#), showing the (lower) bounds on gear ratio imposed by our proposed method, and following the continuously permissible current specification. The black curve here is that obtained from the mass dynamics in 2.2.2, and as such over-estimates the climbing performance obtained when restricting current to i_{cp} .

Simulation Results

In order to test our motor sizing method for use in practice, we performed numerical trials on all of the motors in [Maxon Motors \(2010\)](#). We envision that these simulations will not only enable robot designers to pick out exactly which commercially available motor to use for their robot, but also give feedback about the type of gearbox needed as well as the performance to expect.

Comparing Motor-Sizing Methods A central contribution of this report is the use of a dynamical systems task model that yields a closed form family of trajectories over all possible initial conditions, and, hence, enables motor and gearbox selection over the entire family. Absent this analytically determined design insight, the recourse would be to approximate the “typical” robot speed-torque requirements across a range of “reasonable” example trajectories and iterate through motor/gearbox combinations. Here we assume that the ideas of 2.2.2 are being used, and compare the effect of including the thermal model of 2.2.2 in the design process.

We use our simulation to find the best possible vertical climbing (average) speed that can be obtained by picking the gear ratio (a) without thermal considerations, (b) using the continuously permissible current specification, and (c) with a dynamic thermal model (cf. 2.2.2).

For a specific motor, Fig. 9 demonstrates the nature of the objective function (2.25) as a function of G , as well as the lower bounds imposed by our thermal constraint (cf. 2.2.2), as well as that required to keep motor current under i_{cp} . Note that the latter is more restrictive, while disregarding the constraint entirely gives the best performance (albeit, unacceptably damaging to the motor).

See Fig. 10 for a scatter plot of performance exhibited by the motors in these cases. Note that we have limited the motors displayed to those that can perform the task with a reduction $G \leq 100$. This restricts our results to those motors for which the task parameters (mass and stride length) are roughly appropriate⁷ to the size of the motor.

For our simulations of intermittent operation, we chose the periodic leaping motion defined by fixing a “stride length” as described above.

⁷Situations like (for eg.) a nominal 1W motor attempting to cause a 50kg mass to leap result in extreme gear ratios and/or performance figures that are difficult to represent (owing to plot axis scaling) and physically impractical.

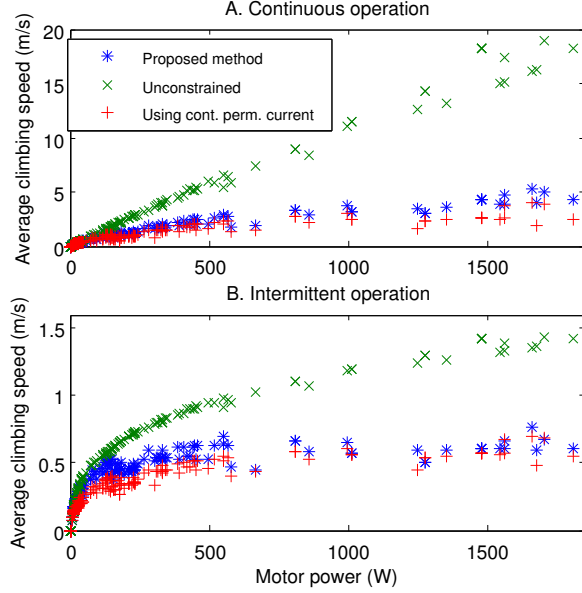


Figure 10: A comparison of the best vertical climbing performance possible picking the gear reduction with the method proposed here, and conventional methods (no thermal constraint, and using continuously permissible current), in continuous (A) and intermittent (B) operation.

We compare our results with those obtained by limiting motor coil current to be under the “continuously permissible current” motor specification, i_{cp} . In continuous operation, motor force $F = mg$, and we need to ensure

$$i_m = \frac{v_{nl}mg}{K_T \omega_{nl}} \leq i_{cp} \implies v_{nl} \leq \frac{i_{cp} K_T \omega_{nl}}{mg}$$

From the result in Fig. 10-A we see that in continuous operation, not considering the thermal effects in the design process [Wollherr et al. \(2002\)](#) allows us to pick a gear ratio which promises very good performance, but would result in thermal damage to the motor.⁸ More interestingly, our method allows us to achieve higher performance than is reachable by restricting motor coil current to values below the continuously permissible current specification of the motor [Clark and Koditschek \(2006\)](#), [Potkonjak \(1989\)](#).

For intermittent operation with a fixed voltage, note that the motor must start from its stall torque (irrespective of the reduction ratio). This means that it is impossible to ensure that the coil current is under the continuously permissible current spec. We chose a slightly less naïve control strategy that uses varying voltage to keep the motor current under i_{cp} . Once the trajectory reaches the highest speed-torque curve (voltage is equal to the maximum supply voltage), we use the same equations as above.

From the performance results displayed in Fig. 10, we note that gearbox selection using a dynamic thermal model (cf. 2.2.2) results in average vertical speed improvement (mean \pm std. dev.)

⁸From the analysis of Section 2.2.2, the blue (*) points correspond to the fastest average speed that can be obtained without overheating the motor core, so all the green (x) points that lie above blue (*) points indicate a gearbox selection that will result in thermal damage.

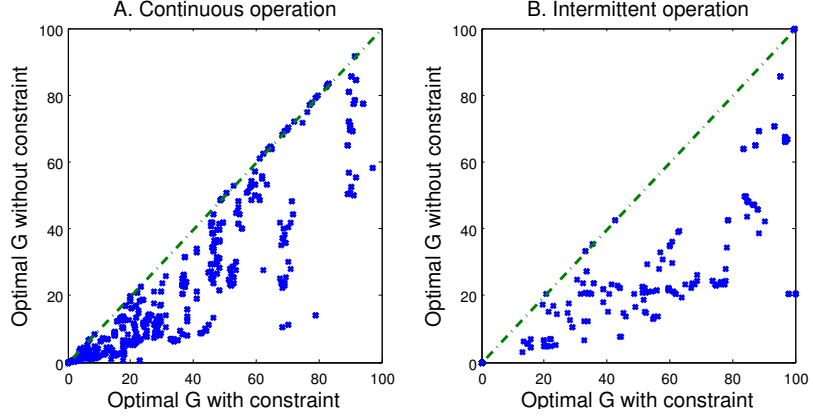


Figure 11: Optimal gear ratios for a subset of the motors, showing how adding the thermal constraints requires a higher reduction. Note that there are fewer motors shown in B as several motors from [Maxon Motors \(2010\)](#) required a much higher gear ratio due to the intermittence penalty described in Section 2.2.2.

of $21.6\% \pm 19.0\%$ (continuous) and $27.7\% \pm 12.3\%$ (intermittent) when compared to restricting coil current to i_{cp} . The maximum improvement seen in intermittent operation was 57.6%. Thus, by explicitly considering thermal behavior instead of simply restricting current to continuously permissible levels, we achieved notably better performance and correspondingly, higher average motor power outputs.

The additional performance improvements from our optimization in the intermittent case are attributable to taking advantage of the short “refractory periods.” While the torque-restricted climber is limited to its continuously permissible current at all times, our thermal model permits us to select a gearbox with the expectation of exceeding the continuously acceptable current and then “resting.” These benefits would undoubtedly be amplified were we to consider thermal constraints over a task with a finite completion time (eg. a specified number of strides), as the thermally optimal behavior would expend a “thermal budget” over the duration of the task, an effect not seen here due to the infinite task timeline.

Thermal Considerations and Gearbox Selection In Fig. 11, we see the effect our thermal constraint has on the selection of v_{nl} , and thus G . Adding thermal considerations necessitates choosing a higher G in order to keep motor torque (and current) lower for the same output torque. Thus, all data points are to the right of the 45° -line in both parts of Fig. 11. Intermittent operation carries an inherent thermal “penalty” (see Section 2.2.2), resulting in a further rightward shift of the data points from Fig. 11-A to Fig. 11-B.

We envision that information similar to what is presented above will be useful to the designer for (a) the identification of motors which can fulfil a given task without needing to recourse to a physically unreasonable gear ratio, and (b) gearbox selection for a specific motor.

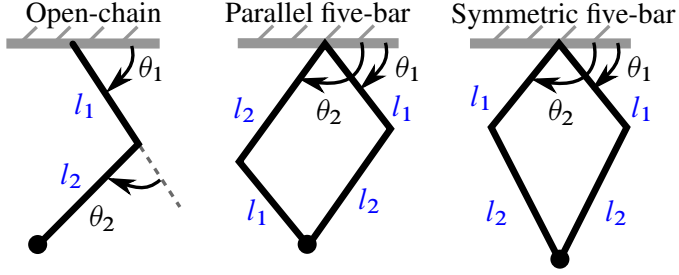


Figure 12: Leg designs considered in Section 2.3.

Conclusion

We have outlined a principled approach (if not an algorithm) to tackle the coupled problems of motor and gearbox selection from both mechanical and thermal dynamic perspectives. In so doing, we introduce a novel concept of task specification and proceed by leveraging optimization, dynamic simulation, and analysis tools. We achieve an analytical result, relevant to any task reasonably well characterized by our simple vertical leaping dynamics, demonstrating the cost of intermittent motor operation. Our result further justifies roboticists’ previous work on the introduction of passive-elastic energy storage to enable more continuous actuator power delivery [Clark et al. \(2007\)](#), [Raibert \(1981\)](#), and gives strong motivation to promote—through mechanical design—an approximately constant motor speed.

To develop and demonstrate our method, we used as an example a 1-DOF vertical climbing robot (with trivial dynamics). Even though this task appears restrictive, it generates motor trajectories across a broad range of regimes in the (fixed-voltage) speed-torque operational plane. Even for applications with strikingly different requirements, a computation such as outlined above can be used to determine the set of motor characteristics that play a similarly crucial role in affecting the execution quality of that task, as well as enable the development of motor-gearbox selection aids akin to Figs. 10-11.

2.3 Actuator Recruitment via Leg Design

2.3.1 Leg Design Preliminaries

The legs of our DD robot family vary in the number of actuated DOF from one to three, and the legs of the two machines with multiply actuated DOF (Minitaur, Delta Hopper) incorporate closed kinematic chains (linkages). Because of the simpler kinematics, the 2-DOF case is analyzed in detail, comparing a serial chain of two revolute joints, (2.28), (denoted by “O”), a parallelogram five-bar, (2.29), (a linkage frequently used in DD robot arms [Asada and Youcef-Toumi \(1987\)](#), denoted by “P”), and a the symmetric five-bar, (2.30), used in the Minitaur robot (denoted by “S”). The Delta Hopper machine uses the 3-DOF generalization of the 2-DOF symmetric five-bar employed in Minitaur⁹. The Jerboa, however, cannot benefit from such analysis of parallel linkages as it has

⁹The linkage in Minitaur consists of two RR chains closing at the toe, while the Delta Hopper linkage has three RR chains that close at the toe. Assuming the same choice of link lengths, the leg kinematics in the two machines are very similar, except that the Delta Hopper’s workspace is cut off at either extreme end of extension because the actuators

only has 1-DOF/leg¹⁰.

Given joint angles $q := (\theta_1, \theta_2) \in T^2$ (see Fig. 12), the forward kinematics for the three candidate leg designs are

$$g_O(q) = \text{Rot}(\theta_1) \begin{bmatrix} l_2 \cos \theta_2 \\ l_1 + l_2 \sin \theta_2 \end{bmatrix}, \quad (2.28)$$

$$g_P(q) = \text{Rot}(\alpha_1) \left(l_1 \text{Rot}(\alpha_2) e_1 + l_2 \text{Rot}(\alpha_2)^T e_1 \right), \quad (2.29)$$

$$g_S(q) = \text{Rot}(-\alpha_1) \begin{bmatrix} 0 \\ l_1 \cos \alpha_2 + \sqrt{l_2^2 - l_1^2 \sin^2 \alpha_2} \end{bmatrix}, \quad (2.30)$$

where $\text{Rot} : S^1 \rightarrow \text{SO}(2)$ is a rotation matrix, e_i denotes the i^{th} standard basis vector, and the $\alpha_1 := (\theta_1 + \theta_2)/2$, $\alpha_2 := (\theta_1 - \theta_2)/2$ coordinate change (for the parallel designs) enables a helpful factoring of the forward kinematics in each case

Proposition 4 (Invariance of Leg Design Measures to Leg Angle). *The singular values of the Jacobian of (2.31), Dg , are invariant to the leg angle, α_1 .*

Proof. For each of the leg designs, there is a linear change of coordinates $L : T^2 \rightarrow T^2$ from the original joint angles such that if $\alpha = Lq$, then α_1 is the “leg angle,” i.e.

$$g(q) = \tilde{g}(Lq), \quad \tilde{g}(\alpha) = \text{Rot}(\alpha_1)h(\alpha_2). \quad (2.31)$$

For the serial design (2.28), $L_S = I$, and for each of the parallel designs (2.29)–(2.30), $L_P := \frac{1}{2} \begin{bmatrix} 1 & 1 \\ 1 & -1 \end{bmatrix}$. At first, we show that if $L = I$, the proposition holds: Using the chain rule on (2.31),

$$Dg = SRhe_1^T + RDh, \quad (2.32)$$

where we drop the dependencies $\text{Rot}(\alpha_1)$, $h(\alpha_2)$ and $Dh(\alpha_2)$ for brevity, $S := \begin{bmatrix} 0 & -1 \\ 1 & 0 \end{bmatrix}$, and $e_1 := \begin{bmatrix} 1 \\ 0 \end{bmatrix}$. Now, multiplying and simplifying (2.32),

$$Dg^T Dg = Dh^T Dh + e_1 h^T h e_1 + Dh^T S h e_1^T + e_1 h^T S^T Dh,$$

and observe that all dependence on α_1 (in the form of Rot in (2.32)) disappears. Thus, $Dg^T Dg$ is invariant to α_1 .

Lastly, since $DL = L$ is constant, and

$$Dg^T Dg = L^T D\tilde{g}^T D\tilde{g} L, \quad (2.33)$$

the linear coordinate change L does not affect this proposition, and the argument above for $L = I$ carries over directly. \square

cannot be made coaxial.

¹⁰The Jerboa benefits from the two major design principles embodied by (2.13) & (2.39). Its inclusion here further serves the important role of illustrating that the additional advantage conferred by the symmetric linkage - while beneficial as manifest in the superior load bearing capabilities revealed by the a_{mcv} values of Table 3 - is not *necessary* to the success of a DD design.

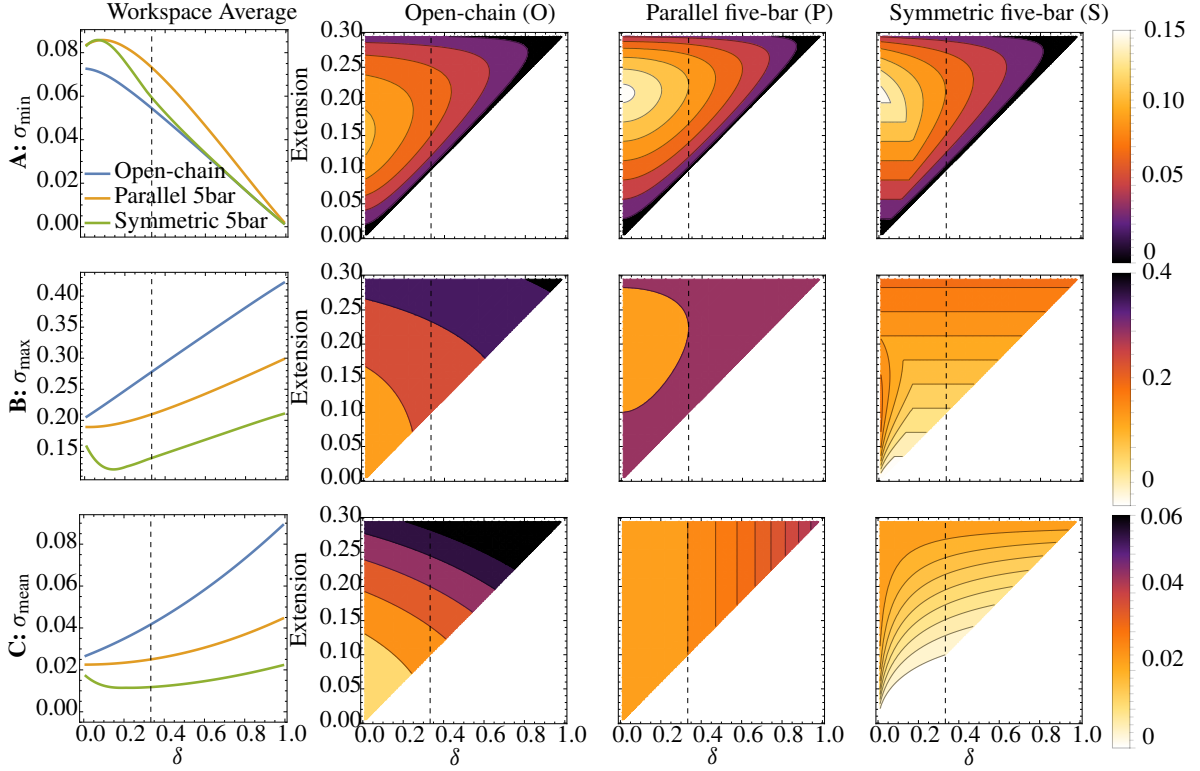


Figure 13: In each of the subfigures (rows) the first column shows the workspace averaged measure of the particular function of singular values, σ , plotted against the ratio of minimal to maximal leg radius, δ . The remaining three columns provide a more detailed view of the particular σ as a function of both δ : higher values yield greater proprioceptive sensitivity. **B:** Leg Jacobian maximum singular values: lower values indicate better minimum force production. **C:** Leg Jacobian mean singular values: lower values indicate smaller thermal cost of producing force. In each figure, the vertical dashed line indicates the linkage used in the Minitaur leg.

Now, if $J := D_q g$ is the Jacobian of the forward kinematics, g , the joint velocities \dot{q} , (Cartesian) toe velocity \dot{p} , joint torques τ , and toe force f satisfy

$$\dot{p} = J \dot{q}, \quad \tau = J^T f. \quad (2.34)$$

Remark 1 (Relation of Measures to Jacobian Singular Values). Let the (ordered) singular values of the square matrix J be $\{\sigma_{\max}, \sigma_{\min}\}$. Observe that

- a) The expression on the left hand side of (2.36) is the Rayleigh quotient for the matrix $J J^T$, which is minimized by its smallest eigenvalue [Horn and Johnson \(1990\)](#). Additionally, J^T and J have the same singular values, and so any measure depending on the singular values of J or of J^T is invariant to leg angle (Prop. 4).
- b) Since the eigenvalues of $(J^T J)^{-1}$ are the reciprocals of eigenvalues of $J^T J$, the singular values of J appear in the denominator of (2.37).
- c) Since $\text{trace}(J J^T) = \text{trace}(J^T J)$, the “thermal cost of force” metric is also independent of leg angle.

2.3.2 Metrics for Leg Design

Additionally, we define the vertical effective mechanical advantage, $\Gamma_v : T^2 \rightarrow \mathbb{R}^2$, as

$$\Gamma_v(q) := [0 \ 1] J(q)^{-T}. \quad (2.35)$$

We compute the singular values of J , σ_i , and then consider standard manipulability measures [Murray et al. \(1994\)](#) for each of the candidate mechanism designs. In each case the workspace is generically an annulus, it is fully defined by r_{\min} (the minimum radius) and r_{\max} (the maximum radius). In each of the following subsections, we have fixed a constant r_{\max} , and plotted a relevant measure over two axes: (a) the design space, $\delta := \frac{r_{\min}}{r_{\max}}$, where $r_{\min} = |l_1 - l_2|$, $r_{\max} = l_1 + l_2$ and

(b) the workspace variable, y representing the radial extension of the leg.¹¹

We propose the following metric

- a) $\sigma_{\min} := \min_i \sigma_i$, **proprioceptive sensitivity**. This measure indicates the minimal speed of the toe in any direction for given motor angular velocities [Murray et al. \(1994\)](#), shown in Fig. 13-A. More importantly in our problem domain, a very small σ_{\min} indicates that some forces at the toe are barely visible to the motor,

$$\min_{\|f\|=1} \tau^T \tau = \min_{\|f\|=1} f^T J J^T f = \sigma_{\min}^2, \quad (2.36)$$

and so higher values of σ_{\min} are favorable (cf. Remark 1a)). From Fig. 13-A, the two parallel mechanisms have better proprioception through a larger portion of their workspace.

- b) $\sigma_{\max} := \max_i \sigma_i$, **force production**. At non-singular configurations, this measure indicates the worst case force at the end effector for bounded motor torque,

$$\min_{\|\tau\|=1} f^T f = \min_{\|\tau\|=1} \tau^T J^{-1} J^{-T} \tau = \frac{1}{\sigma_{\max}^2}. \quad (2.37)$$

(cf. Remark 1b)). Intuitively, this expresses the degree to which an arbitrary external force can be resisted by the (torque-limited) actuators, and so lower values of σ_{\max} are favorable. As shown in Fig. 13-B, the symmetric five-bar does consistently better than the other two mechanisms, in spite of displaying a greater variation over its workspace.

- c) $\sigma_{\text{mean}} := \frac{1}{n} \text{trace}(J J^T)$, **thermal cost of force**. Fixing the motor constant, $K_m = 1$, the thermal cost of force production is a function of the infinitesimal kinematics ([Asada and Youcef-Toumi, 1987](#), pg. 55), given in $\frac{Nm}{W}$. As shown in Fig. 13-C (note that this measure is also leg-angle-invariant; cf. Remark 1c)), the symmetric five-bar has superior design-averaged performance compared to the parallelogram five-bar and series linkages.

2.4 Platform Design

In this section, we present what we know so far about platform design, including morphology and construction. We first outline some general guiding principles (Sec. 2.4.1) in a relatively informal

¹¹We show in Prop. 4 that each of these measures is invariant to the leg angle, making the extension the only relevant workspace parameter.

Table 2: Physical properties of the machines of interest (2.4.1).

Robot	Legs	DOF	L (m)	M (kg)	Mot. (%)	G
Minitaur	4	8	0.2	5	40	N/A
Delta Hopper	1	3	0.2	2.0	38	N/A
Jerboa	2	4	0.105	2.5	40	N/A
MIT Cheetah	4	12	0.275	33	24	5.8
XRL	6	6	0.2	8	11	23
ATRIAS	2	6	0.42	60	11	50
StarlETH	4	12	0.2	23	16	100
Cheetah Cub	4	8	0.069	1	16	300

Table 3: Performance measures of the machines of interest (2.4.1)

Robot	v_{ss} (m/s)	v_{ss} (LL/s)	α_v (m/s) ²	a_{mcv} [DD] (g)	CoT
Minitaur	2	10	4.70	0.69	2.3
Delta Hopper	-	-	3.44	0.59	N/A
Jerboa	1.52	14.5	1.37	0.39	2.5
MIT Cheetah	6	21.8	4.91	1.33 [-0.60]	0.51
XRL	1.54	7.7	4.17	1.14 [-0.91]	0.9
ATRIAS	2.53	6.00	N/A	2.03 [-0.94]	1.46
StarlETH	0.7	3.5	3.09	0.37 [-0.99]	2.57
Cheetah Cub	1.42	20.8	0.20	19.38 [-0.93]	9.8

way,¹² and next we measure how well our designs hold up with respect to some clearly defined metrics (Sec. 2.4.2). We have designed and build three different robot platforms (Fig. 4), but we only discuss the Jerboa in detail (Sec. 2.4.3) in this thesis.

2.4.1 Simple Considerations for Platform Design

Platform Considerations for DD Designs

Mass Budgeting for Robot-specific Power and Force It has long been understood in the legged locomotion design literature that a large fraction of the robot’s mass budget should be reserved for actuation Rad et al. (1993). Our desire for DD designs pushes this notion toward its extreme as the robots in this family all have approximately 40% of total mass taken up by the actuators, compared to 24% for the modestly geared MIT Cheetah and approximately 10-15% for more conventional machines (detailed in Table 2).

“Framing” Costs While increasing the number of active DOF/leg can improve control affordance, distributing actuators incurs inescapable costs (paid in the scarce resource of specific force)

¹²Future work in this area aspires to formalize these notions.

associated with replacing a single larger actuator by multiple smaller ones. When considering how a motor's output torque scales as the characteristic length is modified, the designer must decide which motor scaling is more representative of the actuator choices available namely isometrically, or by assuming a constant cross section and varying the gap radius.¹³ For a constant actuator mass budget, as the number of actuators, n , increases and the actuators scale isometrically, the specific torque scales as $\propto n^0$ if the motors are added in parallel and $\propto n^{-1}$ if they are in series. If the actuators are instead scaled by gap radius, the specific force goes $\propto n^{-1}$ in parallel and $\propto n^{-2}$ in series.¹⁴ This scaling argument represents the minimal characteristic rate of lost specific force production incurred by adding motors whereas, in practice, the additional motors accrue additional cost arising from the further increment of mass (and complexity) needed to frame and attach them. The machines considered here all have one to three active DOF/leg (see Table 2) but humanoids such as Asimo [Sakagami et al. \(2002\)](#) with 57 actuated DOF will incur significant cost.

Self-Manipulability as a Design Principle

Following [Johnson and Koditschek \(2013a\)](#), it is clear that a legged robot has many other available hybrid modes available to it than (vertical) specific agility (which is restricted to measuring work output in “stance”). In Fig. 14 we examine the relevance of these ideas in the simple example of selecting between two competing morphologies (**A**: tail and 1DOF leg¹⁵, versus **B**: a more traditional 2DOF leg). The morphology on the left enjoys more than just “stance” and “flight” contact modes, 3 of which we have found quite useful and list in Fig. 14.

Fig. 14 suggests that **A**, though unconventional, affords a greater possibility for the robot to manipulate its CoM position and orientation over various contact modes.

Delving further into reasons that we are interested in tails, we must acknowledge the past literature in this area [Libby et al. \(2012\)](#). In addition, we observe that

- a) the rank of affordances is higher (as mentioned above);
- b) because of the higher duty cycle of operation (tails can be doing positive work in all contact modes), the average power that can be derived from the actuator before hitting thermal limits is far greater than if it were operating intermittently (Sec. 2.2.2);
- c) the tail can do useful work regardless of which contact mode the robot finds itself in (as contrasted with many robot designs that would be quite stuck when upside down).

2.4.2 Metrics for Platform Design

While there are many performance metrics proposed for robots, we suggest some new ones in [Kenneally et al. \(2016\)](#), and summarize the performance of our robots using traditional as well as some new metrics.

¹³The scaling choice depends on both the design objective and availability of COTS (or feasibility of making custom) actuators.

¹⁴Assuming constant density, the mass budget yields a volume budget, and so the volume of each actuator, v , will be the total volume budget divided by n , so $n \propto v^{-1}$. Scaling isometrically, mass $\propto l^3$ and torque $\propto l^3$ (as both the gap area and radius contribute to torque production), yielding specific torque $\propto n^0$ in parallel. In series, the torque at the end effector is the minimum of the torques in the chain (assuming constant link lengths), so at best $\propto n^{-1}$. If scaling is done according to gap radius, torque $\propto l^3$ but mass $\propto l^2$ resulting in specific force in parallel $\propto n^{-1}$ and similarly in series $\propto n^{-2}$.

¹⁵Modeled on the Jerboa (Sec. 2.4.3)

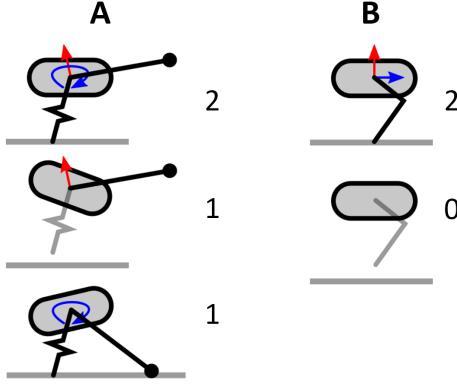


Figure 14: In **A**: leg and tail, while **B** is a more conventional 2DOF leg. Next to each of the contact modes we list the “rank” of available affordances, which should be intuitively understood as the number of independently controllable accelerations that can be imparted on the CoM by the actuators. The red and blue arrows depict these accelerations in cartoon form. The leg is assumed massless.

DD Performance Metrics

Table 2 provides physical properties and Table 3 performance measures for this family of DD robots as well as examples of geared machines over a wide range of mass (1-60 kg).¹⁶

Wherever possible, the maximum experimentally observed forward running **steady velocity** (v_{ss}) of the robots of interest will be provided in m/s, and maximum leg length per second (LL/s).

Specific agility as defined in [Duperret et al. \(2014\)](#) represents the “mass-normalized change in extrinsic body energy [during stance].” Motivated by tasks such as ledge ascent, this measure will be restricted, in this context, to jumps that have a significant vertical component, denoted **vertical specific agility** (α_v). Rotational and horizontal translational components of the energy will be assumed negligible, such that

$$\alpha_v = h_{\max}g, \quad (2.38)$$

where h_{\max} is the maximal experimentally observed vertical jump height of the machine, and g the gravitational constant.

Since specific force is the first limiting resource, a measure is necessary to understand whether a given machine will even be able to support its own weight without thermal damage to the actuators. The leg’s infinitesimal kinematics have significant influence; we consider the minimum continuous vertical force that can be exerted by the machine, and normalize by the gravitational force acting on its mass, then subtract one, yielding an estimate of the **minimal continuous vertical acceleration**

¹⁶Here, L is the mean leg length, Mot. is motor mass fraction, M the mass, and G the gear ratio. For the MIT Cheetah (custom non-COTS motors), motor mass fraction was computed based on the high power actuators only, as the motor mass of the “shape-change” (out of sagittal plane) motors is negligible in comparison, the largest recoverable jump height was from direct correspondence with the author. The XRL (Maxon EC45, 70W, 23:1) v_{ss} is actually XRL data [Galloway et al. \(2010b\)](#). ATRIAS [Grimes and Hurst \(2012\)](#) (Allied Motion MF0150010) v_{ss} is from www.youtube.com/watch?v=U4eBRPHYCdA, and once again only the high power actuators are considered for the mass fraction. The StarlETH [Hutter et al. \(2012\)](#) (Maxon EC4-Pole, 200W, 100:1) jump height was taken from [Gehring et al. \(2015\)](#) by counting pixels in the jump image since COM displacement was not reported. The Kondo KRS2350 servos in the Cheetah Cub [Sprowitz et al. \(2013b\)](#) were assumed to have 1/3 motor mass, and “stall torque” was assumed to correspond to 100°C rise, and jump height was also determined from discussion with the author.

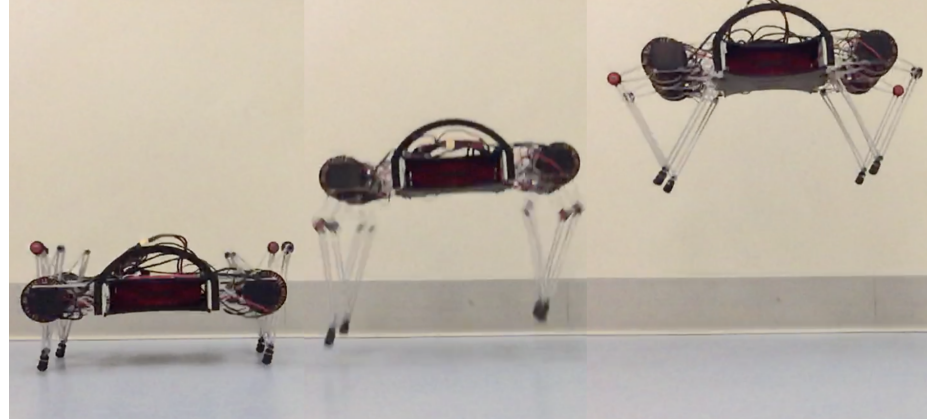


Figure 15: 48cm vertical jump of the Minitaur robot.

(a_{mcv}) :

$$a_{\text{mcv}} := \frac{\tau_c n_l}{mg} \left(\min_q \Gamma_v(q) \right) - 1 \quad (2.39)$$

whereby we assume that all legs have sufficient workspace for the links to be parallel. τ_c denotes the thermally sustainable continuous torque (assumed to be a $100^\circ C$ rise), and n_l the number of legs that can push vertically. This dimensionless number will indicate if the machine will be able to support its own weight at any point in the leg's workspace (≥ 0), and represents the instantaneous vertical acceleration of the body in units of gravitational constant. For comparisons with other machines, the measure is listed both as designed and also as if the machine's gearbox were removed.

The cost of transport (**specific resistance** Ahmadi and Buehler (1999), Gabrielli and von Karman (1950)) is computed using mean voltage (V) and current (i):

$$\text{CoT} := \frac{P_{\text{elec}}}{mg v_{\text{ss}}} \quad (2.40)$$

Performance of the DD machines The family of DD machines here performs similarly or better in conventional measures compared to more established, geared, machines. The Minitaur robot has forward running speed (v_{ss}) of 2 m/s for a bound De and Koditschek (2016), and 0.8 m/s for a prong, competitive for machines around its length scale, and its vertical jump height (represented by α_v , and shown in Fig. 15) is the second best of all the machines considered. The specific resistance of the DD robots is no worse than that of other machines of a similar scale (StarlETH and Cheetah Cub), though the larger machines perform better (as expected). Our machines have proven to be quite robust both mechanically and thermally and have each been run for tens of hours as the gaits were developed. We believe that the true benefits of our DD machines will be realized in tasks that fully exploit the increased proprioception, such as rapid transitions between substrates or locomotion modalities, a topic we leave to future work.

Summary This section outlines a design methodology that brings the well known benefits of DD robotics to legged locomotion. These benefits include significant improvements (3.8x–96x) in

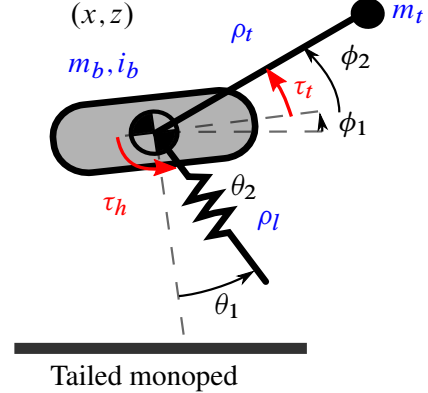


Figure 16: The Jerboa is a 2 Kg robot with hip-actuated legs and a 2DOF tail, pictured on the left as it appeared in the experiments of Chapter 4. On the right is our model for the planarized 4DOF system for comparison.

the constituent components (reflected inertia, and static, kinetic, and viscous friction) of a simple actuator “transparency” model, as well as a 17.4x improvement in rotational bandwidth as compared to a representative geared motor (Maxon EC45 flat, 23:1). The family of machines built with these actuators in accordance with the design principles listed above has proven very competitive with state of the art legged machines, according to a variety of metrics. The diversity of morphologies and similarly competitive running and leaping gaits exhibited by the family of machines we describe suggests that DD legged locomotion may be more readily achievable than its very sparse literature hitherto might suggest.

2.4.3 Jerboa: a Tailed Biped with 4 Actuators

Inspired by the self-manipulability arguments in Sec. 2.4.1, we have built a tailed bipedal robot [De and Koditschek \(2015c\)](#), which (when planarized) we model as shown in Fig. 44. The first two subsections of this section discuss (in an informal manner) the design process of the robot platform we have designed, built, and implemented the tail-energized hopping behavior on.

The Jerboa was designed with the goal of being a dynamic, agile robot with an inertial appendage. We defer an in-depth discussion of morphological constraints and tradeoffs to future work, but present the following basic design decisions here:

- With an eye on power density constraints¹⁷, the robot is underactuated. There are 12 spatial DOFs (6 for the body, 2 for each revolute leg, 2 for the tail) and 4 actuators. When planarized with a boom and virtual constraints on the appendages (as we have done here), there are 6 planar DOFs: 3 for the body, 2 for the single leg and 1 for the pitching tail. Raibert showed that an underactuated robot can be dynamically stable [Raibert \(1986\)](#), and in order to have the best performance, we limited the number of actuators on the robot to the minimum number that we believe is required to achieve a wide variety¹⁸ of behaviors.

¹⁷ Adding actuated DOFs parasitically increases mass, but it is not a direct consequence that a proportionate amount of usable power will be added to the robot body by the extra DOFs.

¹⁸ We have some preliminary empirical evidence that the Jerboa can quasistatically and dynamically balance, in order to sit, stand, walk, hop, run, turn, leap, etc. Careful investigation of each of these behaviors is planned for future work.

Table 4: Jerboa Physical Parameter values

Mass (with battery)	2.419 Kg	Dimensions (without tail)	0.21 m (L) \times 0.23 m (W) \times 0.1 m (H)
Tail length	0.3 m	Tail mass	150 g
Leg length	0.105 m	Leg motor stall torque	3.5 N-m
Peak power density	376 W/Kg	Peak (vertical) force density	46 N/Kg



Figure 17: The Jerboa tail is a 2DOF spherical joint controlled using coaxial motors through a mechanical linkage. Though there are driven sprockets visible in this image, the version of the robot presented here did not have this additional reduction stage.

- b) The body has low inertia (due to the mass of the motors being concentrated near the CoM, and the appendages being light), and the actuators are configured such that they can impart correspondingly large accelerations to the body (with an eye towards “agility”). Future work is planned to reconcile our inclination with emerging definitions of specific agility [Duperret et al. \(2014\)](#), but intuitively it seems as if “integrated magnitude of body acceleration” is a reasonable metric to aim for.
- c) The hips are actuated, but the leg extension is completely passive. This particular form of underactuated leg has been demonstrated to have great versatility in RHex [Saranli et al. \(2001\)](#), for steady-state running as well as transitional maneuvers [Johnson and Koditschek \(2013b\)](#).
- d) The robot contains an inertial appendage which is endowed with the same amount of power as the hips. Recent research in biomechanics [Libby et al. \(2012\)](#) and robotics [Johnson et al. \(2012\)](#) has demonstrated the utility of tails as inertial “self-righting” devices, and on the Jerboa we promote it to a primary source of locomotory energy and control.

In the remainder of this section, we outline the electromechanical aspects of the construction of the robot. A summary of important mechanical measurements is provided in table 4.

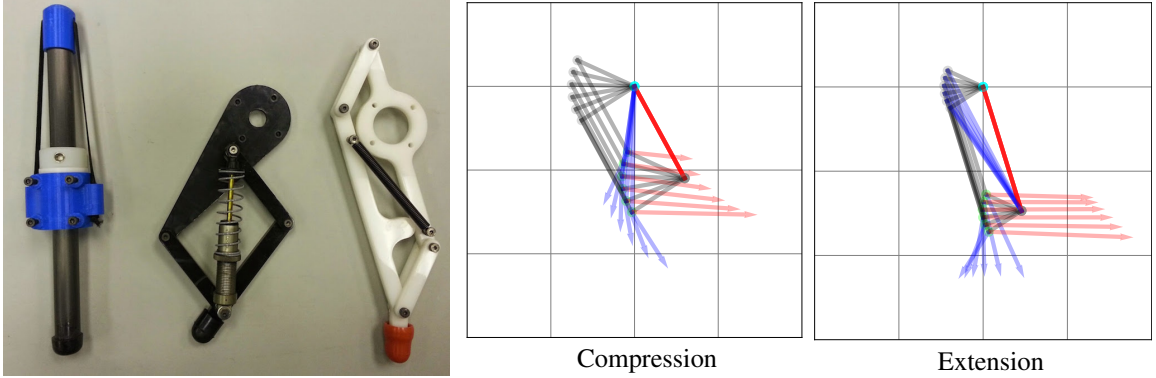


Figure 18: Left: Three leg designs considered for the Jerboa; the prismatic spring is “ideal” (in our model of SLIP, the spring force is dominantly axial, and the actuator force is predominantly tangential) but difficult to manufacture, and the four-bar designs only approximate the desired kinematics. **Right:** Configuration-dependent Jacobians of the compression and extension spring designs, where the displayed arrows map infinitesimal hip torques and spring extension forces to forces represented by red and blue (resp.) arrows at the toe. Out of these designs, the pictured version of the robot in Fig. 44 uses compression springs.

2DOF tail

The tail appendage is configured as a 2DOF spherical joint with a point mass at the distal tip. The joint itself is constructed using a linkage (Fig. 17) such that identical motor displacements result in a pitching motion, and differential motor displacements result in a yawing motion. The forward kinematics map from motor angles $\mu_1, \mu_2 \in T^2$ to the tail pitch and yaw angles, $\phi_2, \phi_{\text{yaw}} \in T^2$ has a simple form when restricted to zero yaw (i.e. $\mu_1 = \mu_2$),

$$\phi_2(\mu_1, \mu_2)|_{\phi_{\text{yaw}}=0} = \mu_1 = \mu_2. \quad (2.41)$$

For the behavior under study here, a virtual constraint ensures that $\phi_{\text{yaw}} = 0$. We leave a full kinematic analysis of the 2DOF mechanism to future work.

Prismatic-compliant revolute-actuated legs

Even though we adopt the underactuated hip-driven legs from RHex, the legs are chosen to have “toes” with point contacts instead of the rolling contact typical of RHex legs for the following reasons:

- Our template plant for fore-aft speed control is an inverted pendulum with a point contact, and in particular, the toe-placement strategy for fore-aft speed control is only (currently) well-understood for this leg structure.
- The Raibert pitch controller Raibert (1986), which we use as part of our attitude control depends on a “rigid” connection between the hip and the toe. With a series-elastic element that may have torsional compliance (such as a C-leg), the ground reaction force would load up the leg spring, introducing the spring dynamics as a “lag” in our pitch control strategy.

The left of Fig. 18 shows three leg designs that were considered for the Jerboa: 1. a prismatic

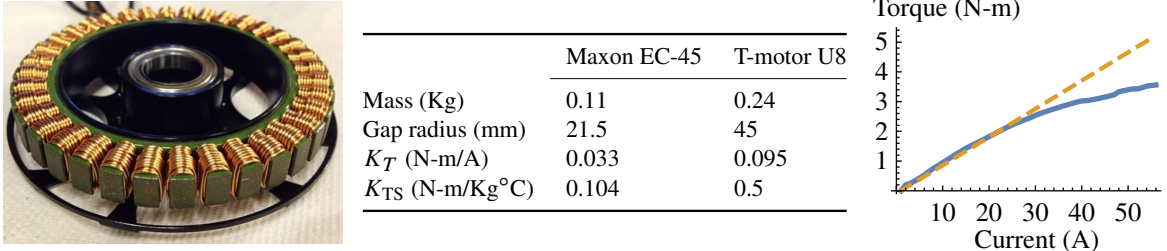


Figure 19: **Left:** The selected actuator for the Jerboa is the **T-motor U8**, showing a thin profile and large gap radius—desireable properties for legged applications [Seok et al. \(2012\)](#). **Middle:** Motor properties relevant to selection for legged applications for the Jerboa motor, and the X-RHex [Galloway et al. \(2010a\)](#) motor. **Right:** A torque-current plot for the U8 when coupled with our custom motor controllers of Fig. 20, showing flux saturation at higher currents and a dashed line for the nominal torque (predicted by K_T).

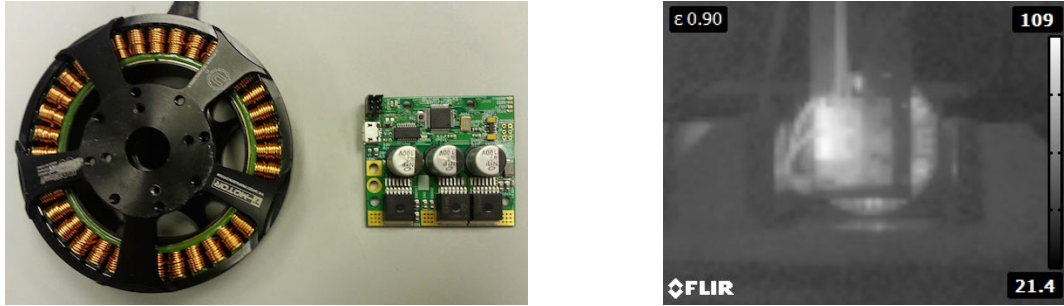


Figure 20: **Left:** The physical dimensions of our motor controller when compared to the motors they are driving. **Right:** Infrared image of of our actuation setup at stall, showing the controller reaching higher temperatures than the motor coils.

mechanism with a nonlinear elastic element, 2. a compression spring in a four-bar mechanism, and 3. an extension spring in a four-bar mechanism. While the kinematic properties of the first design are the closest to our model (the spring force at the toe is purely radial, and the motor force at the toe is purely tangential), this design proved difficult to construct because of the linear bearing required. The kinematics of the “approximate” leg designs are pictorially depicted in Fig. 18.

The experiments in Sec. 4.1 were all performed with the compression-spring legs. The compliant element is an off-the-shelf shock absorber for RC vehicles with lightweight construction, but considerable damping. We believe that the damping in legs was an important limiting factor in the energy of the hopping behavior demonstrated in experiments.

Actuators

The power generated by electromechanical actuators tends to be at unusably high speeds for legged applications, however at the same time, higher gear reductions are undesirable due to a multitude of reasons [Seok et al. \(2012\)](#). To this end, we tune our actuator selection to maximize *thermal specific torque*, K_{ts} —the torque generated by the motor per unit mass per unit temperature rise. This modification to the torque density criterion of [Seok et al. \(2012\)](#) allows us to incorporate

the thermal implications of sustained motor activation¹⁹. Fig. 19 contains a table comparing these metrics for the chosen actuator, a T-motor U8, and the one selected for X-RHex [Galloway et al. \(2010a\)](#), a Maxon EC-45.

Additionally, we developed custom motor controllers built around Infineon BTN8980 integrated half-bridges and an STM32F373 microcontroller that are (a) lightweight (20 g), (b) commutate using field-oriented control (FOC) at 25 KHz (adapted from [Piccoli and Yim \(2014\)](#)), (c) deliver up to 55 A peak current and up to 40 V peak voltage, and (d) have built-in 12-bit rotor position sensing. As a tradeoff for the high power-density of the driving electronics, they are limited by the heat dissipation ability of the half-bridges. Based on some crude testing, we have found that we can source approximately 10 A of steady-state current (thermally limited), corresponding to around 1 N-m of torque. Fig. 20 compares the physical dimensions and thermal performance of the motor controllers to the motors we have chosen. We note the following consequences of our selection of motor and driving electronics:

- a) The high torque density of the chosen motors allows us to completely forgo any static gear-reduction on the Jerboa (although the 2DOF tail makes use of a linkage to transmit power to a spherical joint)—affording benefits of “transparency” and eliminating any transmission losses [Kenneally and Koditschek \(2014\)](#), [Seok et al. \(2012\)](#).
- b) Power dissipation (to heat) in the motors is not a limiting factor in the robot’s performance with the current driving electronics.
- c) By eliminating the need for gearboxes and judicious chassis design, we have been able to reduce the “robot framing cost” to only 40% of the mass of the robot. To put this in context, only 8% of the mass of X-RHex is motors [Galloway et al. \(2010a\)](#).

Lastly, we highlight some of the design aspects of the Jerboa that are particularly relevant to the subject of Sec. 4.1 (tail-energized hopping via parallel playback of decoupled controllers):

Assumption 2 (Design for decoupled control). *The design of the Jerboa specifically ensures (i) leg/tail axes of rotation are coincident at the “hip,” (ii) the tail mass is small, i.e. $m_t \ll m_b$, and (iii) center of mass (approximately configuration-independent by the previous assumption) coincides with the hip.*

¹⁹We are assuming a thermal dissipation model for the motor, but not accounting for temperature effects on magnetic flux density.

CHAPTER 3 : Toward Correct-by-Design Compositions

The contributions in and organization of this chapter are strongly tied to our design paradigm listed in Sec. 1.1.1. Our contribution to the first “task specification” step is that in Sec. 3.1, we describe a small library of templates that we have found useful for our analyses of dynamic locomotion systems (hopping and running in the plane).

The remainder of the chapter is concerned with the crucial second step: providing “solutions” to dynamic steady-state legged locomotion tasks specified by a human operator. Our goal is the development of a correct-by-design approach to synthesis; our contribution in this thesis culminates in a sequence of algorithmic steps (Fig. 40), the outcome of which can be either (a) an analytical stability test for the hybrid nonlinear limit cycle¹, allowing the user to select morphological / control parameters for stability, or (b) a failure of one of the conditions in Fig. 40, indicating an inconclusive result.

In case the procedure is conclusive, our desired outcomes of Sec. 1.1.1 are all satisfied: the behavior is provably correct at design time, in the sense that—subject to any assumptions required to apply Fig. 40 to the ε -parameterized system under consideration—for small enough ε , the physical system has the same stability properties as the analytically found return map linearization. The other benefits (efficient synthesis, . . . , granularity) are all consequences of the design paradigm itself.

From our anecdotal experience², some of the prevalent causes for the procedure being inconclusive include (a) incorrect assignment of states and actuators to templates (see next segment for details); (b) inadequate template library (not rich enough to capture behavior of some body DOFs); (c) reset map perturbs continuous dynamics too aggressively (see Sec. 3.7.2); etc. Future work will focus on eliminating these roadblocks (we speculate on promising solutions in Sec. 5.2).

Conceptual procedure for correct-by-design synthesis

We begin this chapter by introducing the conceptual steps required for correct-by-design synthesis, and formally describe these steps in Sec. 3.2, 3.3, 3.6 as referenced below. This conceptual procedure is quite distinct from the algorithmic procedure for *using* our result (Fig. 40), but we introduce it here as a guide to the reader for interpreting our contributions.

Model mechanical system as coupled oscillators We are interested in reinterpreting our systems of interest as weakly coupled oscillators. Systems of coupled *identical* oscillators have been analyzed in literature in many different contexts such as neural circuitry Proctor et al. (2010) or multilegged coordination Golubitsky et al. (1998). Consider the ε -coupled oscillators with coupling functions χ ,

$$\begin{aligned}\dot{\psi} &= \omega \mathbf{1} + \varepsilon \chi(\psi, a) \\ \dot{a} &= 0,\end{aligned}\tag{3.1}$$

where $\psi \in T^m$ (m -dimensional torus) are the “phases”, $a \in \mathbb{R}^n$ are the “energies”, and $\omega_i \neq 0$ are the frequencies (e.g. Proctor et al. (2010)). Note that conventionally, only the phases are considered part of the state (which we have reflected by using trivial a dynamics above). However, in our

¹To be precise, we compute the stability of an approximation of the physical system, such that the physical system is an ε -perturbation of a trivial model system that we describe in Sec. 3.2.

²Further work is required to formally characterize these algorithmic failures.

case, the oscillators will generally (a) not be identical, and (b) their frequencies may depend on energies, i.e. $\omega = \omega(a)$. Our generalized version of (3.1) is presented in (3.140). Our choices of ψ, a modeling coordinates in Sec. 3.1 reflect this conceptual outline.

One interpretation of this procedure of converting an arbitrary mechanical system to the form (3.1) or (3.140) is that we are simply looking for a local diffeomorphism from the physical states to (ψ, a) . However, this process does not have a generally usable solution. For instance, one of our motivating “model problems” introduced in Sec. 3.6.3 is a spring-loaded inverted pendulum, or SLIP. SLIP with no dissipation in the shank is a Hamiltonian system, and generically Hamiltonian systems admit action-angle coordinates [Goldstein et al. \(2013\)](#). However, to find these coordinates, we must solve the Hamilton-Jacobi equations [Goldstein et al. \(2013\)](#). Additionally, since we have chosen our shank forcing to have ε -dissipation (3.5), it is tempting to pursue the stability analysis as an ε -perturbation about its action-angle representation. However,

- we need the equations of motion in these coordinates, and that the coordinate change persists for weakly dissipative systems, and
- our key criterion is that this coordinate change must be both analytically and computationally tractable (for our analytical and empirical results, respectively).

Thus, absent a generic method to obtain a closed-form coordinate change into action-angle, we compromise and use a cross product of the template coordinate changes (from Sec. 3.1) to rewrite the equations of motion (3.133). This offers the advantage of the coordinate change having a trivial form for both analysis and implementation. The price of this “convenience” is that even a Hamiltonian system may need further approximation to be expressed in the form of (3.140); for instance, assumption 8 is required for us to express SLIP in averageable form (3.143).

When composing the templates on a physical body, implicit in this step is a crucial **assignment** problem: the body’s physical states and actuators must be mapped to those of the template plants. Despite its importance, this step falls out of the scope of this thesis. Further research is needed to formalize this assignment problem; in fact, one of frequent causes for an inconclusive outcome of the algorithmic procedure of Fig. 40 is that the chosen coordinate changes are inappropriate.

Limit cycle stability as regulation and coordination After our $(m + n)$ -dimensional mechanical system is described by (ψ, a) coordinates, we can reinterpret our limit cycle stability goal in these coordinates. From the structure of (3.1) or (3.140) as $\varepsilon \rightarrow 0$ (as well as our intuition), the a coordinates stay relatively constant when the system is on its periodic orbit, but the ψ coordinates continue to oscillate. Conceptually, limit cycle stability consists of two parts: energy regulation, and phase coordination:

Energy regulation intuitively relates to stabilization of the a coordinates to some desired energy set, a^* .

Meanwhile, the m phases can be converted to $m - 1$ relative phases, and the coordination problem intuitively relates to stabilization of the relative phases. There is a large literature on the study of multilegged locomotion as a set of m coupled oscillators [Golubitsky et al. \(1998\)](#), [Haynes et al. \(2012\)](#). Often the phases ψ are assumed to directly correspond to some limb configuration, but there is no coupling to separate energy-like coordinates. [Raibert \(1986\)](#) observed the concept of “neutrality” in his hopping robots. We describe how our notion of coordination formally relates to Raibert’s concept of neutrality in Fig. 39. We depict pictorially a hybrid limit cycle, and these two “regulated” and “coordinated” manifolds in Fig. 21.

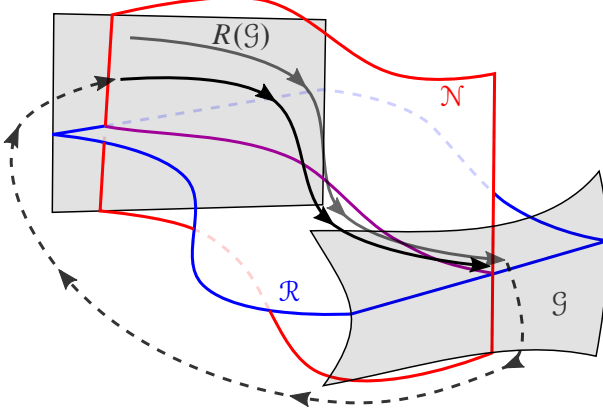


Figure 21: Visual depiction of the limit cycle, guard set, and the \mathcal{R} (3.139) and \mathcal{N} (3.149) submanifolds.

Averaging as a good approximation of coupled continuous flow From the structure of (3.1) or (3.140), we can observe that these systems exhibit a *separation of time-scales*, i.e. $\frac{da}{d\psi_i} = \mathcal{O}(\varepsilon)$. This topic has been the subject of much study in applied dynamical systems (e.g. [Guckenheimer et al. \(2003\)](#), [Hale \(2015\)](#)), and we introduce for the first time dynamical averaging in legged locomotion. Moreover, our prior conceptual decomposition of limit cycle stability into regulation and coordination requires some analytical approximation such as this, since in general, neither the ‘‘regulated’’ nor the ‘‘coordinated’’ submanifolds of the ambient space are invariant in general.

We first introduce dynamical averaging, and our generalization of it to switching systems, and then event-based reset hybrid systems, in Sec. 3.2. These first results (Thm. 2–3) apply to switching / hybrid systems with a single continuous mode, followed by a reset (3.39) (expressed in the form of a vector of slow coordinates $x \in \mathbb{R}^{m+n-1}$, and a single fast coordinates $\sigma \in S^1$). Sec. 3.3 shows how the single-mode result can be applied to certain classes of systems with two non-trivial (but symmetric) continuous modes.

Incorporating time-reversal symmetry The classes of systems we are interested in (representative of steady-state locomotion) are ‘‘close’’ to Hamiltonian systems since, while they typically require dissipative forces in order to stabilize against perturbations, the limiting behavior should have a periodic (and typically roughly constant) total energy.³ Hamiltonian systems are deeply related to time-reversible systems [Lamb and Roberts \(1998\)](#). [Altendorfer et al. \(2004\)](#) first introduced the benefits of time-reversal symmetry to legged locomotion.

In order to use Thm. 2–3 (introduced above), we must first find explicit ‘‘phase difference’’ coordinates in order to express the system in the form (3.39). We have anecdotally found this procedure—as well as verification of the other averageability conditions of Thm. 3—non-trivial even for relatively simple 2 DOF systems (Sec. 3.4–3.5). However, incorporating time-reversal symmetry, we can define a new class of systems (Def. 2) that possess certain symmetry properties.

As a consequence of asserting these new properties (which comparatively add little complexity to the algorithm in Fig. 40, and also have not so far limited its applicability in any instance), we

³While this ‘‘almost-Hamiltonian’’ notion intuitively helpful, our framework is unaffected if the total energy is not roughly constant.

get large simplifications in the averageability conditions, including “automatically” finding appropriate phase difference coordinates. We describe these advances in greater detail in the preamble to Sec. 3.6. Our last result (Thm. 4) can then be applied with far greater ease than the prior result Thm. 2/3.

Applicability and Results

Formally, our classes of applicable systems include any dynamical system expressible as a set of coupled oscillators (3.140), and having a single continuous mode.⁴ Since our contributions in this thesis do not include a solution to the **assignment** problem described above, we are unable to present a formal characterization of the class of applicable systems with our current results.

However, we have successfully applied these results for stability conclusions about planar mechanical systems pertaining to locomotion with up to 2 DOFs, with work currently in progress showing promising applicability to planar systems of up to 3 DOF:

In Sec. 3.4 we analyze a set of two mechanically-uncoupled, informationally-coupled vertical hoppers as a motivating model for the study of virtual bipedal coordination. The analysis informs the development of a new type of coordination controller that not only applies to this 2 DOF model, but also to a physical quadruped (Sec. 4.2).

In Sec. 3.5 we now analyze a set of two mechanically coupled vertical hoppers; in this instance the conclusion enables an analytical resolution to a decades-old stability problem studied in the robotics literature, which previously only had numerical solutions. However, the analysis of Sec. 3.5 poses a great degree of difficulty in the step of finding the phase difference coordinate between two non-identical coupled oscillators (the stance leg and the flight leg)—a required step in order to apply Thm. 2/3.

In Sec. 3.7, we apply the new Thm. 4 to two systems (a 1.5 DOF subspace of SLIP, and the old 2 DOF coupled vertical hoppers), demonstrating the relative ease of application of Fig. 40.

3.1 Templates for Hopping and Running

In this section we present several 1DOF plant models, local diffeomorphisms to (ψ, a) oscillator coordinates for each of these models, and describe the template controller devised to stabilize them.

These template plant models, as well as the feedback controllers presented to stabilize their behavior, are inspired by prior research which we attribute where appropriate. However, the change of coordinates to energy and phase (as detailed in the preamble to this chapter) is a novel contribution.

Pertinent templates serve the following categories of basic functions: control of the velocity of the center of mass (CoM), and control of angular momentum.

CoM control is decomposed into vertical energy regulation in stance and flight (Sec. 3.1.1–3.1.2)—qualitatively expressing how terrestrial running machines must intermittently use ground reaction forces to restore vertical momentum that is constantly lost to gravity—and a template for horizontal plane speed control (Sec. 3.1.3), which find application in control of fore-aft speed in the planar models studied so far.

⁴For all our applications, we integrate the flow in any trivial dynamic modes, such as ballistic flight, and incorporate it as a reset map. Using this procedure, we have not found any obstructions to either monopodal hopping gaits (e.g. SLIP in Sec. 3.7.2), or virtual bipedal gaits (Sec. 3.4, 3.5) leveraging symmetry factoring (Sec. 3.3).

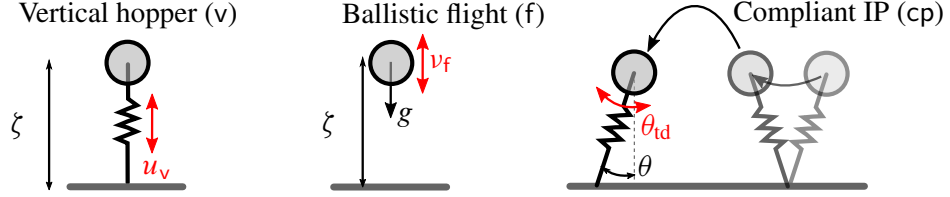


Figure 22: Plant models for the templates in Sec. 3.1.1, 3.1.2, and 3.1.3, showing the physical DOF of interest as a black greek letter, as well as the available actuator input (or perturbative force) in red.

We include two relatively simple expressions of angular momentum control: “attitude control” of a single rigid body introduced prior to its use in Sec. 3.4, a two-jointed planar body with insufficient actuation accessing two hybrid modes (Sec. 3.1.4).

Lastly, in Sec. 3.1.5, we list a few other templates we have studied, but have not been utilized in examples listed in this document.

Throughout this thesis, we use a $\mathsf{mathsf{}}$ subscript to denote the relevant template; for instance ψ_v refers to the “vertical hopper.”

3.1.1 (Vertical) Hopper (v)

This template plant is qualitatively describes a “bouncing” mass, that recovers vertical momentum using a spring-like energy return mechanism, and in addition actively injects dissipative forces to stabilize its bouncing height. Our coordinate transforms here are inspired by [Koditschek and Buehler \(1991\)](#).

Plant model The physical template plant (Fig. 22) is a unit-mass sprung leg in stance,

$$\ddot{\xi} = u_v = \omega_v^2(\rho - \xi) + \varepsilon v_v, \quad (3.2)$$

where ξ is the physical leg length, $\omega_v > 0$ is the chosen or enforced stance frequency, and the nominal extension $\rho \in \mathbb{R}_+$. We observe at the outset that the spring-like force can be generated by a physical spring or a virtually instantiated spring. We assume that the toe-ground interaction is a sticking contact (we do not consider a friction cone), and we ignore collisions between parts of the leg/body other than the toe and the ground, thus making the terrain profile under the toe irrelevant. We also assume there is no gravity, or that it is cancelled by forces in v_v beforehand.

The actuator acts in stance, and so the template controller acts in the continuous dynamics. The reset is trivial and there is no control affordance in the reset map.

Oscillator coordinates The coordinate change to model coordinates is based on the phase vector $p : \mathbb{R}^2 \rightarrow \mathbb{R}^2$,

$$p(\xi, \dot{\xi}) := \begin{bmatrix} (\rho - \xi)\omega_v \\ \dot{\xi} \end{bmatrix}. \quad (3.3)$$

The “square root of energy” coordinate represents the energy (only in stance, i.e. $\zeta < \rho$), and we get the following coordinate change:

$$\psi_v := \angle p(\zeta, \dot{\zeta}) \in S^1, \quad a_v := \|p(\zeta, \dot{\zeta})\| \in \mathbb{R}_+. \quad (3.4)$$

Template controller The controller is based on an energization strategy⁵ from our previous work [De and Koditschek \(2015b\)](#),

This controller is in the continuous mode. We can either operate with a body-fixed or virtually-instantiated (a) Hookean shank spring (frequency ω_v), and (b) viscous damping (coefficient β_v), together with (c) an actively injected additive nonlinear tuned damping term (gain k_v):

$$\nu_v := (k_v - a_v \beta_v) \sin \psi_v \quad (3.5)$$

When the spring is virtually instantiated, we refer to u_v as the control signal, in which case the $\omega_v^2(\rho - \zeta)$ term in (3.2) is simply added on to ν_v .

Closed loop dynamics The physical equation of motion in stance (from (3.2) and (3.5)) is

$$\ddot{\zeta} = \omega_v^2(\rho - \zeta) + \varepsilon \nu_v,$$

and rewritten in terms of $y = p(\zeta, \dot{\zeta})$ are

$$\begin{aligned} \dot{y}_2 &= \ddot{\zeta} = -\omega_v^2(\zeta - \rho) + \varepsilon \nu_v = \omega_v y_1 + \varepsilon \nu_v, \\ \dot{y}_1 &= -\dot{\zeta} \omega_v = -y_2 \omega_v. \end{aligned} \quad (3.6)$$

Using (3.4), $a_v = \|y\|$, and from the equations above,

$$\begin{aligned} a_v \dot{a}_v &= y^T \dot{y} = \varepsilon \nu_v y_2 = \varepsilon \nu_v (a_v \sin \psi_v) \\ \Rightarrow \dot{a}_v &= \varepsilon \nu_v \sin \psi_v, \end{aligned}$$

where we used the polar transform of y , i.e. $y_1 = a_v \cos \psi_v$, and $y_2 = a_v \sin \psi_v$. For the ψ_v dynamics, note that

$$\begin{aligned} \dot{y}_1 &= -a_v \sin \psi_v \dot{\psi}_v + \dot{a}_v \cos \psi_v \\ \dot{y}_2 &= a_v \cos \psi_v \dot{\psi}_v + \dot{a}_v \sin \psi_v \end{aligned}$$

⁵We provide proof of stability using a new controller, but the specific form of the control signal seems anecdotally less important (in our empirical trials) than its closed-loop stability properties. Further work is required to formally justify that compositions are relatively robust to the specific control strategy employed; for instance, we posit that the SLIP composition of Sec. 3.7.2 can display identical averaged dynamics (3.161) with different vertical controllers (3.5). See Sec. 5.2 for a further discussion.

and note that $y_1 \dot{y}_2 - y_2 \dot{y}_1 = a_v^2 \dot{\psi}_v$. Then,

$$\begin{aligned}\dot{\psi}_v &\stackrel{(3.6)}{=} \frac{1}{a_v^2} (\omega_v^2 y_1^2 + \varepsilon v_v y_1 + \omega_v y_2^2) \\ &= \omega_v + \varepsilon v_v \cos \psi_v / a_v\end{aligned}$$

since $y_1^2 + y_2^2 = a_v^2$. Summarizing the above, we get

$$\begin{bmatrix} \dot{\psi}_v \\ \dot{a}_v \end{bmatrix} = \begin{bmatrix} \omega_v \\ 0 \end{bmatrix} + \varepsilon \begin{bmatrix} \cos \psi_v v_v / a_v \\ \sin \psi_v v_v \end{bmatrix}, \quad (3.7)$$

where v_v is given in (3.5).

3.1.2 Ballistic Flight (f)

The ballistic flight template (Sec. 3.1.2) is inspired by the juggling work of [Klavins et al. \(2000\)](#).

Plant model In this template we develop coordinates for a weakly perturbed ballistic mass. The template plant is a unit mass at height $\zeta > 0$, with dynamics

$$\ddot{\zeta} = -g + \varepsilon v_f, \quad (3.8)$$

where v should be interpreted as a “noise” or disturbance function.⁶

For the energy component of the flight coordinates, we use the square root of total energy, and a simple notion of phase originally due to [Klavins et al. \(2000\)](#),

$$a_f := \sqrt{2g(\zeta - \rho) + \dot{\zeta}^2}, \quad \psi_f := \frac{-\dot{\zeta}}{2a_f}. \quad (3.9)$$

Note that $\psi_f = -1/2$ denotes liftoff, and $\psi_f = 0$ denotes apex.

Dynamics With these coordinate we get the flight dynamics (taking a time derivative of (3.9)),

$$a_f \dot{a}_f = \frac{d}{dt} \frac{a_f^2}{2} = g \dot{\zeta} + \dot{\zeta} \ddot{\zeta} = \dot{\zeta} (\ddot{\zeta} + g) \stackrel{(3.9)}{=} -2\varepsilon a_f \psi_f v_f,$$

and from the second row of (3.4),

$$\begin{aligned}\dot{\psi}_f &= \frac{-\ddot{\zeta}}{2a_f} + \frac{\dot{\zeta} \dot{a}_f}{2a_f^2} \stackrel{(3.9)}{=} \frac{g}{2a_f} - \frac{\varepsilon v_f}{2a_f} + \frac{(-2a_f \psi_f)(-2\varepsilon \psi_f v_f)}{2a_f^2} \\ &= \frac{g}{2a_f} + \frac{\varepsilon v_f (4\psi_f^2 - 1)}{2a_f}\end{aligned}$$

⁶The presence of a perturbation force acting on the mass is inspired by our prior work on the slot hopper [De and Koditschek \(2016\)](#). In that instance, the perturbation enters through coupling with a different leg which is in stance.

Inspired by the computation above, we define the flight frequency

$$\omega_f := g/2a_f, \quad (3.10)$$

and can put the above together to get

$$\begin{bmatrix} \dot{\psi}_f \\ \dot{a}_f \end{bmatrix} = \begin{bmatrix} \frac{g}{2a_f} \\ 0 \end{bmatrix} + \varepsilon \begin{bmatrix} \frac{\nu_f(4\psi_f^2-1)}{2a_f} \\ -2\psi_f\nu_f \end{bmatrix}. \quad (3.11)$$

3.1.3 Compliant Inverted Pendulum Horizontal Motion (cp)

This template is inspired by longstanding research on the SLIP model (e.g. [Geyer et al. \(2005\)](#), [Schwind and Koditschek \(1995\)](#)), though the control strategy we use to stabilize fore-aft speed is a reprisal of Raibert’s strategy.

Plant model The physical template plant (Fig. 3.1.3) is of an inverted pendulum of length $r > 0$ (allowed to vary⁷), with leg angle $\theta \in S^1$. The continuous equations of motion are

$$r\ddot{\theta} = -2\dot{r}\dot{\theta} + \varepsilon\nu_{cp}. \quad (3.12)$$

Oscillator coordinates Borrowing from our previous work ([De and Koditschek, 2015a](#), Sec. 3.2), we define (a_{cp}, ψ_{cp}) to capture the leg angle DOF in oscillator coordinates:

$$\psi_{cp} := \theta \quad \text{and} \quad a_{cp} := r^2\dot{\theta}, \quad (3.13)$$

where a_{cp} is the angular momentum about the toe and the leg angle is the proxy for phase. In these coordinates, the dynamics are

$$\begin{bmatrix} \dot{\psi}_{cp} \\ \dot{a}_{cp} \end{bmatrix} = \begin{bmatrix} a_{cp}/r^2 \\ 0 \end{bmatrix} + \varepsilon \begin{bmatrix} 0 \\ r\nu_{cp} \end{bmatrix}. \quad (3.14)$$

3.1.4 Two-link Planar Attitude Control: 2 DOF Hybrid Inertial Reorientation

This template was first introduced in [De and Koditschek \(2015b\)](#), which in turn was inspired by 1 DOF inertial reorientation [Libby et al. \(2015\)](#). Our decision to energize the hopping behavior with a tail leaves introduces a new actuated DOF whose tight dynamical coupling to both the mass center and the body orientation dynamics requires its careful control throughout the locomotion cycle. Recent literature [Johnson et al. \(2012\)](#) has seen the development of a 1DOF “inertial reorientation” template for correcting the “shape” coordinate in a two-link body experiencing free-fall

⁷This template is a specific instance of a variety of models where we can use approximately-conserved quantities to derive the fore-aft energy; for instance in fore-aft compartment of tailed hopping. We defer a full exploration of Lagrangian-derived oscillator coordinates to future work, but observe the following here: If q_i is almost-cyclic in the Lagrangian \mathcal{L} (i.e. $\frac{\partial \mathcal{L}}{\partial q_i} = \mathcal{O}(\varepsilon)$, and $\Upsilon_i = \mathcal{O}(\varepsilon)$). $\frac{\partial \mathcal{L}}{\partial q_i} - \frac{d}{dt} \frac{\partial \mathcal{L}}{\partial \dot{q}_i} = \Upsilon_i$, then we set $a_i = \frac{\partial \mathcal{L}}{\partial \dot{q}_i}$. Clearly $\dot{a}_i = \mathcal{O}(\varepsilon)$. The corresponding phase, ψ_i , can then be found easily if $\mathcal{L}_i = \dot{q}_i^2$ (i.e. decoupled kinetic energy). Then $a_i = \dot{q}_i$, and ψ_i can be q_i , so that $\dot{\psi}_i = a_i$.

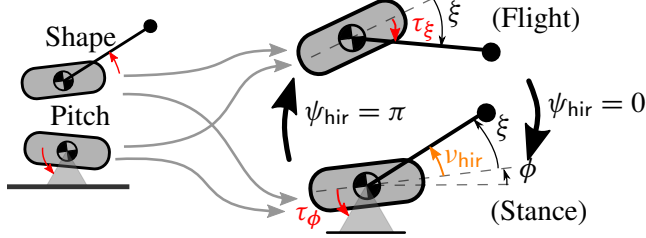


Figure 23: A hybrid 2DOF inertial reorientation template with two segments pinned at the CoM and no gravity. Left: the net angular momentum of the system is constant. Right: the system can correct the net angular momentum using reaction torques on the main body segment, but the tail DOF is subject to an unmodeled disturbance, or ν in (3.15).

(constrained by conservation of angular momentum). Raibert (1986) introduced a pitch stabilization mechanism relying on reaction torques from hip actuation during stance. Here, we adopt the approach of composing these templates for 2DOF stabilization of appropriately defined “pitch” and “shape” coordinates of a two-link body/tail model.

Since in the physical system the tail actuator, τ_2 , is unavailable for attitude control in stance (because it is being “monopolized” as the destabilizing energy source for the SLIP subsystem), and the Raibert pitch correction mechanism (using the hip actuator, τ_1) is unavailable in flight (due to absence of ground reaction force), we present a hybrid inertial reorientation (HIR) template (Fig. 23) as the simplest exemplar body on which this 2DOF template is anchored.

We omit the Lagrangian derivation for this familiar subsystem Johnson et al. (2012), but exploit the fact that when pinned at the CoM, the dynamics are second-order LTI with no Coriolis terms. We perform a change of coordinates (inverting the constant inertia tensor) to obtain the (decoupled) dynamics

$$[\ddot{\phi}, \ddot{\xi}]^T = \begin{cases} [\tau_\phi, \nu_{\text{hir}}]^T & (\text{stance}), \\ [0, \tau_\xi]^T & (\text{flight}), \end{cases} \quad (3.15)$$

where (ϕ, ξ) are the “pitch” and “shape” coordinates, respectively, and ν_{hir} is an unmodeled disturbance term (explicitly added here with an eye toward the use of tail for spring energization in the physical system). In (3.15) we have now represented HIR as two *independent* subsystems on which two identical 1DOF templates will be anchored in parallel (albeit in alternating stages of the hybrid execution).

Taking advantage of the direct affordance (by which we mean that both of the two decoupled 1DOF systems are completely actuated in, one and then other, of the alternating modes of their hybrid dynamics), we employ a graph-error controller Koditschek (1987) as a type of reduction. Our reference first-order dynamics for stabilizing each coordinate in turn are just $\dot{\phi} = -k\phi$ (and similarly for ξ). The independent closed-loop 1 DOF subtemplate vector fields, are defined as

$$\ddot{\phi} = -k_g(\dot{\phi} + k\phi) = -k_g k\phi - k_g \dot{\phi}, \quad (3.16)$$

(and similarly for ξ), where the gain k_g is understood to be high enough to make the transients of the anchoring dynamics irrelevant.

Hybrid Dynamical Model of HIR

Since the isolated model does not have any intrinsic physical mechanism for transitioning between modes, we add an exogenous clock signal, $\psi_a \in S^1$ such that $\psi_{\text{hir}} \in [0, \pi]$ represents stance, and the complement represents flight. Let its frequency be $\omega_{\text{hir}} > 0$. Here we sidestep the issue of phase-synchronization for the various compartments, but simply use ψ_{hir} to ensure our gains are tuned properly for the timescales of the coupled system (we ensure this upon its use in Proposition 8).

HIR stability

Let us denote $\bar{v}_{\text{hir}}[i] := \int v_{\text{hir}} dt$, the interval being over the stance phase of stride i . Also, define $v_{\text{hir}}^{\max} = \max_t \bar{v}_{\text{hir}}[t]$.

Proposition 5 (HIR Stability). *Given arbitrary $\varepsilon > 0$,*

$$k > \frac{2\omega_{\text{hir}}}{\pi} \log(1 + v_{\text{hir}}^{\max}/\varepsilon)$$

results in the desired limiting behavior $\|\mathbf{y}_{\text{hir}}\| \rightarrow \mathcal{B}_{\varepsilon_a}(0)$, a neighborhood of 0 of size ε , where $\mathbf{y}_{\text{hir}} := [\phi, \xi]^T$.

Proof. Simply integrating the first-order dynamics (3.16), we get the touchdown return map

$$P_{\text{hir}}(\mathbf{y}_{\text{hir}}) = \zeta \cdot (a + \bar{v}_{\text{hir}} \begin{bmatrix} 0 \\ 1 \end{bmatrix}),$$

where $\zeta := e^{-k\pi/\omega_{\text{hir}}}(1 - k\pi/\omega_{\text{hir}})$. Iterating this return map, at stride $n \in \mathbb{Z}_+$,

$$\mathbf{y}_{\text{hir}}[n] = \zeta^n \mathbf{y}_{\text{hir}}[0] + (\zeta^n \bar{v}_{\text{hir}}[0] + \cdots + \zeta \bar{v}_{\text{hir}}[n-1])e_2, \quad (3.17)$$

and using the triangle inequality,

$$\|\mathbf{y}_{\text{hir}}[n]\| \leq |\zeta|^n \cdot \|\mathbf{y}_{\text{hir}}[0]\| + v_{\text{hir}}^{\max} \left| \frac{\zeta}{1-\zeta} \right|. \quad (3.18)$$

Note that $\zeta < \frac{1}{1+v_{\text{hir}}^{\max}/\varepsilon}$ is a sufficient condition to ensure that $\|\mathbf{y}_{\text{hir}}[t]\| \leq \varepsilon$ asymptotically stable. Some algebra reveals that

$$k > \frac{2\omega_{\text{hir}}}{\pi} \log \left(1 + \frac{v_{\text{hir}}^{\max}}{\varepsilon} \right) \quad (3.19)$$

is, in turn, a condition sufficient to insure that previous inequality involving ζ . \square

3.1.5 Other Templates Studied

We have studied several other templates in the course of this research, some of which are introduced in detail for the study of specific behaviors / bodies, and others of which were used in research not contained in the thesis.

The following are utilized for various experiments on the Jerboa (Sec. 2.4.3), including those in this thesis (Sec. 4.1):

- two-link spatial attitude control (for 3DOF tail-assisted roll control) [Wenger et al. \(2016\)](#);

- tail-SLIP fore-aft energy (a modification of Sec. 3.1.3 based on the different Langrangian structure induced by an added tail);
- energy pumping tail (in our usage the tail is driven in a phase-locked manner based on the leg shank state, and so we introduce new coordinate changes intricately coupling the tail and leg shank DOFs).

The following are utilized in the bounding quadruped (Sec. 4.2):

- rigid body attitude control (“attitude controller” introduced in Sec. 3.4);
- rigid linear inverted pendulum for horizontal speed control (“linear” version of Sec. 3.1.3, inspired by [Pratt et al. \(2006\)](#))

3.2 Averaging Theory and its Application to Locomotion

The emergence of physically motivated and mathematically tractable hybrid models [Burden et al. \(2015, 2016\)](#), [Johnson et al. \(2016\)](#) offers the prospect of extending classical ideas and techniques of dynamical systems theory for application to new settings arising from the repeated making and breaking of contacts endemic to robotic mobility and manipulation. Here we work at the intersection of a class of tractable hybrid legged locomotion models [Johnson et al. \(2016\)](#) with a class of well-behaved hybrid limit cycle models [Burden et al. \(2015\)](#) to generalize an initial result [De and Koditschek \(2015a\)](#) on the stability of “averageable” hybrid oscillators. Specifically, we extend a classical smooth dynamical averaging technique to a class of hybrid systems with a limit cycle that is particularly relevant to the synthesis of stable gaits.

Relation to prior literature Classical averaging ([Guckenheimer and Holmes, 1990](#), Ch. 4.1) yields a method of approximating (with error bounds) solutions of the T -periodic vector field using the averaged vector field. As in the classical case, our new hybrid results guarantee equivalence in stability type to a simpler approximant (named the *averaged system*) of the system of interest. Specifically, we show that if the return map of the averaged system has a hyperbolic periodic orbit, then so does the original system, and additionally the linearizations of the return maps are ε^2 -close (and thus share the same eigenvalues and eigenvectors to $\mathcal{O}(\varepsilon)$).

This report is also related to previous stability analyses of hybrid oscillators appearing in locomotion for a single vertical hopper [Koditschek and Buehler \(1991\)](#), as well as informationally-coupled, physically-decoupled vertical hoppers [Klavins and Koditschek \(2002\)](#), [Klavins et al. \(2000\)](#). Application of the hybrid averaging result in these instances yields a greater analytical simplification than has been possible before. In fact, we show in our analysis that the nonlinear stance dynamics in our vertical hopper (Example 3) can be reduced to an “averaged” continuous dynamics that appears as a phase-independent proportional controller on the energy (3.47). While single-vertical-hopper stability results have been obtained before without averaging (e.g. [Koditschek and Buehler \(1991\)](#)), the more complex latter instance (informationally-coupled vertical hoppers) has heretofore only been analyzed in the context of a simplified integrable stance model ([Klavins and Koditschek, 2002](#), eqn. (20)). Integrable stance dynamics allowed for a discrete return map control strategy ([Klavins and Koditschek, 2002](#), eqn. (26)), but cannot be extended to more general non-integrable dynamical templates such as the so-called Spring-Loaded Inverted Pendulum (SLIP) [Saranli et al. \(1998\)](#). Hybrid averaging allows us to analyze with relative ease this plant model obviating the need to integrate the time-varying flow and, rather, requiring only examination of its reduced-dimensional,

simplified, averaged approximant. Stability analyses of these kinds of models has not been achieved thus far in the literature, leading past researchers to resort to numerical methods [Poulakakis \(2006\)](#), [Shahbazi and Lopes \(2016\)](#). Further work is currently underway to use hybrid averaging in conjunction with observations on time-reversal symmetry [Altendorfer et al. \(2004\)](#), [Razavi et al. \(2016\)](#) to provide stability analyses of higher dimensional models including fore-aft motion.

3.2.1 Classical Averaging (Background)

Following [Guckenheimer and Holmes \(1990\)](#), consider a time-varying⁸ system

$$\dot{x} = \varepsilon f(x, t, \varepsilon); \quad x \in \mathcal{U} \subset \mathbb{R}^n \quad 0 < \varepsilon \ll 1. \quad (3.20)$$

The averaged system is defined as

$$\dot{y} = \varepsilon \frac{1}{T} \int_0^T f(y, t, 0) dt =: \varepsilon \bar{f}(y). \quad (3.21)$$

Note that y is used instead of x to make clear that these vector fields act on different coordinates. We describe the necessary coordinate change below.

Theorem 1 (Smooth Averaging Theorem [Guckenheimer and Holmes \(1990\)](#)). *There exists a C^r change of coordinates $x = y + \varepsilon w(y, t, \varepsilon)$ under which (3.20) becomes*

$$\dot{y} = \varepsilon \bar{f}(y) + \varepsilon^2 f_1(y, t, \varepsilon). \quad (3.22)$$

Moreover,

- (i) *If $x(t)$ and $y(t)$ are solutions of (3.20) and (3.21) with initial conditions $x(0)$, $y(0)$ respectively, and $|x(0) - y(0)| = \mathcal{O}(\varepsilon)$, then $|x(t) - y(t)| = \mathcal{O}(\varepsilon)$ on a time scale $t \sim 1/\varepsilon$.*
- (ii) *If f is periodic with period T , and if p_0 is a hyperbolic equilibrium of (3.21) then there exists $\varepsilon_0 > 0$ such that, for all $0 < \varepsilon \leq \varepsilon_0$, (3.20) possesses a unique hyperbolic periodic orbit $\gamma_\varepsilon(t) = p_0 + \mathcal{O}(\varepsilon)$, of the same stability type as p_0 .*

Remark 2. The statement (i) does not depend on the periodicity assumption made in [Guckenheimer and Holmes \(1990\)](#); but only (ii). Further, we emphasize that we don't directly compare the behaviors of (3.20) and (3.21); instead we change coordinates for the original vector field from x to y , and then compare the behavior of the original system in the new coordinates, (3.22), to the “model averaged system” (3.21).

Proof. We replicate the proof strategy of (i) from [Guckenheimer and Holmes \(1990\)](#). First we compute the change of coordinates explicitly. Let

$$f(x, t, \varepsilon) = \bar{f}(x) + \tilde{f}(x, t, \varepsilon) \quad (3.23)$$

be split into its mean, \bar{f} , and oscillating, \tilde{f} , parts. Let

$$x = h(y) := y + \varepsilon w(y, t, \varepsilon), \quad (3.24)$$

⁸We prefer to use autonomous systems with a phase coordinate instead of time; point ahead to Sec. 3.2.3.

without yet choosing w . Differentiating the equation above and using (3.20) and (3.23), we have

$$(I + \varepsilon D_y w)\dot{y} = \dot{x} - \varepsilon \frac{\partial w}{\partial t} = \varepsilon \bar{f}(y + \varepsilon w) + \varepsilon \tilde{f}(y + \varepsilon w, t, \varepsilon) - \varepsilon \frac{\partial w}{\partial t},$$

or (expanding in powers of ε , and choosing w such that $\frac{\partial w}{\partial t} := \tilde{f}(y, t, 0)$),⁹

$$\begin{aligned} \dot{y} &= \varepsilon(I + \varepsilon D_y w)^{-1} \left[\bar{f}(y) + \varepsilon D_y \bar{f} \cdot w(y, t, 0) + \tilde{f}(y, t, 0) + \varepsilon \frac{\partial \tilde{f}}{\partial \varepsilon}(y, t, 0) - \tilde{f}(y, t, 0) + \mathcal{O}(\varepsilon^2) \right] \\ &= \varepsilon(I - \varepsilon D_y w) \left[\bar{f}(y) + \varepsilon D_y \bar{f} \cdot w(y, t, 0) + \varepsilon \frac{\partial \tilde{f}}{\partial \varepsilon}(y, t, 0) \right] + \mathcal{O}(\varepsilon^3) \\ &= \varepsilon \bar{f}(y) + \varepsilon^2 \left[\varepsilon D_y \bar{f} \cdot w(y, t, 0) - D_y w(y, t, 0) \bar{f}(y) + \frac{\partial \tilde{f}}{\partial \varepsilon}(y, t, 0) \right] + \mathcal{O}(\varepsilon^3) \\ &=: \varepsilon \bar{f}(y) + \varepsilon^2 f_1(y, t, \varepsilon), \end{aligned} \tag{3.25}$$

as required by (3.22).

We use a version of Gronwall's Lemma (see [Guckenheimer and Holmes \(1990\)](#) for details) to compare solutions of (3.21) and (3.22). If $y(t)$ and $y_\varepsilon(t)$ are their respective solutions, the Lemma says that if $|y(0) - y_\varepsilon(0)| = \mathcal{O}(\varepsilon)$, then $|y_\varepsilon(t) - y(t)| = \mathcal{O}(\varepsilon)$ for $t \in [0, \frac{1}{\varepsilon L}]$. Using the coordinate change (3.24), we know

$$|x(t) - y_\varepsilon(t)| = \varepsilon w(y_\varepsilon(t), t, \varepsilon) = \mathcal{O}(\varepsilon),$$

and using the triangle inequality,

$$|x(t) - y(t)| \leq |x(t) - y_\varepsilon(t)| + |y_\varepsilon(t) - y(t)| = \mathcal{O}(\varepsilon),$$

and we obtain the desired result (i).

To prove (ii), we again follow the proof strategy of [Guckenheimer and Holmes \(1990\)](#), but provide significantly more detail as well as correct some typos in the original. We also enumerate the steps in order to better reference them in the following text.

(a) We consider the Poincare maps P_0 and P_ε associated with (3.21) and (3.22). Rewriting these latter systems as

$$\dot{y} = \varepsilon \bar{f}(y), \quad \dot{\theta} = 1, \tag{3.26}$$

$$\dot{y} = \varepsilon \bar{f}(y) + \varepsilon^2 f_1(y, \theta, \varepsilon), \quad \dot{\theta} = 1, \tag{3.27}$$

where $(y, \theta) \in \mathbb{R}^n \times \mathbb{S}^1$, and $\mathbb{S}^1 = \mathbb{R}/T$ is a circle of length T . We define a global cross-section $\Sigma := \{(y, \theta) : \theta = 0\}$, and the first return or time T Poincare maps $P_0 : \mathcal{U} \rightarrow \Sigma$, $P_\varepsilon : \mathcal{U} \rightarrow \Sigma$ are then defined for (3.26), (3.27) as the flow maps associated with a time- T flow of each of the time-varying dynamics with initial condition $t = 0$, where $\mathcal{U} \subseteq \Sigma$ is some open set.

(b) If p_0 is a hyperbolic equilibrium of (3.21), then $\bar{f}(p_0) = 0$. Using [\(Hirsch et al., 1974\)](#),

⁹Note that we evaluate at $\varepsilon = 0$ since these terms interact with a Taylor expansion at $\varepsilon = 0$ of \dot{y} , as shown in (3.25).

pg. 300), the spatial Jacobian of the flow around and equilibirum is that of a linear time-invariant system, and so^{10,11}

$$DP_0(p_0) = e^{\varepsilon T \overline{Df}(p_0)} = I + \varepsilon T \overline{Df}(p_0) + \mathcal{O}(\varepsilon^2). \quad (3.28)$$

- (c) Note that P_ε is ε -close¹² to P_0 since T is fixed independent of ε , using the result of (i).¹³ Next we show that $DP_\varepsilon(p_0) = DP_0(p_0) + \mathcal{O}(\varepsilon^2)$. For this, consider the time-invariant vector field corresponding to (3.27),

$$\begin{bmatrix} \dot{y} \\ \dot{\theta} \end{bmatrix} = \begin{bmatrix} \varepsilon \overline{f}(y) + \varepsilon^2 f_1(y, \theta, \varepsilon) \\ 1 \end{bmatrix},$$

and define its time- t flow from initial condition (y, θ) as $\Phi_\varepsilon(y, \theta, t)$, versus the corresponding flow $\Phi_0(y, \theta, t)$ for (3.26). Note that, by definition, $P_\varepsilon(p) := \pi_y \Phi_\varepsilon(p, 0, T)$, where π_y is the projection to the y -coordinates. Following (Hirsch et al., 1974, pg. 300) to compute the spatial derivative of the flow, we get the linear time-varying system where $A(t) := D\Phi_\varepsilon(y(t), 0, t)$,

$$\dot{A}(t) = \begin{bmatrix} \varepsilon D\overline{f} + \varepsilon^2 D_y f_1 & \varepsilon^2 D_\theta f_1 \\ 0 & 0 \end{bmatrix} A(t).$$

We can solve this linear time-varying system using the Peano-Baker series. Since we are only interested in the top left block, we can compute it at p_0 ,

$$\begin{aligned} DP_\varepsilon(p_0) &= I + \varepsilon \int_0^T D\overline{f}(\Phi_\varepsilon(p_0, \theta, t)) d\theta + \mathcal{O}(\varepsilon^2) \\ &= I + \varepsilon \int_0^T \left[D\overline{f}(\Phi_\varepsilon(p_0, \theta, t)) - D\overline{f}(\Phi_0(p_0, \theta, t)) + D\overline{f}(\Phi_0(p_0, \theta, t)) \right] d\theta + \mathcal{O}(\varepsilon^2) \\ &\stackrel{*}{=} I + \varepsilon T D\overline{f}(p_0) + \varepsilon \int_0^T \left[D\overline{f}(\Phi_\varepsilon(p_0, \theta, t)) - D\overline{f}(\Phi_0(p_0, \theta, t)) \right] d\theta + \mathcal{O}(\varepsilon^2) \\ &\stackrel{(3.28)}{=} DP_0(p_0) + \varepsilon \int_0^T \left[D\overline{f}(\Phi_\varepsilon(p_0, \theta, t)) - D\overline{f}(\Phi_0(p_0, \theta, t)) \right] d\theta + \mathcal{O}(\varepsilon^2), \end{aligned}$$

where we used the fact that $\Phi_0(p_0, \theta, t) \equiv p_0$ for step \star . From (i), for $\theta \in [0, T]$ we know that $\|\Phi_\varepsilon(p_0, \theta, t) - \Phi_0(p_0, \theta, t)\| = \mathcal{O}(\varepsilon) \implies \Phi_\varepsilon(p_0, \theta, t) = \Phi_0(p_0, \theta, t) + \mathcal{O}(\varepsilon)$. Additionally, $D\overline{f}$ is Lipschitz continuous and so $D\overline{f}(\Phi_\varepsilon(p_0, \theta, t)) = D\overline{f}(\Phi_0(p_0, \theta, t)) + \mathcal{O}(\varepsilon)$. Using this in the block equation above, we have $DP_\varepsilon(p_0) = DP_0(p_0) + \mathcal{O}(\varepsilon^2)$.

- (d) Consider the function $\zeta(p, \varepsilon) := \frac{1}{\varepsilon}(P_\varepsilon(p) - p)$,¹⁴ such that $D_p \zeta = \frac{1}{\varepsilon}(e^{\varepsilon T D\overline{f}(p)} - I)$, and $\lim_{\varepsilon \rightarrow 0} D_p \zeta = T D\overline{f}(p)$. Note that zeros of ζ correspond to fixed points of P_ε , and that

¹⁰Typo in Guckenheimer and Holmes (1990); should have said $D\overline{f}(p_0)$ instead of $Df(p)$.

¹¹This statement means that if p_0 is a hyperbolic fixed point of \overline{f} , by definition, the eigenvalues of $D\overline{f}(p_0)$ have a non-zero real part. Consequently, the eigenvalues of $\exp(\varepsilon T D\overline{f}(p_0))$ do not lie on the unit circle.

¹²Typo in Guckenheimer and Holmes (1990); not ε^2 -close.

¹³Intuitively, the result of (i) holds over a time interval of $\mathcal{O}(1/\varepsilon)$. This statement says that since T doesn't depend on ε , for small enough ε , the $\mathcal{O}(1/\varepsilon)$ time interval over which (i) applies can be $> T$.

¹⁴The $1/\varepsilon$ in ζ is there to maintain invertibility even as $\varepsilon \rightarrow 0$, since $\lim_{\varepsilon \rightarrow 0} DP_\varepsilon \rightarrow I$.

$D_p \zeta(p_0, \varepsilon) = T\bar{f}(p_0)$ is invertible. The implicit function theorem implies that the zeros of $D_p \zeta$ form a smooth curve $(p_\varepsilon, \varepsilon) \in \mathbb{R}^n \times \mathbb{R}$. Thus p_ε are fixed points of P_ε , and further, $p_\varepsilon = p_0 + \mathcal{O}(\varepsilon)$.

(e) Putting together the prior steps, we see that

$$\begin{aligned} DP_\varepsilon(p_\varepsilon) &= \exp[\varepsilon T(Df(p_\varepsilon) + \varepsilon^2 Df_1(p_\varepsilon))] \\ &= \exp[\varepsilon T Df(p_0) + \mathcal{O}(\varepsilon^2) + \varepsilon^2 T Df_1(p_\varepsilon)] = \exp[\varepsilon T Df(p_0)] + \mathcal{O}(\varepsilon^2), \end{aligned}$$

or, $DP_\varepsilon(p_\varepsilon) = DP_0(p_0) + \mathcal{O}(\varepsilon^2)$.

(f) Since both of the matrices above have eigenvalues (at least $\mathcal{O}(\varepsilon)$) away from the unit circle (hyperbolicity of \bar{f}), and an ε^2 perturbation of the entries only perturbs the eigenvalues by $\mathcal{O}(\varepsilon^2)$, the stability properties of DP_ε at its fixed point, p_ε , are the same as that of P_0 at its fixed point, p_0 .

Thus (3.27) has a periodic orbit ε -close to p , and via the change of coordinates (3.24), equation (3.20) has a similar orbit. \square

3.2.2 Switching Systems

Averaging coordinate change

Even though not required for the proof of Thm. 1, we will find it useful to delve deeper into the structure of the coordinate change (3.24). As pointed out in the proof of Thm. 1, w is a solution to the PDE $\frac{\partial w}{\partial t} := \tilde{f}(y, t, 0)$. From this we make the following observations:

- w does not depend on ε ;
- the base value of w at $t = 0$ is not yet constrained, so we are free to choose¹⁵

$$w(y, 0, \varepsilon) \equiv 0 \text{ for all } y, \varepsilon; \quad (3.29)$$

- h in (3.24) is a good change of coordinates for sufficiently small $\varepsilon > 0$, since it is ε -close to the identity map;
- since the right-hand side of $\frac{\partial w}{\partial t} := \tilde{f}(y, t, 0)$ does not depend on w , and also since y is held fixed while taking the partial derivative w.r.t. t , this PDE can be solved by simply integrating over t , i.e.

$$w(y, t, \varepsilon) := \int_0^t \tilde{f}(y, \sigma, 0) d\sigma \quad (3.30)$$

is a solution of (3.24).

We show in several examples below that (3.30) is indeed a coordinate change from (3.20) to (3.22). The examples below can also be viewed in the Wolfram cloud (takes a few moments to load) [here](#).

Example 1 (Explicit averaging coordinate change (vertical hopper)). Consider the system of the form (3.20) with¹⁶ $f(x, t, \varepsilon) = (k_1 - \beta x) \cos^2(t) + \varepsilon k_2 x^2$, with $T = \pi$.

Using Mathematica¹⁷, first we compute $\bar{f} = \frac{1}{2}(k_1 - y\beta)$ according to (3.21). Next, we can find

¹⁵As in (Guckenheimer and Holmes, 1990, Example 1, Sec. 4.2).

¹⁶This is our vertical hopper template with $t \in [0, \pi]$, and a feedforward second-order forcing k_2 added.

¹⁷We used Mathematica version 11, and specifically the functions `D`, `Integrate`, `DSolve`, `Series`.

$w(y, t, \varepsilon) = \frac{1}{4}(k_1 - y\beta) \sin(2t)$ using (3.30), where we see that there is no ε -dependence. In the next crucial step, we check that w accomplishes its role in the proof of Thm. 1, by computing

$$\begin{aligned} & (I + \varepsilon D_y w)^{-1} \left[\varepsilon \bar{f}(y + \varepsilon w(y, t, \varepsilon)) + \varepsilon \tilde{f}(y + \varepsilon w(y, t, \varepsilon), t, \varepsilon) - \varepsilon \frac{\partial w(y, t, \varepsilon)}{\partial t} \right] \quad (3.31) \\ &= \varepsilon \bar{f}(y) + \left(k_2 t y^2 - \frac{1}{16} \beta (k_1 - y\beta) \sin(4t) \right) \varepsilon^2 + \mathcal{O}(\varepsilon^3) = \varepsilon \bar{f}(y) + \mathcal{O}(\varepsilon^2), \end{aligned}$$

as required (compare to (3.25)).

Example 2 (Explicit averaging coordinate change (inverted pendulum)). Now let¹⁸ $f(x, t, \varepsilon) = gx \cos(\alpha t) + \varepsilon x^3 t$, with $T = \pi$.

First we compute $\bar{f} = \frac{1}{\alpha\pi} gy \sin(\alpha\pi)$ according to (3.21). Next, we can find

$$w(y, t, \varepsilon) = gy \left(-\frac{1}{\alpha\pi} t \sin(\alpha\pi) + \frac{1}{\alpha} \sin(\alpha t) \right)$$

using (3.30), where we see that there is no ε -dependence. Next we compute (3.31) and get

$$\begin{aligned} & \varepsilon \bar{f}(y) + \left(\frac{\pi_2 t y^3 \alpha^2 - g^2 \pi t y \alpha \cos(t\alpha) \sin(\pi\alpha) + g^2 t y \sin^2(\pi\alpha) + g^2 \pi^2 y \alpha \cos(t\alpha) \sin(t\alpha) - g^2 \pi y \sin(\pi\alpha) \sin(t\alpha)}{\pi^2 \alpha^2} \right) \varepsilon^2 \\ &+ \mathcal{O}(\varepsilon^3) \\ &= \varepsilon \bar{f}(y) + \mathcal{O}(\varepsilon^2), \end{aligned}$$

as required.

Lemma 3 (Endpoint behavior of averaging coordinate change). *At $t = T$, the coordinate change w has the properties*

- (i) $w(y, T, \varepsilon) = 0$, and
- (ii) $D_y w(y, T, \varepsilon) = 0$.

Proof. We have

$$w(y, T, \varepsilon) \stackrel{(3.24)}{=} \int_0^T \tilde{f}(y, \sigma, 0) d\sigma \stackrel{(3.23)}{=} \int_0^T f(y, \sigma, 0) d\sigma - T \bar{f}(y) \stackrel{(3.21)}{=} 0$$

by the definition of \bar{f} . Similarly,

$$\begin{aligned} D_y w(y, T, \varepsilon) & \stackrel{(3.24)}{=} \int_0^T D_y \tilde{f}(y, \sigma, 0) d\sigma \stackrel{(3.23)}{=} \int_0^T D_y f(y, \sigma, 0) d\sigma - T D_y \bar{f}(y) \\ &= D_y \left(\int_0^T f(y, \sigma, 0) d\sigma - T \bar{f}(y) \right) \stackrel{(3.21)}{=} 0, \end{aligned}$$

where in the penultimate step, we switched the order of the derivative and the integral. \square

We remark here that the result of Lemma 3 is unsurprising: the intuitive purpose of \tilde{f} is to capture

¹⁸This is an inverted pendulum $\ddot{\theta} = \varepsilon g \sin \theta$

the “deviation” between the original vector field f (3.20) and \bar{f} (3.21), and we should expect (from the definition of the “average” vector field) that the deviation integrates to 0.

Switching systems (constant flow time)

Now suppose that instead of a smooth periodic system, we have a switching system with the flow of (3.20) punctuated by a reset, R (acting on the original x -coordinates). We assume for this section that the reset acts after a fixed flow time, T , of (3.20), and relax this assumption in the next section.

Theorem 2 (Switching Averaging Theorem). *Given the “original” and “averaged” switching systems of the forms*

$$\dot{x} = \varepsilon f(x, t, \varepsilon), \quad \dot{\theta} = 1, \quad x(T_+) = R(x(T)), \quad (3.32)$$

$$\dot{y} = \varepsilon \bar{f}(y), \quad \dot{\theta} = 1, \quad y(T_+) = R(y(T)), \quad (3.33)$$

where θ is reset to 0 by the switching event, we assert the following hypotheses on (3.33):

- (i) If the C^r (for $r \geq 2$) reset R (allowed to vary with ε) satisfies (a) $DR(x) = S_0 + \varepsilon S_1(x, \varepsilon)$ (with constant S_0), (b) S_0 is invertible, and its unity eigenvalues have diagonal Jordan blocks¹⁹, and
- (ii) if there is a point p_0 such that (a) it is an equilibrium of \bar{f} , (b) $R(p_0) = p_0$, and (c) the averaged return map is hyperbolic at p_0 ,

then there exists $\varepsilon_0 > 0$ such that, for all $0 < \varepsilon \leq \varepsilon_0$, (3.32) possesses a unique hyperbolic periodic orbit, of the same stability type as p_0 .

Proof. First, we apply the C^r coordinate change (3.24). As shown in the proof of Thm. 1(i), w converts the continuous dynamics in (3.32) to take the form of (3.22). Define the reset after the averaging coordinate change,

$$R_y := h^{-1} \circ R \circ h, \quad (3.34)$$

and convert (3.32) to the switching system

$$\dot{y} = \varepsilon \bar{f}(y) + \varepsilon^2 f_1(y, \theta, \varepsilon), \quad \dot{\theta} = 1, \quad y(T_+) = R_y(y(T)), \quad (3.35)$$

where $(y, \theta) \in \mathbb{R}^n \times \mathbb{S}^1$, and $\mathbb{S}^1 = \mathbb{R}/T$ is a circle of length T . We know that the continuous flow of (3.35) can be approximated by (3.21) after changing coordinates; but we need check how R_y and R are related using (3.34).

First, note that since R_y only acts on $y(T)$, and since the time dynamics in (3.35) are decoupled, we only ever need compute $R_y(y(T))$, and $DR_y(y(T))$. From (3.24) and (3.34),

$$R_y(y(T)) = R(x(T)) - \varepsilon w(x(0), 0, \varepsilon) \stackrel{(3.29)}{=} R(x(T)) = R(y(T)), \quad (3.36)$$

where we used Lemma 3 to observe that $x(T) = y(T) + \varepsilon w(y(T), T, \varepsilon) = y(T)$ for the last equality, and where $T_+ = 0$ after the reset. Similarly, for the spatial Jacobian, first note that $D_y w(y, 0, \varepsilon) = 0$

¹⁹Equivalently, unity eigenvalues have algebraic multiplicity 1.

from the assertion (3.29) for each $y(0)$. Then,

$$DR_y(y(T)) = DR(x(T)) \left[I + \varepsilon D_y w(y(T), T, \varepsilon) \right] = DR(y(T)),$$

where we used Lemma 3 for the last step.

The remainder of this proof follows closely the proof of Thm. 1(ii), and we refer to those steps when convenient. Consider the Poincare maps P_0 , P_ε , and associated with (3.33) and (3.35). Define a section $\Sigma := \{(y, \theta) : \theta = 0\}$, and the first return or time T Poincare maps $P_0 : \mathcal{U} \rightarrow \Sigma$, $P_\varepsilon : \mathcal{U} \rightarrow \Sigma$ are then defined for (3.33), (3.35) as the flow maps associated with a time- T flow of each of the time-varying dynamics, with initial condition $t = 0$, composed with their respective resets

$$P_0 := R \circ Q_0, \quad P_\varepsilon := R_y \circ Q_\varepsilon,$$

where $\mathcal{U} \subseteq \Sigma$ is some open set, and Q_0, Q_ε are the time- T flows.

As shown in steps (b)–(c) in the proof of Thm. 1(ii), $DQ_0(p_0) = \exp[\varepsilon T D\bar{f}(p_0)]$, and $DQ_\varepsilon(p_0) = DQ_0(p_0) + \mathcal{O}(\varepsilon^2)$. Additionally, as shown in step (c), the fundamental averaging result Thm. 1(i) shows that $Q_\varepsilon(p_0) = p_0 + \mathcal{O}(\varepsilon)$. Now incorporating the reset,

$$\begin{aligned} DP_\varepsilon(p_0) &= DR(Q_\varepsilon(p_0)) \cdot DQ_\varepsilon(p_0) = DR(p_0 + \mathcal{O}(\varepsilon)) \cdot DQ_\varepsilon(p_0) \\ &= (S_0 + \varepsilon S_1(p_0 + \mathcal{O}(\varepsilon))) DQ_\varepsilon(p_0) \stackrel{\star}{=} (S_0 + \varepsilon S_1(p_0) + \mathcal{O}(\varepsilon^2)) DQ_\varepsilon(p_0) \\ &= (S_0 + \varepsilon S_1(p_0)) DQ_0(p_0) + \mathcal{O}(\varepsilon^2) = DR(p_0) DQ_0(p_0) + \mathcal{O}(\varepsilon^2) \\ &= DP_0(p_0) + \mathcal{O}(\varepsilon^2), \end{aligned} \tag{3.37}$$

where for the step \star , we used the fact that S_1 is Lipschitz continuous.

By the hypotheses in the statement of Thm. 2(ii), we know that P_0 has a fixed point at p_0 , but we need to show that P_ε has a fixed point that is close. From the block equation above, $DP_\varepsilon(p_0) = S_0 + \varepsilon(S_1 + TD\bar{f}(p_0)) + \mathcal{O}(\varepsilon^2)$. By passing to the Jordan form, without loss of generality we assert that $S_0 = V \begin{bmatrix} I_m & 0 \\ 0 & U \end{bmatrix} V^{-1}$ (using the hypothesis that “1” eigenvalues have algebraic multiplicity 1 from Thm. 2(i)), where U does not have a unity eigenvalue. Now let $E(\varepsilon) := V \begin{bmatrix} I_m/\varepsilon & 0 \\ 0 & I_{n-m} \end{bmatrix} V^{-1}$. Define $\zeta(p, \varepsilon) = E(\varepsilon)(P_\varepsilon(p) - p)$. Note that $\zeta(p, 0) = 0$, and letting $\tilde{S}_1 := S_1 + TD\bar{f}(p_0)$

$$\begin{aligned} V^{-1} D_p \zeta(p_0, \varepsilon) V &= V^{-1} E(DP_\varepsilon - I) V = \begin{bmatrix} I_m/\varepsilon & 0 \\ 0 & I_{n-m} \end{bmatrix} (V^{-1} DP_\varepsilon V - I) \\ &= \begin{bmatrix} I_m/\varepsilon & 0 \\ 0 & I_{n-m} \end{bmatrix} \left(\begin{bmatrix} I_m & 0 \\ 0 & U \end{bmatrix} + V^{-1} \tilde{S}_1 V - I \right) \\ &= \begin{bmatrix} I_m/\varepsilon & 0 \\ 0 & I_{n-m} \end{bmatrix} \left(\begin{bmatrix} 0 & 0 \\ 0 & U - I_{n-m} \end{bmatrix} + \varepsilon V^{-1} \tilde{S}_1 V \right). \end{aligned}$$

In the limit $\varepsilon \rightarrow 0$, the top m rows have rank m , since \tilde{S}_1 is full rank (hyperbolicity of the return map $DP_0(p_0)$ asserted in the hypotheses). The bottom $n - m$ rows evaluate to $U - I_{n-m}$; since U has no unity eigenvalues, $U - I_{n-m}$ is also full rank. For $\varepsilon > 0$, the argument is unchanged for the first m rows. For the bottom rows, the entries of $U - I_{n-m}$ dominate those of $\varepsilon V^{-1} \tilde{S}_1 V$ for sufficiently small ε , and so by continuity of eigenvalue with matrix entries, the right hand is full rank. Thus, $D_p \zeta$ is full rank, and using implicit function theorem, we know there is a family of fixed points p_ε for P_ε , and $p_\varepsilon = p_0 + \mathcal{O}(\varepsilon)$.

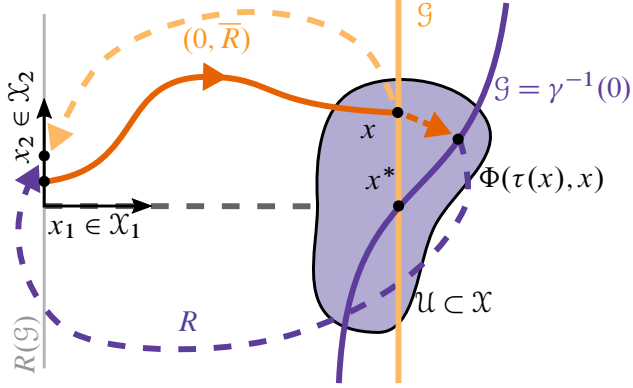


Figure 24: We define a class of hybrid averageable systems (Thm. 3) with a single domain, fast (x_1) and slow (x_2) coordinates, with general conditions on the flow (dark orange), and requirements on fixed points of the flow and the reset, x^* . The calculations in Thm. 3 show how to construct a new hybrid system with constant flow time (yellow, guard $\bar{G} := \{x_1^*\} \times \mathcal{X}_2$) for any hybrid system with variable flow time (purple, guard $\mathcal{G} = \gamma^{-1}(0)$) by augmenting with a flow-to-reset map.

As shown in step (e) in the proof of Thm. 1(ii), we have $DQ_\varepsilon(p_\varepsilon) = DQ_0(p_0) + \mathcal{O}(\varepsilon^2)$, and we showed in the steps leading to (3.37) that $DR(Q_\varepsilon(p_0)) = DR(p_0) + \mathcal{O}(\varepsilon^2)$. Similar to those steps, we can show that $DR(Q_\varepsilon(p_\varepsilon)) = DR(p_0) + \mathcal{O}(\varepsilon^2)$. Putting these together,

$$\begin{aligned} DP_\varepsilon(p_\varepsilon) &= DR(Q_\varepsilon(p_\varepsilon))DQ_\varepsilon(p_\varepsilon) = (DR(p_0) + \mathcal{O}(\varepsilon^2))(DQ_0(p_0) + \mathcal{O}(\varepsilon^2)) \\ &= DP_0(p_0) + \mathcal{O}(\varepsilon^2). \end{aligned} \quad (3.38)$$

Following step (f) in the proof of Thm. 1(ii), we conclude the desired result. \square

3.2.3 Hybrid Systems (Event-Based Switching)

Hybrid systems arising in legged locomotion and other fields often encounter a discrete reset at a state-dependent “event,” unlike the fixed flow time we assumed in the previous section. The event is usually described as the intersection of the continuous flow with a guard surface, \mathcal{G} , which triggers a discrete reset of the system state. The time elapsed between these events generally varies with initial condition.

Theorem 3 (Hybrid Averaging Theorem). *Given the “original” hybrid system and “averaged” switching system of the forms*

$$\dot{x} = \varepsilon f(x, \sigma, \varepsilon), \quad \dot{\sigma} = 1, \quad \gamma(x, \sigma) = 0 \implies x_+ = R(x, \sigma), \quad (3.39)$$

$$\dot{y} = \varepsilon \bar{f}(y), \quad \dot{\sigma} = 1, \quad \sigma = T \implies y_+ = \bar{R}(y), \quad (3.40)$$

where \bar{R} is constructed from R as we show in the proof, we assert the following hypotheses on (3.39)–(3.40). If

(i) the guard set satisfies (a) assuming $D_\sigma \gamma = 1$,²⁰ $D_x \gamma = \mathcal{O}(\varepsilon)$, and (b)

²⁰This can be done without loss of generality by scaling γ as long as $D_\sigma \gamma \neq 0$, which we assert as a condition on the

- (ii) the C^r (for $r \geq 2$) reset R (allowed to vary with ε) satisfies (a) $D_x R(x, \sigma) = S_0 + \varepsilon S_1(x, \sigma, \varepsilon)$ (with constant S_0), (b) S_0 is invertible, and its unity eigenvalues have diagonal Jordan blocks, and
 - (iii) there is a point p_0 and $T > 0$, such that (a) p_0 is an equilibrium of \bar{f} , (b) $\bar{R}(p_0) = p_0$, and (c) $T := \min_{t>0} \{t : \gamma \circ \exp(tD\bar{f}(p_0)) = 0\}$, (d) the matrix $S_0 + \varepsilon(\mathbf{U} + \mathbf{V})$, where $\varepsilon\mathbf{U} := \varepsilon S_1(x, T, \varepsilon) - D_\sigma R \cdot D_x \gamma$, $\mathbf{V} := TD\bar{f}$ is hyperbolic at p_0 ,
- then there exists $\varepsilon_0 > 0$ such that, for all $0 < \varepsilon \leq \varepsilon_0$, (3.39) possesses a unique hyperbolic periodic orbit, of the same stability type as p_0 .

Proof. We first provide a construction that enables us to locally transform a system with variable flow time (3.39), to a system with constant flow time that has equivalent²¹ Poincaré (i.e., flow-and-reset) dynamics. Let $\Phi(x, t)$ denote the maximal flow associated with the continuous dynamics of (3.39) from initial condition $(x, \sigma = T)$.²² Since $\dot{\sigma} \equiv 1$, $\pi_\sigma \Phi = t$. Any initial condition $(x, 0)$ impacts the guard as

$$\gamma \circ \Phi(x, t) = 0, \quad (3.41)$$

where t may be negative. Applying the implicit function theorem (IFT) (Hirsch et al., 1974, App. IV)²³ to (3.41) with respect to t at test point $(x, 0)$ yields a C^1 time-to-event map $\tau : \mathcal{U} \rightarrow \mathbb{R}$ where $\mathcal{U} \subset \mathcal{X} \times \mathbb{R}$ is a neighborhood of $(x, 0)$ (Hirsch et al., 1974, Ch. 11, Sec. 2) such that $\gamma \circ \Phi(x, \tau(x)) \equiv 0$. Note that the image of τ includes negative times. The derivative (i.e. gradient) of τ can be computed at $(x, 0)$ by differentiating (3.41) with respect to x (recall that $D_x \Phi(x, 0) = \begin{bmatrix} I \\ 0 \end{bmatrix}$)

$$D\gamma \cdot (D_x \Phi + D_\sigma \Phi \cdot D\tau) = 0 \implies D\tau = \frac{-D_x \gamma}{\varepsilon D_x \gamma \cdot f + 1}, \quad (3.42)$$

since we assumed $D_\sigma \gamma = 1$ without loss of generality. Define the time- T -flow equivalent reset $\bar{R} : \pi_x \mathcal{U} \rightarrow \mathcal{X}$ by

$$\bar{R}(x) := R \circ \Phi(x, \tau(x)). \quad (3.43)$$

Differentiating with respect to x using chain rule, and substituting using (3.42) we can compute

$$\begin{aligned} D_x \bar{R}(x) &= DR \cdot (D_x \Phi(x, 0) + D_\sigma \Phi \cdot D\tau) \\ &\stackrel{(3.42)}{=} DR \cdot \left(\begin{bmatrix} I \\ 0 \end{bmatrix} - \frac{1}{\varepsilon D_x \gamma \cdot f + 1} \begin{bmatrix} \varepsilon f \\ 1 \end{bmatrix} D_x \gamma \right) \\ &= D_x R - D_\sigma R \cdot D_x \gamma + \mathcal{O}(\varepsilon^2), \end{aligned} \quad (3.44)$$

using the hypothesis that $D_x \gamma = \mathcal{O}(\varepsilon)$.

transversality of the flow and the guard.

²¹We use the term “equivalent” to denote a correspondence stronger than conjugacy; whereas the flows are indeed conjugate, the return maps are identical.

²²This initial condition corresponds to the nominal impact time, not the initialization of the continuous dynamics at $\sigma = 0$. Additionally, the reader should note that we keep “ x ” arbitrary for now, i.e. the following calculations hold for any x .

²³Justified since $D_\sigma \gamma \circ \Phi \neq 0$.

Let Φ_x now denote the flow of the continuous dynamics of (3.39) starting from initial condition $(x, \sigma = 0)$. Consider the switching system

$$\dot{x} = \varepsilon f(x, \sigma, \varepsilon), \quad \dot{\sigma} = 1, \quad \sigma = T \implies x \mapsto \bar{R}(x), \quad (3.45)$$

and its flow-and-reset return map

$$\bar{R} \circ \Phi_x(x, T) \stackrel{(3.43)}{=} R \circ \Phi(\Phi_x(x, T), \tau \circ \Phi_x(x, T)),$$

which corresponds exactly to the return map for (3.39). Additionally, note that $D_x \bar{R} = S_0 + \varepsilon \mathbf{U}$, and that the averaged return map for (3.40) would be

$$D\bar{P}(p_0) = D\bar{R}(p_0)(I + \varepsilon T D\bar{f}) + \mathcal{O}(\varepsilon^2) =: S_0 + \varepsilon(\mathbf{U} + \mathbf{V}) + \mathcal{O}(\varepsilon^2). \quad (3.46)$$

With the hyperbolicity of $D\bar{P}(p_0)$, all of the conditions of Thm. 2 are satisfied by the systems (3.45) and (3.40), and upon its application, we get the desired result. \square

To demonstrate the applicability of hybrid averaging to analysis of physical systems, we first investigate a 1DOF hybrid system. We consider one of the two hoppers depicted in Fig. 25: a unit mass restricted to travel along its vertical axis with an attached massless leg. We choose this as our first example for two reasons. First, despite its apparent simplicity, it serves as a template for ubiquitous running and hopping behavior in robots and animals [Blickhan and Full \(1993\)](#). Variants of this model have been analyzed extensively in the literature, e.g. see [Koditschek and Buehler \(1991\)](#) for analysis of a one degree-of-freedom (1DOF) restriction of this planar point-mass model whose energizing input is inspired by the empirically successful strategies reported in [Raibert \(1986\)](#). Second, the simplicity of the equations of motion mitigate the intricacies of the hybrid averaging, exposing in particular the synergistic relationship of this method with symmetry, which we discuss further in Sec. 3.6.2.

Informed by the structure of the preceding averaging results, we propose an alternative energization scheme (intuitively similar but physically distinct from [Raibert \(1986\)](#)) and apply Thm. 3 to establish an analogous stability result. The analyses in [Koditschek and Buehler \(1991\)](#) relied on two simplified models that both admitted closed form return maps ([Koditschek and Buehler, 1991](#), eqns. (15), (17)). However, hybrid averaging allows a stability analysis without requiring integrable²⁴ stance dynamics (e.g. (3.99)). Recall that even the “simple” 2DOF SLIP dynamics [Saranli et al. \(1998\)](#) are non-integrable, hence motivating an analysis tool that drops this requirement.

Example 3 (Single vertical hopper). Choose the coordinates $\sigma := \psi_1 + \pi/2$, and $x := a_1$. We have the system dynamics (3), and so

$$\frac{da_1}{d\psi_1} = \varepsilon \frac{\cos \psi_1 v_1}{w + \varepsilon \sin \psi_1 v_1} =: \varepsilon f(a_1, \psi_1, \varepsilon).$$

²⁴We remind the readers of the distinction between an integrable flow, and the averaging integral (3.21). In the latter case, we integrate the vector field over a single “phase” parameter while holding the other states constant.

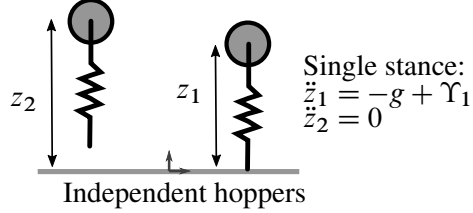


Figure 25: Two decoupled unit mass vertical hoppers, shown here in a single stance mode.

The averaged vector field (3.21) is then (changing variables from σ to ψ_1)

$$\bar{f}(a_1) = \int_{-\pi/2}^{\pi/2} \frac{v_1 \cos \psi_1 d\psi_1}{\pi \omega} = \frac{k - a_1 \beta}{2\omega}. \quad (3.47)$$

Clearly the point

$$a_1^* = k/\beta \quad (3.48)$$

is an equilibrium of the averaged vector field above²⁵.

The guard set is defined by the physical liftoff event when the normal force at the toe-ground interface during stance goes to 0, i.e.

$$\gamma(a_1, \psi_1) := \frac{1}{\tan \psi_1} - \frac{\varepsilon(ka_1 - \beta)}{\omega}, \quad (3.49)$$

scaled such that $D_{\psi_1} \gamma = 1$ at $\psi_1 = \pi/2$. Clearly, $D_{a_1} \gamma = \mathcal{O}(\varepsilon)$.

The massless in-flight leg is reset to its nominal length, ρ . It follows from (3.4) that the touchdown phase, ψ_1 is identically $-\pi/2$ since $z_1 = \rho$ at the touchdown event. Noting from (3.4) that $\dot{z}_1 = -a_1$ at touchdown, and recalling that the mechanical energy a_1 is conserved in flight (3.4), we can solve for a_1 at touchdown, yielding

$$R(a_1, \psi_1) = \sqrt{a_1^2 \sin^2 \psi_1 - 2ga_1 \cos \psi_1 / \omega} \implies D\bar{R} \stackrel{(3.44)}{=} [1, g/\omega]. \quad (3.50)$$

and so we can calculate \mathbf{U} according the definition in Thm. 3,

$$\mathbf{S}_0 = 1, \mathbf{U} = -\frac{g\beta^2}{k\omega^2}.$$

Together with $\mathbf{V} := \pi D\bar{f} = -\frac{\pi\beta}{2\omega}$, we get $D\bar{P}$ (3.46) at its fixed point is $1 - \varepsilon \left(\frac{g\beta^2}{k\omega^2} + \frac{\pi\beta}{2\omega} \right) < 1$. We conclude using Thm. 3 that this hopper is stable.

²⁵In intuitive terms, we point out that the oscillatory control signal introduced in (3.5) has the special property that the k -term possesses a particular symmetry with respect to ψ_1 . Consequently, after the averaging step, k persists in the averaged a_1 -dynamics (3.47), whereas if v_1 contained a $\sin \psi_1$ it would get integrated out. We explicitly show the greater role of symmetries in averaging in Sec. 3.6.2.

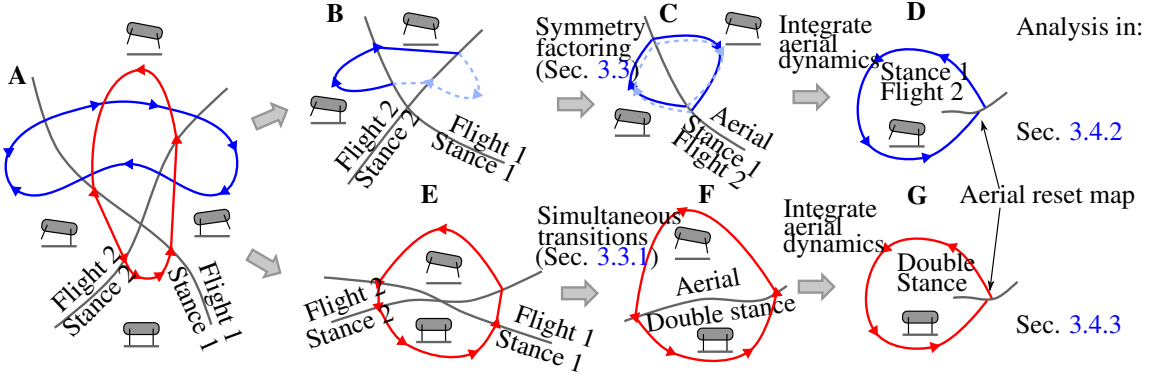


Figure 26: A depiction of the two kinds of hybrid dynamical limit cycles analyzed here. In the full (visualized as two-dimensional) product domain, there are four possible modes corresponding to each of the two legs being in flight or stance. We (locally) analyze two limit cycles (A): one with alternating stances interspersed with aerial phases (blue), and one with “short” single stance periods. In the former case, we use symmetry (Sec. 3.3) to factor the return map into two iterations of a “half return map” (3.54) (B, C), integrate the trivial aerial dynamics, and get a single-mode hybrid system (D). In the latter case, we assume that active toe extension control (Sec. 3.3.1) can be used to eliminate the short single-stance periods and enforce simultaneous transition between aerial and double stance modes (E, F), integrate the trivial aerial dynamics, and recover another single-mode hybrid system (G). In Sec. 3.4.2 and Sec. 3.5.4 we analyze a limit cycle of form D, and in Sec. 3.4.3, Sec. 3.5.5 we analyze a limit cycle of form G.

3.3 Symmetry-Factored Hybrid Averaging

We are able to directly use the single-mode result of Sec. 3.2.3 to demonstrate stability of a “monoped” in the upcoming Example 3. We develop two small extensions to the theoretical result in the following two subsections that allow the result to be applicable in a broader class of “biped” systems that we detail below.

The sagittal plane vertical hopper model we present in Fig. 25 can have four physical modes (resulting from none, one of the two, or both legs in stance), and Fig. 26 suggests how the focus only on in-phase or anti-phase limit cycles leads to a formal reduction to the “single mode with reset” hybrid system (Thm. 3). For the in-phase case (bottom row of Fig. 26) the limit cycle of interest passes through only two modes (double support and flight). In Sec. 3.3.1, we will observe that our control affordance (each leg of the abstract “machine” analyzed here—and indeed the physical machine Minitaur—has two independently actuated degrees of freedom) allows us to force operation into this regime where integrating the aerial dynamics reduces the flight mode to a mere factor of a single mode reset map (as we show in the single-leg example of Example 3). However, for the anti-phase case (top row of Fig. 26), the limit cycle of interest passes through three modes and even after replacing the flight flow with its integrated reset map, we must still extend the Thm. 3 result to a class of hybrid systems with two continuous modes. We achieve this extension by imposing a symmetry condition on the dynamics of the two alternating single stance modes as follows.

We begin by specializing the notion of a standard *hybrid dynamical system* as defined in (Burden et al., 2015, Def. 1).

Definition 1. A K -symmetry-factored hybrid system is a tuple $H_K = (\mathcal{X}, F, \mathcal{G}, R)$ such that

- (i) $(\mathcal{X}, F, \mathcal{G}, R)$ is a hybrid dynamical system as defined in (Burden et al., 2015, Def. 1) with two modes, i.e. index set $J = \{1, 2\} \approx \mathbb{Z}_2$;
- (ii) $\mathcal{X}_{(1)}$ and $\mathcal{X}_{(2)}$ are isomorphic, and $K : \mathcal{X}_{(j)} \rightarrow \mathcal{X}_{(j+1)}$ is an involutive symmetry, i.e. $K^2 = \text{id}$;
- (iii) the vector field, guard, and reset respect the symmetry, i.e. (a) $\text{DK} \cdot F_{(j+1)} \circ K = F_{(j)}$, (b) $\gamma_{(j+1)} \circ K = \gamma_{(j)}$, and (c) $R_{(j+1)} = K \circ R_{(j)} \circ K$, where $\gamma_{(j)}$ is any function such that $\mathcal{G}_{(j)} \equiv (\gamma_{(j)})^{-1}(0)$; and
- (iv) the resets map to the “next” domain, i.e. $R_{(j)} \circ \mathcal{G}_{(j)} \subset \mathcal{X}_{(j+1)}$,

Remark 3. Note that we have made the following notational changes from (Burden et al., 2015, Def. 1): (a) we append the subscript “ K ” to make explicit that these elements are disjoint unions of domains or maps specific to our K –symmetry conditions above, (b) we refer to the domain with the symbol “ \mathcal{X}_K ” instead of “ D ”, (c) we use parenthesized subscripts for the index set, for example, $\mathcal{X}_K := \bigsqcup_{j \in J} \mathcal{X}_{(j)}$, and (d) we make use of a (non-unique) implicit representation of the guard, $\gamma_{(j)}(\mathcal{G}_{(j)}) \equiv 0$.

Remark 4. Symmetry-factoring has been previously exploited to simplify return map calculations in Altendorfer et al. (2004). In that case, *time-reversal symmetry* of Hamiltonian SLIP within a single stance is utilized to factor a SLIP return map, whereas here, we utilize the symmetric steps of a bipedal gait, in order to factor the full return map that represents a complete stride into a “half-return map” (3.54) that only contains a single step.²⁶ More generally, notwithstanding the present-seeming special nature of these factorizations, we suspect that symmetry analysis of this nature will play an important role in many more legged locomotion settings.

Here we exclusively analyze systems with two degrees-of-freedom (DOF). The reset map thus has four dimensions²⁷, i.e. $\mathcal{X} \approx \mathbb{R}^4$. The symmetry map (Def. 1(iii)) we use is

$$K : \mathbb{R}^4 \rightarrow \mathbb{R}^4 : (a_{(j)}, \psi_{(j)}) \mapsto (a_{(j+1)}, \psi_{(j+1)}), \quad (3.51)$$

and specifically, the (reduced dimensional) matrix

$$\overline{K} := \begin{bmatrix} 0 & 1 & 0 \\ 1 & 0 & 0 \\ 0 & 0 & -1 \end{bmatrix} \in \mathbb{R}^{3 \times 3} \quad (3.52)$$

is helpful in defining the reset maps in Sec. 3.4.2 and Sec. 3.5.4.

The first condition in Def. 1(iii) essentially states that $F_{(j)}$ are conjugate through the K ; from this we automatically conclude that

$$K \circ Q_{(j+1)} = Q_{(j)} \circ K, \quad (3.53)$$

where $Q_{(j)}$ is the flow of $F_{(j)}$ till it intersects the guard surface $\gamma_{(j)}$.

²⁶We envision that exploiting within-stance time-reversal symmetry as in Altendorfer et al. (2004) could augment the method here, for further analytical benefit (as we pursue with work already in progress seeking to analyze the composition of in-place behaviors with the fore-aft motions treated as disturbances in Sec. 4.2.3, Sec. 4.2.4).

²⁷We describe in each case which of these four coordinates is averaged.

For such a limit cycle of the kind depicted in Fig. 26B,

$$\begin{aligned}
P_K &= R_{(1)} \circ Q_{(1)} \circ R^{(0)} \circ Q^{(0)} \\
&= (K \circ R^{(0)} \circ K) \circ Q_{(1)} \circ R^{(0)} \circ Q^{(0)} \\
&\stackrel{(3.53)}{=} K \circ R^{(0)} \circ (Q^{(0)} \circ K) \circ R^{(0)} \circ Q^{(0)} \\
&= (P^{(0)})^2,
\end{aligned}$$

i.e. the full return map $P_K = P_{(1)}^2$, where

$$P_{(1)} := K \circ R_{(1)} \circ Q_{(1)} \quad (3.54)$$

is a ‘‘half return map.’’ It is clear from this that the stability properties of the limit cycle are fully described by the half return map. Consider the single-mode hybrid system, $H_{(1)} = (\mathcal{X}_{(1)}, F_{(1)}, \mathcal{G}_{(1)}, K \circ R_{(1)})$. The return map of $H_{(1)}$ is simply $P_{(1)}$ for all limit cycles of the kind shown in Fig. 26B.

Thus, the symmetry properties in Def. 1 allow us to analyze the single-mode system $H_{(1)}$ and make conclusions about limiting behavior of H_K . Accordingly, suppressing the single-mode subscript label, we return to the specialized structure of an averageable hybrid system (Thm. 3) and consider the tuple $H = (\mathcal{X}, F, \mathcal{G}, R, x^*)$, where $\mathcal{X} := \mathcal{X}_{(1)}$, $F := F_{(1)}$, $\mathcal{G} := \mathcal{G}_{(1)}$, $R := K \circ R_{(1)}$ (again, we emphasize that we have dropped the subscripts since we need only analyze behavior in the first mode), and x^* . In the analytical results of Sec. 3.5.2, we prove in each case that H is *averageable* at x^* , and employ Thm. 2 or Thm. 3 for our stability analyses in Sec. 3.4.2 and Sec. 3.5.4.

3.3.1 Near-Simultaneous Transitions

We now consider the in-phase limit cycle depicted in the bottom row of Fig. 26. Specifically, as anticipated above, we bring its analysis under the sway of the restricted single mode framework of Thm. 3 by enforcing transitions through the higher codimension guard set intersections where both toe-touching constraints are active.

Assumption 3. *In the limit cycles of type Fig. 26E–G, active control of the leg extension is used in the aerial phase to execute simultaneous touchdown and liftoff.*

Since the actuators only have to move the toes (small inertia), this action is almost devoid of any energy cost.

We provide numerical and empirical justification for this assumption following the introduction of more physically realistic models (Fig. 27A–C). In Sec. 3.5.6, we compare traces from simulations with active toe extension control in aerial phase either enabled or disabled from a variety of initial conditions Fig. 35 to illustrate how the resulting trajectories become nearly indistinguishable after a few strides. Independently, even without imposing such active control on the physical Minitaur robot, the relative frequency of single stance in empirical pronking is low, is 6.31% in Fig. 51, and 6.65% in Fig. 53, lending support to our ‘‘simultaneous transition’’ assumption for the pronking analysis (Sec. 3.3.1). It is worth noting in passing that these empirical observations, revealing as they do the rarity (even absent active control) of single stance in pronking, lend further support to the suggestion emerging from the analysis of Burden et al. (2016) (motivated by the prevalence

of virtual bipedal and monopodal gaits in biology) that such high codimension transitions might, themselves, be preflexively attracting.

3.4 Application: Coordination of Independent Vertical Hoppers (2DOF)

For the next two sections, we apply hybrid averaging the study of coordination of two vertical hoppers, first mechanically uncoupled (this section), and then with coupling due to the connecting body (Sec. 3.5). For the analytical results in these two sections, we list our models in Fig. 27, and our assumptions in Table 5.

Consider a physical plant with a pair of vertically-constrained masses (of unit mass), suspended by massless legs with nominal extension $\rho \in \mathbb{R}_+$. The configuration variables of interest are physical heights of the masses, $z_i \in \mathbb{R}_+$. This model is depicted in Fig. 27A.

We get two modes, stance and flight, based on whether the height is less than the nominal leg extension (as formalized below in (3.99)). The equations of motion for the two hoppers (indexed by $i \in \mathcal{I} := \{1, 2\}$) are

$$\ddot{z}_i = \begin{cases} -g + \Upsilon_i & z_i < \rho, \text{ and} \\ -g & \text{else,} \end{cases} \quad (3.55)$$

where Υ_i is the shank extension force generated by leg i . We discuss scaling the morphological parameters more in Sec. 3.5, but for this section we assume that the shank extension controller compensates for the known dynamical parameters as

$$\Upsilon_i := g + u_i, \quad (3.56)$$

where u_i is the parameter-agnostic “template controller” signal derived from Sec. 3.1.1.

3.4.1 Oscillatory Energization and Phase Control

In order to express the dynamics of our plant models in terms amenable to application of hybrid averaging, we use our intuition to find appropriate slow “phase difference” coordinates. This idea is inspired by Proctor et al. (2010), where differences of phases of identical coupled oscillators are shown to be slow, and a classical averaging application follows. We introduce the following *local* (by this we mean that δ is a smooth function of the physical states while in a single hybrid mode,

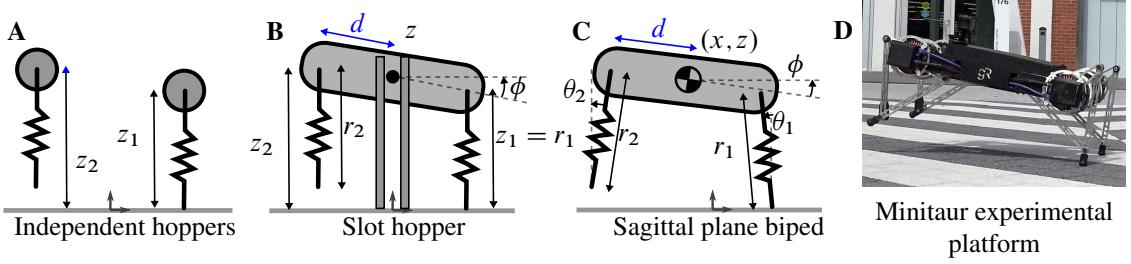


Figure 27: *Virtual biped models of increasing complexity.* Building on our previous work on the coordination of a pair of mechanically decoupled vertical hoppers (A) De et al. (2016), we now introduce the slot hopper (B) as a new template for quadrupedal running. Its coordination stability analysis (Sec. 3.5.2), guides the synthesis of preflexive and feedback coordinated gaits in the progressively more complicated dynamics of the sagittal plane biped (C) and the physical Minitaur robot (D) Kenneally et al. (2016), Minitaur (2016) (Sec. 4.2) that robustly anchor this template (in the sense of Full and Koditschek (1999)) when properly compensated according to our controller designs. Fig. 30 and Table 6 summarize the relationships between these models, our controllers, and our analytical, numerical and empirical results.

but discontinuous across modes²⁸) definition for “phase difference”:

$$\delta := \tau_1 - \tau_2, \text{ where} \quad (3.57)$$

$$\tau_i := \begin{cases} (\psi_i - \pi/2)/\omega_v & z_i < \rho, \text{ and} \\ (\psi_i - 1/2)/\omega_f(a_i) & \text{else,} \end{cases}$$

Note that the coordinates above have the units of time (this is apparent from the definition above, since ψ_i are unitless (3.4), and ω_v (3.5) and ω_f (3.10) both have units of s^{-1}).

The v_i term in our vertical hopper control (3.5) contains the various nonlinearities responsible for asymptotic stability and phase control. This includes a lumped viscous friction term (which is assumed to come from unavoidable parasitic sources), as well as terms introduced by feedback:

$$v_i(x) := -\beta \dot{z}_i - k_a \cos \psi_i + w_i(x), \quad (3.58)$$

where the second summand in the last equation is an oscillatory energization term De and Koditschek (2015b) that can intuitively be thought of as “negative damping”²⁹, and the last summand introduces a new feedback phase-control term. The phase controller expressed in the functional form of $w_i(x)$

²⁸The discontinuity of (3.57) across modes does not introduce any analytical issues: all dynamical models considered here fall within the class of self-manipulation hybrid systems Johnson et al. (2016) and are thus guaranteed to have unique and non-blocking executions. We further show, using the distinct strategies depicted in Fig. 26, that they satisfy the averageability requirements, placing them within the class of “smoothable” hybrid systems (Burden et al., 2015, Thm. 3)—so that their executions are guaranteed as well to vary continuously with respect to initial conditions, and be piecewise smooth. Because our coordinate transformations, e.g., (3.4) are written for convenience across the distinct modes of the original physical coordinates of the self-manipulation system, they are not formally continuous functions. However, as depicted in Fig. 26, both routes to the single mode averageable model subsume into its formal reset map the erstwhile continuous flows through “uninteresting” (and integrable) modes of the physical coordinates, so that (3.4) and (3.57) operate only in a single mode in which they are indeed smooth functions.

²⁹From (3.4), $-k_a \omega \cos \psi_i = (\varepsilon k_a / a_i) \dot{z}_i$ (forcing in the direction of velocity, but normalized by a_i).

is discussed in Sec. 3.4.1.

Coordination controllers

We propose two kinds of coordination controllers. First, we introduce a *phase controller*³⁰ with phase control gain $k_d \in \mathbb{R}$,

$$w_i(x) = (-1)^{i-1} k_d (\dot{z}_1 - \dot{z}_2) \sin \psi_i. \quad (3.59)$$

Looking ahead, setting $k_d > 0$ in Sec. 3.4.2 stabilizes an anti-phase limit cycle (the template for a “bounding” gait, whereas setting $k_d < 0$ in Sec. 3.4.3 stabilizes a limit cycle entraining the two legs in-phase (the template for a “pronking” gait).

Second, we introduce an empirically-motivated *attitude controller* (only for pronk stabilization) which adds a proportional control term to (3.59),

$$w_i(x) = (-1)^{i-1} (k_p(z_1 - z_2) + k_d(\dot{z}_1 - \dot{z}_2)), \quad (3.60)$$

for $i \in \mathcal{J}$.

We verify analytically the efficacy of these controllers with respect to the mechanically isolated hoppers of Fig. 25 in Sec. 3.5.2. In Sec. 3.5 we will show, first, that these stability results persist for a weakly mechanically coupled instance of the hoppers Sec. 3.5.4 and then, turn to a similar but more intricate analysis of what we will term “preflexive” stabilization wherein the influence of two distinct modes of (first, stronger, and then much stronger) mechanical coupling substitutes in place of any feedback control.

We remark here that (3.59) and (3.60) are both trivial to implement on a physical platform, since the only sensory information required is of the coordinate $z_1 - z_2$, and its derivative. For example, on the physical Minitaur robot this information can be measured directly through the physical angle ϕ and its derivative (3.90).

A physical surrogate for abstract phase difference

In each of Sec. 3.4.2–3.4.3, a more straightforward proof involving algebraically simpler terms could have been obtained by introducing instead of (3.59) a coordination term based upon the abstract phase difference

$$w_i(x) = (-1)^{i-1} k_\psi \sin \psi_i \sin(\omega \delta), \quad (3.61)$$

as in (Klavins et al., 2000, eqn. (7)). This is because in both of the preceding averaging analyses, δ is shown to be a “slow” coordinate ($\dot{\delta} = \mathcal{O}(\varepsilon)$), and can be held constant while performing the averaging integral in (3.67) and (3.81).

However, the analytically simpler alternative (3.61) requires computation of the abstract phase difference δ for implementation, which is quite involved (3.57), especially due to the discontinuities in its definition across modes. In comparison, our globally well-defined phase controller (3.59) is

³⁰Though the arguments of (3.59) seemingly involve only physical coordinates, we justify the use of the term *phase controller* by exposing the strong relation between the energetically relevant “proportional / dissipative” form of (3.59)–(3.60), and abstract phase control in Sec. 3.4.1.

a simple function of the physical variables that can be easily measured with sensors. We observe below that, notwithstanding its simplicity, the coordination controller (3.59) actually functions as a physical surrogate for the abstract phase difference, behaving, in both the in-phase and anti-phase cases, like a proportional phase controller *in the averaged sense*. We then discuss the numerical and empirical utility of this simply implemented surrogate in Sec. 3.4.1.

Although a matter of considerable conceptual interest, we are not aware of an analogously equivalent “abstract” version of the attitude controller (3.60) that is a function of the ψ_i coordinates only.

Closed-loop phase-difference dynamics Though our phase controller (3.59) looks quite different from the abstract version (3.61),

- a) an inspection of the last row of (3.67) reveals that $\dot{\delta} \overset{\text{avg}}{\propto} -\delta$, and
- b) inspection of the $\sin(\omega\delta)$ factor in (or application of the **Series** function in Mathematica to) the last row of (3.81) reveals that $\dot{\delta} \overset{\text{avg}}{\propto} -\delta(a_1^2 + a_2^2) + \mathcal{O}(\delta^2)$,

where we use the $\overset{\text{avg}}{\propto}$ symbol and omit constant positive parameters, but include all functions of state explicitly. In both cases, the closed-loop δ dynamics take the form of a proportional control on δ for small δ , which is identical to the (3.61).

Numerical comparison Fig. 29 shows a numerical comparison between the abstract phase control (3.61) and the approximation (3.59) for both positive and negative signs of the gain k_d , respectively stabilizing a bounding and a pronking limit cycle in a pair of independent hoppers.

The simulation in Fig. 30 shows our approximated phase control applied to coupled vertical hoppers, and more importantly, trials on the physical platform show that (3.59) is able to overcome preflexive stability and stabilize the physical platform leg phases to a desired limit cycle Sec. 4.2.3, 4.2.5.

3.4.2 Two Vertical Hoppers: Anti-Phase Limit Cycle (Bounding)

Here we present a local analysis of the anti-phase limit cycle with alternating stances of hoppers 1 and 2, the results of which are borne out in empirical trials in Sec. 4.2.

We appeal to Def. 1 with symmetry (3.51), and study the half return map with the continuous dynamics $F := F_{(1)}$ —where mode “1” we now define as the one where hopper 1 is in stance, hopper 2 in flight—and where the reset $R := K \circ R_{(1)}$, where $R_{(1)}$ maps states from liftoff of hopper 1 to touchdown of hopper as depicted in the upper series of sketches in Fig. 26.

For this subsection and the next, we enforce the following assumption, whose justification is referenced from the second row of Table 5.

Assumption 4. *The stance duration (resulting from a weakly perturbed spring-mass oscillation) is constant.*

As described in the introduction of Sec. 3.5.2, our empirical trials display more-or-less constant flow time, and we find that the further complication in algebra does not buy any new insight. Still, we include a variable-flow-time version of the return map computation (and stability analysis) that appears in Sec. 3.4.2 to demonstrate in a tutorial manner how an application of Thm. 3 would proceed.

Table 5: Assumptions made to facilitate analytical results. We list how they are utilized, and also point to empirical or numerical justification.

Assumption (title)	Application	Benefit	Justification
3 (simultaneous transitions)	Sec. 3.4.3, Sec. 3.5.5	apply single-mode hybrid averaging Thm. 2	Simulation comparison in Fig. 35; < 7% empirical single stance (Sec. 3.5.6)
4 (constant stance duration)	Sec. 3.5.2	simplify reset map (contrast Sec. 3.4.2)	Fig. 54 shows 6.5% deviation despite perturbations (see Sec. 4.2.4 discussion)
5 (linearized stance constraint)	Sec. 3.5.4–3.5.5	simplify single (3.94) and double (3.96) stance dynamics	Fig. 33 trajectory comparison (with / without)
6 (low initial pitch energy)	Sec. 3.5.5	decouple the CoM and pitching dynamics (3.114)	Fig. 53 shows relative magnitudes of a_ϕ and a_z (see Sec. 4.2.3 discussion)
7 (small flight time)	Sec. 3.5.5	prove the time-varying ϕ -reset (3.122) is a contraction	Only restricts analytical scope to low energy pronking; Fig. 37 shows stability for much higher t_f (see Sec. 3.5.5).

Continuous dynamics For the following analysis, we choose the coordinates $\sigma := \psi_1 + \pi/2$, and $x := (a_1, a_2, \delta)$. The continuous dynamics (3.99) can be rewritten (derivation in Sec. 3.1.1) in the coordinates defined in (3.4), so that

$$\begin{aligned} \dot{a}_1 &= -\varepsilon \cos \psi_1 v_1, & \dot{a}_2 &= 0, \\ \dot{\psi}_1 &= \omega + \frac{\varepsilon}{a_1} \sin \psi_1 v_1, & \dot{\psi}_2 &= \omega_f(a_2), \end{aligned} \quad (3.62)$$

where the ε parameter appears in these positions due to our choice of ε –magnitude nonlinearity in the hopper control (3.5) so as to depend upon the anti-phase stabilizing version ($k_d > 0$) of the phase coordination term w_1 defined in (3.59).

Using the phase difference coordinate δ from (3.57) (note that hopper 1 is in stance and hopper 2 is in flight for the analysis in this subsection), we notice that

$$\frac{d}{dt} \delta = \frac{\varepsilon}{\omega a_1} \sin \psi_1 v_1, \quad (3.63)$$

i.e. by inspection, the presence of the “small” parameter, the factor ε in (3.63), reveals that the chosen phase difference coordinate is “slow” ($\mathcal{O}(\varepsilon)$ dynamics). The continuous dynamics in these coordinates are

$$\begin{aligned} \dot{\sigma} &= \omega + \varepsilon \frac{\sin \psi_1 v_1}{a_1} \\ \dot{x} &= \varepsilon \begin{bmatrix} -\cos \psi_1 v_1 \\ 0 \\ \frac{\sin \psi_1 v_1}{\omega a_1} \end{bmatrix}. \end{aligned} \quad (3.64)$$

Consider the prospective anti-phase fixed point,

$$T = \pi, \quad x^* = [\tilde{k}_a/\tilde{\beta}, \tilde{k}_a/\tilde{\beta}, 0]^T, \quad (3.65)$$

where

$$\tilde{k}_a := k_a + \frac{gk_d}{2\omega}, \quad \tilde{\beta} := \beta - \frac{4k_d}{3\pi}. \quad (3.66)$$

Though the last entry of (3.65) is zero, we emphasize that this denotes an “anti-phase” limit cycle: observe in (3.57) that when hopper 2 attains apex, $\tau_1 = 1/2$, then $\delta = 0$ implies that, simultaneously, the hopper must be experiencing its “bottom” (most compressed) event.

Additionally, note from (3.65) that the the k_d gain introduced through our phase controller (3.59) moves the first two components, of the equilibrium, $x^*, a_1^* = a_2^* = \tilde{k}_a/\tilde{\beta}$, smoothly as a function of that controller gain k_d . The limiting $k_d = 0$ case recovers the isolated vertical hopper equilibrium point (3.48). Direct integration of (3.64), using (3.59) with $k_d > 0$, yields

$$\bar{f}(x) := \int_0^\pi \frac{dx}{d\sigma} d\sigma = \frac{1}{2\omega} \begin{bmatrix} \tilde{k}_a - a_1 \tilde{\beta} \\ 0 \\ -\frac{gk_d}{\omega^2 a_1} \delta \end{bmatrix} \quad (3.67)$$

which evaluates to 0 at x_2^* , satisfying Thm. 2(ii). Moreover, anticipating its use in (3.74), we can calculate the Jacobian as

$$D\bar{f}(x_2) = \begin{bmatrix} -\frac{\tilde{\beta}}{2\omega} & 0 & 0 \\ 0 & 0 & 0 \\ \frac{gk_d \delta}{2\omega^3 a_1^2} & 0 & -\frac{gk_d}{2\omega^3 a_1} \end{bmatrix}. \quad (3.68)$$

Reset The touchdown condition is triggered by the event that hopper 2 touches down, or $\psi_2 - 1$ (3.4) crosses zero. Thus, using K as defined in (3.51), $\pi_1 \circ K \circ R_{(1)} \equiv 0$, satisfying Thm. 2(i), where $R_{(1)}$ maps state from liftoff of hopper 1 to touchdown of hopper 2 (as in Def. 1), and is obtained by integrating the trivial aerial dynamics, as detailed below.

Note that the a_i are defined continuously through modes (3.4), and the a_i are unchanged by ballistic flight.

Define t_{LO} as the liftoff time (when hopper 1 is in stance, hopper 2 is in flight) and t_{TD} as the touchdown time (when hopper 1 is in flight, hopper 2 is in stance). In this reset calculation, to avoid confusion, we will be explicit about which row of (3.4) is used in each appearance of ψ_i : e.g., $\psi_f^{(2)} = (a_2 - \dot{z}_2)/(2a_2)$.

First, we integrate the aerial dynamics. Note that the time of flight is t_f is given by

$$\psi_f^{(2)}(t_{\text{LO}}) + \omega_f(a_2)t_f = 1 \implies t_f = \frac{1 - \psi_f^{(2)}(t_{\text{LO}})}{\omega_f(a_2)}.$$

Using this in $\psi_f^{(1)}(t_{\text{TD}}) = \psi_f^{(1)}(t_{\text{LO}}) + \omega_f(a_1)t_f$, and noting from (3.4) that $\psi_f^{(1)}(t_{\text{LO}}) = 0$, we get

the flight map

$$\psi_f^{(1)}(t_{TD}) = \frac{\omega_f(a_1)}{\omega_f(a_2)} (1 - \psi_f^{(2)}(t_{LO})) \quad (3.69)$$

Now we must express the above in terms of δ . Using the appropriate patches at t_{LO} and t_{TD} ,

$$\begin{aligned} \delta(t_{LO}) &= \frac{\psi_v^{(1)}(t_{LO}) - \pi/2}{\omega} - \frac{\psi_f^{(2)}(t_{LO}) - 1/2}{\omega_f(a_2)}, \\ \delta(t_{TD}) &= \frac{\psi_f^{(1)}(t_{TD}) - 1/2}{\omega_f(a_1)} - \frac{\psi_v^{(2)}(t_{TD}) - \pi/2}{\omega}. \end{aligned} \quad (3.70)$$

Per our constant flow-time assumption (Assumption 4), we know that $\psi_v^{(1)}(t_{LO}) = \pi$, and combining with (3.70),

$$\delta(t_{LO}) = \frac{\pi}{2\omega} - \frac{\psi_f^{(2)}(t_{LO}) - 1/2}{\omega_f(a_2)}. \quad (3.71)$$

Since the leg touches down at its nominal extension, by (3.4), $\psi_v^{(2)}(t_{TD}) = 0$, and combining with (3.70),

$$\begin{aligned} \delta(t_{TD}) &= \frac{\psi_f^{(1)}(t_{TD}) - 1/2}{\omega_f(a_1)} + \frac{\pi}{2\omega} \\ &\stackrel{(3.71)}{=} \frac{\psi_f^{(1)}(t_{TD}) - 1/2}{\omega_f(a_1)} + \delta(t_{LO}) + \frac{\psi_f^{(2)}(t_{LO}) - 1/2}{\omega_f(a_2)} \end{aligned} \quad (3.72)$$

Substituting (3.69) into the above,

$$\begin{aligned} \delta(t_{TD}) &= \delta(t_{LO}) - \frac{1}{2\omega_f(a_2)} - \frac{1}{2\omega_f(a_1)} + \frac{1}{\omega_f(a_2)} \\ &= \delta(t_{LO}) + \frac{1}{2\omega_f(a_2)} - \frac{1}{2\omega_f(a_1)} = \delta + \frac{(a_2 - a_1)}{g}. \end{aligned}$$

All together, the slow-coordinate reset is

$$\begin{aligned} R(a_1, a_2, \delta) &= \pi_2 \circ K \circ \begin{bmatrix} \psi_1 \\ a_1 \\ a_2 \\ \delta + (a_2 - a_1)/g \end{bmatrix} \\ &= \bar{K} \begin{bmatrix} a_1, & a_2, & \delta + \frac{(a_2 - a_1)}{g} \end{bmatrix}^T. \end{aligned} \quad (3.73)$$

From the above, we observe that DR has a constant $\mathcal{O}(1)$ part, satisfying Thm. 2(i).

Application of switching averaging Using (3.52), (3.68), and (3.73) and evaluating at (3.65), we get the averaged return map

$$\begin{aligned} \overline{DP} &:= DR \cdot (I + \varepsilon \pi D\overline{f}) \\ &= \left[\begin{array}{cc|c} 0 & 1 & 0 \\ \xi_1 & 0 & 0 \\ \hline \frac{\xi_1}{g} & -\frac{1}{g} & -1 + \frac{\varepsilon g k_d \beta}{2k_a \omega^3} \end{array} \right], \end{aligned} \quad (3.74)$$

where

$$\xi_1 := 1 - \frac{\varepsilon \tilde{\beta}}{2\omega}, \quad (3.75)$$

only depends on constant parameters. The block lower triangular \overline{DP} has eigenvalues $\pm j\sqrt{\xi_1}$ from the upper left block (the upper block has complex conjugates hence the determinant is their magnitude squared), and $-1 + \frac{\varepsilon g k_d \beta}{2k_a \omega^3}$ from the scalar lower right block, which is within the unit circle for small $\varepsilon > 0$.

This computation reveals a condition on allowable parameter values; in (3.59), k_d must be small enough such that $\tilde{\beta} > 0$. Assuming our gains are set appropriately, for small $\varepsilon > 0$, $|\xi_1| < 1$, and also the other eigenvalues are within the unit circle since their product is ξ_1 , and the averaged return map is stable. Additionally, the return map is hyperbolic, and applying Thm. 2, we conclude that the pair of independent hoppers has a stable anti-phase limit cycle ε -close to (3.65).

Variable flow-time (event-based reset) analysis

This section contains a “tutorial” description of how Thm. 3 can be applied (without requiring Assumption 4) to the bounding analysis of Sec. 3.4.2. We point out specific departures from the constant-flow-time version of the analysis below, and end by juxtaposing the return map linearization (3.77) against its constant-flow-time counterpart (3.74).

Guard set First, the guard set is defined by the “normal reaction crossing zero” event as in (3.49).

Reset Next, the reset map is modified in two of its entries:

- Note that a_1 is constant through flight, but we need to convert its stance coordinates at the time of liftoff (depending on when the guard surface (3.49) is intersected) to flight coordinates. Thus, the a_1 -reset is replaced instead by (3.50) (see (3.76) below).
- Additionally, the phase difference reset calculation is modified. We replace (3.71) with the guard (3.49), and get

$$\delta(t_{LO}) = \frac{\tan^{-1}(\varepsilon k_a / (\omega a_1) - \beta)}{2\omega} - \frac{\psi_f^{(2)}(t_{LO}) - 1/2}{\omega_f(a_2)}$$

Using this together with (3.72), we get

$$\delta(t_{\text{TD}}) = \delta(t_{\text{LO}}) + \frac{1}{2\omega_f(a_2)} - \frac{1}{2\omega_f(a_1)} + \frac{\pi - \tan^{-1}(\varepsilon k_a / (\omega a_1) - \beta)}{2\omega}$$

Putting these together, and applying the symmetry operation (3.51)

$$R_{(1)}(x, \psi_1) = \begin{pmatrix} \sqrt{a_1^2 \cos^2 \psi_1 - 2ga_1 \sin \psi_1 / \omega} \\ a_2 \\ \delta + \frac{(a_2 - a_1)}{g} + \frac{\pi - \tan^{-1}(\varepsilon k_a / (\omega a_1) - \beta)}{2\omega} \end{pmatrix}, \quad (3.76)$$

Note from (3.65) that

$$R \begin{pmatrix} \tilde{k}_a / \tilde{\beta} \\ \tilde{k}_a / \tilde{\beta} \\ 0 \end{pmatrix} = \bar{K} \begin{pmatrix} \tilde{k}_a / \tilde{\beta} \\ \tilde{k}_a / \tilde{\beta} \\ 0 \end{pmatrix} = \begin{pmatrix} \tilde{k}_a / \tilde{\beta} \\ \tilde{k}_a / \tilde{\beta} \\ 0 \end{pmatrix},$$

satisfying $\bar{R}(x^*) = x^*$ in Thm. 3(iii). Next, we use (3.44) to find $D\bar{R}$. Using the guard (3.49) and the reset (3.76), and evaluating at the fixed point (3.65), we get

$$D\bar{R}_{(1)}(x^*) = \begin{bmatrix} 1 - \frac{\varepsilon g \beta^2}{k_a \omega} & 0 & 0 \\ 0 & 1 & 0 \\ -1/g & 1/g & 1 \end{bmatrix},$$

which has a constant $\mathcal{O}(1)$ part. We also note the similarity between the top left entry and Example 3. Repeating the steps in Sec. 3.4.2, we obtain the averaged return map

$$D\bar{P} = \left[\begin{array}{cc|c} 0 & 1 & 0 \\ \zeta_1 - \frac{\varepsilon g \beta^2}{k_a \omega} & 0 & 0 \\ \hline \frac{\zeta_1}{g} & -\frac{1}{g} & -1 + \frac{\varepsilon g k_d \beta}{2k_a \omega^3} \end{array} \right], \quad (3.77)$$

Note that the eigenstructure of this matrix is similar to its constant-flow-time counterpart (3.74). In fact, since $\zeta_1 - \frac{\varepsilon g \beta^2}{k_a \omega} < \zeta < 1$ for small ε , the eigenvalues for the block lower triangular matrix above are within the unit circle.

3.4.3 Two Vertical Hoppers: In-Phase Limit Cycle (Pronking)

In this section we show that phase control (3.59) (albeit now with $k_d < 0$) can be applied to the same independent hoppers model as in the previous subsection (Fig. 25) but now used to stabilize a different limit cycle.

As depicted in the lower succession of sketches in Fig. 26, we think of this limit cycle as having a single continuous mode (double stance) followed by a reset (aerial phase), assuming simultaneous transitions as discussed in Sec. 3.3.1. With this assumption in force, we now show, in counterpoint to the previous section (where the introduction of a symmetry operator (3.51) achieves a re-factorization of the three physical modes depicted in Fig. 26B into the “half-stride” paired modes depicted in Fig. 26C), how these different hybrid dynamics can directly be modeled as executions

of a single-mode averageable hybrid system.

In this instance, we again use the switching theorem (Thm. 2) and ignore the small variation in the flow duration.

Continuous dynamics As in (3.62), but this time, since both legs are in stance, for $i \in \mathcal{I}$ we get (3.99) for both legs. Use the phase difference δ in the double stance patch from (3.57), and notice that

$$\begin{aligned} \frac{d}{dt}\delta &= \frac{\varepsilon}{\omega^2} \left(\frac{v_2 \sin(\omega\delta - \psi_1)}{a_2} + \frac{v_1 \sin \psi_1}{a_1} \right) \\ &=: f_\delta(x), \end{aligned} \quad (3.78)$$

i.e. the phase difference is “slow” analogously to its counterpart (3.63) in the anti-phase limit cycle analysis of the preceding Sec. 3.4.2. Once again as in Sec. 3.4.2, we use the coordinates, $\sigma = \psi_1 + \pi/2$ and $x := (a_1, a_2, \delta)$, and see that

$$\begin{aligned} \dot{\sigma} &= \omega + \frac{\varepsilon}{a_1} \sin \psi_1 v_1 \\ \dot{x} &= \varepsilon \begin{bmatrix} -\cos \psi_1 v_1 \\ -\cos(\omega\delta - \psi_1) v_2 \\ f_\delta(x) \end{bmatrix}, \end{aligned} \quad (3.79)$$

where $f_\delta(x)$ is defined above in (3.78). Recall we are using the same phase controller (3.59) as in Sec. 3.4.2, but now with $k_d < 0$. Introducing the prospective in-phase fixed point,

$$T = \pi, \quad x^* = [k_a/\beta, k_a/\beta, 0]^T, \quad (3.80)$$

we point out here that the equilibrium phase difference above is very different from the one in (3.65) despite the visual similarity, due to the different definition of δ (which is, as before in Sec. 3.4.2, local). For recall, once again, that in Sec. 3.4.2 we considered hopper 1 to be in stance and hopper 2 to be in flight, whereas now both hoppers are assumed to be in stance. Consequently, (3.57) shows that δ is zero iff both hoppers attain “bottom” simultaneously.

Note that using (3.80) in (3.79) and integrating (we used the **Integrate** function in Mathematica 10.2 to perform this integral),

$$\bar{f}(x) = \begin{bmatrix} \frac{(k_a - a_1 \beta)}{2\omega} - \frac{2k_d(a_1 - a_2 c)}{3\pi\omega} \\ \frac{(k_a - a_2 \beta)}{2\omega} - \frac{2k_d(a_1(c^2 - s^2) - a_2 c^3)}{3\pi\omega} \\ \frac{-2k_d s (2a_2^2 + a_1 a_2 s^2 + 2a_1^2 c)}{3\pi\omega^3 a_1 a_2} \end{bmatrix}, \quad (3.81)$$

where $s := \sin(\omega\delta)$, and $c := \cos(\omega\delta)$. Despite the complexity, we observe the following about the averaged vector field (3.81):

- a) the preflexive $k_d = 0$ case recovers the isolated vertical hopper a_i -dynamics (3.99) for both hips (first summand in each of the first two rows);
- b) when $\delta = 0$, and $a_1 = a_2$, we also recover isolated vertical hopper dynamics in the first two rows, suggesting that behavior close to the equilibrium resembles that of independent vertical

- hoppers;
- c) in 3.4.1 we provide an interpretation of the last row as a proportional controller on the phase difference, δ .

The averaged vector field (3.81) evaluates to 0 at x^* , satisfying Thm. 2(ii). Moreover, we can calculate the Jacobian and evaluate at x^* to get

$$D\bar{f}(x_2^*) = \left[\begin{array}{cc|c} -\zeta_2 - \zeta_3 & \zeta_3 & 0_{2 \times 1} \\ \zeta_3 & -\zeta_2 - \zeta_3 & \\ \hline 0 & & -\frac{8k_d}{3\pi\omega^3} \end{array} \right], \quad (3.82)$$

where we define the new constants $\zeta_2 := \frac{\beta}{2\omega}$, and $\zeta_3 := \frac{2k_d}{3\pi\omega}$.

Reset The touchdown condition is the touchdown of hopper 1 after its flight phase, or when $\psi_1 - 1$ (3.4) crosses zero. As in Sec. 3.4.2, a_i are not modified by the aerial dynamics. To integrate the aerial dynamics, note first that since the touchdown event is at the zero of $1 - \psi_f^{(1)}$, and $\psi_f^{(1)}(t_{LO}) = 0$, the time of flight is simply $t_f = 1/\omega_f(a_1)$. In this time, hopper 2 must finish its stance phase, complete its flight phase, and proceed through its stance phase (where some of these times may be negative):

$$t_f = \frac{\pi - \psi_v^{(2)}(t_{LO})}{\omega} + \frac{1}{\omega_f(a_2)} + \frac{\psi_v^{(2)}(t_{TD})}{\omega}. \quad (3.83)$$

To express in terms of δ , note that $\delta(t_{LO}) = \frac{\pi - \psi_v^{(2)}(t_{LO})}{\omega}$, $\delta(t_{TD}) = -\frac{\psi_v^{(2)}(t_{TD})}{\omega}$. Using the above in (3.83), we get

$$\frac{1}{\omega_f(a_1)} = \delta(t_{LO}) - \delta(t_{TD}) + \frac{1}{\omega_f(a_2)}.$$

Rearranging, using (3.10), and putting together with the energy coordinates, we get

$$\bar{R}(a_1, a_2, \delta) = \left[a_1, \quad a_2, \quad \delta + \frac{2(a_2 - a_1)}{g} \right]^T. \quad (3.84)$$

Just as in Sec. 3.4.2, x^* in (3.80) when substituted into the equation above yields $\bar{R}(x^*) = x^*$, satisfying Thm. 2(ii), and also we note that $D\bar{R}$ has a constant $\mathcal{O}(1)$ part, satisfying Thm. 2(i).

Note that unlike the reset map for the anti-phase limit cycle (3.73), \bar{K} does not appear here, since we only have a single-mode hybrid system in consideration for the in-phase limit cycle.

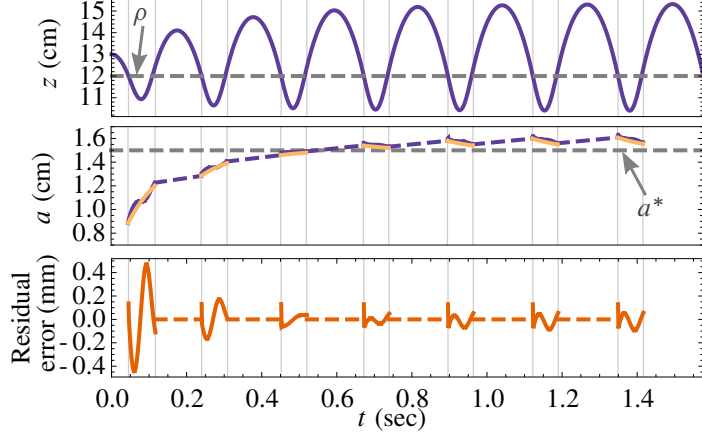


Figure 28: (top) displacement of vertical hopper in physical z coordinates (thin vertical lines separate stance and flight); (middle) abstract energy coordinate a (3.99) in purple (dashed: flight), and, in gold, the equivalent continuous dynamical system (3.47) over several hops. (bottom) residual error in the a coordinate between trajectories of the averaged and original systems.

Application of switching averaging Using (3.82), and (3.84) and evaluating at (3.80), we get the averaged return map

$$\begin{aligned} D\bar{P} &:= D\bar{R} \cdot (I + \varepsilon\pi D\bar{f}_1) \\ &= \left[\begin{array}{cc|c} 1 - \varepsilon(\zeta_2 + \zeta_3) & \varepsilon\zeta_3 & 0 \\ \varepsilon\zeta_3 & 1 - \varepsilon(\zeta_2 + \zeta_3) & 0 \\ \hline -\frac{2(1-\varepsilon(\zeta_2+2\zeta_3))}{g} & -\frac{2(1-\varepsilon(\zeta_2+2\zeta_3))}{g} & 1 - \frac{\varepsilon 8 k_d}{3\pi\omega^2} \end{array} \right], \end{aligned} \quad (3.85)$$

where ζ_i are as defined in Sec. 3.4.3. This lower triangular matrix has $1 - \frac{\varepsilon 8 k_d}{3\omega}$ as one of its eigenvalues, which is within the unit circle for small $\varepsilon > 0$. The symmetric upper left block has the simple eigenvalues $\{1 - \varepsilon\zeta_2, 1 - \varepsilon\zeta_2 - 2\varepsilon\zeta_3\}$, which are also within the unit circle for small $\varepsilon > 0$. Moreover, $D\bar{P}$ is hyperbolic, and using Thm. 3, we conclude that the pair of independent hoppers has a stable in-phase limit cycle ε -close to (3.80).

3.4.4 Numerical Results

In this section we present simulation results of the model systems discussed here. In Sec. 3.4.4 we display overlapping traces of “unaveraged” and “averaged” dynamics on an isolated vertical hopper, showing the correspondence that is formally established by Thm. 1. In Sec. 3.4.4, we demonstrate the efficacy of the new coordination controllers introduced in Sec. 3.4.1 on a pair of informationally-coupled, mechanically-decoupled vertical hoppers.

We would like to remind the reader that Sec. 3.5.6 and Sec. 4.2 contain a much larger swath of not just numerical but also empirical results benefitting from the theoretical contributions here.

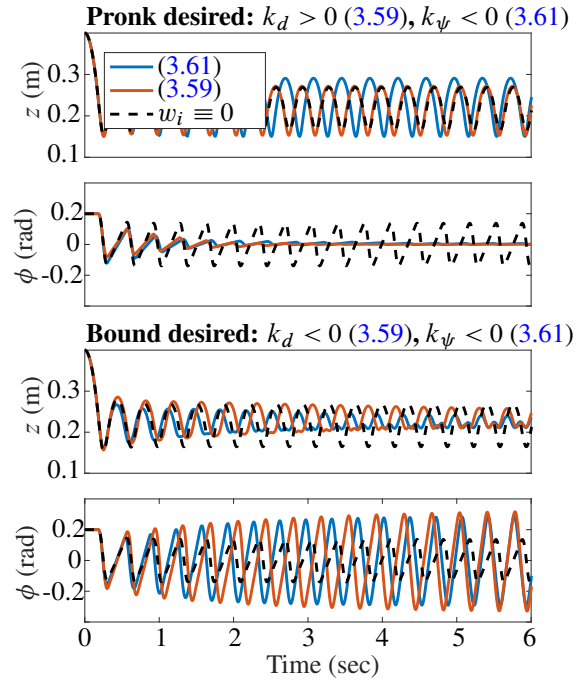


Figure 29: Comparison of coordination through pure ‘abstract’ phase (3.61) vs. its perceptually direct surrogate (3.59). Simulation runs of a pair of independent vertical hoppers with $z = (z_1 + z_2)/2$ (Fig. 25) where, comparing no phase control (dashed black), the abstract phase control (3.61) (blue), and our new phase controller (3.59) (red) which introduces complexity in our analysis here, but leads to more simple and robust physical implementation in De and Koditschek (2016). Note that the sign of k_p is the same for both limit cycles due to our local definition of δ , as discussed after (3.66).

1DOF vertical hopper

Using parameters $\omega = 50$ rad/s, $k = 0.4$ N·s/m², $\beta = 10$ N/(m/s) and $\varepsilon = 2$, numerical simulations of the vertical hopper with **Mathematica 10**, using **NDSolve** and **WhenEvent** show that

- a) the fixed point of the averaged system is approximately 0.15 mm away from the original system’s fixed point (Fig. 28 middle, difference between purple a and dashed gray a^*), and
- b) the residual error between trajectories of the averaged and original systems are an order of magnitude smaller than $a^* = k/\beta = 0.04$ m (Fig. 28, bottom).

Remark 5 (approximating continuous control with discrete steps). Note that the averaged vector field (3.47) has the form of a proportional controller on total energy. Thus Thm. 1 enables us to conclude that the cumulative control effect on body height from multiple isolated steps through a second-order ODE is approximately equivalent to that of a first-order ODE acting on body height (as shown in Fig. 28(middle)): the gold traces in the middle plot correspond to the averaged system, and ‘snipping away’ the resets recovers a smooth energy dynamics corresponding to (3.47).

Pair of vertical hoppers

In Fig. 29 we illustrate numerically the analytical results just derived in Sec. 3.4.2–3.4.3. The physical model we use is the pair of vertical hoppers of Fig. 25, and we demonstrate that our new phase controller (3.59) can stabilize both anti-phase and in-phase limit cycles by changing the sign of the scalar parameter k_d .

We provide empirical demonstration of the phase controller on a physical platform as well as empirical application of the attitude controller (3.60) in Sec. 4.2.3.

We also show in 3.4.1 how the phase controller (3.59) behaves in closed loop like an abstract phase control such as previously analyzed in Klavins et al. (2000). The empirical benefit of (3.59) is that it is a smooth function of data $\phi, \dot{\phi}$ measured from sensors on the robot, whereas the abstract phase difference (3.57) is not only an involved calculation, but also a discontinuous function of the physical state.

3.5 Application: Coordination of Coupled Vertical Hoppers (2DOF)

Contributions

Fig. 27B introduces the “slot hopper” model (inspired by in-place biped models in prior literature, such as Berkemeier (1998), Burden et al. (2007)), wherein we add a notional mechanical coupling between the two independent vertical hoppers (Fig. 27A), taking the form of a connecting bar pivoting freely around a vertically-sliding pin. The central contribution as stated at the outset is the proposal of the slot hopper as a template for all “virtual bipedal” quadruped gaits, a stability analysis of the target limit cycles that encode them in that model, and the empirical demonstration of their anchoring in the physical Minitaur quadruped (Fig. 27D). The analysis and data presented here to establish these claims is summarized in Fig. 30 as follows:

Analysis We provide the first correctness proofs for in-place dynamical virtual bipedal gaits by adapting the hybrid averaging analysis of De et al. (2016) to the three distinct (overlapping) physical regimes of the slot-hopper template determined by its “non-dimensional inertia” (3.86) as depicted along the abscissa of Fig. 30.

Preflexive stability In so doing, we show how these regimes elicit preflexive stabilization for both in-phase (pronking) and out-of-phase (bounding) quadrupedal hopping behavior by interpreting the stable limit cycles of the slot-hopper template (whose relative phase is plotted by the black dots in Fig. 30) as being anchored by closely matching periodic motions of the appropriately loaded preflexively stable physical Minitaur (corresponding to the green and magenta vertical lines in Fig. 30).

Implementation Using only shank extension actuators and the same three template controllers (3.5)–(3.60) with few parameters³¹, we can demonstrate all in-place virtual bipedal quadruped gaits on Minitaur, as shown Table 6. We show how the preflexive behavior can be robustly either countermanded or reinforced by simple sign adjustments to the coordination control law gains introduced in (3.59)–(3.60) when applied to the slot-hopper template (plotted as blue and red dots in Fig. 30), to achieve correspondingly enhanced or disrupted pronking or bounding on the anchoring physical Minitaur (plotted as colored open diamonds in Fig. 30).

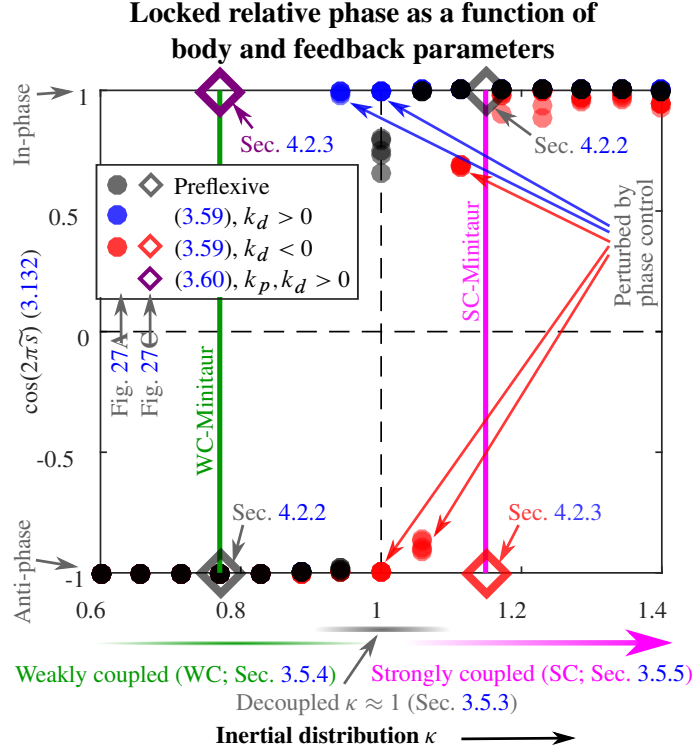


Figure 30: Phase locking at non-extreme κ . Stable steady-state relationships between leg phases for simulation and physical runs of the models depicted in Fig. 27 in relation to the inertia parameter κ (3.86). Solid round dots represent the limiting relative phase between the two legs of the slot hopper model (Sec. 3.5.1, Fig. 27A). Each translucent dot is the result of a single trial (5 trials are plotted at each κ value, though in many of the trials, the dots overlap and appear as a single dot of increased opacity) which is $t_{\max} = 5$ seconds long, and the phase offset is calculated at the end. The gray dots refer to a preflexive control only ($k_d = 0$ in (3.59)), whereas, in contrast, the blue and red dots contain trials with some phase control (3.59). The hollow diamonds are data points representing Minitaur’s preflexive and feedback-stabilized gait coordination behavior in the physical world (Sec. 4.2.2–4.2.3). Please see Sec. 3.5 for our contextualization of the major claims in terms of this figure.

Template composition We empirically compose these vertical hopping coordination controllers with fore-aft and yaw controllers to get useful and robust locomotion performance (Table 7). The stability results propose for the first time a formal explanation for the preflexive in-place coordination, extending the results of Berkemeier (1998) to include the stabilization effects of the $\varepsilon \neq 0$ dynamics, showing that the preflexes are effective for a vastly different shank energization strategy, as well as then showing that these results bear out on a physical platform.

We apply a dynamical systems method for coupling hybrid oscillators De et al. (2016) to achieve formally specified, physically effective and robust instances of all virtual bipedal gaits on a quadrupedal robot. Gait specification takes the form of a three-parameter family (k_a , k_p , and k_d to be introduced in (3.58)–(3.60)³¹) of coupling rules used to entrain an otherwise independent pair of virtual vertical

³¹For example, for 3D bounding-in-place in Fig. 32, in addition to the two “morphological” parameters per (identical)

leg hopping controllers.

3.5.1 Linearized 2 DOF Slot Hopper

In prior literature, there are several instances of a 2DOF vertically-constrained biped (Fig. 27B), such as [Berkemeier \(1998\)](#), [Burden et al. \(2007\)](#). We include a complete Lagrangian derivation of its equations of motion³² below, and also derive a simplified analytically tractable version subject to an assumption that we present below (similar to the small-angle assumption made by [Berkemeier \(1998\)](#)).

Define the “non-dimensionalized inertia” parameter (originally due to [Murphy and Raibert \(1985\)](#)) which we shall henceforth refer to simply as the “inertia parameter”,

$$\kappa := \frac{i_b}{m_b d^2}, \quad (3.86)$$

where m_b is the body mass (without loss of generality, we set to $m_b = 1$ kg, and we justify doing so in Sec. 3.5.1), d is half the hip-to-hip distance and i_b is the rotational inertia about the center of mass.

The configuration variables (including those for massless limbs) are $\mathbf{q} := [r_1, r_2, z, \phi]^T$, where $r_i \in \mathbb{R}_+$ are the lengths of the legs, $z \in \mathbb{R}_+$ is the height of the center of mass, and ϕ is the “body angle.” Despite the four entries, the number of dynamical DOFs accounting for constraints and degeneracies is only two, as shown below. The kinetic and potential energies are respectively

$$T(\mathbf{q}, \dot{\mathbf{q}}) := \frac{1}{2} m_b \dot{z}^2 + \frac{1}{2} i_b \dot{\phi}^2, \quad V(\mathbf{q}) := m_b g z.$$

Actuation enters this model only through the stance legs, i.e. $\Upsilon_i \in \mathbb{R}$ are the forces acting on the r_i prismatic joints. The model has two possible contacts—the two toes located at

$$\mathbf{a}_i(\mathbf{q}) := z + (-1)^{i-1} d \sin \phi - r_i. \quad (3.87)$$

The following assumption allows us to derive simplified equations of motion for the slot hopper,

Assumption 5. *To derive the constrained slot hopper dynamics (3.94), (3.96), we substitute the linearized version,*

$$\bar{\mathbf{a}}_i(\mathbf{q}) := z + (-1)^{i-1} d \phi - r_i, \quad (3.88)$$

of the exact constraint in (3.87).

As a plot of bounding data from the physical platform shows (Fig. 54), the oscillation in the body angle for Minitaur bounding is in the order of ± 0.3 radians, where the small angle approximation

virtual leg (which only require rough guesses, cf. Fig. 36), the required parameters are k_a in (3.5) (which controls vertical hopping height), and k_p and k_d in (3.60) for roll control. If preflexive coordination is insufficient (e.g. bounding-in-place on SC-Minitaur in Fig. 52), we compose a phase controller (3.59) (with one additional parameter). These parameters only require very rough guesses as shown in Sec. 3.5.6.

³²The reader may note the close correspondence between ([Burden et al., 2007](#), eq. (1)) and the double stance equations of motion we find for the slot hopper (3.96).

error is less than 1.5%. Secondly, since our proofs only provide sufficient (not necessary) conditions for stability, we often find that the basin of stability is much larger than the scope of the analysis (whether it be in relation to Assumption 5, or the magnitude of the perturbation parameter). We compare the behavior of this simplified model to a higher fidelity hybrid system simulation as well as data from Minitaur in Fig. 32 to corroborate the validity of this assumption.

Lastly, define the virtual leg index set $\mathcal{J} \approx \mathbb{Z}_2$, where the members $i \in \mathcal{J}$ are “1” and “2”, but we use “ $i - 1$ ” and “ $i + 1$ ” to refer to the other element in the set. Also, define $z_i \in \mathbb{R}_+$, the heights of the hips, as

$$z_i := z + (-1)^{i-1} d\phi \quad (3.89)$$

(anticipating the imposition of assumption 5). Clearly

$$2d\dot{\phi} = \dot{z}_1 - \dot{z}_2, \quad (3.90)$$

which we use to change coordinates in Sec. 3.5.1. In the following, we will think of an abstract “hopper i ” being located at height z_i .

The continuous dynamics vary according to which constraints from (3.88) are active (physically corresponding to one or both toes contacting the ground). The different “modes” are thus: “double stance” (both $\bar{\mathbf{a}}_i$ active), “single stance” (only one active), and “aerial” (no constraints).

Controller parameter scaling We endeavor to apply the same scalar control feedback signals developed for vertical hopper control Sec. 3.4 (recorded in (3.5)–(3.60)) to the slot hopper analyses (Sec. 3.5.2), simulations (Sec. 3.5.6), and Minitaur experiments (Sec. 4.2.1). This “template” controller feedback law, $u_i : \mathcal{X} \rightarrow \mathbb{R}$, is related to the physical input signal $\Upsilon_i \in \mathbb{R}$ (Sec. 3.5.1) through

$$\Upsilon_i(x) := \alpha_0 + \alpha_1 u_i(x), \quad (3.91)$$

where $\alpha_i \in \mathbb{R}$ are constant parameters that we modify according the physical parameters of various plant models considered here (Table 6). The formal effect of this affine transform (i.e., its role in facilitating the proofs of Sec. 3.5.2) is to cancel extraneous constant terms in the equations of motion (effectively mass and gravity-like parameters) and reduce to a form close to (3.99). This is a kind of morphological reduction as defined in Libby et al. (2015), however the details and physical implications of the reduction map are beyond the scope of this report.

Lagrangian setup For the derivation of the equations of motion, we use the notation of Johnson et al. (2016). In each hybrid mode (subsections below) we define (a) the configuration variables \mathbf{q} , (b) the unconstrained (aerial) inertia tensor $\mathbf{M}(\mathbf{q})$, (c) the Lagrangian constraint $\mathbf{a}(\mathbf{q})$, whose rows are comprised of the exact “toe pinned” constraint (3.87), and (d) the input vector Υ . Let $\mathbf{A} := \mathbf{D}_{\mathbf{q}}\mathbf{a}(\mathbf{q})$. Note that the gravity-like potential is the same in each case, and so the gravity-like forces are $\mathbf{N}(\mathbf{q}) = \mathbf{D}_{\mathbf{q}}V(\mathbf{q}) = \mathbf{D}_{\mathbf{q}}(m_b g z)$. Lastly, the unconstrained inertia tensor happens to be

constant in each case below, and so as in [Johnson et al. \(2016\)](#), we get the equations of motion from

$$\begin{bmatrix} \mathbf{M} & \mathbf{A}^T \\ \mathbf{A} & 0 \end{bmatrix} \begin{bmatrix} \ddot{\mathbf{q}} \\ \lambda \end{bmatrix} = \begin{bmatrix} \Upsilon - \mathbf{N} \\ \dot{\mathbf{A}}\mathbf{q} \end{bmatrix}, \quad (3.92)$$

where λ are the constraint forces at the toe. Lastly, in each case below, we use a [text color](#) to highlight terms in the equations of motion that are present *without* Assumption 5. When Assumption 5 is used, these terms get simplified as $\sin\phi \mapsto \phi$, $\cos^2\phi \mapsto 1$, and $\dot{\phi}^2 \mapsto 0$. Note that we prefer to impose the “small angle” approximation before taking derivatives (following Assumption 5) rather than after (which requires making the substitutions described in this paragraph and the following subsubsections). We include the dynamics sans Assumption 5 below for completeness.

Single stance

Without loss of generality, we consider the case where hopper 1 is in stance, and hopper 2 is in flight. The toe of hopper 1 is pinned to the ground, and so only constraint 1 is active in (3.88), or $\mathbf{a}(\mathbf{q}) = \bar{\mathbf{a}}_1(\mathbf{q})$.

Without small angle In single stance, we have $\mathbf{q} = [r, z, \phi]$

$$\begin{aligned} \mathbf{M}(\mathbf{q}) &= \text{diag}[0, m_b, \kappa m_b d^2], \\ \mathbf{a}(\mathbf{q}) &= z + d \sin\phi - r \\ \Upsilon &= \Upsilon_1 \end{aligned}$$

We can solve for $\ddot{\mathbf{q}}$ by inverting the block matrix on the left of (3.92) (which is non-singular as long as there are no massless free DOFs or kinematic singularities [Johnson et al. \(2016\)](#)),

$$\ddot{\mathbf{q}} = \begin{bmatrix} -g + \frac{\Upsilon_1}{m_b} (1 + \cos^2\phi/\kappa) - d \sin\phi \dot{\phi}^2 \\ -g + \Upsilon_1/m_b \\ \frac{\Upsilon_1 \cos\phi}{dm_b \kappa} \end{bmatrix}. \quad (3.93)$$

Even though the system has two dynamical DOF, we have three rows here, since the three (originally unconstrained) variables r, z, ϕ are now related through the toe–ground constraint. Additionally, to get the second row of (3.94), we use (3.89) with the first two rows of (3.93), and so the $\cos\phi$ in last row of (3.93) does not need to be approximated.

With small angle Using the change of coordinates from center-of-mass (z, ϕ) to “hip height” z_i coordinates in (3.89), we get $m_b \ddot{z} = -m_b g + \Upsilon_1$, and $m_b \ddot{z}_1 = -m_b g + (1 + 1/\kappa) \Upsilon_1$. As per Sec. 3.5.1 and as listed in Table 6, we substitute (3.91), and get

$$\ddot{z}_1 = u_1, \quad \ddot{z}_2 = -\frac{1 - \kappa}{1 + \kappa} u_1, \quad (3.94)$$

which can be compared to the exact version (3.93). We outline in Sec. 3.5.1 how the control input u_1 is set as a function of the robot state.

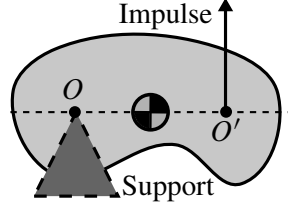


Figure 31: Center of percussion. From Symon (1971): “The point O' about which a blow must be struck in order that no impulse be felt at the point O is called the *center of percussion* relative to O . If the body is unsupported, and is struck at O' , its initial motion will be a rotation about O ”.

The physical implications of different values of κ are noted in Table 6, and an intuitive interpretation of κ is that it moves the center of percussion (see Fig. 31), where the net force on the hip over the stance duration plays the role of the “impulse.” As (3.94) shows, a $\kappa = 1$ configuration results in a complete lack of coupling interaction, equivalent to the “rotation about O' ” condition of Fig. 31. In Table 6, we depict the location of the mass concentration as well as of the CoP as κ is varied.

Double stance

Without small angle Using $\mathbf{q} = [r_1, r_2, z, \phi]$,

$$\mathbf{M}(\mathbf{q}) = \text{diag}[0, 0, m_b, \kappa m_b d^2],$$

$$\mathbf{a}(\mathbf{q}) = \begin{bmatrix} z + d \sin \phi - r \\ z - d \sin \phi - r \end{bmatrix},$$

$$\Upsilon = \begin{bmatrix} \Upsilon_1 \\ \Upsilon_2 \end{bmatrix}$$

in (3.92),

$$\ddot{\mathbf{q}} = \begin{bmatrix} -g + \frac{\Upsilon_1 + \Upsilon_2}{m_b} + \frac{(\Upsilon_1 - \Upsilon_2) \cos^2 \phi}{m_b \kappa} - d \sin \phi \dot{\phi}^2 \\ -g + \frac{\Upsilon_1 + \Upsilon_2}{m_b} + \frac{(\Upsilon_2 - \Upsilon_1) \cos^2 \phi}{m_b \kappa} + d \sin \phi \dot{\phi}^2 \\ -g + \frac{\Upsilon_1 + \Upsilon_2}{m_b} \\ \frac{(\Upsilon_1 - \Upsilon_2) \cos \phi}{d m_b \kappa} \end{bmatrix}. \quad (3.95)$$

Even though the system has two dynamical DOF, we have four rows here, since the four (originally unconstrained) variables r_1, r_2, z, ϕ are now related through two instances of the toe-ground constraint. Additionally, as above, the $\cos \phi$ in the last row does not need to be approximated when Assumption 5 is in place:

With small angle After replacing Υ_i as in Table 6, using Assumption 5 we get:

$$\begin{aligned} m_b \ddot{z} &= -m_b g + \Upsilon_1 + \Upsilon_2, \\ \ddot{\phi} &= \frac{\Upsilon_1 - \Upsilon_2}{d m_b \kappa}. \end{aligned}$$

Using Table 6 and substituting in (3.91), we get

$$\ddot{z} = \frac{u_1 + u_2}{2}, \quad \ddot{\phi} = \frac{u_1 - u_2}{2d\kappa}, \quad (3.96)$$

which can be compared to the exact version (3.95).

Aerial

In this case, Assumption 5 makes no difference. Using $\mathbf{q} = [z, \phi]$, no constraint \mathbf{a} , and no input Υ ,

$$\mathbf{M}(\mathbf{q}) = \text{diag}[m_b, \kappa m_b d^2],$$

$$\ddot{\mathbf{q}} = \begin{bmatrix} -g \\ 0 \end{bmatrix},$$

we get the equations

$$\ddot{z} = -g, \quad \ddot{\phi} = 0, \quad (3.97)$$

and using (3.90) we can reinterpret these in the z_i coordinates,

$$\ddot{z}_1 + \ddot{z}_2 = -2g, \quad \ddot{z}_1 - \ddot{z}_2 = 0 \implies \ddot{z}_i = 0, \quad (3.98)$$

that is, the aerial phase is identical to the flight of two independent vertical hoppers (De et al., 2016, (3.99)).

Decoupled case

First consider the stance dynamics of the decoupled ($\kappa = 1$) slot hopper. In double stance, using (3.89) in (3.96), and also setting $\kappa = 1$, we get

$$\ddot{z}_i = \ddot{z} \pm d\ddot{\phi} = u_i,$$

and in single stance, setting $\kappa = 1$ in (3.94), we see that

$$\ddot{z}_1 = u_1, \quad \ddot{z}_2 = 0.$$

In aerial phase, (3.97) is already decoupled. All together, we see that the decoupled slot hopper has the equations of motion (for each $i \in \mathcal{I}$)

$$\ddot{z}_i = \begin{cases} -g + u_i & \text{(stance)} \\ -g & \text{(flight).} \end{cases} \quad (3.99)$$

Limiting value of $\kappa \rightarrow 0$

The first row of Table 6 refers to a degenerate condition, where all the mass of the body is concentrated at its center. In this configuration, the ϕ degree of freedom is degenerate (since $i_b = \kappa m_b d^2 = 0$).

Thus, we are effectively reduced to a 1DOF vertical hopper without any physical relevance, since the model in Fig. 27B possesses a body whose orientation now cannot be controlled.

Phase differences and phase control

In the present case, the two coupled hips of the slot hopper are not identical oscillators, and we rely on intuition in each different non-degenerate regime in Sec. 3.5.2 to construct a modified phase difference coordinate (compared to (3.57)), such as (3.102) in Sec. 3.5.4.³³

In addition to the feedback coordination controllers (3.59)–(3.60), the slot hopper exhibits *preflexive* phase control terms, i.e. their more complex equations of motion contain terms qualitatively resembling w_i in (3.58) even without any feedback control. The specific form of w_i in these cases is more difficult to express via a single equation, but we provide at the outset an intuitive description of the stability mechanism that is borne out by our analysis here. Following the last two rows of Table 6,

- a) the weakly coupled hoppers are stabilized through an interaction between the continuous dynamics of a_2 (3.103), and the reset map (3.108), resulting from a confluence of the stance influence of the phase difference on the energy level of hopper 2 (description after (3.105)), and the reset influence of the energy level of hopper 2 on the phase difference (description after (3.108));
- b) the strongly coupled hoppers are stabilized through the leg damping acting as a phase controller (cf. Sec. 3.5.5).

3.5.2 Slot Hopper Analytical Results

First in Sec. 3.5.3, we discuss the $\kappa \approx 1$ “decoupled” regime of the slot hopper (as an extension of the $\kappa = 1$ case identified in Sec. 3.5.1). In Sec. 3.5.4–3.5.5, we set the input $w_i \equiv 0$ in (3.58)) of (a) out-of-phase hopping at $\kappa < 1$ (which we term in the *weak coupling* regime in Table 6), and (b) in-phase hopping at $\kappa \gg 1$ (which we term the *strong coupling* regime).³⁴ In Sec. 3.5.5 we reintroduce phase control (3.59) and attitude control (3.60) through w_i , and show that it is possible to augment preflexive pronking with feedback. We present many more numerical and empirical instances of feedback augmentation / disruption of preflexive stability in the next section.

3.5.3 The “Decoupled” $\kappa \approx 1$ Case

We saw that the return maps for bounding (3.74) and pronking (3.85) are hyperbolic with eigenvalues $\mathcal{O}(\varepsilon)$ within the unit sphere. From the slot hopper dynamics in (3.94), (3.96), and (3.97), we see that the dynamics (specifically the coupling forces) depend smoothly on κ . Now suppose $\kappa = 1 + \mathcal{O}(\varepsilon^2)$. Then, coupling forces of $\mathcal{O}(\varepsilon^2)$ magnitude appear in the continuous dynamics in (3.62) or (3.79), and are consequently ignored in the averaging step in (3.67) or (3.81). Thus, the

³³We wish to emphasize that our present understanding necessitates in each physical regime a different intuitive choice of the “correct” phase ψ_i and the appropriate phase difference δ . Work currently underway is making progress towards replacing this intuitive step with a uniformly defined and algorithmically implemented procedure.

³⁴Note that despite this nomenclature, in some sense the nature of the coupling “changes sign” as the decoupled regime lies at an intermediate κ -value (Fig. 30).

Table 6: Behavioral regimes and analytical results. As the inertia κ (3.86) of a slot-hopper (Fig. 27A) is varied (mass concentration depicted as red disks) along the abscissa of the plot in Fig. 30, we observe the following systematic changes in its morphological, analytical and behavioral features which are echoed by the sagittal plane biped (Fig. 27B) and Minitaur robot (Fig. 27C) in close correspondence: (a) the center of percussion (CoP, Fig. 31, depicted as blue disk) moves (cf. Sec. 3.5.1), (b) the preflexive control stabilizes different limit cycles (cf. numerical results in Fig. 30 with superimposed markings locating the corroborating in-place empirical Minitaur experiments of Sec. 4.2.2–4.2.2), and (c) we are able to prove stability of five of these limit cycles (corresponding to either preflexive or feedback stabilization of both relative phase targets) as listed below.

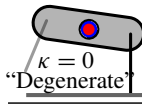
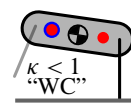
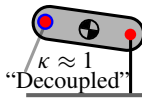
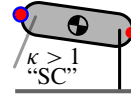
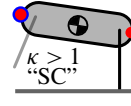
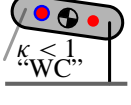
Regime	Relative phase	Coordination control	α_0 (3.91)	α_1 (3.91)	Analysis	Numerical/empirical demonstration		
						Reduces to single leg		
	anti-phase	Preflexive (3.103), (3.108)	$\frac{m_b g}{1+1/\kappa}$	$\frac{m_b}{1+1/\kappa}$	Proof Sec. 3.5.4	in	Minitaur (Sec. 4.2.2)	bounding
	in-phase	Attitude (3.60)					Minitaur (Sec. 4.2.3)	pronking
						Fig. 29, SC-Minitaur bounding (Sec. 4.2.3)		
	anti-phase	Phase (3.59), $k_d > 0$	g	1	Proof Sec. 3.4.2	in	Fig. 29	
	in-phase	Phase (3.59), $k_d < 0$	g	1	Proof Sec. 3.4.3	in	SC-Minitaur pronk (Sec. 4.2.2)	
	in-phase	Preflexive (3.117)	$\frac{m_b g}{2}$	$\frac{m_b}{2}$	Proof Sec. 3.5.5	in	SC-Minitaur pronk (Sec. 4.2.2)	
	in-phase	Attitude (3.60)	$\frac{m_b g}{2}$	$\frac{m_b}{2}$	Proof Sec. 3.5.5	in		
	anti-phase	Phase (3.59), $k_d > 0$			Suggested by Sec. 3.4.2	by	Minitaur (Sec. 4.2.5)	pacing
	anti-phase	Retraction (Sec. 4.2.5)			Suggested by Example 3	Ex-	Minitaur (Sec. 4.2.5)	trotting

Table 7: Empirical extensions via template composition. Parallel composition of the new slot-hopper template with the existing SLIP template [De and Koditschek \(2015b\)](#) can be directly embedded into the Minitaur dynamics to achieve stable running and leaping, while relying on the analytically supported vertical energization and coordination strategies in Table 6.

Regime	Controller(s) composed	Empirical demonstration
	Stepping fore-aft controller (4.17), yaw controller (4.19)	Bounding at commanded velocities up to 5 body lengths / second (Fig. 54)
	Increased vertical gain k_a (3.58) for a single stride	Leaping from and returning to steady state bounding / pronking (Fig. 55, Fig. 56)

averaged return map is perturbed by $\mathcal{O}(\varepsilon^2)$, and the stability conclusions in Sec. 3.4.2, 3.4.3 still hold.

3.5.4 Weak Coupling: Preflex Anti-Phase Stability

In this subsection, we use ε as a perturbation parameter perturbing both (a) the dissipation in the shank forcing controller (3.5), and (b) κ (3.86), by setting $\kappa = \frac{1-\varepsilon}{1+\varepsilon}$. Specifically, we can reparameterize the dynamics (3.94) in terms of $\varepsilon = \frac{1-\kappa}{1+\kappa}$ to get

$$\ddot{z}_1 = u_1, \quad \ddot{z}_2 = -(1+\varepsilon)g - \varepsilon u_1; \quad (3.100)$$

so that there is now a weak coupling interaction between the two hoppers for small $\varepsilon > 0$.³⁵

As in the prior bounding analysis, we capitalize on step-to-step symmetry and use the “half return map” analysis as depicted in the upper series of sketches in Fig. 26, but suppress the parenthetical subscripts, $F := F_{(1)}$, $R := R_{(1)}$ for ease of reading.

Continuous dynamics

From (3.94), the stance dynamics of hopper 1 are free of any influence from hopper 2, and so $\dot{a}_1, \dot{\psi}_1$ can be computed as for an isolated vertical hopper De et al. (2016). However, there is coupling from hopper 1 into the dynamics of hopper 2, suggesting (for reasons to be motivated directly below in the discussion of (3.102)) the following coupled phase definition as a replacement for ψ_2 in (3.4):

$$\tilde{\psi}_2 := \psi_2 + \frac{\varepsilon a_1 \cos \psi_1}{2a_2}. \quad (3.101)$$

Owing to the new mechanical coupling, here we must define the following modified δ (specifically in the patch where hopper 1 is in stance and hopper 2 is in flight):

$$\tilde{\delta} := \frac{\psi_1 - \pi/2}{\omega} - \frac{\tilde{\psi}_2 - 1/2}{(1+\varepsilon)\omega_f(a_2)}. \quad (3.102)$$

Again, this definition is motivated by the aim to find a “slow” coordinate, $\frac{d}{dt}\tilde{\delta} = \mathcal{O}(\varepsilon)$, which is in equilibrium on the limit cycle.³⁶ With these new definitions, using the flight energy coordinate from

³⁵Note that for purposes of analysis, we merely require the coefficient of u_1 above to be $\mathcal{O}(\varepsilon)$, but for the sake of not introducing a new constant into our perturbation analysis around $\varepsilon = 0$, we choose the equality above.

³⁶Intuitively, in the averaging of a single vertical hopper in De et al. (2016), the introduction of the even function (with respect to the half-orbit center angle $\pi/2$), $\sin \psi_i$, in the coordination term, w_i (3.59), leaves a proportionally stabilizing δ term in \bar{f} . However, now with w_i set to 0, the odd function ($\cos \psi_i$) arising from the vertical energization term in v_i (3.58), can have no effect on relative phase (intentionally, since we prefer the vertical energization control not affect phase relations) and integrates out of the averaged vector field (3.105). The determination of the “right” phase coordinate $\tilde{\psi}_2$ (3.101) is, in this light, informed by the computation of $\frac{d}{dt}\tilde{\delta}$ as to not “disturb” the odd factor v_i in (3.104).

Research is currently under way to facilitate algorithmic generation of slow and fast coordinates for averaging.

(3.4) in (3.94),

$$\begin{aligned}
a_2 \dot{a}_2 &= \dot{z}_2(g + \ddot{z}_2) = -\varepsilon \dot{z}_2(u_1 + g) \\
&\stackrel{(3.4)}{=} -\varepsilon a_2(1 - 2\psi_2)(u_1 + g) \\
&\stackrel{(3.5)}{=} -\varepsilon a_2(1 - 2\psi_2)(\omega a_1 \sin \psi_1 + g) + \mathcal{O}(\varepsilon^2) \\
&\Rightarrow \dot{a}_2 \stackrel{(3.101)}{=} -\varepsilon(1 - 2\tilde{\psi}_2)(\omega a_1 \sin \psi_1 + g) + \mathcal{O}(\varepsilon^2).
\end{aligned}$$

Using (3.102) to replace $\tilde{\psi}_2$ with $\tilde{\delta}$, we get

$$\dot{a}_2 = -\frac{g\varepsilon(2\omega\tilde{\delta} - 2\psi_1 + \pi)(\omega a_1 \sin \psi_1 + g)}{2\omega a_2} \quad (3.103)$$

To calculate, $\frac{d}{dt}\tilde{\delta}$, first we calculate $\frac{d}{dt}\tilde{\psi}_2$. From (3.4), $\dot{\psi}_2 = -\frac{\ddot{z}_2}{2a_2} + \frac{\dot{z}_2 \dot{a}_2}{2a_2^2}$. Using (3.100) and (3.103),

$$\begin{aligned}
\dot{\psi}_2 &= \frac{g}{2a_2} + \varepsilon \left(\frac{g(g + u_1)(2\psi_2 - 1)(2\omega\tilde{\delta} - 2\psi_1 + \pi)}{4\omega a_2^2} \right. \\
&\quad \left. + \frac{g + u_1}{2a_2} \right) + \mathcal{O}(\varepsilon^2),
\end{aligned}$$

and then using (3.5) and the newly defined phase coordinate (3.101),

$$\begin{aligned}
\frac{d}{dt}\tilde{\psi}_2 &= \dot{\psi}_2 - \frac{\varepsilon a_1 \omega \sin \psi_1}{2a_2} + \mathcal{O}(\varepsilon^2) = \frac{g}{2a_2} + \\
&\quad \frac{\varepsilon g \left(\frac{(2\psi_2 - 1)(2\omega\tilde{\delta} - 2\psi_1 + \pi)(\omega a_1 s_1 + g)}{\omega} + 2a_2 \right)}{4a_2^2} + \mathcal{O}(\varepsilon^2).
\end{aligned}$$

Now we move on to using this to calculate $\frac{d}{dt}\tilde{\delta}$. Using (3.102) and also substituting in $\dot{\psi}_1$, we get

$$\frac{d}{dt}\tilde{\delta} = \frac{\varepsilon \sin \psi_1 v_1}{\omega a_1} + \mathcal{O}(\varepsilon^2).$$

Now we can complete the continuous dynamics for $\sigma := \psi_1, x := (a_1, a_2, \tilde{\delta})$,

$$\begin{aligned}
\dot{\sigma} &= \omega + \frac{\varepsilon}{a_1} \sin \psi_1 v_1 \\
\dot{x} &= \varepsilon \begin{bmatrix} -\cos \psi_1 v_1 \\ \frac{-g(2\omega\tilde{\delta} - 2\psi_1 + \pi)(\omega a_1 \sin \psi_1 + g)}{2\omega a_2^2} \\ \frac{\sin \psi_1 v_1}{\omega a_1} \end{bmatrix},
\end{aligned} \quad (3.104)$$

where v_1 is defined in (3.58) but now time with a silenced active phase coordination term $w_1 \equiv 0$. The form of (3.104) yields $\frac{dx}{d\sigma} = \mathcal{O}(\varepsilon)$ as required by Thm. 2. Comparing to the dynamics of the independent hoppers in De et al. (2016), we notice that $\dot{\sigma}, \dot{a}_1$ are identical (a consequence of the

lack of coupling from hopper 2 to hopper 1 in (3.94)), and second, in sharp contrast, that the \dot{a}_2 dynamics (3.103) are intricately coupled with the phase difference $\tilde{\delta}$.

Anticipating an anti-phase limit cycle, we consider the same x^* as for the independent hoppers (3.65), and averaging with respect to the fast variable ψ_1 after substituting in (3.58) gives us

$$\bar{f}(x) = \begin{bmatrix} \frac{k_a - a_1 \beta}{2\omega} \\ \frac{-g\tilde{\delta}(g\pi + 2a_1\omega)}{a_2\pi\omega} \\ 0 \end{bmatrix}, \quad (3.105)$$

which evaluates to 0 at x^* , satisfying Thm. 2(ii). Note that δ has an averaged effect on the energy level of the flight hopper (second row above). This departure from the mechanically decoupled hoppers De et al. (2016) contributes to the preflexive stabilization of the bounding limit cycle. Intuitively, if the flight hopper is leading in phase ($\tilde{\delta} < 0$), a_2 is increased, and vice versa. This effect over stance interacts with the reset (see text after (3.108)). Moreover, we can calculate the Jacobian at the fixed point,

$$D\bar{f}(x^*) = \begin{bmatrix} -\frac{\beta}{2\omega} & 0 & 0 \\ 0 & 0 & -g\xi_4 \\ 0 & 0 & 0 \end{bmatrix}, \quad (3.106)$$

where

$$\xi_4 := \frac{g\beta}{k_a\omega} + \frac{2}{\pi} \quad (3.107)$$

is a scalar only depending on constant parameters.

Reset

Since the aerial dynamics are the same as for isolated hoppers, the reset for the a_i components are the same as in (3.73). We now calculate the reset for the last coordinate $\tilde{\delta}$.

We use the explicit superscripts $.^f$ or $.^f$ to denote which coordinate patch (case of (3.4)) is being used. We use “ c_1 ” as shorthand for $\cos \psi_1^f$ in this calculation. At liftoff,

$$\begin{aligned} \delta(t_{LO}) &= \frac{\psi_1^f(t_{LO}) - \pi/2}{\omega} - \frac{\psi_2^f(t_{LO}) - 1/2}{\omega_f(a_2)} \\ &\stackrel{(3.101)}{=} \frac{\psi_1^f(t_{LO}) - \pi/2}{\omega} - \frac{\tilde{\psi}_2(t_{LO}) - 1/2}{\omega_f(a_2)} + \frac{\varepsilon c_1 a_1}{g} \\ &\stackrel{(3.102)}{=} \tilde{\delta} + \varepsilon \left(\tilde{\delta} + \frac{c_1 a_1}{g} - \frac{\psi_1^f(t_{LO}) - \pi/2}{\omega} \right). \end{aligned}$$

Similarly, but bearing in mind that at the touchdown patch hopper 1 is in flight and hopper 2 is in

stance, and accordingly modifying (3.102), we get

$$\begin{aligned}\delta(t_{\text{TD}}) &= \frac{\psi_1^f(t_{\text{TD}}) - 1/2}{\omega_f(a_1)} - \frac{\psi_2^f(t_{\text{TD}}) - \pi/2}{\omega} \\ &\stackrel{(3.101)}{=} \frac{\psi_1^f(t_{\text{TD}}) - 1/2}{\omega_f(a_1)} - \frac{\psi_2^f(t_{\text{TD}}) - \pi/2}{\omega} - \frac{\varepsilon c_2 a_2}{g} \\ &\stackrel{(3.102)}{=} \tilde{\delta} + \varepsilon \left(\tilde{\delta} - \frac{c_2 a_2}{g} + \frac{\psi_2^f(t_{\text{TD}}) - \pi/2}{\omega} \right).\end{aligned}$$

Using the boundary conditions $\psi_1^f(t_{\text{LO}}) = \pi$ (constant flow-time assumption in Table 5), and $\psi_2^f(t_{\text{TD}}) = 0$ (initial condition for the flow of Thm. 2) in the equations above,

$$\begin{aligned}\delta(t_{\text{LO}}) &= \tilde{\delta} + \varepsilon \left(\tilde{\delta} - \frac{a_1}{g} - \frac{\pi}{2\omega} \right), \\ \delta(t_{\text{TD}}) &= \tilde{\delta} + \varepsilon \left(\tilde{\delta} - \frac{a_2}{g} - \frac{\pi}{2\omega} \right).\end{aligned}$$

Substituting this into (3.73), and dividing through by $(1 + \varepsilon)$,

$$\tilde{\delta}(t_{\text{TD}}) = \tilde{\delta}(t_{\text{LO}}) + \frac{a_2 - a_1}{g}.$$

Putting everything together,

$$\bar{R}(a_1, a_2, \tilde{\delta}) = \bar{K} \begin{bmatrix} a_1, & a_2, & \tilde{\delta} + \frac{a_2 - a_1}{g} \end{bmatrix}^T. \quad (3.108)$$

We see that x^* in (3.65) when substituted into the equation above yields $\bar{R}(x^*) = x^*$, and $D\bar{R}$ has a constant $\mathcal{O}(1)$ part, together satisfying Thm. 2(i).

The influence of the energy levels a_i on the phase difference $\tilde{\delta}$ (apparent in the last entry above) results in a coupled interaction of a_2 and $\tilde{\delta}$ through the continuous dynamics (3.105) and the reset (3.108). Intuitively, following along the example in the discussion after (3.105), if the flight hopper is leading in phase ($\delta < 0$), then a_2 is increased during stance (as discussed before). From (3.108), the flight hopper now has a shorter flight period, and so δ is increased.

Stability test

Using (3.106) and (3.108), we can compute the averaged return map and evaluate at x^* (3.65),

$$D\bar{P}(x_2^*) = \left[\begin{array}{cc|c} 0 & 1 & -\varepsilon g \zeta_4 \\ \zeta_5 & 0 & 0 \\ \hline \zeta_5/g & -1/g & -(1 - \varepsilon \zeta_4) \end{array} \right], \quad (3.109)$$

where ζ_4 is defined in (3.107), and

$$\zeta_5 := 1 - \frac{\varepsilon \beta}{2\omega}. \quad (3.110)$$

Now we calculate the eigenvalues of (3.109). The characteristic polynomial is

$$\begin{aligned} m_\varepsilon(\lambda) &= \lambda^3 - \lambda^2(-1 + \varepsilon\zeta_4) - \zeta_5(1 - \varepsilon\zeta_4)\lambda - \zeta_5 \\ &=: \lambda^3 + c_2(\varepsilon)\lambda^2 + c_1(\varepsilon)\lambda + c_0(\varepsilon). \end{aligned} \quad (3.111)$$

The roots are an ε -parameterized family of scalars $\rho : \mathbb{R}_{\geq 0} \rightarrow \mathbb{C}$. The eigenvalues at $\varepsilon = 0$ are the roots of $m_0(\lambda) = \lambda^3 + \lambda^2 - \lambda - 1 = (\lambda^2 - 1)(\lambda + 1)$ (noting that $\zeta_5|_{\varepsilon=0} = 1$ from (3.110)), which are $\{-1, -1, 1\}$, and thus $\rho_1(0) = -1, \rho_2(0) = 1, \rho_3(0) = -1$.

Now we consider two cases: as $\varepsilon > 0$, either the eigenvalues remain all real, or two of them move into the complex plane as a complex conjugate pair:

- i) $\rho_i \in \mathbb{R}$: To do this, we find $\rho'_i(0)$. Note that the characteristic polynomial is alternatively expressed as

$$\begin{aligned} m_\varepsilon(\lambda) &= \prod_{i=1}^3(\lambda - \rho_i(\varepsilon)) = \lambda^3 + (-\rho_1 - \rho_2 - \rho_3)\lambda + \\ &\quad (\rho_1\rho_2 + \rho_1\rho_3 + \rho_2\rho_3)\lambda - \rho_1\rho_2\rho_3. \end{aligned}$$

Using the chain rule, we equate $D_\varepsilon c(\varepsilon) = D_\rho c(\varepsilon) \cdot \rho'(\varepsilon)$ and evaluate at $\varepsilon = 0$. However, the matrix $D_\rho c(\varepsilon)|_{\varepsilon=0}$ is singular, indicating that not all the eigenvalues remain real as $\varepsilon > 0$.

- ii) $\rho_1 \in \mathbb{R}, \rho_2, \rho_3 \in \mathbb{C}$: We reparameterize $\rho_2, \rho_3 = \zeta_6 \pm j\zeta_7$, and define $\zeta_8 := \zeta_6^2 + \zeta_7^2$. The characteristic polynomial is now

$$\begin{aligned} m_\varepsilon(\lambda) &= \prod_{i=1}^3(\lambda - \rho_i(\varepsilon)) = \lambda^3 + (-\rho_1 - 2\zeta_6)\lambda + \\ &\quad (2\rho_1\zeta_6 + \zeta_8)\lambda - \rho_1\zeta_8. \end{aligned}$$

We can equate the coefficients with (3.111), and differentiate with ε on both sides to get

$$\begin{aligned} -2\zeta'_6 - \rho'_1 &= c'_2, \\ \zeta'_8 - 2\zeta_6\rho'_1 + 2\zeta'_6\rho_1 &= c'_1, \\ -\rho'_1\zeta_8 - \rho_1\zeta'_8 &= c'_0, \end{aligned}$$

where $'$ denotes ε -derivative. Now evaluating both sides at $\varepsilon = 0$, we get a linear system of equations

$$\begin{bmatrix} -1 & 0 & -2 \\ -2 & 1 & 2 \\ -1 & -1 & 0 \end{bmatrix} \begin{bmatrix} \rho'_1(0) \\ \zeta'_8(0) \\ \zeta'_6(0) \end{bmatrix} = c'(0),$$

which is readily solved to yield $\rho'_1(0) = -\frac{\beta}{4\omega}$, and $\zeta'_8(0) = -\frac{\beta}{4\omega}$. Thus the first-order Taylor expansion of the roots is

$$\begin{aligned} \rho_1 &= 1 - \frac{\varepsilon\beta}{4\omega} + \mathcal{O}(\varepsilon^2), \\ |\rho_2|^2 &= |\rho_3|^2 = 1 - \frac{\varepsilon\beta}{4\omega} + \mathcal{O}(\varepsilon^2), \end{aligned}$$

and we are guaranteed that all the roots move inside the unit circle for small $\varepsilon > 0$.

So, the return map is hyperbolic, and so we can apply Thm. 2 to conclude that the weakly coupled hoppers have a stable anti-phase limit cycle ε -close to (3.65); we tabulate this result in Table 6.

Disruption with feedback

The preflexive stability we just proved is demonstrated in empirical results in Sec. 4.2.2, 4.2.4. We also demonstrate (though we do not analyze) the disruption of this preflexive stability using the phase controller (3.59) in Sec. 4.2.3. As argued in Remark 3.5.3, we expect the hyperbolic phase-controlled limit cycles to persist in a sufficiently small neighborhood of κ around 1. In interests of space we omit a full analysis of the weakly coupled slot hopper as detailed in this section with w_i set according to (3.59) (which would proceed almost identically to the proof presented here, with the incorporation of the feedback as shown in [De et al. \(2016\)](#)).

3.5.5 Strong Coupling: Preflex In-Phase Stability

In this subsection we consider the “strongly coupled” mass-parameter regime $\kappa \gg 1$ (last row of Table 6), where the body’s mass concentration beyond the hips moves the center of percussion far from the mass center, thus diminishing the moment associated with differences in the ground reaction forces of one leg vs. the other. Unlike in Sec. 3.5.4, where we used an explicit analytical relation between κ and ε made in (3.94), κ and ε are unrelated in this section. The regime of operation here is one of “large κ ,” but still “small ε .” As in [De et al. \(2016\)](#), we instead now interpret ε as the magnitude of the (naturally occurring) dissipative forces along with the underlying hopping energization terms (second summand in (3.58) originally introduced in [De and Koditschek \(2015b\)](#)) applied to the vertical hopper according to (3.5).

Because of the strong coupling, we find it helpful to work in the physical (z, ϕ) coordinates (center of mass location and body angle), subject to Assumption 5 as in Sec. 3.5.1. First, we introduce an assumption on the initial “attitude” energy:

Assumption 6. *The initial conditions lie within the “low a_ϕ ” set $\mathcal{L} := \{x : a_\phi/(\kappa a_z) = \mathcal{O}(\varepsilon^{1/2})\}$.*

Our justification for the assumption is listed in the next-to-last row of Table 5; specifically, we show empirical evidence of its applicability in Fig. 53. It allows us to decouple the vertical and attitude dynamics (Sec. 3.5.5). Next, we show that the vertical dynamics are stable (Sec. 3.5.5), which is unsurprising since the decoupled dynamics resemble that of an isolated vertical hopper.

Then, in Sec. 3.5.5–3.5.5, we tackle stability of the “attitude” coordinate, ϕ . First, we rigorously prove in Sec. 3.5.5 that the continuous-time orbits of r_ϕ followed by its resets render \mathcal{L} (of Assumption 6) positive invariant, subject to the following additional assumption:

Assumption 7. *The flight time is bounded above: $t_f < \varepsilon \pi \beta \sqrt{d/\kappa} / \omega^2$.*

This assumption (and the contraction proof it enables) is necessary because the stability of the ϕ -dynamics depend on the flight time of the slot hopper, thus rendering the ϕ -return map time-varying. However, numerical and empirical exercise of all these models shows that the time-variation in the return map is indeed insignificant; we offer evidence that Assumption 7 is unnecessary both in simulation (Sec. 3.5.6), as well as in data taken from the physical Minitaur experiments summarized in Fig. 51. In Sec. 3.5.5, we discuss an assumed time-invariant version of the ϕ -stability analysis, exposing the relation of the shape parameter κ to the behavior of ϕ , not subject to Assumption 7.

Coordinate changes

Similar to the map p in Sec. 3.1.1, we define the “ ϕ –phase”

$$p_\phi := d \begin{bmatrix} -\dot{\phi} \\ -\phi \omega \end{bmatrix}^T, \quad a_\phi := \|p_\phi\|, \quad (3.112)$$

as in (3.4). Unlike the complete polar transformation for the shank coordinate in (3.4), in this instance we only need the body angle energy a_ϕ for analysis. This is because in this subsection, the desired limiting behavior is a point attractor for ϕ (not an oscillatory behavior), and consequently a “ ϕ –phase” ψ_ϕ is neither well-defined nor required for analysis. In contrast, because vertical oscillations of the mass center are of key interest, we will need to define the vertical hopping energy and phase,

$$a_z := \|p(z, \dot{z})\|, \quad \psi_z := \angle p(z, \dot{z}) \quad (3.113)$$

as in (3.4) respectively. Note that the vertical energy coordinate a_z has units of m/s as before in (3.4), and the new attitude energy coordinate a_ϕ also has the same units (since in (3.112), d is a length, and ϕ is an angle).

Decoupling

Substituting our controllers (3.5), (3.58) with the attitude controller (3.60)³⁷ into the double stance equations of motion (3.96), we see that in closed loop,

$$\begin{aligned} \ddot{z} &= \omega^2(\rho - z) - \varepsilon\beta\dot{z} - \varepsilon k_a(\cos\psi_1 + \cos\psi_2)/2, \\ \kappa\ddot{\phi} &= -d(\omega^2 + k_p)\phi - d(\varepsilon\beta + k_d)\dot{\phi} \\ &\quad - \varepsilon k_a(\cos\psi_1 - \cos\psi_2)/2. \end{aligned} \quad (3.114)$$

Now we simplify the sum and difference cosines in the equation above. Define the variables $p_i := p(z_i, \dot{z}_i)$ (where the map p is as defined in Sec. 3.1.1), and $p_z := p(z, \dot{z})$. From (3.98), note that $p_1 = p_z + p_\phi$, and $p_2 = p_z - p_\phi$, where p_ϕ is defined in Sec. 3.5.5. To approximate $\cos\psi_i$ in (3.114), we need to approximate $1/\|p_i\|$:

$$\begin{aligned} \frac{1}{\|p_z + p_\phi\|^2} &= \frac{1}{p_z^T p_z + p_\phi^T p_\phi + 2p_z^T p_\phi} \\ &= \frac{1}{\|p_z\|^2} \left(\frac{1}{1 + (a_\phi/a)^2 + p_z^T p_\phi/a^2} \right) \end{aligned}$$

where note that from assumption 6, $(a_\phi/a)^2 + p_z^T p_\phi/a^2 = \mathcal{O}(\varepsilon)$. Taking a square root, we get

$$\frac{1}{\|p_z + p_\phi\|} = \frac{1}{\|p_z\|} (1 - \delta_+/2) + \mathcal{O}(\varepsilon),$$

³⁷Note that setting $k_p = k_d = 0$ recovers the preflexive case which we again remind the reader will be treated in Sec. 3.5.5–3.5.5, before returning to investigate the effect of coordination feedback in Sec. 3.5.5.

where we define $\delta_+ := (a_\phi/a)^2 + p_z^T p_\phi/a^2$. Similarly, we can calculate

$$\frac{1}{\|p_z - p_\phi\|} := \frac{1}{\|p_z\|}(1 - \delta_-/2) + \mathcal{O}(\varepsilon),$$

where $\delta_- := (a_\phi/a)^2 - p_z^T p_\phi/a^2$. We can now use these to calculate

$$\begin{aligned} \cos \psi_1 + \cos \psi_2 &= e_1^T \left(\frac{p_1}{\|p_1\|} + \frac{p_2}{\|p_2\|} \right) \\ &= \frac{e_1^T}{\|p_z\|} ((p_z + p_\phi)(1 - \delta_+/2) + (p_z - p_\phi)(1 - \delta_-/2)) \\ &= \frac{e_1^T}{\|p_z\|} \left(p_z \left(2 - \frac{\delta_+ + \delta_-}{2} \right) - p_\phi \frac{\delta_+ - \delta_-}{2} \right) + \mathcal{O}(\varepsilon) \\ &= \cos \psi (2 + \mathcal{O}(\varepsilon^2)) + \mathcal{O}(\varepsilon) = 2 \cos \psi + \mathcal{O}(\varepsilon), \end{aligned} \quad (3.115)$$

since a_ϕ/a appears in the p_ϕ term (use Assumption 6 again). Similarly,

$$\begin{aligned} \cos \psi_1 - \cos \psi_2 &= \frac{e_1^T}{\|p_z\|} \left(p_\phi \left(2 - \frac{\delta_+ + \delta_-}{2} \right) - p_z \frac{\delta_+ - \delta_-}{2} \right) + \mathcal{O}(\varepsilon) \\ &= \mathcal{O}(\varepsilon) - \cos \psi (p_z^T p_\phi/a^2) = \mathcal{O}(\varepsilon), \end{aligned} \quad (3.116)$$

using Assumption 6 again. Using (3.115) and (3.116) in (3.114),

$$\begin{aligned} \ddot{z} &= \omega^2(\rho - z) - \varepsilon \beta \dot{z} - \varepsilon k_a \cos \psi_z, \\ \kappa \ddot{\phi} &= -d(\omega^2 + k_p)\phi - d(\varepsilon \beta + k_d)\dot{\phi}, \end{aligned} \quad (3.117)$$

where $\psi_z = \angle p(z, \dot{z})$. Again, we emphasize that it is Assumption 6, empirically justified in the last row of traces in Fig. 53, which allows us to decouple the z and ϕ dynamics in stance to $\mathcal{O}(\varepsilon)$.

Additionally, note that the aerial dynamics in (3.97) are decoupled already, enabling completely isolated analyses of the vertical “ z ” DOF (in Sec. 3.5.5) and the attitude “ ϕ ” DOF (in Sec. 3.5.5–3.5.5).³⁸

CoM vertical dynamics stability

The z continuous dynamics (first row of (3.117)) are exactly the same as of a single “virtual” leg located at the center of mass [Raibert \(1986\)](#), [Saranli and Koditschek \(2003\)](#). The analysis of this subsystem proceeds identically to the analysis of a single vertical hopper [De et al. \(2016\)](#), and we obtain the same stability result.

³⁸Lastly, we point out that this decoupling of the vertical and pitch oscillations is in some sense necessary for a limit cycle analysis: as the last two rows of Fig. 37 show, the body angle oscillations generally occur at a different time scale than the stance/flight vertical hopping cycle of z , without any sign of phase-locking.

Attitude continuous dynamics: preflexive

For Sec. 3.5.5–3.5.5, we examine preflexive stability by setting $k_p = k_d = 0$ in (3.117). First we reparameterize the $\ddot{\phi}$ equation in (3.117) with

$$\omega_\phi := \omega \sqrt{d/\kappa}, \quad \beta_\phi := \frac{\varepsilon\beta}{2\omega} \sqrt{d/\kappa}, \quad (3.118)$$

to yield $\ddot{\phi} = -\omega_\phi^2(1 + \beta_\phi^2)\phi - 2\omega_\phi\beta_\phi\dot{\phi}$. Using the linear coordinate change

$$y_\phi := \begin{bmatrix} \omega_\phi \sqrt{1 + \beta_\phi^2} & \beta_\phi / \sqrt{1 + \beta_\phi^2} \\ 0 & 1 / \sqrt{1 + \beta_\phi^2} \end{bmatrix} \begin{bmatrix} \phi \\ \dot{\phi} \end{bmatrix} \quad (3.119)$$

from (Koditschek and Buehler, 1991, A.1), we get

$$\dot{y}_\phi = (-\omega_\phi\beta_\phi I - \omega_\phi J)y_\phi, \quad (3.120)$$

where $J := \begin{bmatrix} 0 & -1 \\ 1 & 0 \end{bmatrix}$ is the skew form of a rotation in the plane. Directly solving this linear system, we get the time- t_f flow of the vector field (3.120),

$$Q_\phi(y_\phi; t) = e^{-\beta_\phi\omega_\phi t_f} \text{Rot}(-\omega_\phi t_f)y_\phi, \quad (3.121)$$

where $\text{Rot} : S^1 \rightarrow \mathbb{R}^{2 \times 2} : \theta \mapsto \exp(\theta J)$ is the rotation matrix on the plane.

The reset for the ϕ coordinates (from the decoupled $\ddot{\phi} = 0$ aerial ϕ -dynamics) is a “time of flight” t_f -parameterized map,

$$R_\phi(y_\phi) = (I + \omega_\phi t_f N)y_\phi, \text{ where } N := \begin{bmatrix} 0 & 1 \\ 0 & 0 \end{bmatrix}. \quad (3.122)$$

Attitude stability: preflexive

Since the ϕ -dynamics are decoupled from the z -dynamics to $\mathcal{O}(\varepsilon)$ in both the flow (3.117) and reset (3.122), we can analyze the ϕ -stability separately. Direct computation yields the return map

$$\begin{aligned} P_\phi(y_\phi) &= R_\phi \circ Q_\phi(y_\phi; t_f) \\ &= e^{-\beta_\phi\omega_\phi t_f} (I + \omega_\phi t_f N) \text{Rot}(-\omega_\phi t_f)y_\phi. \end{aligned} \quad (3.123)$$

We next prove that P_ϕ is a contraction subject to Assumption 7. First, we need a Lemma:

Lemma 4. For $\chi \geq 0$, $e^\chi \geq 1 + \chi^2/2 + \chi\sqrt{1 + (\chi/2)^2}$.

Proof. First, note that

$$\begin{aligned} \frac{d}{d\chi} \left(1 + \frac{\chi^2}{2} + \chi\sqrt{1 + \chi^2/4} \right) &= \chi + \frac{2+\chi^2}{\sqrt{4+\chi^2}} \\ &\leq \chi + \frac{2+\chi^2}{2} = 1 + \chi + \frac{\chi^2}{2} \leq e^\chi, \end{aligned}$$

whereas the last expression is the derivative of e^χ . Since both expressions equal 1 at $\chi = 0$, and the derivative of e^χ is pointwise greater for $\chi \geq 0$, e^χ is the larger expression for all $\chi \geq 0$. \square

Let us define $\theta_f := \omega_\phi t_f$, and $\theta_f := \omega_\phi t_f$. To check if P_ϕ is a contraction, we need to check that the largest eigenvalue of $P_\phi^T P_\phi$ lies within the unit cycle, since this is the largest value that $y^T P_\phi^T P_\phi y / y^T y$ can take. The largest eigenvalue is

$$\lambda_{\max} \leq \frac{e^{-2\beta_\phi \theta_f}}{2} (2 + \theta_f^2 + \theta_f \sqrt{4 + \theta_f^2}) \leq e^{-2\beta_\phi \theta_f + \theta_f},$$

where we use the Lemma above for the last inequality. Since the exponential is monotonic, we only need check

$$-2\beta_\phi \theta_f + \theta_f < 0 \iff t_f - \frac{\varepsilon \pi \beta \sqrt{d/\kappa}}{\omega^2} < 0$$

which is ensured by Assumption 6. Thus, P_ϕ is a contraction. The continuous ϕ dynamics already (3.117) strictly contract a_ϕ , and so \mathcal{L} is positive invariant.

In summary, the decoupling described in Sec. 3.5.5, the proof of vertical stability of the CoM in Sec. 3.5.5, and the proof of ϕ -stability in this subsection together guarantee stability of the in-phase limit cycle; we list this result in Table 6. We continue below to make further observations about the behavior when Assumption 7 is not made, or in the presence of feedback.

Attitude stability: time-invariant, preflexive

Making instead the approximation that both the stance time t_f and flight time t_f are constant (justified by observing their small variance in empirical trials such as the one in Fig. 51), we now have a time-invariant ϕ -return map (3.123), and we can look at the *eigenvalues* of P_ϕ to discern stability.

Define $\widetilde{P}_\phi := (I + \theta_f N) \text{Rot}(-\theta_f)$ such that $P_\phi(y_\phi) = e^{-\beta_\phi \theta_f} \widetilde{P}_\phi y_\phi$. Note that

$$\det \widetilde{P}_\phi = 1, \quad \text{tr } \widetilde{P}_\phi = 2 \cos \theta_f - \theta_f \sin \theta_f.$$

Next, we prove and use the following Lemma:

Lemma 5. *If $\det \widetilde{P}_\phi = 1$ and $|\text{tr } \widetilde{P}_\phi| \leq 2$, then $\widetilde{\lambda}_i$, the eigenvalues of P_ϕ , are complex conjugate with unit magnitude.*

Proof. Since the determinant is identically 1, $\widetilde{\lambda}_i = \text{tr}/2 \pm \sqrt{(\text{tr}/2)^2 - 1} =: \xi_0 \pm j \xi_1$, and $|\widetilde{\lambda}_i|^2 = \xi_0^2 + \xi_1^2 = 1$. \square

Note from (3.118) that $\omega_\phi \propto 1/\sqrt{\kappa}$, and so when κ is made arbitrarily large, $|\text{tr } \widetilde{P}_\phi| \rightarrow 2$. The eigenvalues of P_ϕ are $\lambda_i = e^{-\beta_\phi \theta_f} \widetilde{\lambda}_i$, and so (using the Lemma above) λ_i lie within the unit circle. We conclude that the return map P_ϕ is stable, without requiring the restrictive Assumption 7.

We show numerically (in Sec. 3.5.6) as well as empirically, by mechanically reconfiguring Minitaur to have two different κ values (in Sec. 4.2.2), that this condition on κ is important, and that instability of the in-phase limit cycle results when κ is not large enough. In other words, the “weakly coupled” body of Sec. 3.5.4 (as well as our physical platform Minitaur arranged with its “native” intended body mass distribution) does not possess a stable in-phase limit cycle, and requires feedback control (which we discuss next) to render it attracting, thereby eliciting a pronk.

Attitude stability: feedback

Now, we augment the preflexive stability to reinforce the in-phase (pronking) limit cycle by reintroducing feedback through positive k_p and k_d in (3.60). From (3.117), we have enough control affordance to stabilize the ϕ dynamics to a point within a single stance phase as follows.

First, we reparameterize the constants k_p and k_d in terms of a new parameter, $k_\phi > 0$, such that

$$\frac{d(\omega^2 + k_p)}{\kappa} = k_\phi, \quad \frac{d(\varepsilon\beta + k_d)}{\kappa} = \frac{k_\phi^2}{2}.$$

Using this in the second row of (3.117), we get

$$\ddot{\phi} = -k_\phi \dot{\phi} - k_\phi^2 \phi / 2. \quad (3.124)$$

Now define the “graph error” [Koditschek \(1987\)](#) $e_\phi := \dot{\phi} + k_\phi \phi$. Using (3.124), we get

$$\dot{e}_\phi = -2k_\phi e_\phi \implies e_\phi(t) := e^{-2k_\phi t} e_\phi(0), \quad (3.125)$$

and so k_ϕ can be made arbitrarily large to get $e_\phi(t)$ arbitrarily small in stance. Consequently, in arbitrarily small time, the flow collapses to the $e_\phi^{-1}(0)$ submanifold, where by definition of e_ϕ ,

$$\dot{\phi} = -k_\phi \phi \implies \phi(t) = e^{-k_\phi t} \phi(0), \quad (3.126)$$

and with large k_ϕ , both $\phi(t), \dot{\phi}(t)$ are also driven to zero arbitrarily fast. Denote this deadbeat stance map as

$$Q_{\phi, \text{FB}} : (\phi, \dot{\phi}) \mapsto \text{“arbitrarily close to 0”}. \quad (3.127)$$

Choosing a Poincaré section at liftoff, we get the return map

$$P_{\phi, \text{FB}} \left(\begin{bmatrix} \phi \\ \dot{\phi} \end{bmatrix} \right) = Q_{\phi, \text{FB}} \left((I + t_f N) \begin{bmatrix} \phi \\ \dot{\phi} \end{bmatrix} \right). \quad (3.128)$$

In summary, despite the flight destabilization, the deadbeat nature of the stance stabilization guarantees stability in the return map sense. We list this result in Table 7.

Though this discussion of feedback stability is for the strongly coupled plant (3.114), we employ this controller on the physical platform Minitaur, and empirically find that even in the “weakly coupled” regime ($1 - \kappa \approx 0$) it is able to overcome preflexive bounding stability and exhibit a pronking gait (Sec. 4.2.3).

3.5.6 Numerical Results

In this subsection, we use numerical simulation (all created using [MATLAB R2016a](#) with `ode45`) to, first, test the efficacy of our slot hopper model and justify the various assumptions that were made for our analyses (Table 5) in Sec. 3.5.6–3.5.6. In Sec. 3.5.6, we use numerical study to get a global view of the closed-loop behavior when subject to a κ –sweep (3.86). An exhaustive κ –sweep would be impractical with the physical platform, though we present empirical results at two interesting values as suggested by our analysis (Fig. 30).

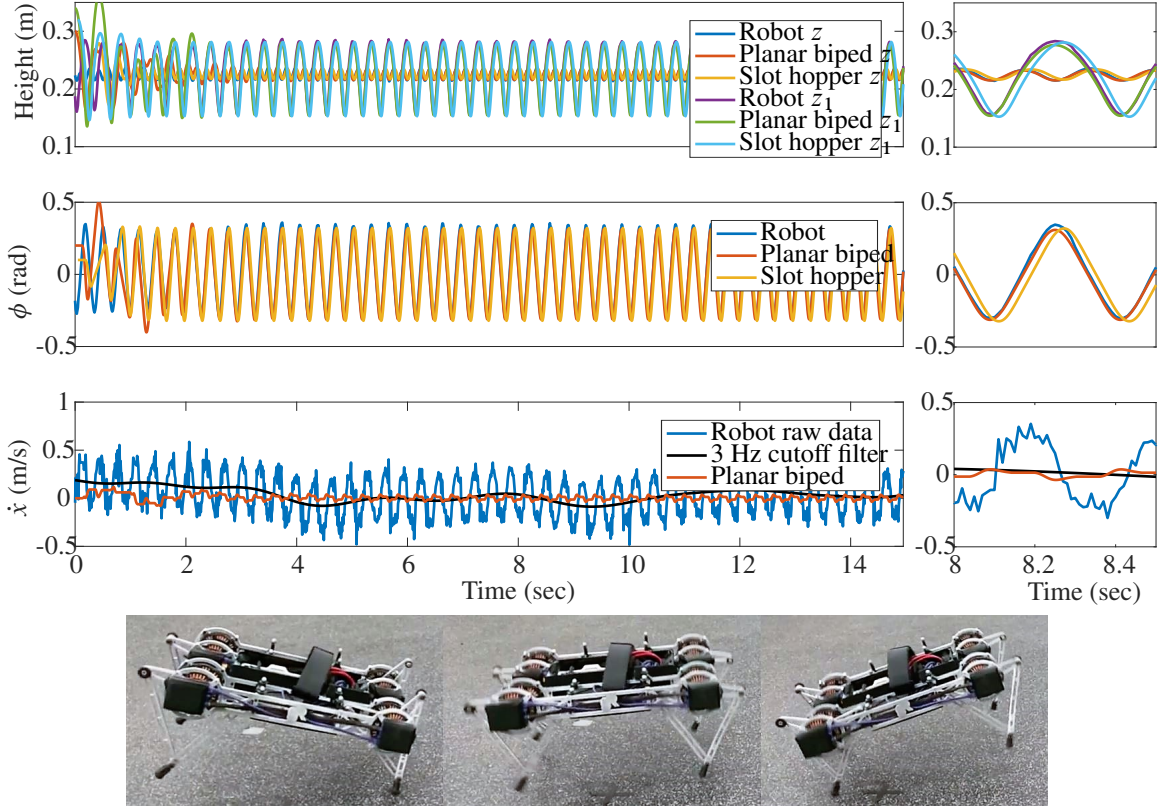


Figure 32: Projecting Minitaur and sagittal plane biped trajectories onto the slot hopper DOF. **Top:** A comparison of empirical data from Minitaur bounding in place (Fig. 27C) with simulations of a high-fidelity sagittal biped model (Sec. 3.5.6, Fig. 27B) and the more abstracted slot hopper model (Sec. 3.5.1, Fig. 27A). Note that the x DOF only appears in models B–C, and its velocity is displayed here (third plot of traces) for a full account of the physical machine’s behavior as it bounds in place (see Sec. 3.5.6). We provide a “zoomed-in” version on the right so that some of the almost-overlapping traces are visible (e.g. the z coordinate in the first row is almost overlapped by the red/yellow traces). **Bottom:** Snapshots of WC-Minitaur bounding in place (taken at rear stance, aerial, and front stance) from this experiment.

2DOF slot-hopper as a model for Minitaur

We posit the 2DOF slot hopper model (Sec. 3.5.1) as a template—analytically tractable and effectively representative of the locomotion tasks of interest [Full and Koditschek \(1999\)](#)—to be anchored in a physical platform possessing far greater dynamical complexity. Even assuming massless limbs, and considering operation in only the sagittal plane, a physically realistic Lagrangian model requires working with at least 5DOF kinematics, suggesting the sagittal plane biped (Fig. 27B) as an intermediate model.

In this section, we present plots comparing the template and appropriately projected numerical and empirical body trajectories that establish: (i) the accuracy of a linearized approximation (Assumption 5) to that template; (ii) the precision with which the sagittal plane biped model (Fig. 27B) anchors that template; and (iii) initial empirical data suggesting the efficacy of that intermediate

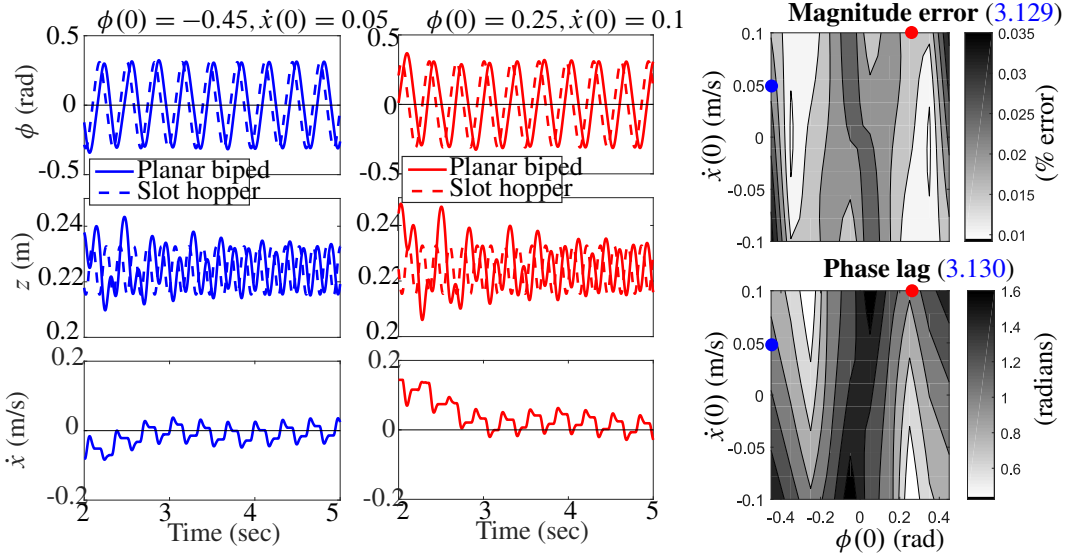


Figure 33: 2DOF slot-hopper as a template anchored by the Sagittal Plane biped. Numerical comparison of steady state behavior in the sagittal biped (Fig. 27B, Sec. 3.5.6) and in the slot-hopper (Fig. 27A, Sec. 3.5.1) models presenting error between the corresponding state trajectories from a variety of initial conditions. **Left:** time trajectories from two different initial conditions in the two columns. Note that the last traces on the left are non-existent for slot-hopper and only show that the sagittal plane biped settles down to zero-net horizontal velocity. **Right:** a frequency domain comparison of the resulting ϕ and z oscillations obtained from 100 initial conditions (10 along each axis; see Sec. 3.5.6 for details). Even though the phase lag can be quite large, it converges to a constant which is generally small (as shown in the right hand sweep, and which, in any case, does not diminish the qualitative match), and the error in oscillation magnitude is bounded above by 3.5% (as discussed in Sec. 3.5.6). With the exception of the added x -DOF, the primary distinction between these two models is our Assumption 5; the qualitative similarity in the limiting behavior of the two models thus justifies the assumption.

model as a description of the sagittal plane behavior of the Minitaur robot (Fig. 27C) at steady state. We reserve for Sec. 4.2.2 a more extensive empirical study detailing the utility of the template model's preflexive and feedback-based stability analyses for commanding and executing useful running behavior in the physical machine.

This intermediate numerical model of the anchoring sagittal plane system (Fig. 27B) can be derived using the self-manipulation modeling paradigm of Johnson et al. (2016). As shown in Fig. 27 (third column), the body is allotted 3 DOF's, and each leg is modeled as a massless revolute-prismatic joint, suggesting

$$\mathbf{q} := [\theta_1, \ r_1, \ \theta_2, \ r_2, \ x, \ z, \ \phi]^T,$$

and the kinetic and potential energies are respectively

$$T(\mathbf{q}, \dot{\mathbf{q}}) := \frac{1}{2}m_b(\dot{x}^2 + \dot{z}^2) + \frac{1}{2}i_b\dot{\phi}^2, \quad V(\mathbf{q}) := m_bgz.$$

Additionally, we consider two possible active contacts at the massless toes,

$$\mathbf{a}_i(\mathbf{q}) := \begin{bmatrix} x \\ z \end{bmatrix} + (-1)^{i-1} d \begin{bmatrix} \cos \phi \\ -\sin \phi \end{bmatrix} + r_i \begin{bmatrix} -\sin(\theta_i - \phi) \\ \cos(\theta_i - \phi) \end{bmatrix},$$

and depending on which contacts are active, one or both constraints are activated, and appear as rows in $\mathbf{a}(\mathbf{q})$. We omit a full hybrid system description of this model, but we follow the modeling procedure of [Johnson et al. \(2016\)](#).

In Fig. 32, we plot data from Minitaur and data from both the sagittal biped simulation and the slot hopper simulation. Since the body inertia i_b is not known accurately for Minitaur, we tuned that parameter from the simulation; $\kappa = 0.77$ proved to be a good estimate. In the last row, the speed of the robot from raw motion capture data is plotted alongside a filtered version (obtained by truncating the Fourier transform at 3 Hz—approximately the stride rate of bounding Minitaur). We believe that the speed oscillations are caused in part because of the motion capture rigid body CoM being located vertically above the actual CoM, and also because the body speed \dot{x} does indeed oscillate in a manner that averages out over a stride due to imperfect tuning of the nominal leg angles. The leg angles and fore-aft behavior are out of the analytical scope here (though we describe our implementation in Sec. 4.2.4).

The sagittal biped simulation’s speed is also plotted, but note that the slot hopper model does not even have an x degree of freedom. The fore-aft energy can be considered a “perturbation” to the slot hopper model we have analyzed here, and the persistence of the expected vertical oscillations and phase relationships testifies further to the robustness of the analytical results.

All in all, Fig. 32 indicates that at least for bounding in place, both models provide good agreement in the z and ϕ degrees of freedom (to each other and to empirical data), over the region of state space most pertinent to the bounding task. A comparison of the slot hopper and sagittal biped models over a much larger region of state space (more trials than is practical to run on the physical platform) is shown in Fig. 33.

The left panels of Fig. 33 show time trajectories for some relevant coordinates comparing the sagittal biped simulation to the slot hopper simulation. The simulations are started with both models in aerial phase, with different initial $\phi(0)$, $\dot{x}(0)$ conditions, but from the same $z(0)$. Note from Fig. 32 and Fig. 54 that the initial ϕ on touchdown for bounding seems to be within $|\phi| < 0.4$ radians empirically. The range of speeds chosen was small since this simulation does not implement the fore-aft control necessary to stabilize large speeds (in Sec. 4.2.4, we describe a controller used for this purpose on the physical platform).

The leftmost columns show time-trajectories of the resulting hybrid executions, and even though the two models are drastically different in dimension and complexity, the resulting behavior is a characteristic z and ϕ oscillation in either case. The only discernible qualitative difference is a phase shift in the resulting steady-state oscillation.

In the top right column of Fig. 33, we compare the resulting oscillations in the frequency domain. Suppose $\mu_z(\mathbf{M})$ is the z -oscillation magnitude at the predominant frequency, where $\mathbf{M} \in \{\mathbf{A}, \mathbf{B}\}$ (referring to the model from Fig. 27), and a similar quantity is defined for ϕ . In Fig. 33 (top right) we plot the quantity

$$\left\| \begin{bmatrix} \mu_\phi(\mathbf{B})/\mu_\phi(\mathbf{A}) \\ \mu_z(\mathbf{B})/\mu_z(\mathbf{A}) \end{bmatrix} - \begin{bmatrix} 1 \\ 1 \end{bmatrix} \right\| \tag{3.129}$$

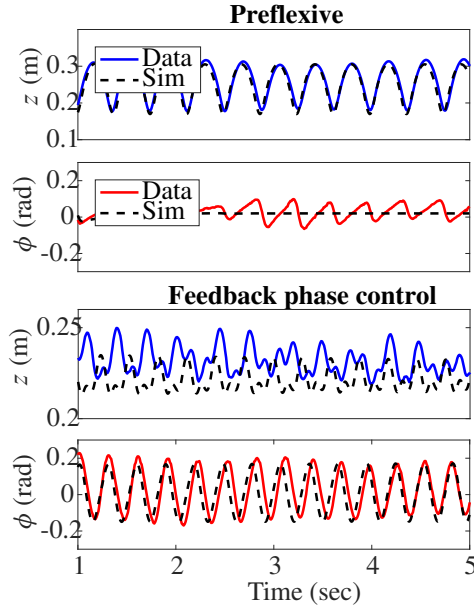


Figure 34: Comparison of slot hopper simulation to SC-Minitaur. The empirical data (in contrast to the numerically computed dotted traces) for this plot is from Fig. 51 and Fig. 52, and we have now used the value of κ in (4.16). Note the different z -scales in the two sets of plots. See the last paragraph of Sec. 3.5.6 for further discussion.

as a metric of the normalized dissimilarity in the ϕ , z oscillations in the two cases. Note that each entry of the vector inside the $\|\cdot\|$ above is a “% error” in the oscillation of the ϕ , or z trace (respectively), and we plot the norm of this vector in the top right of Fig. 33. As the legend reveals, the error is less than 3.5% over the range of initial conditions considered.

In the Fig. 33 (bottom right), we compare the phase offset of the resulting ϕ -oscillations,

$$\angle_\phi(\mathbf{B}) - \angle_\phi(\mathbf{A}) \quad (3.130)$$

showing a larger range of phase lags between the two simulations (generally more strongly related to $\phi(0)$ than $\dot{x}(0)$). These discrepancies in steady state phase as a function of initial condition don’t affect qualitative behavior on the limit cycles, hence, the stabilizing effects of body and feedback parameters proven mathematically for the slot-hopper (Sec. 3.4.2, 3.4.3, 3.5.4, 3.5.5) achieve correspondingly stabilizing results in the qualitative behavior of the sagittal biped and physical robot as we will detail in the next section.

In addition to the numerical and empirical comparisons in Fig. 32–33, we include in Fig. 34 another comparison of the slot hopper’s preflexive and feedback–stabilized behavior at a different κ value (4.16) to data from SC-Minitaur. The top two rows demonstrate preflexive (pronking) behavior, and with the same κ value, we apply the phase controller (3.59) to both simulation and physical platform, and plot the results in the bottom rows (bounding in both cases). The ϕ -traces in the top row, and the z -traces in the bottom row both exhibit small amplitude variations, where various perturbation sources in the physical world cause apparent discrepancies between physical data and simulation. However, there is a very close match in the more pronounced z , and ϕ –

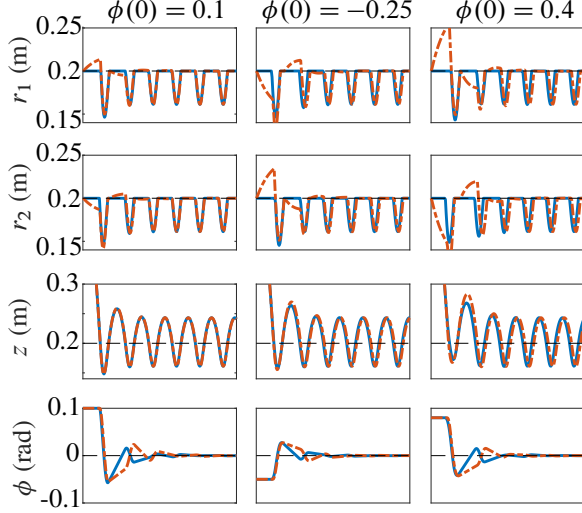


Figure 35: Qualitative effect of active toe extension for simultaneous transitions. Simulation runs of the slot hopper (Sec. 3.5.1, Fig. 27A) testing the simultaneous transition assumption (third row of Table 5) with some plots of executions from different initial conditions (in columns). In the traces with **dashed lines**, active toe extension control in aerial phase (see Sec. 3.5.6) is enabled, whereas for the **solid lines** it is disabled. The resulting qualitative behavior is almost identical in either case.

oscillations that are observed in the top and bottom rows respectively between the simulation and the empirical data. This provides more evidence that the template and the analytical conclusions garnered from Sec. 3.5.5 and Sec. 3.4.3 are representative of Minitaur’s behavior in the real world.

Near-simultaneous transitions

As Sec. 3.3.1 describes, an assumption on active toe extension control is required for the application of the single-mode hybrid averaging theory De et al. (2016) to our analyses in Sec. 3.4.3 and Sec. 3.5.5 (to ensure simultaneous transitions between aerial and double stance modes as intuitively illustrated in the lower series of Fig. 26). However, in practice, the resulting hybrid executions of the four-mode system (allowing for single stance) are quite similar.

In Fig. 35, we compare simulated executions of the slot hopper model (Sec. 3.5.1) from three different initial $\phi(0)$ conditions ($z(0) = 0.4$ m in each case), with executions of a version of this model modified as follows. In the aerial phase, we apply the following acceleration to the toe (though the mass is non zero)

$$\ddot{r}_i := k_p \left(\rho + (-1)^{i-1} \phi d - r_i \right) - k_d \dot{r}_i,$$

for $i \in \mathcal{I}$, where r_i is the extension of the toe in flight. Though the model assumes massless toes, this imposed feedback results in simultaneous touchdown as long as $|\phi| < \pi/2$. In Fig. 35, the solid lines correspond to executions going through all 4 hybrid modes, and the broken lines are with simultaneous touchdown.

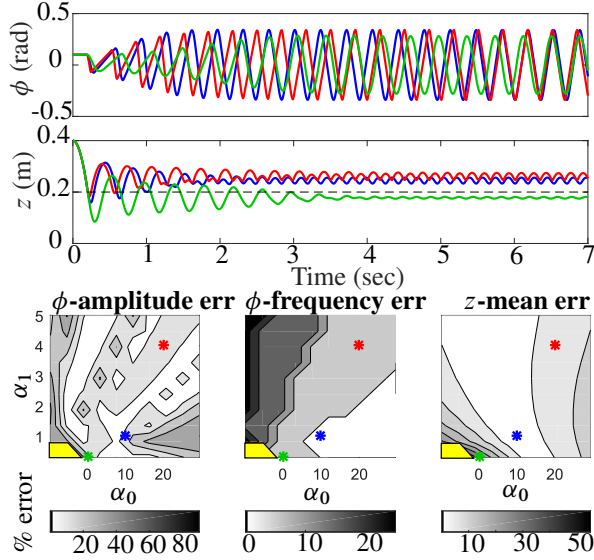


Figure 36: Robustness to parametric inaccuracy. Simulation of the slot hopper model (Fig. 27A) testing the effect of poorly chosen physical mass and inertial matching parameters, α_i in Sec. 3.5.1. Despite the large and varied discrepancies between assumed (applied in the control (3.91)) and actual α_i captured in the bottom plot, there is a stable limit cycle everywhere except for a region contained within the yellow polygon. The colors in the top plot correspond to the applied parameters designated by the “*” in the bottom row. The “correct” parameters (Table 6) are at the blue “*” (i.e. there is no parameter mismatch); we chose the green “*” to be deliberately close to the yellow “failure region” (the lowered energy results in almost no aerial phase, causing the z -oscillations to be diminished; cf. Sec. 3.5.6), and the red “*” in a disparate region of the parameter space. The percentage errors in the last row measure the relative discrepancy between the intended response to “correct” (blue) control parameters vs. that achieved by the actually applied parameters as described in (3.131) and the text following.

As expected, the larger $|\phi(0)|$ results in the most disparate behavior³⁹, but in all cases, the asymptotic resulting behavior is identical, with small phase shifts in the z -oscillations. This supports our analytical Assumption 3 of simultaneous transitions in Sec. 3.4.3 and Sec. 3.5.5, even though we do not enforce it on the physical platform (Sec. 4.2.1) when employing the controller (3.5) with v_i as in (3.58). Still, as referenced from Table 5, the relative frequency of single stance periods observed in pronking trials is quite low (< 7%).

Robustness to parametric inaccuracy

The simple form our controller takes (3.5), (3.58) is relatively robust to parametric inaccuracy. In Fig. 36, we numerically explore the results of a mismatch in the two parameters α_i in (3.91) of Sec. 3.5.1. In the wide range of parameters shown in the bottom row ($g \in [-10, 40]$ m/s² and one order of magnitude of variation in the assumed body mass m_b)⁴⁰, the qualitative behavior still

³⁹Because larger ϕ results in longer unmodeled single stance periods when the active policy of Sec. 3.3.1 is not applied.

⁴⁰Even non-physical $g < 0$ values result in observable hopping since the spring-like forces in (3.5) dominate the constant term in (3.91).

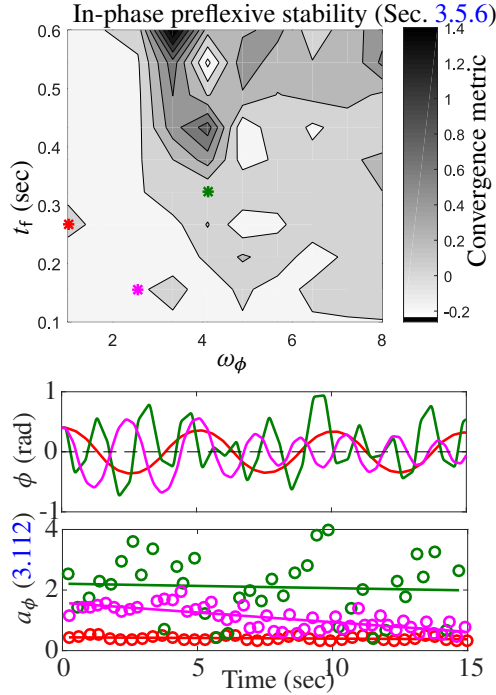


Figure 37: *Strongly coupled in-phase stability vs. κ .* Simulations of a slot hopper (Sec. 3.5.1, Fig. 27A) testing the convergence of an in-phase limit cycle as the parameters ω_ϕ (equivalently, κ through (3.118)) and the flight time t_f . The “convergence metric” is an estimate (described in Sec. 3.5.6) where negative values indicate stability. We chose the pink and green parameter vectors on either side of a posited stability “boundary” supported by the findings of Sec. 3.5.5, and the red point to illustrate that the behavior for small- ω_ϕ is convergent (albeit slow due to the small ω_ϕ) despite the dark patch surrounding it. The plots in the bottom row are discussed in the text.

displays a stable limit cycle for almost⁴¹ the entire region. We chose $\kappa = 0.9$ for each simulation in this subsubsection.

The top rows of Fig. 36 plot executions from three different parameter sets (shown in the bottom row with a “*” corresponding to the color of the solid line in the top row). The bottom row of Fig. 36 displays the discrepancy

$$100 \left(\mu_i(\alpha) / \mu_i(\alpha^*) - 1 \right) \quad (3.131)$$

in the resulting ϕ and z oscillations for some parameter vector $\alpha = [\alpha_0, \alpha_1]$ relative to the result with the correct parameters, α^* (blue “*” in Fig. 36), for three different “measures” μ_i chosen for the three columns along the bottom row of Fig. 36: the magnitude of the ϕ -oscillation (**left**), frequency of the ϕ -oscillation (**center**), and mean of the limiting CoM height z (**right**).

We can see from the contours on the bottom row that excluding the yellow region⁴¹ that in each case, even large parametric mismatches in (3.91) result in less than 30% error as compared to the designer’s intention.

⁴¹Except the region within the depicted yellow polygon, where the applied radial force (3.91) is insufficient to overcome gravity and sustain oscillations.

Strongly coupled in-phase stability vs. κ

In Sec. 3.5.5, we showed that the assumption of constant flight time permits a conclusion that “high enough” κ (consequently, “low enough” ω_ϕ in (3.118)) results in preflexive pronking. In simulation, we test a range of values of ω_ϕ across an order of magnitude to explore its interaction with a primary destabilizing influence absent this assumption. Intuitively, a greater excursion of pitch in flight should disrupt the sagittal plane gaits and, indeed, recall from the return map expression (3.123), the flight time t_f provides a destabilizing effect. Motivated by this, in Fig. 37, we plot a metric of stability (which we describe below) on a ω_ϕ – t_f^* plane. The flight time is not constant, however we provide the vertical hopper with a desired energy $a^* = gt_f^*/2$.

The bottom rows of Fig. 37 display both the physical ϕ coordinate, as well as values of a_ϕ (3.112) sampled at successive transitions into aerial mode (liftoff). The slope of the solid line⁴² in the bottom row is the “convergence metric” we use in the top row of Fig. 37. We use this unconventional metric since (as the green time-series plot shows), in large parts of this “ungoverned” region of the parameter space, the behavior is somewhat chaotic (as apparent from the a_ϕ plot), and conventional numerical estimates of the return map eigenvalues return uninterpretable or inaccurate results. Nonetheless, negative values indicate “convergent” behavior, and positive values correspond to divergence.

The plot results agree with our analytical result in Sec. 3.5.5 even without a time-invariant assumption: for each t_f^* , there is a “low enough” ω_ϕ that results in convergence to the in-phase limit cycle, and for smaller t_f^* allows for a larger range of ω_ϕ that result in stability. These findings are corroborated by empirical results in Sec. 4.2.2; in particular, Fig. 51 shows a stable empirical preflexive pronk obtained by simply modifying the κ of the physical platform with no feedback-generated control signals (i.e. $w_i \equiv 0$ in (3.58)).

Phase locking at intermediate κ

In our analysis of the case $\kappa < 1$ in Sec. 3.5.4, we showed the anti-phase limit cycle is preflexively stabilized, whereas in Sec. 3.5.5 we argued that there is a preflexive stability for the in-phase limit cycle when $\kappa \gg 1$. These analyses motivate an inquiry into the behavior of the system for intermediate values of κ (i.e., comprising a range of values around the third row of Table 6). As previously argued in Sec. 3.5.3, we expect the phase control to be effective in a sufficiently small neighborhood of κ around 1; numerically and (as we show in Sec. 4.2.3) also empirically, we are able to explore a much larger neighborhood.

Fig. 30 shows the limiting (after $t = 10$ seconds of execution) “touchdown offset”,

$$\cos(2\pi\tilde{s}), \text{ where } \tilde{s} := \frac{s_i - s_{i-1}}{s_i - s_i^-} \quad (3.132)$$

for leg $i \in \mathcal{I}$, s_i is the latest touchdown time of leg i , and s_i^- is the previous touchdown time. This calculation essentially returns $\tilde{s} = 0$ for the in-phase limit cycle, and $\tilde{s} = 1/2$ for an anti-phase limit cycle.

⁴²The solid line is obtained as a least-squares degree-1 polynomial fit. While in a linear system we would expect an exponential trend, due to the chaotic nature of the section data, in our experience a degree-1 fit proved relatively more reliable.

The black dots in Fig. 30 summarize simulation runs that corroborate the analytical results of this section for the slot-hopper model (Fig. 27A) at the left and right extremes of the plot (Sec. 3.5.4 and Sec. 3.5.5, respectively), and strongly suggest that there is a sharp “phase transition” in a tight neighborhood of $\kappa = 1$ regarding which our analysis is silent absent the specific sensorimotor feedback policies analyzed in Sec. 3.4.2–3.4.3. Looking ahead to the empirical study of the next section, the superimposed vertical green and magenta lines correspond roughly to the values of κ exhibited by Minitaur without weights (see Sec. 4.2.2 reporting reflexive bounding via an anti-phase fore-aft oscillation) and with weights (see Sec. 4.2.3 reporting preflexive pronking via an in-phase fore-aft oscillation) added to distribute the mass center. Their correspondence with this section’s analysis of the slot-hopper model further attests to our hypothesis that its dynamics are anchored by preflex in the physical machine.

In contrast, we use colored dots in Fig. 30 to depict the capacity of the sensorimotor feedback policy (3.59) to override the preflexive coordination patterns as proven in Sec. 3.4.2–3.4.3 for the case $\kappa = 1$ and shown in Sec. 3.5.3 to apply in the “approximately decoupled” $\kappa \approx 1$ regime (depicted in gray along the abscissa of Fig. 29). Specifically, the red dots summarize the simulated results of applying (3.59) with $k_d < 0$ (commanding an anti-phase limit cycle) while the blue dots correspond to the case $k_d > 0$ (commanding an in-phase limit cycle) for the slot-hopper model (Fig. 27A), with a range of coupling values including the effectively decoupled situation of $\kappa = 1$ illustrated in Fig. 25. While the phase control is insufficient to overcome the preflexive stability at extreme values of κ , the figure shows regions near $\kappa = 1$ where the feedback control is able to stabilize near-independent hoppers to a desired limit cycle. The disruptive influence of feedback is also empirically demonstrated in the Minitaur in Sec. 4.2.3.

3.6 Time-Reversal Symmetry and its Relation to Averaging

Our previous mathematical formulation (Sec. 3.2, De et al. (2016)) has brought classical dynamical averaging theory to bear on a (restricted) class of hybrid systems: averageable single-mode hybrid systems (HAS). However, the difficulty in applying our previous result (Thm. 2/3) is threefold:

- a) A HAS as listed in conditions of Thm. 3 must have a single “fast” mode (3.39). Our interest in compositions generically take the form of coupling several oscillators together (as in a tailed biped that translates while hopping De and Koditschek (2015b), a composition of two virtual legs in a virtual biped (Sec. 3.5, De and Koditschek (2016)), coupled oscillator formulations of multilegged coordination Righetti and Ijspeert (2008), Owaki et al. (2013), etc. Thus in order to apply the theorem, coordinate changes to appropriate slow phase differences must be constructed. While phase differences are easily constructed for identical coupled oscillators Proctor et al. (2010), they must be hand-crafted in the case of non-identical oscillators , as in Sec. 3.5.4.
- b) The equilibrium condition of Thm. 3(iii) is non-trivial to verify, especially since it is heavily related to the coordinate change to phase-difference coordinates.
- c) The linearization of the averaged return map is difficult to compute in some cases (e.g. Sec. 3.5.4) without any prior simplifications.

One of the major contributions here is to simplify the conditions for hybrid averaging by relaxing the need for a single fast coordinate, and simultaneously to ease the application of the averaging theorem. Exploiting time-reversal symmetry aids us on both counts, and helps alleviate difficulties

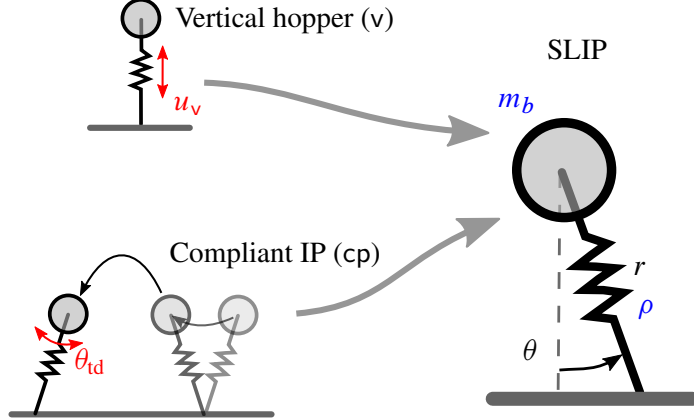


Figure 38: A spring-loaded inverted pendulum (SLIP).

(a)–(c) as shown below:

- a) There is no need to either hand-craft the coordinate changes for phase differences (as in (3.102)), or explicitly define the slow vector field in the form of (3.39). The newly-introduced coordinate change Def. 4 is proven to transform a general network of coupled oscillators (3.140) the form of (3.39) in Lemma 6).
- b) There is no need to check the equilibrium condition in Thm. 3(iii), since the correctness of (3.159) as an equilibrium is proved in Lemma 8.
- c) The averaged return map (3.163) is subject to symmetry-induced algebraic simplifications, expressed by the simplifications in (3.163) (Lemma 9).

These simplifications (which we detail in Sec. 3.6.3) allow us to present stability analyses of higher-dimensional systems with relative computational ease in Sec. 3.7.

In Sec. 3.7, we present two applications of the results in this section.

3.6.1 Motivating Example: SLIP (2 DOF)

We analyze SLIP (Fig. 38) as a composition of the vertical hopper (Sec. 3.1.1) and compliant inverted pendulum (Sec. 3.1.3) templates. We show through the use of examples in this section how each of the benefits a)–c) apply to this particular system.

Continuous Dynamics Referring to Fig. 38, the SLIP model consists of a massless leg with length r (nominal length ρ), attached to a mass m_b . We assume that there is a shank actuator which can apply an axial force $\Upsilon_r \in \mathbb{R}$ in stance. The angle of the leg from the vertical axis is $\theta \in S^1$.

In stance (toe pinned), the kinetic and potential energies are

$$\text{KE} = \frac{m_b}{2}(\dot{r}^2 + r^2\dot{\theta}^2), \quad \text{PE} = m_b gr \cos \theta.$$

Using the Lagrangian, the continuous dynamics in physical coordinates are

$$\begin{aligned}\ddot{r} &= \Upsilon_r/m_b - g \cos \theta + r \dot{\theta}^2 \\ \ddot{\theta} &= g \sin \theta / r - 2\dot{r}\dot{\theta} / r.\end{aligned}\tag{3.133}$$

We use the vertical hopper feedback control strategy u_r with the following affine transformation (related to the “mass” and “gravity” parameters),

$$\Upsilon_r := m_b(g + u_r).\tag{3.134}$$

Guard Set As presented in [De et al. \(2016\)](#), the constant flow-time assumption is reasonably justified⁴³. By enforcing that assumption, the physical liftoff event is now $\{r = \rho, \dot{r} > 0\}$. From [\(3.3\)–\(3.4\)](#), we get

$$\gamma_y(y) = \psi_r - \pi/2.\tag{3.135}$$

Reset Map The leg angle during flight is reset according to a “stepping” strategy, as discussed in [Sec. 3.1.3](#).

3.6.2 Averageability of Coupled Oscillators

Prior work [Altendorfer et al. \(2004\)](#) introduced the formal role in locomotion of a time-reversal symmetric system, which we use below. Suppose we have a dynamical system on space $\mathcal{Y} := \mathbb{T}^{m+1} \times \mathbb{R}^n$ partitioned into “phase” and “energy” compartments⁴⁴ as $\mathbf{y} = [\psi, a]^T$, with dynamics represented by the ε -parameterized vector field,

$$\dot{\mathbf{y}} = F_{\mathbf{y}}(\mathbf{y}, \varepsilon).\tag{3.136}$$

Additionally, let $G_{\mathbf{y}}$ be a *time-reversal symmetry* ([Altendorfer et al., 2004](#), Def. 2), such that

$$G_{\mathbf{y}} : (\psi \mapsto -\psi, a \mapsto a).\tag{3.137}$$

Without loss of generality, $F_{\mathbf{y}}$ can be split into “odd” and “even” parts based on the involution $G_{\mathbf{y}}$ [\(3.137\)](#),

$$F_{\mathbf{y}} = F_{\mathbf{y}}^o + F_{\mathbf{y}}^e,\tag{3.138}$$

$$\text{where } \begin{cases} F_{\mathbf{y}}^o := (F_{\mathbf{y}} - (DG_{\mathbf{y}} \cdot F_{\mathbf{y}}) \circ G_{\mathbf{y}})/2, \\ F_{\mathbf{y}}^e := (F_{\mathbf{y}} + (DG_{\mathbf{y}} \cdot F_{\mathbf{y}}) \circ G_{\mathbf{y}})/2. \end{cases}$$

where we have nominally used Raibert’s notation ([Raibert, 1986](#), Ch. 5) for the components, and demonstrate later our justification for using superscripts denoting “odd” and “even” for these mul-

⁴³A comparison of analysis with and without the “constant flow time” assumption for a similar vertical hopper is included in [\(De et al., 2016, A.5.3\)](#).

⁴⁴Note that $m = n$ for non-critically-damped autonomous Lagrangian mechanical systems. Accordingly, we define the projections in [Def. 3](#).

tivariate quantities. It is easy to check that the two formulae just above uniquely solve (3.138) and the desired symmetries

$$F_y^o \circ G_y = -DG_y \cdot F_y^o, \quad F_y^e \circ G_y = DG_y \cdot F_y^e.$$

As shall be apparent from examples that follow, F_y^e can be thought to comprise forces added that are dissipative (and hence includes both perturbative forces which are destabilizing along with the compensating forces that we add using our available control authority to be restorative), while the conservative forces are represented in F_y^o .

In the upcoming Def. 2 describe a generalization of (3.1) to *non-identical* coupled oscillators (representative of a large class of mechanical systems), and provides an explicit coordinate change to averageable (Sec. 3.2.1). The embedding of the periodic orbit in \mathcal{Y} can be thought of as being the intersection of the “regulated” set

$$\mathcal{R} := \{\mathbf{y} \in \mathcal{Y} : a = a^*\}, \quad (3.139)$$

where a^* is a specific energy level stabilized by the dynamics (as formalized below in Def. 2(ii)), and the “coordinated” set, which we define later in (3.149).

Definition 2 (Weakly-coupled almost-reversible continuous dynamics). (3.136) *satisfies the following:*

(i) *the vector field is of the form*

$$F_y(\mathbf{y}, \varepsilon) = \begin{bmatrix} F_0(a) \\ 0 \end{bmatrix} + \varepsilon F_1(\mathbf{y}, \varepsilon); \quad (3.140)$$

- (ii) *the first element of $F_0 > 0$, and F_0 is odd;*
- (iii) *there is a^* such that $F_1^e(\mathcal{R}) = 0$ (see (3.139)).*

Remark 6 (Intuition behind Def. 2). Note that our requirements above are a strict generalization of (3.1) (i.e. (3.1) automatically satisfies Def. 2). Instead of constant ω_0 , we allow the phase dynamics to be a function of the state. In the first part of (ii), we are setting up conditions for the first element of ψ defining the “master” phase, and the a^* that satisfies (iii) essentially defines \mathcal{R} (3.139).

Example 4 (Oscillator coordinates for SLIP). From the second-order equations of motion (3.133), we use the coordinate changes from the previous section (3.4) and (3.13) to rewrite (3.133) in our model coordinates $\mathbf{y} := [\psi_v, \psi_{cp}, a_v, a_{cp}]^T$, where we choose, for SLIP, a_{cp} to be the angular momentum about the toe (first option in (3.13)). However, in order to do so, we require an assumption, which we formalize by relating ε to the important physical scale variables.

Assumption 8 (SLIP). *We assume*

- a) *the gravitational force in stance (relatively to the leg extension force) is $\mathcal{O}(\varepsilon)$, i.e. we can substitute $g = \varepsilon \tilde{g}$ in the stance dynamics;*⁴⁵
- b) *the leg stiffness is $\mathcal{O}(\varepsilon^{-2})$, i.e. we can substitute $\omega_v = \tilde{\omega}_v/\varepsilon$.*

⁴⁵We are positing the spring potential as inserting much greater forces than can gravity. We retain the original gravity parameter, g , in flight since (as the only force acting on the body in flight), its effect is non-negligible.

Intuitively, the $\varepsilon = 0$ system is a restricted version of SLIP which has no gravity⁴⁶ and an infinitely stiff spring (purely pendular swing) in stance. Using (3.134) in (3.133), we get $\ddot{r} = u_r + g(1 - \cos \theta) + r\dot{\theta}^2$. Using Assumption 8b), we can simplify

$$\begin{aligned} r\dot{\theta}^2 &\stackrel{(3.13)}{=} \frac{a_{cp}^2}{r^3} = \frac{a_{cp}^2}{\rho^3} - \frac{3a_{cp}^2(r - \rho)}{\rho^4} + \mathcal{O}(r - \rho)^2 \\ &\stackrel{(3.4)}{=} \frac{a_{cp}^2}{\rho^3} + \frac{3\varepsilon a_{cp}^2 a_v \cos \psi_v}{\tilde{\omega}_v \rho^4} + \mathcal{O}(\varepsilon^2). \end{aligned}$$

Using this and the template controller (3.5), we get

$$\begin{aligned} \ddot{r} &= \omega_v^2(\tilde{\rho} - r) + \varepsilon \tilde{v}_v + \mathcal{O}(\varepsilon^2), \text{ where } \tilde{\rho} := \rho + \frac{a_{cp}^2}{\omega_v^2 \rho^3}, \\ \tilde{v}_v &:= v_v + \tilde{g}(1 - \cos \psi_{cp}) + \frac{3a_{cp}^2 a_v \cos \psi_v}{\tilde{\omega}_v \rho^4}. \end{aligned} \quad (3.141)$$

However, note that using Assumption 8b), $\frac{a_{cp}^2}{\omega_v^2 \rho^3} = \varepsilon^2 \frac{a_{cp}^2}{\tilde{\omega}_v^2 \rho^3}$, and so $\tilde{\rho} = \rho + \mathcal{O}(\varepsilon^2)$, and we may rewrite the above as

$$\ddot{r} = \omega_v^2(\rho - r) + \varepsilon \tilde{v}_v + \mathcal{O}(\varepsilon^2).$$

Comparing to the closed-loop equations of motion of the template (3.2) in physical coordinates, we see that subject to Assumption 8, the SLIP radial dynamics are an ε^2 -perturbation of a decoupled vertical hopper (3.99).

Now turning our attention to the angular dynamics, using Assumption 8b) again as above,

$$\dot{\psi}_{cp} \stackrel{(3.13)}{=} \frac{a_{cp}}{r^2} = \frac{a_{cp}}{\rho^2} + \frac{2\varepsilon a_{cp} a_v \cos \psi_v}{\tilde{\omega}_v \rho^3} + \mathcal{O}(\varepsilon^2). \quad (3.142)$$

Using Assumption 8a) as well as 8b) in \dot{a}_{cp} , we have

$$\dot{a}_{cp} = \varepsilon \tilde{g} r \sin \psi_{cp} = \varepsilon \tilde{g} \rho \sin \psi_{cp} + \mathcal{O}(\varepsilon^2).$$

With these, we get the system dynamics

$$\dot{\mathbf{y}} = F_0(a) + \varepsilon F_1(\mathbf{y}, \varepsilon), \text{ where} \quad (3.143)$$

$$F_0 = \begin{bmatrix} \omega_v \\ a_{cp}/\rho^2 \\ 0 \\ 0 \end{bmatrix}, \quad F_1 = \begin{bmatrix} \frac{1}{\omega_v a_v} \cos \psi_v \tilde{v}_v \\ \frac{2a_{cp} a_v \cos \psi_v}{\tilde{\omega}_v \rho^3} \\ \sin \psi_v \tilde{v}_v \\ \tilde{g} \rho \sin \psi_{cp} \end{bmatrix} + \mathcal{O}(\varepsilon).$$

⁴⁶This approximation has been previously employed in the literature either directly Schwind and Koditschek (1995) or in a relaxed form by aligning it with the leg angle Geyer et al. (2005).

where \tilde{v}_v was defined in (3.141). Using (3.137), we can find

$$F_1^o = \begin{bmatrix} \frac{c_v}{\omega_v} \left(\frac{\tilde{g}(1-c_{cp})}{a_v} + \frac{3a_{cp}^2 c_v}{\tilde{\omega}_v \rho^4} \right) \\ \frac{2a_{cp} a_v c_v}{\tilde{\omega}_v \rho^3} \\ \left(\tilde{g}(1-c_{cp}) + \frac{3a_{cp}^2 c_v}{\tilde{\omega}_v \rho^4} \right) s_v \\ \tilde{g} \rho s_{cp} \end{bmatrix}, \quad F_1^e = (k_v - a_v \beta) \begin{bmatrix} \frac{c_v s_v}{\omega_v a_v} \\ 0 \\ s_v^2 \\ 0 \end{bmatrix}, \quad (3.144)$$

where we use the shorthand $c_v := \cos \psi_v$, $s_v := \sin \psi_v$. Clearly, with

$$a_v^* = k_v / \beta, \quad (3.145)$$

we can define \mathcal{R} as in Def. 2 and have $F_1^e(\mathcal{R}) = 0$.

Changing to averageable coordinates

We define some new coordinates that intuitively change slowly near the limit cycle. As a preliminary, we define the following new notation:

Definition 3 (Projections of state space). *Define the following projections of arbitrary $\mathbf{v} \in \mathbb{R}^{m+n+1}$:*

$$\begin{aligned} \pi_\sigma \mathbf{v} &:= [1, 0, \dots, 0] \mathbf{v} \in \mathbb{R}; \\ \pi_\delta \mathbf{v} &:= [0_{m \times 1}, I_m, 0_{m \times n}] \mathbf{v} \in \mathbb{R}^m; \\ \pi_a \mathbf{v} &:= [0_{n \times (m+1)}, I_n] \mathbf{v} \in \mathbb{R}^n. \end{aligned} \quad (3.146)$$

Definition 4 (Slow coordinates). *Given the parameter vector $\omega \in \mathbb{R}^m$, $\mathbf{y} = (\sigma, \psi_1, \dots, \psi_m, a_1, \dots, a_n) \in \mathcal{Y}$, define the σ -varying coordinate change $h : \mathbb{R}^{m+n} \times \mathbb{R} \rightarrow \mathbb{R}^{m+n}$*

$$\mathbf{x} = h_\omega \left(\begin{bmatrix} \pi_\delta \mathbf{y} \\ \pi_a \mathbf{y} \end{bmatrix}, \sigma \right) := \begin{bmatrix} \sigma \mathbf{I} - \Delta(\omega) \pi_\delta \mathbf{y} \\ \pi_a \mathbf{y} \end{bmatrix}, \quad (3.147)$$

where $\Delta(v)$ is a diagonal matrix with diagonal entries v .

Remark 7 (Intuition behind Def. 4). For each σ along the limit cycle, we define a set of coordinates $\mathbf{x} = (\delta, a)$ where δ is a vector of phase differences. We show in the following how to find the relative frequencies ω . The reader may intuitively relate the \mathbf{x} variables to concepts in the literature such as transverse coordinates [Hauser and Chung \(1994\)](#), and floquet coordinates [Guckenheimer and Holmes \(1990\)](#). However, as we shall show, we can *explicitly* define the coordinate change h and use it for analysis.

Remark 8 (Properties of h). Note that the “inverse” of this coordinate change (at a given σ) is

$$h_\omega^{-1}(\mathbf{x}, \sigma) = \begin{bmatrix} \Delta(\omega)^{-1}(\sigma \mathbf{1} - \pi_\delta \mathbf{x}) \\ \pi_a \mathbf{x} \end{bmatrix}. \quad (3.148)$$

Now we define the “coordinated” set, \mathcal{N} , (as anticipated in the preamble to this chapter) contain-

ing orbits of (3.136) that maintain a specific relation between the different phase variables, i.e.,

$$\mathcal{N} := \{\mathbf{x} \in \mathcal{X} : \pi_\delta \mathbf{x} = 0\}. \quad (3.149)$$

For instance, in the 2DOF SLIP system, the bottom right cartoon in (De and Koditschek, 2015b, Fig. 5) depicts a neutral orbit (in \mathcal{N}), but the other two cartoons depict orbits which have a different phase relation between the vertical and angular DOFs. Thus, the limit cycle is an ψ_0 -cycle, with constant \mathbf{x} at

$$\mathbf{x}^* = [0, a^*]^T \in \mathcal{X}, \quad (3.150)$$

i.e. intuitively the system has achieved the steady state energies and all the phases are locked in their steady state delays relative to the “master phase,” ψ_0 .

Using \mathbf{x} from (3.150) in (3.148), the condition in Def. 2(iii) is ensures that

$$F_1^e \circ h^{-1}(\mathbf{x}^*) = 0. \quad (3.151)$$

Finding the relative frequencies We have not yet defined $\omega \in \mathbb{R}^m$ as it appears in Def. 4. We posit the form $\omega(a) = \omega_0(a) + \varepsilon \omega_1(a)$, and we define each of the summands in the following.

Lemma 6 (Slow dynamics). *Choosing*

$$\omega_0 := \pi_\sigma F_0 \Delta(\pi_\delta F_0)^{-1} \mathbf{I}, \quad (3.152)$$

and defining $H_0(a) := \begin{bmatrix} 0 & -\Delta(\omega_1) & 0_{m \times n} \\ 0 & 0 & 0 \end{bmatrix}$, $H_1(a, \psi) := \begin{bmatrix} \mathbf{I} & -\Delta(\omega_0) & -\Delta(\pi_\delta \mathbf{y}) D\omega_0 \\ 0 & 0 & I_n \end{bmatrix}$, the dynamics of the \mathbf{x} variables are $\frac{d\mathbf{x}}{d\sigma} = \varepsilon f(\mathbf{x}, \sigma, \varepsilon)$, where

$$f(\mathbf{x}, \sigma, \varepsilon) = \frac{H_0 F_0 + H_1 F_1}{\pi_\sigma F_0} \circ h_{\omega_0}^{-1}(\mathbf{x}, \sigma) + \mathcal{O}(\varepsilon), \quad (3.153)$$

and $\Delta(\cdot)$ denotes a diagonal matrix with diagonal entries given by its argument.

Proof. Differentiating (3.147), we get

$$\begin{aligned} \dot{\mathbf{x}} &= \mathbf{D}_y h \cdot \dot{\mathbf{y}} + \mathbf{D}_\sigma h \cdot \dot{\sigma} \\ &= \begin{bmatrix} \mathbf{1} \\ 0 \end{bmatrix} \pi_\sigma F + \begin{bmatrix} -\Delta(\omega) & \Delta(\pi_\delta \mathbf{y}) D\omega \\ 0 & \mathbf{I} \end{bmatrix} \begin{bmatrix} \pi_\delta F_0 + \varepsilon \pi_\delta F_1 \\ \varepsilon \pi_\sigma F_1 \end{bmatrix} \\ &= \underbrace{\begin{bmatrix} \mathbf{1} \\ 0 \end{bmatrix} \pi_\sigma F_0}_{\equiv 0 \text{ by defn. of } \omega_0} - \begin{bmatrix} \Delta(\omega_0) \pi_\delta F_0 \\ 0 \end{bmatrix} + \varepsilon (H_0 F_0 + H_1 F_1) + \mathcal{O}(\varepsilon^2) \end{aligned}$$

Dividing by $\dot{\sigma} = \pi_\sigma F = \pi_\sigma F_0 + \mathcal{O}(\varepsilon)$, we get (3.153). \square

We observe here that Lemma 6 does not rely on the symmetry properties of Def. 2; it relies on our judicious coordinate change (Def. 4). We leverage symmetry to show how to simplify stability calculations in the upcoming subsubsection.

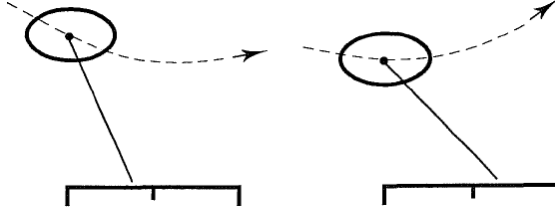


Figure 39: Asymmetric monoped trajectories (Raibert, 1986, Fig. 2.11) that would be assigned $\delta_{cp} < 0$ on the left (note at $\sigma = 0$, the leg angle would be ahead) and $\delta_{cp} > 0$ on the right.

Remark 9 (Convergence rates to the limit cycle). As apparent from (3.153), in our modeling, the “regulation” and “coordination” aspects of stabilization both occur at the same $\mathcal{O}(\varepsilon)$ (relative to phase) rate. For contextualization, the reader may want to juxtapose against isochrons Guckenheimer (1975), where regulation is posited to occur at a faster timescale than coordination, resulting in a reduced-dimensional phase-coordination problem (of the kind studied in, e.g. Golubitsky et al. (1998), Haynes et al. (2012)). In contrast, we consider both regulation and coordination aspects of stabilization simultaneously (non-negligible in highly-dynamic settings such as hopping and running).

Example 5 (SLIP slow coordinates). Continuing from Example 4, we can explicitly compute the change to averageable coordinates. We emphasize here that the **steps in this example are not required for a stability test** (which we distill into the form of an algorithm in Fig. 40). However, we expose all the details in these examples for the benefit of readers.

From (3.152), we get

$$\omega_0(a) = \omega_v \rho^2 / a_{cp}. \quad (3.154)$$

We can directly use the coordinate change (3.147) and (3.143) to get

$$\dot{\mathbf{x}} = \varepsilon \begin{bmatrix} -\frac{c_v s_v \beta}{\omega_v} - \frac{\omega_1 a_{cp}}{\rho^2} + \frac{3c_v^2 a_{cp}^2}{\rho^4 \omega_v \tilde{\omega}_v} + \frac{c_v \tilde{g}}{\omega_v a_v} - \frac{c_{cp} c_v \tilde{g}}{\omega_v a_v} + \frac{c_v k_v s_v}{\omega_v a_v} - \frac{2c_v \omega_v a_v}{\rho \tilde{\omega}_v} + \frac{\tilde{g} s_{cp} \rho^3 \omega_v \psi_{cp}}{a_{cp}^2} \\ \tilde{g} s_v - c_{cp} \tilde{g} s_v + k_v s_v^2 - s_v^2 \beta a_v + \frac{3c_v s_v a_{cp}^2 a_v}{\rho^4 \tilde{\omega}_v} \\ \tilde{g} s_{cp} \rho \end{bmatrix} + \mathcal{O}(\varepsilon^2). \quad (3.155)$$

Alternatively, using our formula (3.153), we can compute the matrices, $H_0(a) = \begin{bmatrix} 0 & -\omega_1 & 0 & 0 \\ 0 & 0 & 0 & 0 \\ 0 & 0 & 0 & 0 \end{bmatrix}$, $H_1(a) = \begin{bmatrix} 1 & -\omega_0 & 0 & \frac{\psi_{cp} \rho^2 \omega_v}{a_{cp}^2} \\ 0 & 0 & 1 & 0 \end{bmatrix}$. Then $\dot{\mathbf{x}} = \varepsilon(H_0 F_0 + H_1 F_1) + \mathcal{O}(\varepsilon^2)$. Comparing the result to the block equation above, we get identical $\mathcal{O}(\varepsilon)$ terms.

Averaging the continuous dynamics

We have showed in (3.153) that the dynamics are in the averageable form (Guckenheimer and Holmes, 1990, eq. (4.1.1)). Next, we observe that the reversibility properties in the original \mathbf{y}

coordinates (3.137) can be interpreted very simply as $\sigma \mapsto -\sigma$ reversal.⁴⁷

Lemma 7 (Master phase reversal symmetry). *For any $\mathbf{x} \in \mathcal{N}$ (3.149), and any ω ,*

- (i) $h^{-1}(\mathbf{x}, -\sigma) = G_y \circ h^{-1}(\mathbf{x}, \sigma)$;
- (ii) if f at $\varepsilon = 0$ (3.153) can be decomposed into “odd” and “even” parts

$$f^o(\mathbf{x}, \sigma) = \frac{H_0 F_0 + H_1 F_1^o}{\pi_\sigma F_0} \circ h_{\omega_0}^{-1}(\mathbf{x}, \sigma), \quad f^e(\mathbf{x}, \sigma) = \frac{H_1 F_1^e}{\pi_\sigma F_0} \circ h_{\omega_0}^{-1}(\mathbf{x}, \sigma), \quad (3.156)$$

then $f = f^o + f^e$, and $f(\mathbf{x}, -\sigma) = -DG_y f^o(\mathbf{x}, \sigma) + DG_y f^e(\mathbf{x}, \sigma)$.

Proof. Let us start with arbitrary $\mathbf{y} = (\sigma, \psi_1, \dots, \psi_m, a_1, \dots, a_n) \in \mathcal{Y}$. Applying (3.138) to (3.148), we get

$$G_y \circ h^{-1}(\mathbf{x}, -\sigma) = G_y \left(\begin{bmatrix} \Delta(\omega)^{-1}(-\sigma \mathbf{1} - \pi_\delta \mathbf{x}) \\ \pi_a \mathbf{x} \end{bmatrix} \right) = \begin{bmatrix} \Delta(\omega)^{-1}(\sigma \mathbf{1} + \pi_\delta \mathbf{x}) \\ \pi_a \mathbf{x} \end{bmatrix},$$

which is equal to $h^{-1}(\mathbf{x}, \sigma)$ iff $\pi_\delta \mathbf{x} = 0$ (from (3.148)), i.e. for $\mathbf{x} \in \mathcal{N}$ (3.149). As a corollary, $h(G_y(\mathbf{y}), -\sigma) = h(\mathbf{y}, \sigma)$, using the fact that G_y is idempotent.

To prove the second part, note from (3.153) and the first part of this Lemma that

$$\begin{aligned} f(\mathbf{x}, -\sigma, 0) &= \frac{H_0 F_0 + H_1 F_1}{\pi_\sigma F_0} \circ h_{\omega_0}^{-1}(\mathbf{x}, -\sigma) \\ &\stackrel{(3.140)}{=} \frac{(H_0 F_0) \circ h_{\omega_0}^{-1}(\mathbf{x}, \sigma) + (H_1 F_1) \circ h_{\omega_0}^{-1}(\mathbf{x}, -\sigma)}{\pi_\sigma F_0 \circ h_{\omega_0}^{-1}(\mathbf{x}, \sigma)}, \end{aligned}$$

since F_0 is odd. Additionally, looking at each component of F_1 separately,

$$\begin{aligned} (H_1 F_1^o) \circ G_y &= \begin{bmatrix} \mathbf{1} & -\Delta(\omega_0) & \Delta(\pi_\delta \mathbf{y}) D\omega_0 \\ 0 & 0 & I_n \end{bmatrix} \begin{bmatrix} I & \\ & -I \end{bmatrix} F_1^o \\ &= \begin{bmatrix} \mathbf{1} & -\Delta(\omega_0) & -\Delta(\pi_\delta \mathbf{y}) D\omega_0 \\ 0 & 0 & -I_n \end{bmatrix} F_1^o, \end{aligned}$$

i.e. $\pi_\delta(H_1 F_1^o) \circ G_y = \pi_\delta(H_1 F_1^o)$, and $\pi_a(H_1 F_1^o) \circ G_y = -\pi_a(H_1 F_1^o)$. Similarly, we can compute and find that $\pi_\delta(H_1 F_1^e) \circ G_y = -\pi_\delta(H_1 F_1^e)$, and $\pi_a(H_1 F_1^e) \circ G_y = \pi_a(H_1 F_1^e)$. Putting these together, we get the desired conclusion. \square

Using σ , the master phase as, “time” in classical averaging (Sec. 3.2.1), the *averaged vector field* is defined as in the classical definition (Guckenheimer and Holmes, 1990, eq. (4.1.2)),

$$\overline{f}(\mathbf{x}) := \frac{1}{T} \int_{\mathcal{T}} f(\mathbf{x}, \sigma, 0) d\sigma, \quad (3.157)$$

where f , the slow vector field, was defined in (3.153), and we use $\mathcal{T} := [-T/2, T/2]$.

⁴⁷As Altendorfer et al. (2004) shows, reversible systems of the kind (3.137) possess certain time-reversible orbits. As shown in Lemma 7, in our coordinates (Def. 4) this property corresponds to a \mathcal{N} -restriction.

In order to pin down the value ω_1 (the missing component of (3.152)), we first remind the reader of the intuitive aim of the averaging method. As described in our prior averaging work (as well as in classical texts, such as (Guckenheimer and Holmes, 1990, Thm. 4.1.1(ii))), the averaging method uses as its approximant the behavior of the averaged system from (3.157) at its equilibrium, i.e. $\bar{f}(\mathbf{x}^*) = 0$. Thus, we use as “constraint” that with our proposed (Def. 4) ω -parameterized coordinate change, (3.157) must have a zero at the equilibrium state (3.150).

The pair of propositions below contain the main contribution of this section: simplified analytical expressions for the averaged properties of the system (3.136).

Lemma 8 (Averaged properties). *Choosing*

$$\omega_1(a) := \Delta(\pi_\delta F_0)^{-1} \int_{\mathcal{T}} (\pi_\sigma F_1 \mathbf{1} - \Delta(\omega_0) \pi_\delta F_1 - \Delta(\pi_\delta \mathbf{y}) D\omega_0 \pi_a F_1) \circ h_{\omega_0}^{-1}([0, a], \sigma) d\sigma, \quad (3.158)$$

the averaged vector field (3.157), when evaluated at the equilibrium (3.150), satisfies

$$\bar{f}(\mathbf{x}^*) = 0. \quad (3.159)$$

Proof. In order to prove (3.159), first we observe that for the bottom n rows in (3.157)

$$T \pi_a \bar{f}(\mathbf{x}) = \int_{\mathcal{T}} \pi_a f(\mathbf{x}, \sigma, 0) d\sigma = \int_0^{T/2} (\pi_a f(\mathbf{x}, \sigma, 0) + \pi_a f(\mathbf{x}, -\sigma, 0)) d\sigma,$$

where we have simply split up the integral into two pieces using a trivial change of variables. Now observe that at \mathbf{x}^* , using Lemma 7, the second integrand turns into $2\pi_a f^e(\mathbf{x}^*, \sigma) d\sigma$. By Def. 2, $F_1^e \circ h_{\omega_0}^{-1}(\mathbf{x}^*, \sigma) \equiv 0$. Thus the integrand above is pointwise zero, and the π_a integral is zero.

For the top $m-1$ rows, symmetry does not help directly; instead we leverage our choice of ω_1 (3.158). Averaging the first $m-1$ rows of (3.153),

$$T \pi_\delta \bar{f}(\mathbf{x}^*) = \int_{\mathcal{T}} \frac{\pi_\sigma F_1 \mathbf{1} - \Delta(\omega_0) \pi_\delta F_1 - \Delta(\omega_1) \pi_\delta F_0 - \Delta(\pi_\delta \mathbf{y}) D\omega_0 \pi_a F_1}{\pi_\sigma F_0} \circ h_{\omega_0}^{-1}(\mathbf{x}^*, \sigma) d\sigma.$$

Now recall that $\pi_\sigma F_0$ does not depend on σ (3.140), and can thus be pulled out of the integral. Our definition of $\omega_1(a)$ (3.158) exactly cancels out the remaining terms for any $\mathbf{x} = [0, a]$, i.e. $\pi_\delta \bar{f}^o([0, a]) \equiv 0$ for any a , and in particular, also for a^* . \square

Example 6 (SLIP averaged system equilibrium). Continuing from Example 5, we can divide (3.155) by $\pi_\sigma F_0 = \omega_v$ (from (3.143)) to get $\frac{d\mathbf{x}}{d\sigma}$.

First, note that $\pi_\delta h_{\omega_0}^{-1}(x, \sigma) = (\psi_v - \delta_{cp})/\omega_0$, which we replace ψ_{cp} with. We can now integrate at $\delta_{cp} = 0$ over $\mathcal{T} = [-\pi/2, \pi/2]$ to get

$$\bar{f}([0, a]) = \frac{1}{\pi} \int_{-\pi/2}^{\pi/2} f([0, a], \sigma, 0) d\sigma \quad (3.160)$$

$$= \begin{bmatrix} -\frac{\omega_1 a_{cp}}{\rho^2 \omega_v} + \frac{3a_{cp}^2}{2\rho^4 \omega_v^2 \tilde{\omega}_v} + \frac{\tilde{g} \rho^3 (2s_\omega \rho^2 \omega_v / \pi - c_\omega a_{cp})}{a_{cp}^3} + \frac{2\tilde{g}}{\pi \omega_v^2 a_v} - \frac{4a_v}{\pi \rho \omega_v} - \frac{2\tilde{g} \rho^4 c_\omega}{\pi (\rho^4 \omega_v^2 a_v - a_{cp}^2 a_v)} \\ \frac{k_v - \beta a_v}{2\omega_v} \\ 0 \end{bmatrix}, \quad (3.161)$$

where $c_\omega := \cos(\pi/(2\omega_0))$, $s_\omega := \sin(\pi/(2\omega_0))$. Clearly, the lower rows are zero at (3.145). For the upper rows, first compute ω_1 according to (3.158) to get

$$\begin{aligned}\omega_1(a) &= \frac{1}{\pi\pi_\delta F_0} \int_{-\pi/2}^{\pi/2} (\pi_\sigma F_1 - \omega_0\pi_\delta F_1 - \psi_{cp}D\omega_0 \cdot \pi_a F_1) \circ h_{\omega_0}^{-1}([0, a], \sigma) d\sigma \\ &= \frac{\rho^2 \left(-\frac{2c_\omega \tilde{g}\rho^4\omega_v}{\rho^4\omega_v^2 a_v - a_{cp}^2 a_v} + \frac{\tilde{g}\rho^3\omega_v(2\rho^2 s_\omega \omega_v - \pi c_\omega a_{cp})}{a_{cp}^3} + \frac{3\pi a_{cp}^2}{2\rho^4\omega_v \tilde{\omega}_v} + \frac{2\tilde{g}}{\omega_v a_v} - \frac{4\omega_v a_v}{\rho \tilde{\omega}_v} \right)}{\pi a_{cp}},\end{aligned}\quad (3.162)$$

substituting which into the preceding block equation correctly ensures $\bar{f}(\mathbf{x}^*) = 0$.

Lemma 9. *Evaluated at the equilibrium (3.150), the averaged vector field (3.157) satisfies*

$$D\bar{f}(\mathbf{x}^*) = \begin{bmatrix} D_\delta \pi_\delta \bar{f}^o(\mathbf{x}^*) & 0 \\ D_\delta \pi_a \bar{f}^o(\mathbf{x}^*) & D_a \pi_a \bar{f}^e(\mathbf{x}^*) \end{bmatrix}, \quad (3.163)$$

where the odd/even components are as defined in Lemma 7.

Proof. First, we calculate the right hand block columns, i.e. $D_a \bar{f}$. Note that for these columns, δ is evaluated at 0, and so we can use Lemma 7 to see that the top right block is $\pi_\delta \bar{f}^o([0, a]) \equiv 0$ by our definition (3.158) (as shown in the proof of Lemma 8). In the bottom right block, we use Lemma 7 to see that (as in the proof of Lemma 8)

$$\pi_a \bar{f}(\mathbf{x}^*) = \frac{1}{T} \int_{\mathcal{T}} \pi_a f^e(\mathbf{x}^*, \sigma) d\sigma \implies D_a \pi_a \bar{f} = D_a \pi_a \bar{f}^e(\mathbf{x}^*).$$

For the left blocks, we cannot use Lemma 7 since $\delta \neq 0$. However, since we can evaluate a at a^* , note that $f^e([\delta, a^*], \sigma) \equiv 0$ (from Def. 2), and so only f^o appears. Consequently, differentiating the respective blocks with δ , we get (3.163). \square

Remark 10 (Symmetry-induced algebraic simplification). The computation (3.163) benefits greatly from symmetry: note the block structure of $D\bar{f}$ where there is a zero in the top right block in (3.163). Further, we have shown that an explicit form for ω_1 (3.158) is not required; we only need to compute ω_0 (3.152), $\pi_a f^e$, f^o for (3.163) from the vector field.

Example 7 (SLIP averaged system linearization). Continuing from Example 6, we can explicitly compute $D\bar{f}$ from our \bar{f} by brute force, getting

$$D\bar{f}(\mathbf{x}^*) = \begin{bmatrix} 0 & 0 & 0 \\ \frac{-c_\omega \tilde{g} a_{cp}^2}{\pi \rho^4 - \pi \omega_v a_{cp}^2} & \frac{-\beta}{2\omega_v} & 0 \\ \frac{-2\tilde{g} s_\omega \rho}{\pi \omega_v} & 0 & 0 \end{bmatrix}. \quad (3.164)$$

Note immediately that the top right block is 0, as we proved in Lemma 9. Now we instead use our formula in (3.163) to compute $D\bar{f}$. First we compute f^o and $\pi_a f^e = \begin{bmatrix} (k_v - \beta a_v) s_v^2 / \omega_v \\ 0 \end{bmatrix}$. Then averaging these quantities over $\sigma = \psi_v$, we get the same result as (3.164).

3.6.3 Averageable Symmetric Hybrid Systems (HSAS)

Building on Def. 2, we are now ready to define an *averageable single-mode symmetric hybrid system (HSAS)*, which we view as a specialization⁴⁸ of a HAS (introduced in Sec. 3.2.3), and a specialization of a symmetric hybrid system (SHS) Razavi et al. (2016) (see Sec. 3.8).

Compared to our prior Thm. 2 or Thm. 3, this next result directly applies to systems with multiple phases (a network of coupled oscillators), instead of requiring a system already in coordinates with a single fast mode.

Theorem 4 (Coupled Oscillator Hybrid Averaging Theorem). *Given the “original” hybrid system satisfying Def. 2,*

$$\dot{\mathbf{y}} = F_{\mathbf{y}}(\mathbf{y}, \varepsilon), \quad \gamma_{\mathbf{y}}(\mathbf{y}) = 0 \implies \mathbf{y}_+ = R_{\mathbf{y}}(\mathbf{y}), \quad (3.165)$$

and with ω as in (3.152), define (a) $R(\mathbf{x}, \sigma) := h_{\omega}(R_{\mathbf{y}}(h_{\omega}^{-1}(\mathbf{x}, \sigma)), -\sigma)$, and (b) $\gamma(\mathbf{x}, \sigma) = \gamma_{\mathbf{y}} \circ h_{\omega}^{-1}(\mathbf{x}, \sigma)$. If

$$(i) D_{\sigma} \gamma_{\mathbf{y}} = 1, \quad \frac{\partial \gamma_{\mathbf{y}}}{\partial y_i} = \mathcal{O}(\varepsilon) \text{ for each } i > 1,$$

(ii) with $\bar{R}(\mathbf{x})$ defined from (R, γ, T) as in Thm. 3, the C^r (for $r \geq 2$) reset R (allowed to vary with ε) satisfies (a) $D\bar{R}(\mathbf{x}) = \mathbf{S}_0 + \varepsilon \mathbf{U}(\mathbf{x})$ (with constant \mathbf{S}_0)⁵⁰, (b) \mathbf{S}_0 is invertible, its unity eigenvalues have diagonal Jordan blocks, and

(iii) there is an \mathbf{x}^* such that (a) $\bar{R}(\mathbf{x}^*) = \mathbf{x}^*$; (b) with $\mathbf{V} := T D \bar{f}(\mathbf{x})$ (3.163), the matrix $\mathbf{Z} := \mathbf{S}_0 + \varepsilon (\mathbf{U} + \mathbf{S}_0 \mathbf{V})$ evaluated at \mathbf{x}^* has no eigenvalues on the unit circle,

then there exists $\varepsilon_0 > 0$ such that, for all $0 < \varepsilon \leq \varepsilon_0$, (3.165) possesses a unique hyperbolic periodic orbit with stability determined by eigenvalues of \mathbf{Z} .

Proof. Our coordinate change of Def. 4 is used throughout to convert (3.165) to a hybrid system of the form (3.39) (for which we have already developed a stability result in Thm. 3).

Now, consider the hybrid system

$$\frac{d\mathbf{x}}{d\sigma} = \varepsilon f(\mathbf{x}, \sigma, \varepsilon), \quad \dot{\sigma} = 1, \quad \gamma(\mathbf{x}, \sigma) = 0 \implies \mathbf{x}_+ = R(\mathbf{x}, \sigma). \quad (3.166)$$

Lemma 6 shows that the \mathbf{x} -dynamics appear as in the left column of (3.166). Based on the hypotheses on $D_{\mathbf{y}} \gamma_{\mathbf{y}}$,

$$D\gamma = D_{\mathbf{y}} \gamma_{\mathbf{y}} \begin{bmatrix} 0 \\ I \end{bmatrix} D_{\mathbf{x}} h_{\omega}^{-1}(\mathbf{x}, T/2)$$

satisfies the hypotheses for $D\gamma$ in Thm. 3, and based on hypotheses on $DR_{\mathbf{y}}$, $\mathbf{S}_0 + \varepsilon \mathbf{U}$ satisfies the conditions on the reset in Thm 3. In particular, the Lipschitz condition on $D\bar{R}$ can indeed be verified from \mathbf{S}_0 .

Lemma 8 shows that \mathbf{x}^* is an equilibrium of \bar{f} , and the theorem statement assures us that it is a fixed point of \bar{R} .

⁴⁸Although the specialization to systems with some symmetry conditions (Def. 2) precludes application to some classes of systems, the explicitly constructed coordinate change (3.147) to directly address multiple fast modes (a ubiquitous feature of the high-DOF systems we are interested in) greatly expands the applicability of hybrid averaging.

⁴⁹This can be done without loss of generality by scaling $\gamma_{\mathbf{y}}$ as long as $D_{\sigma} \gamma_{\mathbf{y}} \neq 0$, which we assert as a condition on the transversality of the flow and the guard.

⁵⁰The $\mathcal{O}(1)$ part comes from $D_{\mathbf{y}} R_{\mathbf{y}}$ and is constant by hypothesis, and the $\mathcal{O}(\varepsilon)$ terms are contributed by both the state-dependent part of $D_{\mathbf{y}} R_{\mathbf{y}}$ as well as $D_{\sigma} R_{\mathbf{y}} \cdot D_{\mathbf{y}} \gamma_{\mathbf{y}} \begin{bmatrix} 0 \\ I \end{bmatrix}$, where $D_{\mathbf{y}} \gamma_{\mathbf{y}} \begin{bmatrix} 0 \\ I \end{bmatrix} = \mathcal{O}(\varepsilon)$ by hypothesis.

- C1)** Find template CC, check that system dynamics can be written in the form $\dot{\mathbf{y}} = F_{\mathbf{y}}(\mathbf{y}, \varepsilon) = \begin{bmatrix} F_0(a) \\ 0 \end{bmatrix} + \varepsilon F_1(\mathbf{y}, \varepsilon)$ (3.140).
- C2)** Compute odd and even parts of components of $F_{\mathbf{y}}$ using $\begin{cases} F_{\mathbf{y}}^o &:= (F_{\mathbf{y}} - (DG_{\mathbf{y}} \cdot F_{\mathbf{y}}) \circ G_{\mathbf{y}})/2, \\ F_{\mathbf{y}}^e &:= (F_{\mathbf{y}} + (DG_{\mathbf{y}} \cdot F_{\mathbf{y}}) \circ G_{\mathbf{y}})/2 \end{cases}$ (3.138), and check that F_0 is odd;
 compute $\begin{cases} \omega_0(a) &\leftarrow \pi_{\sigma} F_0 \Delta(\pi_{\delta} F_0)^{-1} \mathbf{1} \text{ (3.152),} \\ \omega_1(a) &\leftarrow \Delta(\pi_{\delta} F_0)^{-1} \int_{\mathcal{T}} (\pi_{\sigma} F_1 \mathbf{1} - \Delta(\omega_0) \pi_{\delta} F_1 \\ &\quad - \Delta(\pi_{\delta} \mathbf{y}) D\omega_0 \pi_a F_1) \circ h_{\omega}^{-1}([0, a], \sigma) d\sigma \text{ (3.158).} \end{cases}$
- C3)** Check the existence of a^* such that for each $\mathbf{y} : \pi_a \mathbf{y} = a^*$, $F_1^e(\mathbf{y}) = 0$ (Def. 2).
- C4)** Defining $\begin{cases} H_0(a) &\leftarrow \begin{bmatrix} 0 & -\Delta(\omega_1) & 0_{m \times n} \\ 0 & 0 & 0 \\ 0 & 0 & I_n \end{bmatrix} \\ H_1(a, \psi) &\leftarrow \begin{bmatrix} 1 & -\Delta(\omega_0) & -\Delta(\pi_a \mathbf{y}) D\omega_0 \\ 0 & 0 & I_n \end{bmatrix} \end{cases}$, and $\begin{cases} f^o(\mathbf{x}, \sigma) &\leftarrow \frac{H_0 F_0 + H_1 F_1^o}{\pi_{\sigma} F_0} \circ h_{\omega_0}^{-1}(\mathbf{x}, \sigma) \\ f^e(\mathbf{x}, \sigma) &\leftarrow \frac{H_1 F_1^e}{\pi_{\sigma} F_0} \circ h_{\omega_0}^{-1}(\mathbf{x}, \sigma) \end{cases}$,
 compute $\mathbf{V} \leftarrow T \begin{bmatrix} D_{\delta} \pi_{\delta} \bar{f}^o(\mathbf{x}^*) & 0 \\ D_{\delta} \pi_a \bar{f}^o(\mathbf{x}^*) & D_a \pi_a \bar{f}^e(\mathbf{x}^*) \end{bmatrix}$ (3.163).
- C5)** Scale $\gamma_{\mathbf{y}}$ such that $D_{\sigma} \gamma_{\mathbf{y}} = 1$. Check that $D \gamma_{\mathbf{y}} \begin{bmatrix} 0 \\ I \end{bmatrix} = \mathcal{O}(\varepsilon)$ (Thm. 4(i)).
- C6)** With $\omega = \omega_0 + \varepsilon \omega_1$ (3.152), compute $R(\mathbf{x}, \sigma) \leftarrow h_{\omega}(R_{\mathbf{y}}(h_{\omega}^{-1}(\mathbf{x}, \sigma)), -\sigma)$; compute \bar{R} (Thm. 3); check $\bar{R}(\mathbf{x}^*) = \mathbf{x}^*$; compute $\mathbf{S}_0 + \varepsilon \mathbf{U}(\mathbf{x}) \leftarrow D\bar{R}(\mathbf{x})$.
- C7)** Check that \mathbf{S}_0 is constant, invertible, and its unity eigenvalues have diagonal Jordan blocks (Thm. 4(ii)).
- C8)** Check that the eigenvalues of $\mathbf{Z} = \mathbf{S}_0 + \varepsilon(\mathbf{U} + \mathbf{S}_0 \mathbf{V})$ are hyperbolic to $\mathcal{O}(\varepsilon)$, for small $\varepsilon > 0$. If they are all within the unit circle, Thm. 4 guarantees stability.

Figure 40: A computational recipe for stability analysis: We repeat parts of previous definitions, but also include references for the reader, in order to keep this section self-contained. We apply these steps systematically to the examples in Sec. 3.7.1–3.7.2. We posit that some of these steps can be simplified in special classes of systems; we leave an exploration of this to future work.

Lemma 9 gives us a formula for $D\bar{f}$, using which we can compute the averaged return map in \mathbf{x} coordinates, which equals \mathbf{Z} . By the hypothesis in the theorem statement, it is hyperbolic to $\mathcal{O}(\varepsilon)$, and so using Thm. 3 we conclude that the original hybrid system has stability properties given by \mathbf{Z} . \square

The conditions of Thm. 4 are ensuring that the hybrid properties of the system are synergistic with the symmetry in its continuous dynamics (Def. 2). Note that conditions (i)–(ii) together assert that the set \mathcal{R} is invariant to the reset event, although \mathcal{N} (3.149) is not necessarily so.⁵¹ This mechanism of modifying the coordination properties through the reset is key in the functioning of the stepping control of horizontal speed for a monoped (e.g. Sec. 3.1.3).

Additionally, (ii) stipulates that the limit cycle of the averaged system, $\mathcal{N} \cap \mathcal{R}$, has $\pi_{\delta} \mathbf{x} \equiv 0$, i.e. using Lemma 7, the orbit is $\mathcal{G}_{\mathbf{y}}$ -invariant, coinciding with the definition of a *symmetric orbit* (Al-

⁵¹To see this, note that it is possible that the pre-reset state is $\mathbf{y} \in \mathcal{N} \setminus \mathcal{R}$, such that $\pi_a R_{\mathbf{y}}(\mathbf{y}) \neq \pi_a \mathbf{y}$ (the energy is changed by the reset), and due to the now-changed definition of $\omega(a)$, $\pi_{\delta} R_{\mathbf{y}}(\mathbf{y}) \neq 0$, i.e. $R_{\mathbf{y}}(\mathbf{y}) \notin \mathcal{N}$.

tendorfer et al., 2004, Def. 3). We emphasize though that the original system is only approximated by the averaged system, and the orbit in the original system may not hold the sets \mathcal{N} or \mathcal{R} invariant, nor may it be symmetric in the sense of Altendorfer et al. (2004).

In summary, the main contribution of this section was to present constructively a judicious change of coordinates (3.147) that converts a network of coupled oscillators to a hybrid averageable system (HAS) that we defined in Thm. 3. We summarize a “computational recipe” for stability analysis in Fig. 40.

3.7 Applications of HSAS

In this section, we present two applications for the results of Sec. 3.6.3 (specifically in the algorithmic summary form of Fig. 40).

We first present an application to the weakly coupled slot hopper of Sec. 3.5.4 in Sec. 3.7.1, chosen specifically to convey the simplifications enabled by incorporating time-reversal symmetry (including the algorithmic generation of a phase difference coordinate, as opposed to the hand-generated definition of (3.102)). By contrasting with Sec. 3.5.4, we hope the reader can get a clear idea of the contribution made by the coordinate change introduced in Sec. 3.6.3.

We next present an application to a 1.5 DOF version of SLIP, chosen specifically as a continuation of our examples throughout Sec. 3.6.3, which demonstrated the benefits of our coordinate change (Def. 4) in simplifying the coupled continuous SLIP dynamics into an explicit linearization of its flow (3.164).

Additionally, in the context of SLIP, we also show below how our new analytical tools help obtain a new superior approximation (3.168) to the “neutral point” (essentially a return map approximation) initially suggested by Raibert (1986).

However, we are unable at this time to present a full 2 DOF stability proof since the SLIP reset appears to be unaverageable with two existing reset strategies. This “case study” demonstrates the seemingly crucial dependence of averageability (a tool employed to approximate the continuous dynamics) on the reset map in a hybrid system.

Nonetheless, work in progress now suggests applicability to certain systems up to 3 DOF—such as hopping on a 2.5 DOF tailed SLIP system (model for the empirical trials in Sec. 4.1), bounding on a 3 DOF sagittal plane biped of Fig. 27C—with relative ease.

3.7.1 Slot Hopper (2 DOF)

We revisit the slot hopper model of Fig. 27B, however, now we apply the steps in Fig. 40. The reader may choose to contrast the analytical work in Sec. 3.5.4 to the algorithmic procedure below.

We apply the vertical hopper (Sec. 3.1.1) coordinate change to the stance leg’s vertical height, z_1 , to get its energy-phase coordinates, (a_v, ψ_v) , and the ballistic flight (Sec. 3.1.2) coordinate change to the flight hip height, z_2 , to get (a_f, ψ_f) . Let $\mathbf{y} := (\psi_v, \psi_f, a_v, a_f)$.

Hybrid averaging

C1) As shown in Sec. 3.5.1, we get the single stance equations of motion (3.100)

$$\ddot{z}_1 = u_v, \quad \ddot{z}_2 = -g + \varepsilon(-g - u_v),$$

where $u_v = \omega_v a_v \cos \psi_v + \varepsilon v_v$ is the template control signal based on z_1 's states. Since the z_1 dynamics are decoupled, $\dot{a}_v, \dot{\psi}_v$ are the same as in (3.99). For the flight dynamics, we follow Sec. 3.1.2, with $v_f = -g - \omega_v a_v \cos \psi_v + \mathcal{O}(\varepsilon)$, to get

$$\dot{\mathbf{y}} = \begin{bmatrix} \omega_v \\ \frac{g}{2a_f} \\ 0 \\ 0 \end{bmatrix} + \varepsilon \begin{bmatrix} \frac{\cos \psi_v v_v}{\omega_v a_v} \\ \frac{(-g - \omega_v a_v \cos \psi_v)(4\psi_f^2 - 1)}{2a_f} \\ \sin \psi_v v_v \\ -2\psi_f(-g - \omega_v a_v \cos \psi_v) \end{bmatrix} + \mathcal{O}(\varepsilon^2).$$

C2) We find that

$$F_1^o = \left[0, \frac{(-1 + 4\psi_f^2)(g + \omega_v a_v \cos \psi_v)}{2a_f}, 0, 2\psi_f(g + \omega_v a_v \cos \psi_v) \right]^T$$

$$F_1^e = (k_v - a_v \beta) \left[\cos \psi_v \sin \psi_v / (a_v \omega_v), 0, \sin^2 \psi_v, 0 \right]^T$$

$$\text{and } \omega_0 = \frac{2\omega_v a_f}{g}.$$

C3) Clearly, using $a_v^* = k_v / \beta$ satisfies this.

C4) Computing using the provided formulae, we get $\mathbf{V} = \begin{bmatrix} 0 & 0 & 0 \\ 0 & -\frac{\pi\beta}{2\omega_v} & 0 \\ \frac{-g(\pi g + 2k_v \omega_v / \beta)}{\omega_v^2 a_f} & 0 & 0 \end{bmatrix}$.

C5) Using the constant flow time assumption (as in Sec. 3.5.4), we have $\gamma_y = \sigma - \pi/2$, which is already scaled correctly. Also, $D\gamma_y \begin{bmatrix} 0 \\ 1 \end{bmatrix} = 0$.

C6) For the reset, we use symmetry factoring of the return map as described in Sec. 3.3, introducing the map K as a pre-multiplier of the map taking liftoff of hopper 1 to touchdown of hopper 2, i.e. $R_y = K \circ R_{y(1)}$.

The duration of the aerial phase, t_f , (before leg 2 touches down) is calculated from $\psi_f + \frac{g}{2a_f} t_f = \frac{1}{2}$. Integrating the trivial aerial dynamics $\ddot{z}_i = 0$ forward for this duration, we get

$$R_y = \left[-\frac{\pi}{2}, -\frac{1}{2} - \frac{a_f(-1 + 2\psi_f)}{2a_v}, a_f, a_v \right] \text{ (after applying the symmetry factoring map } K\text{).}$$

Using (3.147) and (3.148), we get $R = h_\omega(R_y \circ h_\omega^{-1}(\mathbf{x}, \pi/2), -\pi/2)$, and can compute

$$DR = \mathbf{S}_0 + \varepsilon \mathbf{U} + \mathcal{O}(\varepsilon^2) = \begin{bmatrix} -1 & \omega_v/g & -\omega_v/g \\ 0 & 0 & 1 \\ 0 & 1 & 0 \end{bmatrix} + \varepsilon \begin{bmatrix} 0 & \zeta & -\zeta \\ 0 & 0 & 0 \\ 0 & 0 & 0 \end{bmatrix} + \mathcal{O}(\varepsilon^2),$$

where $\zeta := -\frac{2k_v \omega_v^2}{g^2 \pi \beta}$ is a constant independent of ε .

C7) We observe above that \mathbf{S}_0 is indeed constant and has the requisite spectral properties.

C8) Now we can compute the averaged return map

$$D\bar{P}_{sh} = (S_0 + \varepsilon U)(I + \varepsilon V) = \begin{bmatrix} 1 - \varepsilon \left(2 + \frac{g\pi\beta}{k_v\omega_v}\right) & \varepsilon\xi + \frac{\omega_v - \pi\beta\varepsilon/2}{g} & -\frac{\varepsilon g \xi + \omega_v}{g} \\ -\frac{\varepsilon g(g\pi\beta + 2k_v\omega_v)}{k_v\omega_v^2} & 0 & 1 \\ 0 & 1 - \frac{\varepsilon\pi\beta}{2\omega_v} & 0 \end{bmatrix}. \quad (3.167)$$

The eigenvalues of $D\bar{P}_{sh}$ are $\{\lambda_1, \lambda_1^*, 1 - \frac{\varepsilon\pi\beta}{4\omega_v}\} + \mathcal{O}(\varepsilon^2)$, where λ_1^* is the complex conjugate of λ_1 . We can check the magnitude of the complex conjugate pair: $\lambda_1\lambda_1^* = 1 - \frac{\varepsilon\pi\beta}{4\omega_v} + \mathcal{O}(\varepsilon^2)$. Thus, all the eigenvalues are within the unit circle.

Applying Thm. 4, we concluded that this antiphase limit cycle of the slot hopper is stable (as in Sec. 3.5.4).

3.7.2 SLIP without Leg Angle (1.5 DOF)

We have already formulated the SLIP dynamics and described its averageability in detail in preceding examples throughout Sec. 3.6.3. However, in this section, we use the procedure in Fig. 40 for a SLIP stability analysis from the perspective of a “user” of the Thm. 4.

Averageability of SLIP reset strategies

For SLIP, the control affordance available is the freely selectable touchdown leg angle, θ_{td} . Though many strategies for selecting θ_{td} have been empirically successful, it has generally not been easy to show analytically that the resulting hybrid limit cycle is stable with the exception of a few isolated cases [Ghigliazza et al. \(2005\)](#), or with simplified models [De and Koditschek \(2015b\)](#), [Geyer et al. \(2005\)](#), [Schwind and Koditschek \(1995\)](#). By using this well-known model as an initial “test” for our new analytical tools, we hope to better contextualize its strengths and weaknesses.

For stepping strategies, we showed in ([De and Koditschek, 2015a](#), Sec. 4.2) that given a touchdown angle $\theta_{td}(y)$ (usually chosen as a function of state), the energy reset (with $a := [a_v, a_{cp}]^T$) follows

$$R_y(y) = \begin{bmatrix} -\pi/2 \\ \theta_{td}(y) \\ R_a(y, \theta_{td}) \end{bmatrix}, \text{ where} \quad (3.168)$$

$$R_a(y, \theta_{td}) := \begin{bmatrix} 1 & \rho \end{bmatrix} \text{Rot}(\psi_{cp} + \theta_{td}) \begin{bmatrix} 1/\rho & 1 \end{bmatrix} a$$

and ψ_{cp} is the lift-off leg angle, since y is on the guard set (3.135). With (3.168), we can evaluate several stepping strategies in terms of their satisfaction of the conditions of Thm. 4 below. For this section, we assume the flow time is fixed, i.e. $D\gamma_y \begin{bmatrix} 0 \\ 1 \end{bmatrix} = 0$, and consequently, we know that $\sigma(t_{TD}) = -\pi/2$, and $\sigma(t_{LO}) = \pi/2$ (from (3.4)).

Proposition 6 (SLIP reset fixed point). *The reset equilibrium condition of Thm. 4(iii) is equivalent to⁵² the condition $\theta_{td}(y^*) = \frac{-\pi}{2\omega(a^*)}$.*

⁵²We would like to evaluate the averageability of different stepping strategies, and so a necessary condition lets us prune infeasible ones.

Proof. First, note that at a^* , the argument of the rotation in (3.168) must be zero to get $R_a = \text{id}$ (necessary for Thm. 4(iii)). Thus a necessary condition is that

$$0 = \psi_{\text{cp}}(t_{\text{LO}}) + \theta_{\text{td}}(a^*) \stackrel{(3.148)}{=} \frac{\pi/2 - \delta(t_{\text{LO}})}{\omega(a(t_{\text{LO}}))} + \theta_{\text{td}}(a^*) = \frac{\pi}{2\omega(a^*)} + \theta_{\text{td}}(a^*),$$

evaluating at $a(t_{\text{LO}}) = a^*, \delta(t_{\text{LO}}) = 0$ according to (3.150). So, we see that the condition above is necessary. Additionally, note that $R_\delta = \delta(t_{\text{TD}}) = -\pi/2 - \theta_{\text{td}}\omega(a(t_{\text{TD}}))$, and when evaluated at (3.150) we get

$$R_\delta(\mathbf{x}^*) = -\frac{\pi}{2} - \left(\frac{-\pi}{2\omega(a^*)} \omega(a^*) \right) = 0,$$

and so it is sufficient for satisfying the reset fixed point condition in Thm. 4(iii) as well. \square

Reduction to 1.5 DOF

The reader will note that the 2 DOF SLIP mechanical system has 4 dimensions; however, we show next that with our assumptions, both the continuous and reset dynamics are equivariant with respect to the leg angle, θ . This justifies a “quotient space” analysis excluding the leg angle DOF, which is formally justified in the averaged system.⁵³ To this end, define the reduced averaging coordinate vector, $\tilde{\mathbf{y}} := [\psi_v, a_v, a_{\text{cp}}]^T$.

Continuous dynamics are invariant to θ_a -translation First, in the continuous dynamics, note from our coordinate change (3.148), and the previously calculated ω_0 (3.154),

$$|\psi_{\text{cp}}| = \frac{|\sigma - \delta_{\text{cp}}|}{\omega} \leq \frac{\pi a_{\text{cp}}}{2\omega_v \rho^2} + \mathcal{O}(\varepsilon) \quad (3.169)$$

which is $\mathcal{O}(\varepsilon)$ since $\omega_v = \mathcal{O}(1/\varepsilon)$ by assumption 8b), i.e. because of the stiff leg, the leg angle remains small during stance. Consequently

- a) combining with assumption 8a), we have $g \sin \psi_{\text{cp}} = \mathcal{O}(\varepsilon^2)$, and
- b) $\cos \psi_{\text{cp}} = 1 + \mathcal{O}(\varepsilon^2)$.

Using these simplifications, note that the continuous dynamics (3.143) become

$$\dot{\tilde{\mathbf{y}}} = \begin{bmatrix} \omega_v \\ 0 \\ 0 \end{bmatrix} + \varepsilon \begin{bmatrix} \frac{1}{\omega_v a_v} \cos \psi_v \tilde{v}_r \\ \sin \psi_v \tilde{v}_r \\ 0 \end{bmatrix} + \mathcal{O}(\varepsilon^2), \quad (3.170)$$

in which $\psi_{\text{cp}} = \theta_a$ does not appear.

⁵³However, a stability conclusion about 2 DOF physical SLIP would now require a conjecture about the leg angle DOF being appropriately stabilized in the unaveraged system.

Reset dynamics are invariant to θ_a -translation We choose to employ⁵⁴ the modified scissor strategy [De and Koditschek \(2015a\)](#):

$$\theta_{\text{td}}(\mathbf{y}) := -\psi_{\text{cp}} + \varepsilon u_{\text{cp}}(a), \quad (3.171)$$

where $u_{\text{cp}}(a)$ is a simple servoing function such as $u_{\text{cp}}(a) = k_{\text{cp}}(a_{\text{cp}} - a_{\text{cp}}^*)$. Note that at the equilibrium, using the G_y symmetry of Def. 2, the reset satisfies Prop. 6. Additionally, applying to (3.168), we see that

$$R_{\widetilde{\mathbf{y}}} = \begin{bmatrix} -\pi/2 \\ \text{diag}(1, \rho) \text{Rot}(\varepsilon u_{\text{cp}}(a)) \text{diag}(1, 1/\rho) \end{bmatrix}, \quad (3.172)$$

which again is independent of ψ_{cp} .

Hybrid averaging

C1) We have listed this above in (3.170).

C2) We find $F_1^o = \left[\frac{3a_{\text{cp}}^2 \cos^2 \psi_v}{\rho^4 \omega_v \tilde{\omega}_v}, \frac{3a_{\text{cp}}^2 a_v \cos \psi_v \sin \psi_v}{\rho^4 \tilde{\omega}_v}, 0 \right]^T$, and $F_1^e = (k_v - a_v \beta) \left[\frac{\cos \psi_v \sin \psi_v}{\omega_v a_v}, \sin^2 \psi_v, 0 \right]^T$.

There is no ω_0 , since $m = 0$ in this instance.

C3) Clearly, $a_v^* = k_v/\beta$ satisfies this.

C4) Using the given formula, we get $\mathbf{V} = \begin{bmatrix} -\frac{\pi\beta}{2\omega_v} & 0 \\ 0 & 0 \end{bmatrix}$.

C5) Using the constant flow time assumption, we have $\gamma_y = \sigma - \pi/2$, which is already scaled correctly. Also, $D\gamma_y \begin{bmatrix} 0 \\ I \end{bmatrix} = 0$.

C6) From (3.172), we can directly compute the reset in $\mathbf{x} = a$ coordinates (trivial due to the absence of any phase difference coordinates). Evaluating at the equilibrium (setting $u_{\text{cp}}(a_{\text{cp}}^*) = 0$, we get $\mathbf{S}_0 + \varepsilon \mathbf{U} = I_2 + \varepsilon \begin{bmatrix} 0 & -a_{\text{cp}}^* u'_{\text{cp}}/\rho \\ 0 & k_v \rho u'_{\text{cp}}/\beta \end{bmatrix}$.

C7) From the expression above, we can verify the requisite properties of \mathbf{S}_0 .

C8) We can directly compute $D\bar{P} = (\mathbf{S}_0 + \varepsilon \mathbf{U})(I + \varepsilon \mathbf{V}) = \begin{bmatrix} 1 - \frac{\varepsilon\pi\beta}{2\omega_v} & -\varepsilon a_{\text{cp}}^* u'_{\text{cp}}/\rho \\ 0 & 1 + \varepsilon k_v \rho u'_{\text{cp}}/\beta \end{bmatrix}$, whose eigenvalues can be read off the diagonal. For sufficiently small $\varepsilon > 0$, and $k_v > 0, u'_{\text{cp}} < 0$ (both of which are controller tuning parameters), we are guaranteed that $D\bar{P}$ is stable.

Using Thm. 4 we conclude that 1.5 DOF SLIP has a stable limit cycle in the \mathbf{y} coordinates.⁵⁵

Averageability of 2 DOF SLIP

Our theoretical result Thm. 4 is capable of addressing the issue of multiple fast modes (the leg shank phase and the leg angle in SLIP); however the current obstruction to its averageability is the reset dynamics. We next describe (in the hope that it communicates to the reader effectively our current

⁵⁴We show the analytical result of using a neutral point controller at the end of this subsection.

⁵⁵See footnote 53.

understanding of averageability of hybrid systems) the obstructions with two strategies we have used with past empirical success.

Modified scissor reset strategy We used this strategy for our 1.5 DOF stability proof; however, the obstruction to its application for a 2 DOF proof (including the leg angle) is that the resulting averaged return map is not hyperbolic to $\mathcal{O}(\varepsilon)$.

In the 2DOF calculation, we get \mathbf{V} from $D\tilde{f}$, which is given in (3.164). We now use the full reset

$$R_y = \begin{bmatrix} -\pi/2 \\ -\psi_{cp} + \varepsilon u_{cp}(a_{cp}) \\ \text{diag}(1, \rho) \text{Rot}(\varepsilon u_{cp}(a)) \text{diag}(1, 1/\rho) \end{bmatrix} \quad (3.173)$$

instead of (3.172). We can convert to \mathbf{x} coordinates, and calculate

$$\mathbf{S}_0 + \varepsilon \mathbf{U} = \begin{bmatrix} -1 & 0 \\ 0 & I_2 \end{bmatrix} + \varepsilon \begin{bmatrix} 0 & 0 & -\frac{(2\rho^2\omega_v - \pi\rho a_v^*)u'_{cp}}{2a_{cp}^*} \\ 0 & 0 & a_{cp}u'_{cp}/\rho \\ 0 & 0 & -\rho a_v^* u'_{cp} \end{bmatrix}.$$

Lastly, we can compute the averaged return map:

$$\overline{DP} = \begin{bmatrix} -1 & 0 & -\varepsilon \frac{(2\rho^2\omega_v - \pi\rho a_v^*)u'_{cp}}{2a_{cp}^*} \\ \frac{-2\varepsilon\tilde{g}a_{cp}^2c}{\omega_v(\rho^4\omega_v^2 - a_{cp}^2)} & 1 - \frac{\varepsilon\pi\beta}{2\omega_v} & a_{cp}u'_{cp}/\rho \\ \frac{-2\varepsilon\tilde{g}s}{\omega_v} & 0 & 1 - \rho a_v^* u'_{cp} \end{bmatrix},$$

where c and s stand for the cosine and sine of $\frac{\pi a_{cp}}{2\rho^2\omega_v}$. This matrix has eigenvalues $\{1 - \frac{\varepsilon\pi\beta}{2\omega_v}, 1 - \varepsilon\rho a_v^* u'_{cp}, -1\} + \mathcal{O}(\varepsilon^2)$ which does not satisfy the structural stability needed for our result, since Thm. 2 only assures us that the original system has stability properties $\mathcal{O}(\varepsilon^2)$ close to the averaged system.

Raibert's neutral point strategy This stepping strategy is also due to Raibert, although we can now present a superior neutral point approximation (as we show with numerical results below). Let us define

$$\theta_{td}(\mathbf{y}) = \underbrace{\frac{-\pi}{2\omega(a)}}_{=: \theta_{np}(a)} + \varepsilon u_{cp}(a), \quad (3.174)$$

where the first summand should be interpreted as the “neutral point” function. [Raibert \(1986\)](#) approximated the neutral point by a linear function of forward speed; using our averaging tools we now present a closed-form expression that is (as we show below) a more accurate representation of the neutral point.

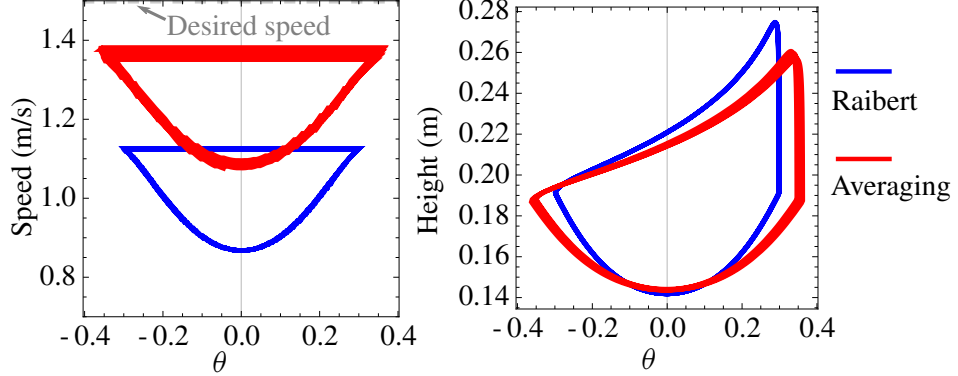


Figure 41: Demonstration that the “neutral point” approximation found using our averaging method (3.175) (in red) outperforms the classic Raibert approximation (blue) Raibert (1986).

From (3.174), clearly Prop. 6 is satisfied. Unfortunately, we get

$$D\bar{R} = \begin{bmatrix} -\frac{\pi a_v}{2\rho\omega_v} & 0 & 0 \\ -\frac{a_{cp}^2}{\rho^3\omega_v} & 1 & 0 \\ \frac{a_{cp}a_v}{\rho\omega_v} & 0 & 1 \end{bmatrix},$$

which is not constant in its $\mathcal{O}(1)$ terms, violating Thm. 4(ii). At present, this places the neutral point stepping algorithm outside the class of averageable systems.

Neutral point approximation using averaging

Using both (3.152) and (3.158) we can compute a closed form expression for the “neutral point” (3.174),

$$\theta_{np}(a) = \frac{-2\rho^3 a_{cp}^3 \left(\frac{2g\rho^5 \cos\left(\frac{\pi a_{cp}}{2\rho^2\omega_v}\right)}{\rho^4\omega_v^3 a_v - \omega_v a_{cp}^2 a_v} - \frac{2g\rho}{\omega_v^3 a_v} + \frac{4a_v}{\omega_v^2} + \frac{\pi\rho}{\omega_v} \right) + 4g\rho^9 \sin\left(\frac{\pi a_{cp}}{2\rho^2\omega_v}\right) - \frac{2\pi g\rho^7 a_{cp} \cos\left(\frac{\pi a_{cp}}{2\rho^2\omega_v}\right)}{\omega_v} + \frac{3\pi a_{cp}^5}{\omega_v^4}}{4\rho^6 a_{cp}^2}, \quad (3.175)$$

$$= \frac{-\pi}{2\omega_0(a)} + \mathcal{O}(\varepsilon) = \frac{-\pi a_{cp}^2}{2\omega_v\rho} + \mathcal{O}(\varepsilon), \quad (3.176)$$

where for the cruder approximation in the second row, we used only $\omega_0(a)$ and left out the contribution of $\varepsilon\omega_1$ in (3.152).

In Fig. 41, we show a numerical comparison of our averaging neutral point approximation to the one in Raibert (1986). For this simulation, we used the crude approximation (3.176) when the horizontal frequency (proportional to a_{cp} as shown in (3.143)) is low, since the expression (3.175) is singular when the oscillator frequency is close to 0.⁵⁶

We believe that the *closed form* return map approximations obtainable using averaging (as demonstrated here) is one of the key benefits of this analysis mode. Once a closed-form expression such

⁵⁶This singularity is clear from our initial coordinate change (3.147)–future work will focus on a modification to the coordinate change to allow for oscillators with close to zero frequency without numerical issues.

as (3.175) is obtained, it can then be approximated to a desired level of precision and deployed on robots. In this particular example, it results in superior speed control (compared to an implementation [Raibert \(1986\)](#)), and for more complex models, a closed form return map approximation would make online reactive planning (e.g. [Arslan and Saranli \(2012\)](#)) a possibility.

3.8 Discussion

We have presented in Thm. 4 and its “corollary,” Fig. 40, the most generally applicable version of hybrid averaging so far. We have successfully applied this result to various mechanical systems appearing in legged locomotion with up to 2 DOF in Sec. 3.7, and work in progress suggests applicability to some 3 DOF systems such as Fig. 27C.

Relation to other coordinate systems for limit cycle analysis Our main advance in Sec. 3.6.3–3.7 (over the hybrid averaging results in Sec. 3.2) can be summarized as the development and application of a judicious coordinate change (Def. 4). In a similar vein, we may now juxtapose this contribution against other coordinate systems suggested in the literature to study limit cycle stability.

Transverse coordinates [Hauser and Chung \(1994\)](#), [Manchester et al. \(2011\)](#) are a set of local coordinates about a periodic orbit typically used to view the linearization of the limit cycle dynamics in a special {tangential, transverse} moving coordinate frame. The reader may compare averageable coordinates (3.20) to ([Hauser and Chung, 1994](#), eq. (5)) or ([Manchester et al., 2011](#), eq. (9)–(10)) to see that in our averageable systems, the “master phase” σ relates to the “tangential” dynamics, and the “slow variables” \mathbf{x} relate to the “transverse” dynamics of the approximated averageable system.

However, note that an explicit description of the orbit is required for analysis using traditional transverse coordinates (for example, ([Manchester et al., 2011](#), eq. (27))). Typically, an explicit description of the periodic orbit is non-trivial to obtain. In comparison, in our approach, we have restricted ourselves to using the template coordinate changes from Sec. 3.1, and an explicit description of the orbit is only required in the (trivial) $\varepsilon = 0$ case.

Secondly, for a stability analysis, in the linearization theory one needs to compute linearization terms using the actual orbit (and Coriolis terms from the moving coordinate frame appear when changing from physical to transverse coordinates along the flow), whereas we can provide a relatively simple analytically tractable closed-form version of the final spatial flow Jacobian (3.163). Our analyses in progress are beginning to address 3 DOF dynamic systems, whereas the application of transverse linearization to a 2 DOF system already presents significant computational challenges [Manchester et al. \(2011\)](#).

Floquet coordinates [De \(2010\)](#), [Revzen \(2009\)](#) are a special form of moving orbit-coincident coordinate frame such that the transverse dynamics are that of an LTI system; they come with the same analytical tractability drawbacks as transverse coordinates.

Phase response curves (PRC’s) [Brown et al. \(2004\)](#) are used in the study of neural circuits; they describe the phase response of the oscillator to perturbations in various states that couple into the phase dynamics. There are no general analytical tools for PRC computation, and results so far use numerical tools for their computation. In contrast, it would be possible to derive a first-order approximation to a PRC from an averageable system in the same way we approximated the SLIP neutral point in Sec. 3.7.2.

Relation to prior usage of time-reversal symmetry in legged locomotion Razavi et al. (2016) utilizes a special class of “symmetric hybrid systems” (SHS’s) with time-reversal symmetry for development of bipedal gaits. As in Altendorfer et al. (2004), a SHS requires strict conditions on symmetry, lack of dissipation in the continuous dynamics, and conditions on the reset. Unfortunately, these Hamiltonian systems are not structurally stable, resulting in practical difficulties to their empirical fielding (since perturbations are not dissipated). Control strategies such as Raibert’s neutral point stepping algorithm would be inadmissible in an SHS scheme as well.

The authors add a slight generalization with scalar dissipation of kinetic energy. However, a specific desired limit cycle (such as desired hopping height, running speed) cannot be freely selected and stabilized using this strategy from a far away initial condition.

Because of these reasons, we find it prudent to incorporate dissipation in our model, which adds the $\mathcal{O}(\varepsilon)$ terms in the dynamics of (3.140).

Relation to other “anchoring” notions Two conceptual notions in the literature of “anchoring” or dynamical dimension reduction are (a) the classical notion of invariant attracting submanifolds Full and Koditschek (1999), and (b) (hybrid) zero dynamics introduced in Westervelt et al. (2003), intuitively a two-step anchoring process Ames et al. (2014).

In contrast, in our experience, these conventional notions of anchoring are too rigid to allow for the kinds of compositions we would like to describe. For instance, our desire to express SLIP (from Sec. 3.6.3) as a composition of a vertical hopper and a fore-aft component would require a dynamical decoupling of the two DOFs in order to apply classical anchoring Full and Koditschek (1999). This is known to not be possible, as evidenced by long-standing SLIP research. In contrast, the averaged vector field (3.161) displays decoupled *average* vertical and fore-aft energy dynamics. Our interpretation is that in Fig. 21, neither of the \mathcal{N} nor \mathcal{R} manifolds are invariant in the unaveraged continuous flow, but they are invariant in the averaged continuous flow.

CHAPTER 4 : Empirical Compositions

As shown in Fig. 1, some of our empirical results are extensions suggested by our analytical work in Chapter 3, and we list them separately in this Chapter. [Raibert \(1986\)](#) pioneered the kind of empirical composition we explore here. We take inspiration from Raibert’s work, but also extend it (a) controlling a planar hopping machine with an asymmetric (tailed) body design and no shank actuator (Sec. 4.1); and (b) controlling a physical quadruped with the same gaits as [Raibert et al. \(1989\)](#) but with fewer actuators (Sec. 4.2).

Though the empirical demonstrations in this section go beyond the scope of our analytical results, they are each distinctly relevant to the topic of compositions: (a) fore-aft quadrupedal bounding (Sec. 4.2.4) and tail-energized hopping (Sec. 4.1) demonstrate robustness to *persistent periodic perturbations* from coupling interactions with the fore-aft DOFs; (b) horizontal-plane quadrupedal yaw control (Sec. 4.2.4) demonstrates the utility of the coordination controllers developed in Sec. 3.5 as well as the attitude controller used in the roll plane when subjected to *aperiodic perturbations* when turning; (c) quadrupedal leaping and return to steady motion (Sec. 4.2.4) demonstrates the robustness of the (preflexive or feedback) coordination controller to *large instantaneous perturbations* in the relative phase of the two legs. Further, in Sec. 4.2.5, we show how the various regimes (Table 6) of the simple 2DOF slot hopper model introduced in this paper also pertain to trotting and pacing, covering the full gamut of virtual bipedal quadruped gaits.

4.1 Tailed Planar Hopping (4 DOF)

In the previously introduced Jerboa (Sec. 2.4.3), we have built a 12DOF, passive-compliant legged, tailed biped actuated by four brushless DC motors. We anticipate that this machine will achieve varied modes of quasistatic and dynamic balance, enabling a broad range of locomotion tasks including sitting, standing, walking, hopping, running, turning, leaping, and more. Achieving this diversity of behavior with a single under-actuated body, requires a correspondingly diverse array of controllers, motivating our interest in compositional techniques that promote mixing and reuse of a relatively few base constituents to achieve a combinatorially growing array of available choices. Here we report on the development of one important example of such a behavioral programming method, the construction of a novel monopodal sagittal plane hopping gait through parallel composition of four decoupled 1DOF base controllers.

For this example behavior, the legs are locked in phase and the body is fastened to a boom to restrict motion to the sagittal plane. The results cited here were reported in [De and Koditschek \(2015b\)](#), with the exception of the preliminary hip-energized numerical results in the introduction.

Contribution: Empirical Hopping on a New Underactuated Legged Morphology

This section contributes both to the theory and practice of dynamical legged locomotion. The principal new theoretical contribution is an invariance proof (modulo a restrictive assumption 9) of the parallel composition of Raibert’s [Raibert \(1986\)](#) stepping controller with our new energy pump (4.1).

The empirical contributions of the paper are the the physical demonstration of the new oscillatory spring-energization scheme for vertical hopping using a tail actuator, and experimental evidence

supporting the hypothesis that our final parallel composition of the four isolated controllers does indeed anchor the corresponding templates in the Jerboa body (Fig. 48).

While the idea of parallel composition is appealing, the difficulty of such a composition arises from the natural transfer of energy between different compartments Eriksson (1971)¹ in a mechanical system operating in a dynamical regime. In our setting, some degree of coupling across compartments is crucial to the underlying design concept of driving the leg spring through torques generated “far away” in the tail. Thus, a naive approach of looking for exactly decoupled body dynamics is not fruitful². Instead, we analyze stability properties of (hybrid) closed-loop templates—which are not specifically associated to any body—without paying attention to the input structure. In agreement with intuition, we find (Sec. 4.1.3) that minimization of cross-template transfer of energy—through either the flows or the reset maps—results in a successful composition.

Superscripts on each of these symbols denote the *hybrid template* that it is a part of, e.g. for controlled vertical hopping (Sec. 3.1.1). The layout of the paper roughly reflects the template-anchor hierarchy depicted in Fig. 42. Namely, there are two intermediate 2DOF templates—the SLIP, and the inertial reorientation—that comprise the tailed monoped. They, in turn, are comprised of the vertical, and fore-aft, 1DOF templates, and respectively, the shape, and pitch, 1DOF templates. We endow the 1DOF templates at the lowest level with an exemplar plant, with respect to which we will develop controllers for the four template plants, in isolation.

SLIP, and Sec. 3.1.4 present the 2DOF templates that are directly anchored in the robot body, and within them contain descriptions of the subtemplates (e.g. Sec. 3.1.1, 3.1.3)—as simple exemplar 1DOF anchoring bodies and corresponding control laws—that comprise in isolation the constituent desired limiting behaviors that we seek to embody simultaneously in our physical system. Each of the template controllers in this suite is necessarily simple by dint of its origin as a feedback law for a highly abstract 1DOF task exemplar. We hypothesize that this combination of algorithmic simplicity and task specialization may lend robustness in the empirical setting since control policies are not sensitive to, and certainly avoid cancellation of, forces arising from dynamical coupling in the anchoring body.

We emphasize that these coupling-naive feedback laws (summarized in Sec. 4.1.2) are simply “played back” (modulo scaling) in the 6DOF body with all its complicated true dynamical coupling. We show formally through various propositions in this paper that nevertheless the stability of the templates and subtemplates persists through composition for the distal segments of the tree (Fig. 42)—SLIP as a composition of vertical hopping and fore-aft speed control, and attitude stabilization as a composition of inertial reorientation and Raibert’s pitch control. We provide some preliminary suggestions about the composition of SLIP (s) with attitude (a) compartments (center of Fig. 42), but a full analysis is left to future work. However, we offer empirical data in Sec. 4.1.4 showing how this idea has resulted in promising qualitative behavior on the Jerboa robot (Fig. 48, video attachment).

As depicted in Fig. 42, the platform’s locomotion is powered by the hip motor that adjusts leg touchdown angle in flight and balance in stance, along with a tail motor that adjusts body shape in flight and drives energy into the passive leg shank spring during stance. The motor control signals

¹We use this term here to stand for subsystems (here, disjoint subsets of the physical degrees of freedom) that exchange a resource (here, energy).

²For instance, for hopping with the tailed monoped, the tail actuator and hip actuator seemingly work on differently “binned” tail and leg DOFs, but we energize the robot body with the tail through the leg spring.

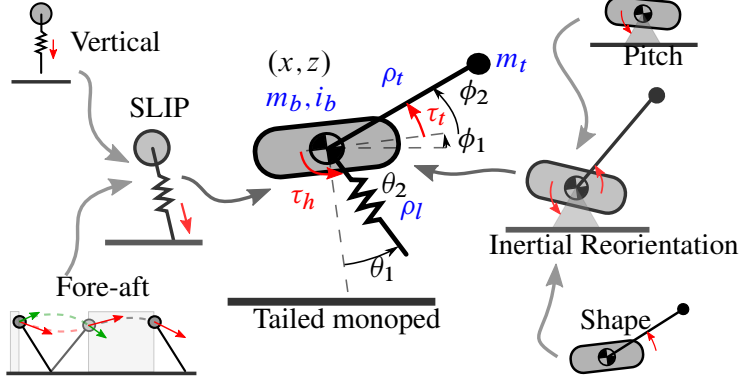


Figure 42: Control of a tail-energized hopping behavior expressed as a hierarchical composition of closed-loop templates. Notionally, the grey arrows represent directed template→anchor relations. **Center:** A model of the tailed monoped physical platform on which we implement tail-energized planar hopping, labeled with configuration variables (black), actuators (red), and model parameters (blue).

arise from the application in parallel of four simple, completely decoupled 1DOF feedback laws that provably stabilize in isolation four corresponding 1DOF abstract reference plants. Each of these abstract 1DOF closed loop dynamics represents some simple but crucial specific component of the locomotion task at hand. We present a partial proof of correctness for this parallel composition of “template” reference systems along with data from the physical platform suggesting these templates are “anchored” as evidenced by the correspondence of their characteristic motions with a suitably transformed image of traces from the physical platform (Sec. 4.1.4).

We present, at the outset, the assumption we make in order to simplify our theoretical invariance result.

Assumption 9 (Pendular stance). *During stance,*

- (i) *the effects of gravity are negligible³ compared to spring potential / damping forces,*
- (ii) *radial deflections are negligible,*
- (iii) *time of stance is constant, and*
- (iv) *the angle swept by the leg admits a small-angle approximation.*

4.1.1 Two Solutions: Tail-Energized vs. Hip-Energized

For this simple planar hopping task, specified simply as a composition of a vertical hopping and fore-aft speed control template for the CoM, we observe that even the 4DOF (planarized) Jerboa body offers “multiple solutions.” This reveals for the first time one of the great benefits of modularity: if an autonomous robot has a solution for flexibly anchoring combinations of templates (motivating our Chapter 3 work), changing environment and task conditions can be used to trigger more suitable anchoring choices in order to improve performance or efficiency.

In this thesis, we only motivate these potential benefit with anecdotal findings, and our detailed presentation in this section only pertains to the tail-energized solution.

³We suspect that the less restrictive Geyer approximation Geyer et al. (2005) is sufficient, but leave this generalization to future work.

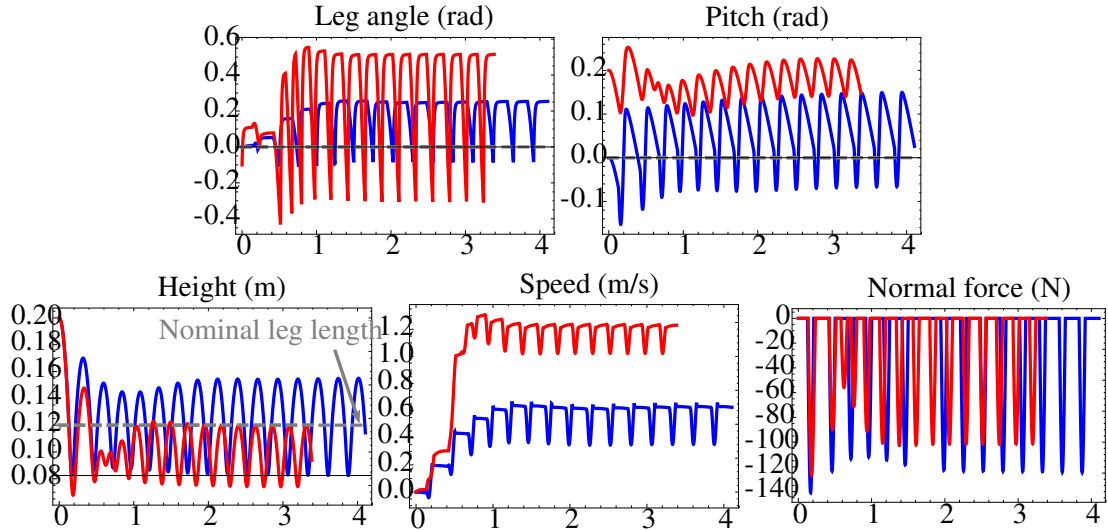


Figure 43: Simulation traces of tail-energized (blue) and hip-energized (red) hopping on the Jerboa. Both simulations used a composition of simple controllers, one of which (tail-energized) we describe in detail in Sec. 4.1.2. Both simulations ran for 15 hops, though the hip-energized simulation took a shorter time because of its higher step frequency.

However, we present in this short subsection a single numerical trial (Fig. 43) in which we overlay results from two different strategies. We discuss below how Fig. 43 clearly suggests the benefits of the tail-energized composition on rougher terrain, and of the hip-energized composition for higher speed on more predictable terrain.

Tail-energized In this mode, we can see that the simulated robot generates far greater hopping height, as well as greater normal force. The larger hopping height is clearly desirable when the terrain gets rough and obstructs the swing path of the leg (toe stubbing), and similarly, the greater normal forces produce a bigger friction cone in order to maintain traction in unpredictable, loose, or slippery terrain.

Hip-energized In this mode, we can see that the robot attains almost twice the speed (with the same speed command as the tail-energized version). However, the hopping height is much lower, increasing vulnerability to stubbing if implemented on a physical platform.

Our preliminary attempts to implement this strategy on the physical platform failed due to insufficient traction causing the toe to SLIP before any successful hops.

Table 8: Jerboa control parameters (all scalars unless noted)

k_t	Tail gain (4.1)
k_p	Raibert speed controller gain (4.2)
k	Inertial reorientation generalized damper gains (4.4)
k_g	Inertial reorientation graph error gain (4.4)
β, ω	Dissipation, frequency of spring-damper (Sec. 3.1.1)
ε	Saturation parameter for tail controller (4.1))
ε_r	Arbitrarily small orientation error (Proposition 5)
m_b, i_b	Mass, inertia of robot body (Sec. 2.4.3)
ρ_l, ρ_t	Leg, tail link lengths (Sec. 2.4.3)
k_s	Hooke's law leg spring constant (Sec. 2.4.3)

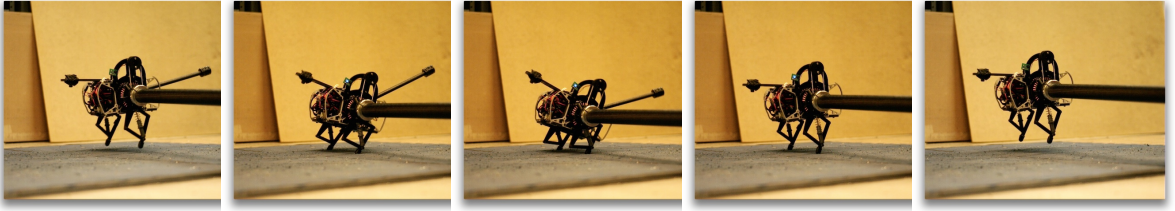


Figure 44: Snapshots from apex to apex of tail-energized planar hopping implemented on a new robot platform—the Penn Jerboa (Sec. 2.4.3).

4.1.2 Implementation Details

We use the following controllers,

$$\text{Tail energy pump (Sec. 3.1.1)} \quad u_v(x) = k_t \cos(\angle x) \quad (4.1)$$

$$\text{Raibert neutral point (Sec. 3.1.3)} \quad u_{cp}(\dot{x}) = \beta^*(\dot{x}) + k_p(\dot{x} - \dot{x}^*) \quad (4.2)$$

$$\text{Pitch correction} \quad u_{att_1}(a_1, \dot{a}_1) = -k_g k a_1 - k_g \dot{a}_1 \quad (4.3)$$

$$\text{Shape reorientation Johnson et al. (2012)} \quad u_{att_2}(a_2, \dot{a}_2) = -k_g k a_2 - k_g \dot{a}_2 \quad (4.4)$$

applied to generate the torque signals for the tail, hip, hip, and tail actuators respectively.

4.1.3 Modeling for Planar Hopping

Raibert's planar hopper [Raibert \(1986\)](#) empirically demonstrated stable hopping using a rigid body with a springy leg, and in this paper we pursue the same idea, but instantiate vertical hopping by coupling the 1-DOF leg-spring excitation controller (physically acting through the tail). In flight, the tail actuator grants us a new affordance that we only use here to regulate the added “shape” DOF. Our physical model is shown in Fig. 44. The system has a single massless leg with joints $\theta = (\theta_1, \theta_2) \in S^1 \times \mathbb{R}_+$, a rigid body $(x, z, \phi_1) \in \text{SE}^2$, and a point-mass tail with revolute DOF ϕ_2 , such that the full configuration is $\mathbf{q} := (\theta_1, \theta_2, x, z, \phi_1, \phi_2) \in \mathcal{Q}$.

Assumption 10. We make the following design-time assumptions⁴ relating to the physical construction parameters of the robot:

- (i) leg/tail axes of rotation are coincident at the “hip;”
- (ii) tail mass is small, i.e. $m_t \ll m_b$;
- (iii) center of mass (configuration-independent by the previous assumption) coincides with the hip; and
- (iv) body, tail have high inertia, i.e. $i_b, i_t \rightarrow \infty$.⁵

Equations of Motion

Using the self-manipulation [Johnson and Koditschek \(2013a\)](#) formulation of hybrid dynamics, the inertia tensor is

$$\mathbf{M} = \begin{bmatrix} 0 & \\ & \mathbf{M}_b \end{bmatrix}, \text{ where } \mathbf{M}_b := \begin{bmatrix} \mathbf{M}_1 & \mathbf{M}_o^T \\ \mathbf{M}_o & \mathbf{M}_2 \end{bmatrix}. \quad (4.5)$$

Note that $\mathbf{M}_1 = (m_b + m_t)I$ and $\mathbf{M}_2 = \begin{bmatrix} i_b + i_t & i_t \\ i_t & i_t \end{bmatrix}$ are constant, and \mathbf{M}_o contains the critical cross-compartment interaction, by way of which we can use our tail actuator (formally acting on an attitude DOF, ϕ_2) for energizing the shank DOF, θ_2 .

Let the forward kinematics of the leg be $\mathbf{g} : \theta \mapsto \mathbb{R}^2$. The constraint in the stance contact mode is

$$\mathbf{a}_1(\mathbf{q}) = \begin{bmatrix} x \\ z \end{bmatrix} - R(\phi_1)\mathbf{g}(\theta), \quad (4.6)$$

such that $\mathbf{A}_1(\mathbf{q}) = [RD\mathbf{g} \quad I \quad JR\mathbf{g} \quad 0]$. In flight mode, $\mathbf{a}_2(\mathbf{q}) \equiv 0$. As in [Johnson and Koditschek \(2013a\)](#), the dynamics can be expressed as

$$\begin{bmatrix} \mathbf{M} & \mathbf{A}_i^T \\ \mathbf{A}_i & 0 \end{bmatrix} \begin{bmatrix} \ddot{\mathbf{q}} \\ \lambda \end{bmatrix} = \begin{bmatrix} \mathbf{Y} - \mathbf{N} \\ 0 \end{bmatrix} - \begin{bmatrix} \mathbf{C} \\ \dot{\mathbf{A}}_i \end{bmatrix} \dot{\mathbf{q}}.$$

Define the linear coordinate change $\mathbf{h} : \mathcal{Y} = \mathcal{S} \times \mathcal{A} \rightarrow \mathcal{Q}$, and $\mathbf{H} := \mathbf{D}\mathbf{h}$ such that

$$\mathbf{h}^{-1} : \mathbf{q} \mapsto \begin{bmatrix} (\theta_1 + \phi_1, \theta_2, x, z)^T \\ \mathbf{M}_2 \begin{bmatrix} \phi_1 \\ \phi_2 \end{bmatrix} \end{bmatrix}, \quad (4.7)$$

and the projections $\pi_s := [I_4 \quad 0]\mathbf{h}^{-1}$, $\pi_a := [0 \quad I_2]\mathbf{h}^{-1}$. The equations of motion are generated

⁴These assumptions were informed by analytical simplifications in the dynamics which follow.

⁵Even though the dynamic task here is quite different from free-fall, in the language of [Johnson et al. \(2012\)](#), the tail should be light but *effective*.

in the new coordinates, $\ddot{\mathbf{y}} = \mathbf{H}^{-1} \mathbf{M}^\dagger (\Upsilon - \mathbf{N}) - \mathbf{H}^{-1} (\mathbf{M}^\dagger \mathbf{C} + \mathbf{A}^\dagger T \dot{\mathbf{A}}) \mathbf{H} \dot{\mathbf{y}}$. In stance,

$$\begin{bmatrix} \ddot{s}_1 \\ \ddot{s}_2 \end{bmatrix} = \begin{bmatrix} \frac{\tau_h}{m_b \theta_2^2} - \frac{2\dot{\theta}_2 \dot{\theta}_s}{\theta_2} \\ \frac{k_s(\rho_t - \theta_2)}{m_b} + \theta_2 \dot{\theta}_s^2 \end{bmatrix} + \frac{\tau_t}{\rho_t m_b} \begin{bmatrix} \sin \xi / \theta_2 \\ -\cos \xi \end{bmatrix}, \quad (4.8)$$

$$\ddot{a} = \begin{bmatrix} -\tau_h \\ \tau_t \end{bmatrix}, \quad (4.9)$$

where $\xi := \theta_1 - \phi_2$ (the tail-leg angle), and the right summand in (4.8) is quite clearly the disturbance caused due to the added attitude degrees of freedom. With the same choice of \mathbf{H} , we can similarly recover weakly decoupled flight dynamics:

$$\begin{bmatrix} \ddot{x} \\ \ddot{z} \end{bmatrix} = \begin{bmatrix} 0 \\ -g \end{bmatrix} + \frac{\tau_t}{\rho_t m_b} \begin{bmatrix} \sin(\phi_1 + \phi_2) \\ -\cos(\phi_1 + \phi_2) \end{bmatrix}, \quad (4.10)$$

$$\ddot{a} = \begin{bmatrix} 0 \\ \tau_t \end{bmatrix}. \quad (4.11)$$

“Physical” Decoupling and Anchoring

With the highly restrictive assumption 10 (allowing for infinite tail inertia), the tail motion is essentially negligible. Under these conditions, we show the emergence of the beginnings of a classical anchoring relation [Full and Koditschek \(1999\)](#), via a natural (weak) decoupling of the 6DOF dynamics into “point-mass” and attitude compartments.

Proposition 7 (Jerboa flow anchoring). *Under assumption 10, in each hybrid mode, (i) the submanifold $\mathcal{U} = \{T\mathbf{q} \in T\mathcal{Q} : T\phi_1 = T\phi_2 = 0\}$ is invariant under the action of the closed-loop flow, and (ii) in each hybrid mode, the closed-loop flow restricted to \mathcal{U} is a cross-product of the template vector fields,*

$$f_{\text{tm}}|_{\mathcal{U}} = f_{\text{slip}} \circ \pi_{\text{slip}} \times f_{\text{att}} \circ \pi_{\text{att}},$$

where π_{slip} and π_{att} represent projections to the SLIP and attitude components of \mathbf{q} respectively.

Proof. Applying assumption 10.(ii) to the equations of motion, the plant dynamics $p_{\text{tm}}(T\mathbf{q}, (\tau_h, \tau_t))$ are

$$\begin{aligned} \ddot{\theta}|_{\text{stance}} &= \begin{bmatrix} \frac{\tau_h}{m_b \theta_2^2} - \frac{2\dot{\theta}_2 \dot{\theta}_s}{\theta_2} \\ \frac{k_s(\rho_t - \theta_2)}{m_b} + \theta_2 \dot{\theta}_s^2 \end{bmatrix} + \frac{\tau_t}{\rho_t m_b} \begin{bmatrix} \sin \xi / \theta_2 \\ -\cos \xi \end{bmatrix}, \\ \ddot{a}|_{\text{stance}} &= \begin{bmatrix} -\tau_h \\ \tau_t \end{bmatrix}, \\ \begin{bmatrix} \ddot{x} \\ \ddot{z} \end{bmatrix}|_{\text{flight}} &= \begin{bmatrix} 0 \\ -g \end{bmatrix} + \frac{\tau_t}{\rho_t m_b} \begin{bmatrix} \sin(\phi_1 + \phi_2) \\ -\cos(\phi_1 + \phi_2) \end{bmatrix}, \\ \ddot{a}|_{\text{flight}} &= \begin{bmatrix} 0 \\ \tau_t \end{bmatrix}, \end{aligned} \quad (4.12)$$

We can check that we have available affordances through our two actuators to assign (scaled versions of) our template controllers in Sec. 4.1.2, (i) $\tau_h|_{\text{stance}} = -u_{\text{att}_1}(a_1, \dot{a}_1)$ to control a_1 , and $\tau_h|_{\text{flight}} = u_{\text{cp}}(\dot{x})$ to control \dot{x} , and (ii) $\tau_t|_{\text{flight}} = u_{\text{att}_2}(a_2, \dot{a}_2)$ to control a_2 , and $\tau_t|_{\text{stance}} = -\rho_t \theta_2 m_b \cdot u_v(\dot{z})$ to control hopping height⁶.

Under assumptions 9.(iv) and 10.(iv), we show that the highlighted terms in (4.12) vanish inside \mathcal{U} :

- a) $\mathbf{M}_2 \rightarrow \infty$, so in the dynamics equations $\ddot{a} = 0$. Restricted to \mathcal{U} , $a \equiv 0$. This proves part (i) of the claim.
- b) From $\ddot{a} \equiv 0$ and (4.4), $\tau_h|_{\text{stance}} = \tau_t|_{\text{flight}} = 0$.
- c) Since $\phi_2 = 0$, $\xi = -\phi_1 \approx 0$ (from assumption 9.(iv)).

By comparing the thus-restricted plant dynamics (4.12) to the SLIP equations of motion (3.133) and (3.15), we obtain part (ii) of the result. \square

We observe here that this stronger invariance condition of Prop. 7 requires the restrictive assumption 10. Future work will apply our averaging approximation of Sec. 3 to instead seek an averaged invariance that will hopefully obviate the need for such a restrictive assumption.

Proposition 8 (Jerboa return-map anchoring). *The set \mathcal{U} is invariant under the return map $F_{\text{tm}}(T \mathbf{q}|_{\mathcal{U}})$, and restricted to \mathcal{U} , $F_{\text{tm}} = F_{\text{slip}} \circ \pi_{\text{slip}} \times F_{\text{att}} \circ \pi_{\text{att}}$.*

Proof. We first define the return map F_{tm} by instantiating a “cross-product” hybrid system with domain, vector field, and return map $(D_{\text{tm}}, f_{\text{tm}}, R_{\text{tm}})$ as (a) $D_{\text{tm}} := D_{\text{slip}} \times D_{\text{att}}$, (b) $R_{\text{tm}} := R_{\text{slip}} \times R_{\text{att}}$, and (c) f_{tm} as defined in Proposition 7, where $D_{\text{att}_i} := TS^2 \times S^1$ for each i (ensuring $\partial D_{\text{att}} = \emptyset$) and $R_{\text{att}_i} : D_{\text{att}_i} \rightarrow D_{\text{att}_{i+1}}$ is defined

$$\widetilde{R}_{\text{att}_i} : \begin{bmatrix} T_{\text{att}} \\ \psi_{\text{att}} \end{bmatrix} \mapsto \begin{bmatrix} T_{\text{att}} \\ i\pi \bmod 2\pi \end{bmatrix}. \quad (4.13)$$

With these modifications, the ψ_{att} dynamics (3.16) are ignored, and the clock of the HIR subsystem is being driven by the SLIP subsystem⁷. This ensures that the conditions of Proposition 5 still hold, i.e. $\pi_{\text{att}} \circ F_{\text{tm}} = F_{\text{att}} \circ \pi_{\text{att}}$.

Additionally, the decoupled nature of $f_{\text{tm}}|_{\mathcal{U}}$ (Proposition 7) allows us to conclude that $\pi_{\text{slip}} \circ F_{\text{tm}} = F_{\text{slip}} \circ \pi_{\text{slip}}$, so that

$$F_{\text{tm}} = \pi_{\text{slip}} \circ F_{\text{tm}} \times \pi_{\text{att}} \circ F_{\text{tm}} = F_{\text{slip}} \circ \pi_{\text{slip}} \times F_{\text{att}} \circ \pi_{\text{att}},$$

which concludes the proof. \square

We leave to future work (using results from Chapter 3) a proof that \mathcal{U} is attracting, which is a requirement for demonstration of anchoring **Full and Koditschek (1999)**.

⁶We observe that by assumption 9.(ii), $\theta_2 \approx \rho_l$ is roughly constant, so the scaling need not be configuration dependent.

⁷This coupling interaction importantly invalidates the ω_{att} -dependent bound on k (3.19). Our solution is to scale the input such that k is high enough for the shortest feasible transition time in vertical hopping.

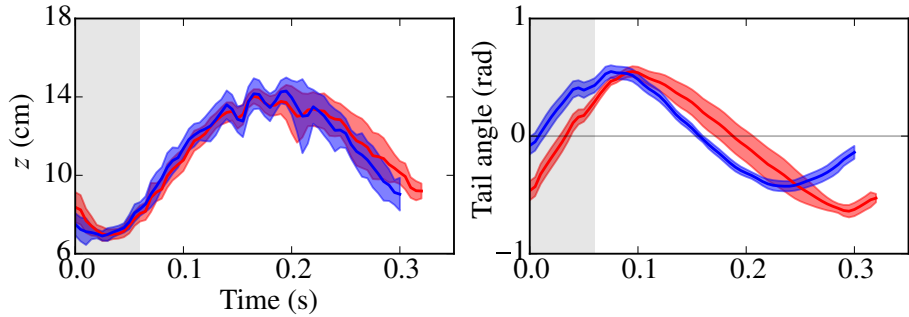


Figure 45: Two datasets corresponding to different tail masses: The blue traces use the $m_t = 150$ g (as in Table 4), but the red traces use $m_t = 100$ g. Note that the tail displacement is larger for the lighter tail mass, although vertical behavior is largely unaffected.

4.1.4 Experimental Results

In this section we present empirical data obtained from the Jerboa (Sec. 2.4.3). In the first three subsections, we present data from a few “nodes” of our composition tree (Fig. 42). Finally, a crucial examination of our idea of composition of templates, when implemented on the Jerboa, is presented in Sec. 4.1.4.

Effect of Varying Tail Mass on Vertical Hopping

The first empirical result we present corresponds to the top left leaf of Fig. 42—empirical vertical hopping. In order to facilitate the analysis in this paper, in assumption 10 we stipulated an ideally effective Johnson et al. (2012) tail, with negligible mass and infinite inertia. We connected the robot (Fig. 44) to a boom and constrained the body pitch as well as the fore-aft DOF. By varying the tail mass (with a fixed tail length given in Table 4), we obtained two vertical hopping datasets plotted in Fig. 45.

We observe the following:

- a) Increasing tail mass results in smaller tail displacements. Taken to the limit, this sheds some light on assumption 10: a large tail mass would indeed render the tail motion negligible.
- b) The hopping height remains relatively unchanged in spite of this physical variation. From (4.8), the force acting on the leg-spring depends only on the (feedforward) tail torque, τ_t (as in Sec. 4.1.2).

Consequently, we see that the tail mass is a *tunable design parameter* that allows us to trade off the conditions of assumption 10 (negligible mass versus large inertia—both affecting coupling interactions) without affecting the vertical behavior.

Empirical Validation of Attitude-Decoupling Change of Coordinates

An important foundation of our attitude control strategy is the decoupling of the two attitude DOFs (Sec. 3.1.4), such that a_1 is controlled in stance, and a_2 is controlled in flight (3.15). However, the body pitch and tail angle are clearly coupled in flight⁸. To resolve this, as shown in (4.7), we use

⁸Since the tail actuator is attached between the body and the tail, tail torques are felt by the body.

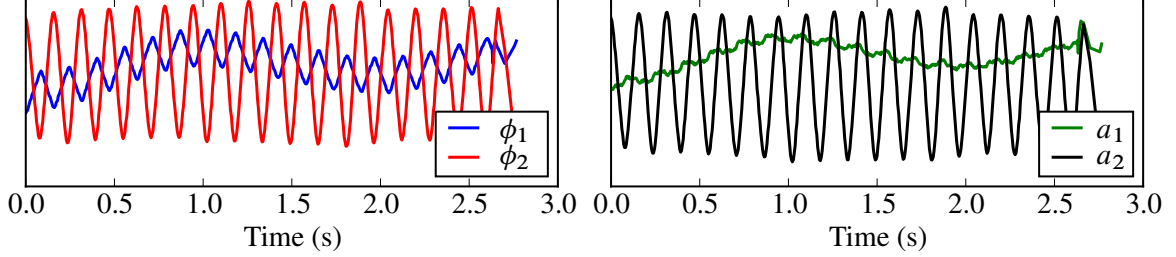


Figure 46: Testing our decoupling change of coordinates from the physical body pitch, tail angle coordinates (ϕ_1, ϕ_2) to our chosen attitude coordinates (a_1, a_2) by suspending the robot about its CoM (see Sec. 4.1.4).

\mathbf{M}_2^{-1} as a decoupling change of coordinates.

In terms of implementation this strategy requires the estimation of a single scalar parameter that defines \mathbf{M}_2 up to scale (see the text just after (4.5)). To test our the change of coordinates empirically, we suspended the robot about the CoM and applied a feedforward sinusoidal τ_t signal. The resulting traces for the physical attitude coordinates are shown in Fig. 46.

Recall from (4.11) that in flight, $\ddot{a}_1 = 0$. In practice, we observe from the right of Fig. 46 that there are small a_1 -variations are at a much slower time scale than a_2 -variations. The reason that \ddot{a}_1 is not zero is that we were unable to suspend the robot at precisely the CoM, and so gravity exerts a net moment on the body—appearing as a slow a_1 -oscillation. Other than this minor deviation of our physical platform from assumption 10, it appears as if the attitude-decoupling change of coordinates is indeed effective.

Trading off Forward Speed and Hopping Height for “Leaping”

The “stepping” fore-aft control using the touchdown angle as a control input essentially allows us to trade off vertical and fore-aft energy—appearing as a pure rotation. Even though for steady-state behavior we choose the touchdown angle to stabilize forward speed, it also allows for transient behaviors such as a one-shot “leaping” motion (term coined by Raibert [Raibert \(1986\)](#)). In particular, choosing a larger (in magnitude from vertical) touchdown angle than that dictated by the neutral point controller results in added vertical height and reduced fore-aft speed.

The results of an empirical test of this one-shot leaping strategy are showing in Fig. 47: we can indeed get a large increase in apex height using this strategy. This kind of “asymmetry” [Raibert \(1986\)](#) or deviation from steady-state may have important applications in behaviors that require rapid changes in the body energy, and we plan to explore more such behaviors in future work.

Empirical Validation of Composition

By physically constraining some of the DOFs, we test our hierarchical composition (Fig. 42) at as many “nodes” of the composition tree as possible. Note that it is infeasible to isolate the fore-aft or the closed-loop pitch correction templates in a physical setting. The results are summarized in Fig. 48. Five strides are averaged within each category, and aligned with ground truth knowledge of the touchdown event. We observe that

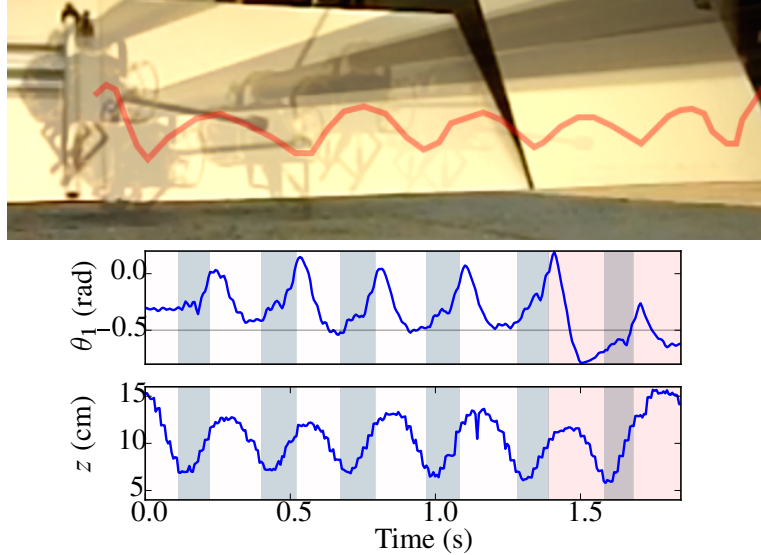


Figure 47: **Top:** Snapshots of fore-aft hopping behavior in a trial where we test a “leaping” motion Raibert (1986)—the robot stubs its toe at the last touchdown in order to gain a boost in vertical height at the expense of forward speed (see Sec. 4.1.4). The red line shows the CoM-trajectory of the robot. **Bottom:** Corresponding traces showing near-steady-state behavior in the fore-aft compartment (leg angle, θ_1 and vertical height, z are plotted) before the “stutting” event (red overlay). The leg angle shows the “neutral angle” with a thin horizontal line, and in order to leap; note that a much larger (in magnitude from vertical) touchdown angle is chosen in order to leap. The leg height (z) plot shows the robot getting around 50% larger apex height in the subsequent flight phase.

- a) there is a vertical limit cycle that retains its rough profile and magnitude through three anchoring bodies,
- b) the hip angle roughly satisfies $\ddot{\theta}_1 = 0$ in stance and the stance duration is roughly constant (corroborating assumptions 9(ii)-(iii)),
- c) the shape coordinate is destabilized in stance and stabilized in flight, and the pitch-deflections are small in magnitude over the stride, and in agreement with (3.16).

Qualitatively, the “tailed point-mass hopper” configuration attained stable forward hopping at controlled speeds upwards of 20 strides, only limited by space. The fully unlocked system has so far hopped for about 10 strides at multiple instances before failing due to accumulated error causing large deviations from the limit cycle. We believe the prime reason for this is that the CoM is significantly aft of the hip (violating assumption 10(i)). We attempted to compensate for this effect with a counterbalance visible in Fig. 44, but an unacceptably large weight would have been required to completely correct the problem.

4.2 3D Virtual Bipedal Running (6 DOF)

Moving beyond our previous results on correct-by-design in-place preflexive and feedback coordination, we now present empirical results of composition with other templates including horizontal plane speed and yaw control, as well as running leaps.

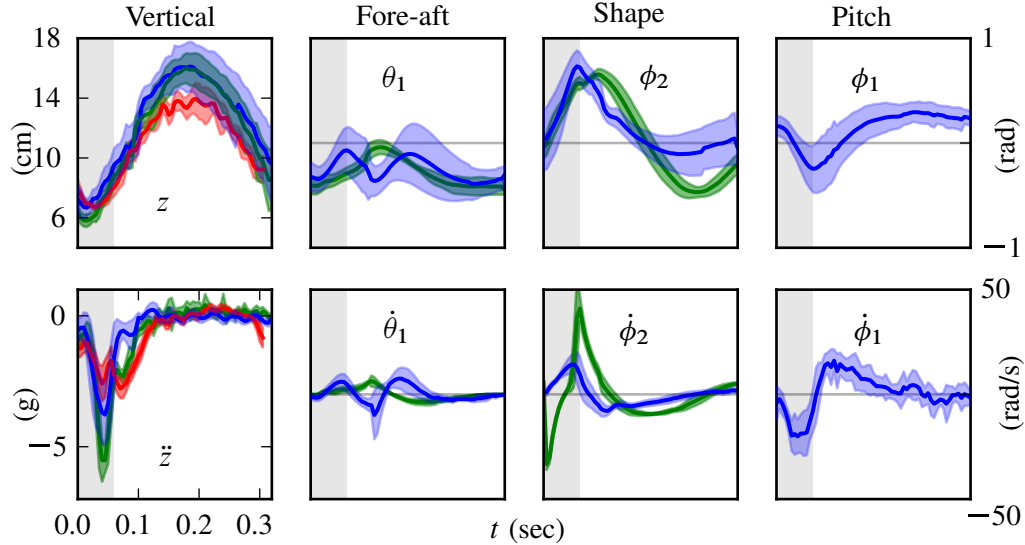


Figure 48: A single stride (stance with shaded background followed by flight), where each column corresponds to some representative time series from each of the relevant 1DOF templates from Sec. 3.1, and the traces (mean and standard deviation) correspond to different “bodies” realized by variably constraining the robot—red: tailed vertical hopper (i.e. (θ_1, x, ϕ_1) locked), green: tailed point-mass hopper (i.e. ϕ_1 locked), blue: tailed planar hopper (all free)—in which these templates are being anchored.

Our empirical results are from a physical platform: Ghost Robotics’ **Minitaur** (2016), a $m_b = 6$ kg direct-drive quadrupedal robot introduced in [Kenneally et al. \(2016\)](#). Each of Minitaur’s legs has two actuated degrees of freedom capable of independently controlling toe extension and hip flexion, with no ab/adduction joints and no passively compliant elements. The distance from the center of mass to each hip is $d = 0.2$ m. Minitaur is equipped with encoders on each of its motors, as well as an inertial measurement unit (IMU). No exteroceptive sensing is required for the experiments reported here. The computationally simple controllers (leg extension controller (3.5) as well as other controllers mentioned below) are implemented on a [STM32F303 microcontroller](#) running at 72 MHz.

In Sec. 4.2.1 we provide details of our implementation for all the gaits demonstrated on the physical platform, and empirical results in Sec. 4.2.2 onward. All of these experiments are also included in the video attachment.

4.2.1 Implementation Details

In this paper we primarily view Minitaur as a composition of two hoppers in the sagittal plane (with exceptions in Sec. 4.2.5). The various aspects of implementation and control are described in this subsection, and the experimental results are presented in the following subsections.

Table 9: Comparison to prior virtual leg management. We refer to Raibert et al. (1989) for baseline prior practice, as it remains the most complete reference to Raibert’s pioneering ideas that continue to dominate most experimental quadruped work, including our own. The analytical insights reported here afford similar behavioral results from less prescribed (event-based) compensators requiring fewer actuated degrees of freedom.

Name	Raibert et al. (1989)	Our implementation	Possible benefit / discussion
State machine	Prescribed alternating stance / flight (Fig. 6-6), cf. note 12	Independent hips with event-based (non-prescribed) mode switching ⁹	Robustly handles unexpected perturbations. ¹⁰
Virtual leg flight control	Identical hip-relative horiz plane displacement: eqs. (6.5)–(6.6)	Same as Raibert (Sec. 4.2.4)	
Virtual leg event synchronization	Actively enforced simultaneous touchdown	Simultaneous touchdown not enforced	Minimal qualitative effect (Sec. 3.5.6), not reliant on flat ground (Sec. 4.2.1)
Virtual leg stance control	Equal axial leg forces: eq. (6.7)	Each leg independently applies (3.91)	Shank actuators control both height and roll/pitch (see below and Sec. 4.2.1)
Vertical control	Increased “rest length” at bottom	Negative damping (3.5)	Smoothly defined through stance
Fore-aft speed control	Positioning flight toe at “neutral point:” eqs. (6.1)–(6.2)	Same as Raibert (Sec. 4.2.4)	
Pitch/roll control	Hip torques (flexion/extension and ab/adduction): eqs. (6.3)–(6.4)	Coordination controllers (3.59)–(3.60)	Hip actuators not needed (Sec. 4.2.1)
Yaw control	Positioning flight toe using ab/adduction: eqs. (6.9)–(6.10)	Fore/aft hip joint torques in stance (4.19)	Ab/adduction joints not needed (Sec. 4.2.4)

Template control implementation

The overall implementation proceeds as follows (and is further detailed throughout this subsection): (a) a virtual leg grouping is selected; (b) physical touchdown and liftoff detection is implemented; (c) the controller (3.5) (and recursively, (3.58), and when applicable, (3.59) and/or (3.60)) is used to formulate the stance control signal; (d) this control signal is applied to the stance leg through the process described in Sec. 4.2.1; (e) to additionally move the in-place-hopping robot in the horizontal plane, the fore-aft (4.17) and yaw (4.19) controllers are applied.

In this paper we assume control authority over the radial leg force for implementation of (3.5). On Minitaur, this force can be controlled at a very high bandwidth using the microcontroller and drive electronics documented in De and Koditschek (2015c), Kenneally et al. (2016), and the motor encoders enable 12-bit measurements of the motor position and velocity. The accumulated losses from motor back-EMF and bearing friction are represented in the lumped damping term in (3.5). Whereas there is no torsional control asserted for the in-place gaits discussed in this and the next two

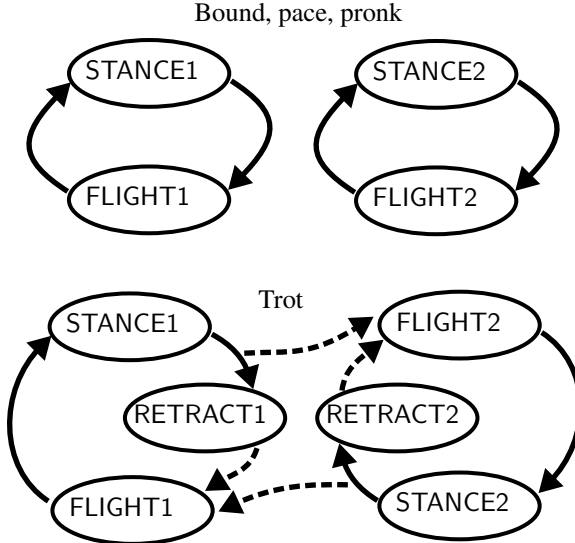


Figure 49: State machines utilized to implement the various gaits. Our work is inspired by Raibert, and this figure is meant to elicit connections to (Raibert et al., 1989, Fig. 6-6, 6-11). However, unlike Raibert’s implementation (we summarize in Table 9 our departures from Raibert’s implementation, and provide further details in Sec. 4.2.1 as well as Sec. 4.2.5), our scheme enables bounding, pacing, and pronking with independent virtual legs and fewer actuators (only using radial leg extension), whereas Raibert’s reported pace and trot results used the more aggressive sequenced coordination of (Raibert et al., 1989, Fig. 6-6), as well as two additional actuators at each hip.

subsections, 4.2.2 and 4.2.3, please see Sec. 4.2.1 for an account of additional controllers introduced to coordinate other actuated and unactuated DOFs.

Touchdown detection

A major design consideration for Minitaur was drivetrain transparency, as described in Kenneally et al. (2016). In flight, we set the toe extension using a PD controller with low gains, and on physical toe-touchdown, the vertical force on the toe manifests as a deflection in the motor angles (through the well-conditioned leg Jacobian Kenneally et al. (2016)). An above-threshold deflection (corresponding exactly to an above-threshold toe force) causes the TOUCHDOWN event to be triggered. This scheme allows for touchdown detection in as little as 6 milliseconds with no additional sensors, as shown in (Kenneally and Koditschek, 2017, Fig. 4, 5). Further research is underway to establish which behaviors on the Minitaur machine are crucially dependent upon this high bandwidth proprioceptive capability.

Virtual leg groups

As (Raibert, 1986, Ch. 4) describes, we use the term “virtual leg” in this paper to refer to a group of physical legs (on Minitaur) coordinated to operate in synchrony as per the three rules detailed below. In each case, we first present our implementation, and then highlight below the similarities and differences between our implementation and that of (Raibert, 1986, pg. 92). We point out here

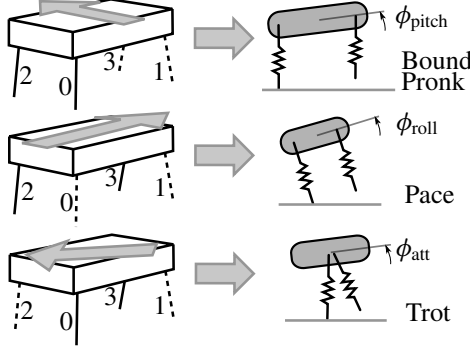


Figure 50: Virtual bipedal gaits on a quadruped. Sec. 4.2.1 discusses the feedback coordination needed for these “groupings.” On the left, the solid lines are grouped together into a single virtual leg, and the dashed lines into a second one. The solid arrow connotes the “projection” of the dynamics manifesting formally as a dimension reduction of the state space considered in the analysis. The nominal leg numbering we use is also depicted in the figure, and is helpful for interpreting the empirical data in Fig. 54–59.

that though we use the simulation paper [Murphy and Raibert \(1985\)](#) and book [Raibert \(1986\)](#) as the main expository sources of Raibert’s insights, some of the implementation details pertaining to the quadrupedal gaits demonstrated by him and his collaborators are only present in the technical report [Raibert et al. \(1989\)](#). We consider the latter as the definitive representation of “prior art” when juxtaposing with our own implementation, but refer to the book [Raibert \(1986\)](#) on occasion when the requisite descriptions are missing from the technical report.

a) Event synchronization.

Our implementation. As shown in Fig. 49, each virtual leg has an independent mode, STANCE or FLIGHT. Transitions between these modes are triggered by events: TOUCHDOWN (described in Sec. 4.2.1) and LIFTOFF (elapse of π/ω seconds since TOUCHDOWN, following the constant flow-time assumption (Table 5). The specific STANCE and FLIGHT controllers are presented next.

Comparison to Raibert. This part of our implementation is a simpler version of the “Synchronization” rule in ([Raibert, 1986](#), pg. 93). Our justification for this is our comparative numerical work in Sec. 3.5.6 showing that the qualitative effect of active toe extension is relatively minor. Additionally, feedback synchronization in flight relies heavily on the ground being particularly flat.

b) Mean-difference coordinates in stance.

Our implementation. Our analytical result of Sec. 3.5.5 showed that using only shank extension actuators, (3.60) can be applied to two stance legs to feedback-stabilize the body orientation for the in-phase (pronking template) limit cycle. Noting from (3.60) that the two legs receive equal and opposite control signals, we introduce the following “mean-difference” input coordinate change:

For a desired virtual leg radial force Υ_1 (given by (3.91)), suppose the physical radial forces commanded of the within-group legs are Υ_{1+} and Υ_{1-} in a manner we now specify. In Fig. 50, we show which legs are grouped together into virtual legs for each of the gaits discussed in this paper, as well as the leg numbering scheme we use for Minitaur. E.g., in the

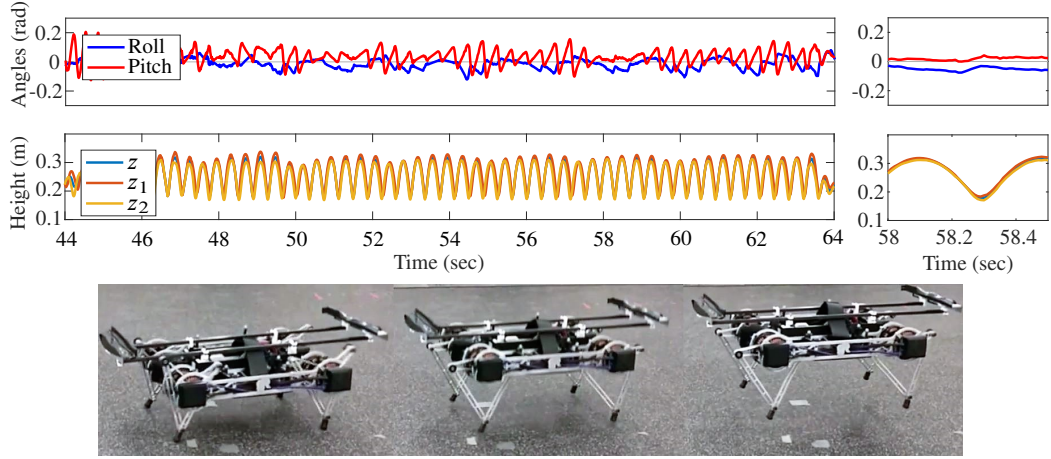


Figure 51: SC-Minitaur preflexive pronking. **Top:** Empirical data from Minitaur (Fig. 27C) in its “high-inertia” configuration (Sec. 4.2.2) showing stable preflexive pronking (note that the hip heights z_1, z_2 oscillate in phase). We compare this empirical data to our simulation models in Fig. 34. Additionally, by examining successive touchdown and liftoff times from the log file, we get statistics for the time of stance $t_f = 0.139 \pm 0.013$ seconds, and time of flight $t_f = 0.233 \pm 0.026$ seconds. The deviation in flight time is thus 11% including the initial transients, justifying our investigation into “constant flight time” in Sec. 3.5.5. **Bottom:** Snapshots of SC-Minitaur (taken roughly at bottom, liftoff, and apex) from this experiment, showing the newly attached 0.5 kg weights on either end (compared to Fig. 32) to modify κ (3.86).

bounding gait, legs “0” and “2” receive radial actuation signals Υ_{1+} and Υ_{1-} , and legs “1” and “3” receive radial actuation signals Υ_{2+} and Υ_{2-} , respectively.

Additionally, define the attitude controller for within-group stabilization

$$\Upsilon_{wg} := k_p \phi_{wg} + k_d \dot{\phi}_{wg}, \quad (4.14)$$

where ϕ_{wg} is the body angle in the plane containing the within-group legs (e.g. for bounding, ϕ_{wg} is the roll angle; for pacing, ϕ_{wg} is the pitch angle; for trotting, ϕ_{wg} is the body angle projected in the plane containing the diagonally paired legs). Then, in stance the physical legs are commanded the radial forces

$$\Upsilon_{1+} := \Upsilon_1 + \Upsilon_{wg}, \quad \Upsilon_{1-} := \Upsilon_1 - \Upsilon_{wg}. \quad (4.15)$$

We point out here the ϕ_{wg} is not visible in right column of Fig. 50 since it is the angle of the body about an axis on the plane of the page. We also observe that (4.14) is a mere copy of our previously defined attitude controller (3.60) (after Assumption 5 is incorporated), simply applied about a different axis. We define it separately here in order to be explicit about within-group feedback stabilization in the remainder of the paper.

Comparison to Raibert. This part of our implementation differs from the “Force Equalization” rule in (Raibert, 1986, pg. 93), since we explicitly command radial forces that are unequal across the leg groups and utilize this affordance for feedback attitude stabilization. A later account of Raibert’s implementation on his quadruped Raibert et al. (1989) reveals

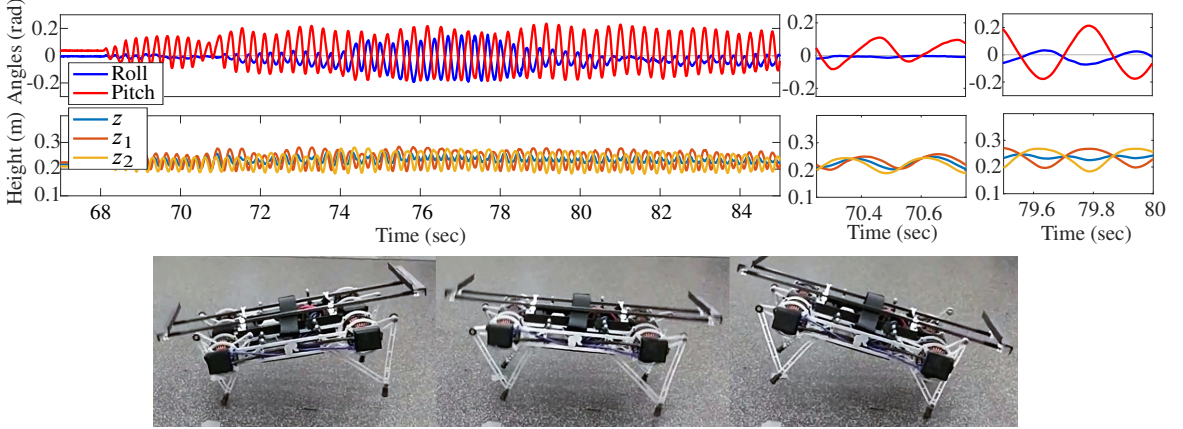


Figure 52: SC-Minitaur feedback-stabilized bounding. **Top:** Empirical data from Minitaur (Fig. 27C) in its “high-inertia” configuration (Sec. 4.2.2), but with feedback phase control (3.59), showing stable bounding (note that while in the initial transient phase (first inset), the hip heights z_1, z_2 oscillate without a specific relative phase, after some time they stabilize to being out of phase, and the pitch oscillations are much more pronounced). We compare this empirical data to our simulation models in Fig. 34, and discuss in Sec. 4.2.3. **Bottom:** Snapshots of SC-Minitaur bounding in place (roughly at front stance, aerial, and rear stance) from the same experiment.

that two additional actuators (which we don’t need with our method) are used for feedback attitude stabilization (see Sec. 4.2.5 for further details about trot implementation).

c) *Toe positioning in flight.*

Our implementation. In flight, the radial forces simply act to keep each toe at the nominal leg extension, ρ . The hip actuators are used to servo the toes to a desired absolute leg angle, θ^* using the controller described in (4.17). We furnish additional details about the hip actuation in Sec. 4.2.4.

Comparison to Raibert. This part of our implementation is equivalent to the “Positioning” rule in (Raibert, 1986, pg. 92).

In future work we plan to explore a more sophisticated version of our intra-group control such that a “virtual leg” is formally anchored in the physical leg groups transmitting ground reaction forces to the robot body, as in Saranli and Koditschek (2003).

4.2.2 Preflexive Stability

First, we leverage the preflexive stability properties analyzed in Sec. 3.5.4 and 3.5.5 to get stable limit cycles on Minitaur without any feedback coordination of the phases of the two hips. We program each of the sagittal plane legs (virtualized according to the top row of Fig. 50) as a vertical hopper, using the controller (3.5) with $w_i \equiv 0$ in (3.58).

Bounding in place

The first result we obtain is that Minitaur bounds in place (Fig. 32). In that figure we compare the resulting time-behavior of the appropriately chosen physical coordinates to simulations of the

numerical models depicted in Fig. 27, and find that $\kappa \approx 0.77$ is a good fit. This matches our expectation, since most of Minitaur’s mass is concentrated at the hips (where the motors are attached), but some mass is concentrated near the center where the battery is housed. This preflexive stability is a demonstration of our analytical result in Sec. 3.5.4, and also shows remarkable agreement of empirical data to the simulated sagittal plane biped (Fig. 27B) and only slightly more distinguishable traces relative to the slot-hopper template (Fig. 27A).

Pronking in place

In the next experiment, we artificially modify κ by attaching two weights on top of Minitaur (we deem the modified model “SC-Minitaur” or strongly-coupled Minitaur). These outrigger payloads have a total mass of 1 kg, are added at a distance of 0.37 m from the center of mass, and primarily serve to increase the rotational inertia about the center of mass (Fig. 51, bottom). Using the parallel axis theorem, the resulting inertia is

$$\begin{aligned} i'_b &= \kappa m_b d^2 + 1 \cdot 0.37^2 =: \kappa'(m_b + 1)d^2 \\ &\implies \kappa' = 1.149, \end{aligned} \quad (4.16)$$

using values for m_b , d and κ mentioned in Sec. 4.2.2.

We find that the modified SC-Minitaur exhibits a preflexively stable pronking in place, as shown in Fig. 51. We reiterate to emphasize that the controller was not modified between Fig. 32 and Fig. 51, only the physical parameters of the body. This preflexive stability is an empirical demonstration of our stability analysis in Sec. 3.5.5.

Qualitatively, we observe that preflexively, the legs z_i are in phase in SC-Minitaur Fig. 51, but out of phase in unloaded Minitaur (Fig. 32 and Fig. 54). We did not include z_2 in the top row of Fig. 32 for clarity, but the different asymptotic relative phases can be seen by comparing the zoomed-in panels in Fig. 32 to Fig. 51; specifically, the reader should compare the relative phases of the red and yellow traces. This empirical outcome is expected from our analytical results of Sec. 3.5.4 (preflexive bounding) and Sec. 3.5.5 (preflexive pronking), and the simulation results generated from our slot hopper model in Fig. 30. Additionally, the pitch shows a pronounced oscillation in both Fig. 32 and Fig. 54 (instances of bounding), but the magnitude of the pitch is very small in Fig. 51 (instance of pronking).

4.2.3 Feedback Synchronization

Simulations in the companion paper showed that the coordination controllers (3.59)–(3.60) can establish either bounding or pronking limit cycles in the decoupled slot hopper. In this paper, we show that the same controllers can reinforce or disturb the slot hopper’s preflexive stability (proved in Sec. 3.5.2) when applied to a slot hopper simulation (Fig. 30). In this subsection, we now apply the feedback phase control ideas of Sec. 3.5.1 to attempt to disrupt the limit cycles of Sec. 4.2.2.

We first point out that the two Minitaur configurations listed in Sec. 4.2.2 are indicated with the vertical green (WC-Minitaur, Fig. 27C) and magenta (SC-Minitaur, Fig. 51) lines in Fig. 30. Our empirical trials reveal that the phase control (3.59) is able to overcome the preflexive stabilization in the magenta configuration (see Sec. 4.2.3 below) to disrupt the mechanically entrained pronking in favor of the “commanded” bounding gait. On the other hand, more aggressive feedback

coordination (3.60) is required to overcome the preflexive stability in the green configuration (see Sec. 4.2.3 below) to disrupt the mechanically entrained bounding in favor of the “commanded” pronking gait.¹¹ We remind the reader that these experiments are recorded in the video attachment as well.

Using phase control to disrupt preflexive pronking and impose bounding

We implement the feedback controller (3.59) on SC-Minitaur, and plot the results in Fig. 52. Compared to the results with the preflexive control only (Fig. 51), a pitch oscillation can be observed, and furthermore, the second row reveals an alternating front/rear touchdown in z_1 and z_2 , indicating that the anti-phase limit cycle characteristic of bounding has been stabilized. In the region $t \in [74, 79]$ seconds of Fig. 52, the robot rolls in an underdamped fashion due to the attitude controller applied in the frontal plane (4.14) not being tuned ideally. The sagittal plane behavior is mostly unaffected by this rolling.

We can conclude that the κ of SC-Minitaur (magenta line in Fig. 30) allows the phase control (3.59) to overcome the preflexive control analyzed in Sec. 3.5.5. We display this data point in Fig. 30 as well.

An additional example of the application of phase control can be found in the application to the pacing gait presented in Sec. 4.2.5. However, note that this application is beyond the analytical scope of the present paper, since Minitaur does not possess hip ab/adduction joints. Consequently, the body-leg angle is rigidly set at $\pi/2$, and (a) the legs cannot be positioned vertically with respect to the ground, and (b) ground reaction forces are not always directed vertically as they are in the slot hopper.

Using attitude control to disrupt preflexive bounding and impose pronking

The phase controller (3.59) is not successful in overcoming the preflexive control in WC-Minitaur (green line in Fig. 30), indicating that the preflexive controller is “stronger.” We apply the more aggressive attitude-servoing controller (3.60) in order to attempt to stabilize an in-phase limit cycle (pronking).

The results in Fig. 53 show an in-phase pattern for z_1, z_2 , indicating stability of the in-phase limit cycle. Moreover, the magnitude of the body pitch has been reduced to approximately 0.15 radians, compared to the much larger pitch oscillations seen in the bounding trial in Fig. 32. We display this data point in Fig. 30 as well.

4.2.4 Parallel Template Compositions for Translation and Rotation of the CoM

Raibert (1986) pioneered a kind of empirical *composition*—decoupled controllers, each designed to stabilize an isolated 1DOF “template plant,” which, when utilized in tandem, empirically stabilize a high-DOF body. The empirical success betrays the difficulty in obtaining provable guarantees,

¹¹It is worth noting in passing that there seems to be no analogous path to destabilizing the very strongly preflexive pronking regime (the far right hand side of Fig. 30 with κ values well beyond unity) because it is not clear what configuration setpoint to furnish—an observation that might lead us toward consideration of feedforward excited (“clocked”) gaits Haynes et al. (2011) or potentially, a refinement via appeal to higher period orbits of the “factored map” expressions.

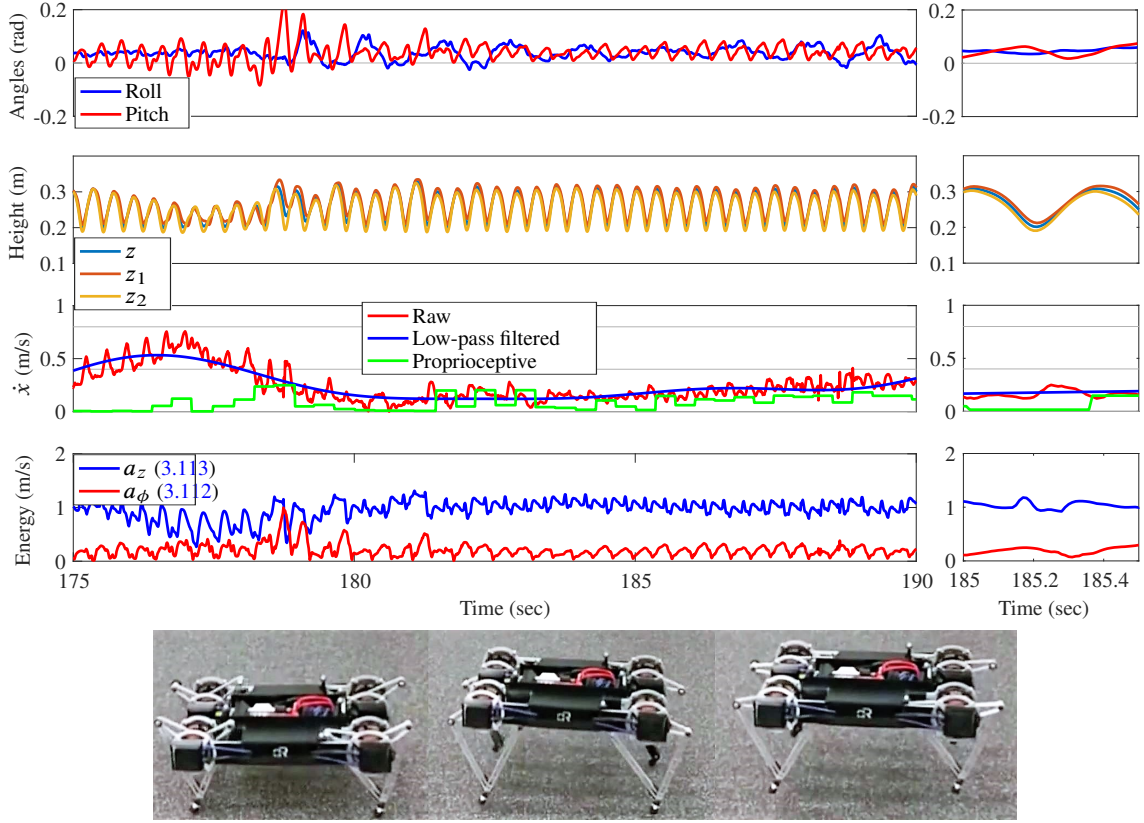


Figure 53: Minitaur feedback-stabilized pronking. **Top:** Empirical data from Minitaur (Fig. 27C) in its default configuration, but with feedback attitude control (3.60) stable pronking (note that the hip heights z_1, z_2 oscillate in phase). As described after (3.113), the “energy” coordinates have units of speed. See Sec. 4.2.3 for more discussion. **Bottom:** Snapshots of WC-Minitaur pronking (taken roughly at bottom, liftoff, and apex) from this experiment.

however: coupling in mechanical systems can move energy between the different compartments, either stabilizing or destabilizing the template plant.

In Murphy and Raibert (1985), the following quote appears shortly after the one we have used before: “*there was a limit on forward velocity. As the model bounded faster, the height of centre of gravity of the body decreased along with the magnitude of its angular oscillation. These two factors reduced the ground clearance of the foot as it swung forward. Eventually, the model stubbed its toe, tripped and fell.*” This anecdote confirms the difficulties of composing fore-aft control with the vertical energization (3.5) and coordination (3.59)–(3.60) discussed thus far. This motivates further analytical work to discover and prove stability of feedback-stabilization of other DOFs, but we restrict the scope of this paper to empirical composition of controllers. We find empirically that the simplicity of our template controllers (3.5)–(3.60) affords robustness against large amounts of coupling energy (arising from the significant cross talk injected by these erstwhile decoupled controllers) before destabilization.

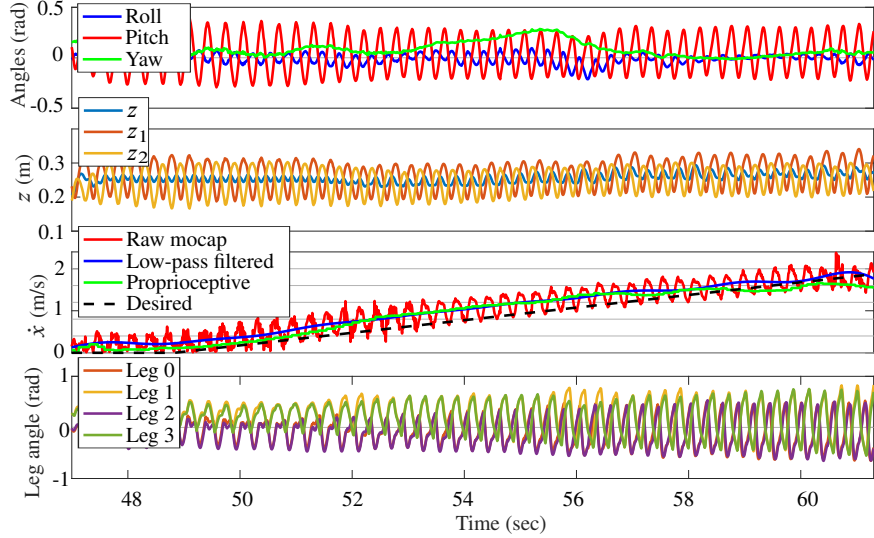


Figure 54: Minitaur preflextive bounding. Empirical data from Minitaur (Fig. 27C) exhibiting bounding with preflextive coordination (pitch) control (Sec. 3.5.4), feedback roll control (3.60) (roll angle is also displayed in the first row), moving at a range of commanded forward speeds (Sec. 4.2.4) up to 4.8 body lengths / sec, as well as yaw rates (Sec. 4.2.4), controlled using a parallel composition of decoupled controllers. See the last paragraph of Sec. 4.2.4 for discussion. Lastly, numerical post-processing of this data reveals that despite the strong fore-aft and yaw perturbations in this trial, the stance duration is 109 ± 7.5 ms (mean and standard deviation): a 6.5% deviation. As in [Raibert \(1986\)](#), this motivates our constant stance duration assumption in Table 5.

Fore-aft speed control

We adapt the monopodal fore-aft speed controller described in [Raibert \(1986\)](#), and we review it briefly here. Our decoupled control strategy (3.5) already encourages thinking of sagittal plane Minitaur as a composition of a “front” and “rear” monopod, and so we apply the fore-aft control to each monopod independently. The control input is the touchdown angle of the virtual leg in flight, which is easy to actuate with very little energetic cost by using the hip actuators, since the toes are light. Specifically, we set

$$\ddot{\theta}_i = k_p(\theta^*(\dot{x}) - \theta_i) - k_d \dot{\theta}_i, \quad (4.17)$$

where the desired touchdown angle, $\theta^*(\dot{x})$ is defined as a function of the current speed \dot{x} according to the “neutral point” ideas of [Raibert \(1986\)](#),

$$\rho \sin(\theta^*(\dot{x})) = -\frac{\pi \dot{x}}{2\omega} + k_{\dot{x}}(\dot{x}^* - \dot{x})$$

for $i \in \mathcal{I}$, where note that π/ω is the stance duration (assumed constant as in Table 5). Recall that θ_i is the *absolute* leg angle, and an estimate of the body pitch, ϕ , is required as well to command the leg angle correctly.

An important part of this controller is an estimate of the current speed, \dot{x} . We obtain a proprioceptive forward speed estimate in Minitaur by using encoder-measured joint angles and velocities

together with the forward kinematics $g : \mathbb{R}_+ \times S^1 \rightarrow \mathbb{R}^2$ of the leg,

$$\dot{x} = Dg(r_i, \theta_i) \begin{bmatrix} \dot{r}_i \\ \dot{\theta}_i \end{bmatrix} \quad (4.18)$$

for $i \in \mathcal{I}$, where Dg is the leg Jacobian derived in (Kenneally et al., 2016, eqn. (6)).

Applying this controller to preflexively bounding Minitaur (shown bounding in place in Fig. 32) along with a roll controller (4.14) to stabilize out-of-sagittal-plane motion, results in fore-aft motion as shown in Fig. 54, while not disturbing the front/rear preflexive phase coordination at a range of speeds. The desired speed \dot{x}^* is set by an external signal (often an operator, but in this case we used a ramp function showed in dashed black). In the last row of Fig. 54, we use a 3Hz cutoff filter to low-pass the raw speed measurements from motion capture. The step rate of Minitaur (each front or rear stance is counted as a “step”) is about 3Hz, and a distinct oscillation can be noticed at around this frequency in the forward speed. We hypothesize that this is an artifact of imperfect tuning between the front and rear hips; a full analysis of the fore-aft stability (that we defer to future work) should illuminate this issue further.

Even with this decoupled compositional control, it is still possible to attain traveling speeds of 1.92 m/s (4.8 body lengths / second, or 11 leg lengths / second), comparing favorably to quadrupeds of a similar size (as listed in Sprowitz et al. (2013a)), keeping in mind that Minitaur is a general-purpose quadruped with onboard power. Further, since this gait is the result of a smoothly parametrized family of control policies (3.5), (4.14) (rather than, e.g., empirically optimized parameter set points as in Weingarten et al. (2004)), stable bounding can be accessed at a continuum of traveling speeds and yaw rates (as demonstrated in Fig. 54), as well as vertical height (shown below in Sec. 4.2.4). We posit that the limit to even higher speeds in these trials is primarily due to:

- a) *inaccuracy in \dot{x} estimate*: as observed in Fig. 54, the proprioceptive speed estimate (4.18) systematically underestimates the actual speed of the robot past around 1.5 m/s. This usually results in incorrect toe placement, and the robot stumbles forward. The reason for this inaccuracy could be toe slip (see next point) or minor delays in estimation of touchdown and liftoff (which are on the order of 5-10 ms as stated in Sec. 4.2.1);
- b) *loss of traction*: yaw correction in stance (Sec. 4.2.4) requires a large amount of friction, and especially at higher speeds small amounts of toe slip can cause failure;
- c) *destabilization of pitch oscillation*: the preflexive stabilization we analyzed in Sec. 3.5.4 maintains the desired pitch oscillations for a range of speeds, but as seen between $t \in [52, 56]$ seconds in Fig. 54, the pitch oscillations can reduce in magnitude, or worse, get out of synchronization with the leg touchdowns when a lot of energy is injected at higher traveling speeds.

The last point motivates us to incorporate the fore-aft degree of freedom in our analysis in the future, as well as to augment the bounding coordination with additional coordination control.

While the phase controller (3.59) is successful at disrupting preflexive pronking in SC-Minitaur (Sec. 52), it is unable to disrupt preflexive bounding (as we observed in Sec. 4.2.3). Likewise, we did not observe any empirical benefit to the application of (3.59) to “augment” Minitaur’s preflexive bounding stability (as analyzed in Sec. 3.5.4). However, we posit that for a physical machine with $\kappa \approx 1$ (no preflexive stability), (3.59) could be used to feedback-stabilize bounding (as analyzed in De et al. (2016)).

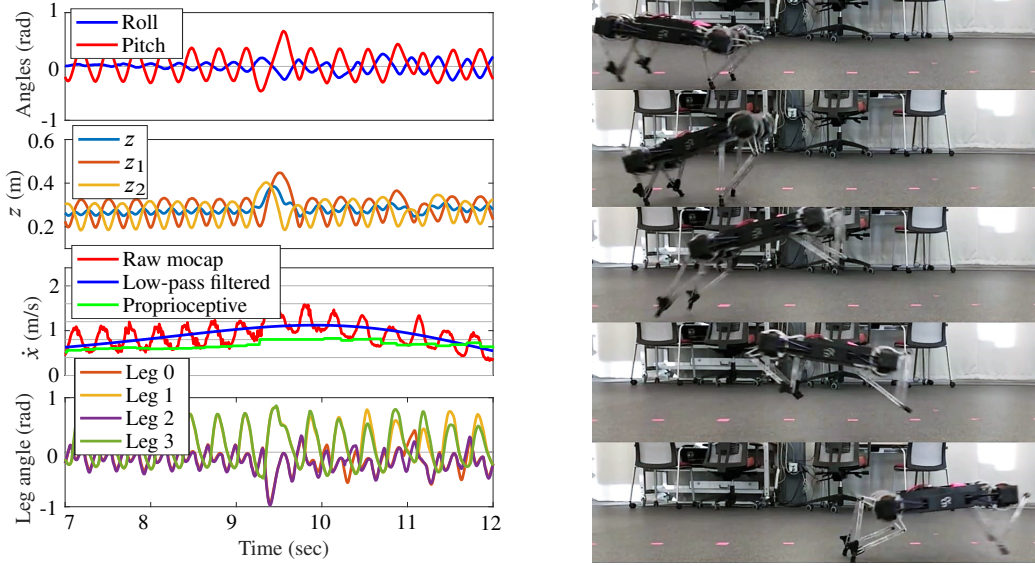


Figure 55: Minitaur bounding leap. **Left:** Empirical data from Minitaur (Fig. 27C) exhibiting bounding (Sec. 4.2.4), with a discrete “leap” command send at $t = 9$ seconds (higher desired vertical energy for a single stride at both hips) resulting in a vertical displacement of the center of mass while bounding. **Right:** Snapshots of WC-Minitaur performing a bounding leap, showing that this simple strategy allows the robot to clear a gap larger than 1.5 times its body length.

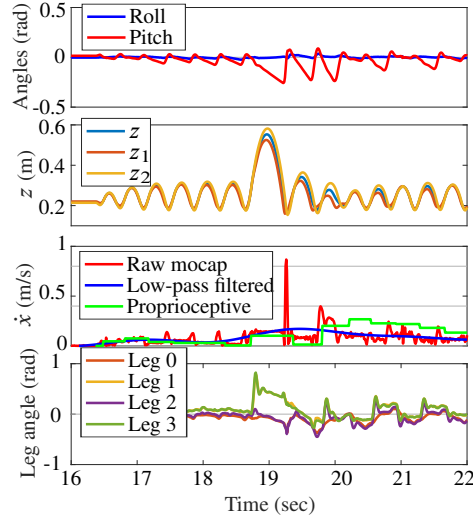


Figure 56: Minitaur pronking leap. Empirical data from Minitaur (Fig. 27C) exhibiting pronking (3.60), with a discrete “leap” command send at $t = 18.5$ seconds (higher desired vertical energy for a single stride at both hips) resulting in a vertical displacement of the center of mass while pronking.

The fore-aft control above is also applied to pronking (Fig. 53) as well as trotting (below, in Sec. 4.2.5) to obtain modest traveling speeds of 1 and 2 body lengths / second respectively. The inaccuracy in the proprioceptive speed estimate was much larger in these other gaits, so we believe

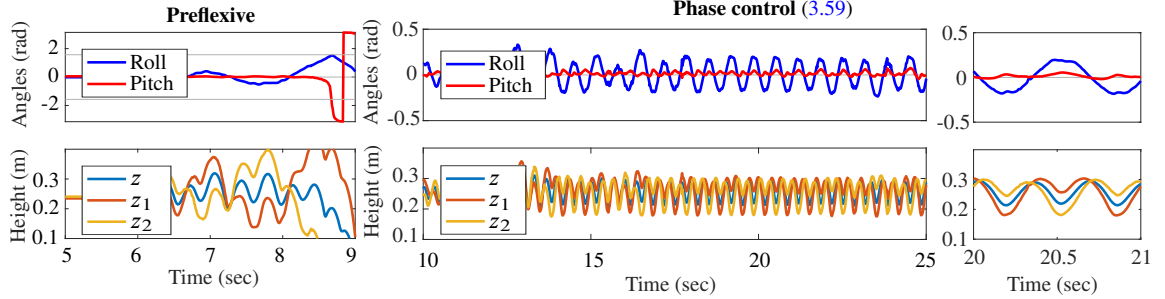


Figure 57: Minitaur preflexive and feedback-stabilized pacing. Empirical data from Minitaur (Fig. 27C) with decoupled vertical hopping controllers applied to “left” and “right” virtual hips, revealing no preflexive stability (**left**) resulting in a roll over (note faint horizontal lines are at $\pm\pi/2$, and the IMU Euler angles pass through a parameterization singularity), but a stable roll oscillation (**center, right**) with our feedback phase controller (3.59). The zoomed-in segment (**right**) reveals interesting comparisons to preflexive (Fig. 32) and forced (Fig. 52) sagittal plane bounding. See Sec. 4.2.5 for discussion.



Figure 58: Snapshots of pacing in place (taken roughly at left stance, aerial, right stance) from the experiment in Fig. 57(**center, right**).

that these gaits can travel at much faster speeds with some more tuning. Since the focus of this paper is the coordination control of the z, ϕ degrees of freedom, we defer to future work the analysis of vertical and fore-aft coupling that would facilitate extracting faster translational speeds from these other gaits.

Yaw control while bounding

We also compose an empirically motivated yaw controller, that makes use of the available hip torques in stance. Specifically, the two legs comprising the “virtual leg” in stance apply differential hip torques in order to impart a yawing moment on the body (in the horizontal plane).

If $\zeta \in S^1$ is the yaw angle, $\dot{\zeta}^* \in \mathbb{R}$ is the desired yaw rate, and τ_j is the hip torque applied to the left and right hips in stance, we set

$$\tau_j = (-1)^j k_{\dot{\zeta}} \dot{\zeta}^* \quad (4.19)$$

where $j \in \{\text{left, right}\}$. Note that we intentionally use a different index than $i \in \mathcal{I}$ used in Sec. 3.5.1 and throughout the paper to refer to the two virtual legs, since in (4.19) we are referring to legs grouped within an erstwhile “single” virtual leg.

This is a different strategy than the horizontal-plane toe placement strategy in [Raibert et al. \(1989\)](#), which requires 2DOF control of toe position in the horizontal plane (an ab/adduction joint)

and is thus inaccessible to Minitaur.

This strategy results in controllable yaw in bounding Minitaur. As an example, in Fig. 54, the yaw of the robot begins to drift at around $t = 54$ seconds, and the yaw controller (with desired yaw being supplied by an operator) allows the robot to be brought back on course. As expected, this introduces a rolling disturbance that can be seen at around $t = 56$ seconds, but the roll is eventually stabilized by the attitude controller (4.14).

Further characterization of the fore-aft and yaw controllers is needed to argue that bounding Minitaur anchors a unicycle in the horizontal plane; we defer this topic to future work. Experiments in the lab are already underway employing higher-level control schemes designed for unicycle plants, such as [De and Koditschek \(2013\)](#), [Lopes and Koditschek \(2007\)](#).

Running leaps

As mentioned in Sec. 4.2.4, our template-based control (3.5) affords the operator the ability to control the height setpoint a^* through k_a . Even though in our analysis we have kept a^* constant, in practice, we can increase a^* for a single stride to get a running leap. This results in a large perturbation off the limit cycle (both in bounding and pronking), but the large stability basin of the (preflexive or feedback) coordination of Sec. 4.2.2–4.2.3 helps restore the nominal gait pattern within 1-2 strides.

Fig. 55 shows a bound leap: though there is a large pitching disturbance before the body recovers, the fore-aft speed of the body as well as the z_1, z_2 stepping pattern is maintained through the leap, demonstrating the large stability of basins of the template controllers. Fig. 56 shows a pronk leap at around $t = 18.5$ seconds, where again a large pitching disturbance is introduced by the leap, but the z -oscillations are not disturbed.

4.2.5 Pacing and Trotting

So far we have presented data from Minitaur bounding and pronking. However, moving beyond the sagittal plane (while still only using the controllers (3.5), (3.59) and (3.60) as applicable), Minitaur is able to exhibit the remaining virtual bipedal gaits: pace and trot. A pictorial description of these gaits from the virtual leg viewpoint is in Fig. 50.

Our implementation of pacing and trotting on a physical machine differs from that reported in [Raibert et al. \(1989\)](#), in ways that we summarize below:

- a) we are able to exhibit these gaits while using fewer actuators: only shank actuators in our case as compared to two actuators (fore-aft and ab/adduction) at the hip ([Raibert et al., 1989](#), eqs. (6.3), (6.4)) due to the analytical insights from [De et al. \(2016\)](#) suggesting the use of the w_i term in (3.58) for phase (3.59) or attitude (3.60) control;
- b) the state machine in ([Raibert et al., 1989](#), Fig. 6-6) forces a prescribed alternating stance / flight sequence, whereas our state machine (Fig. 49) bears more resemblance to Raibert's "independent" version in ([Raibert et al., 1989](#), Fig. 6-11) which is reportedly only used for bounding and pronking.¹² One advantage of using a less prescriptive state machine is that

¹²The reported "pronk" observed with the independent state machines in [Raibert et al. \(1989\)](#) is possibly due to the added hip actuation stabilizing the attitude DOFs. Per our analytical result of Sec. 3.5.4, Raibert's quadruped ([Raibert et al., 1989](#), Table 6-1) with only shank actuation would exhibit preflexive bounding stability, as corroborated by the prior simulation study in [Murphy and Raibert \(1985\)](#).

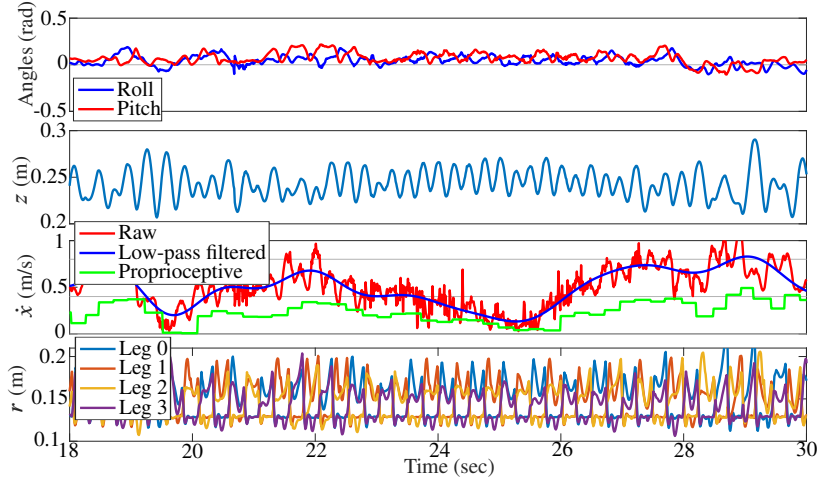


Figure 59: *Minitaur feedback-stabilized trotting.* Empirical data from WC-Minitaur exhibiting trotting implemented by commanding two diagonally paired virtual legs as vertical hoppers (3.5), but with added coordination logic (Sec. 4.2.5).

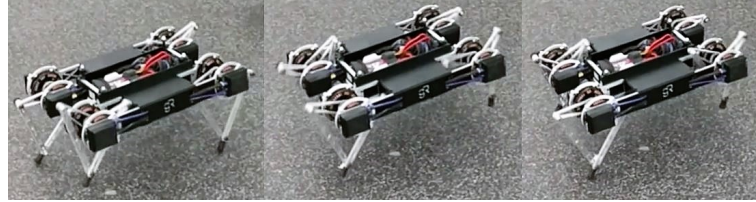


Figure 60: Snapshots of trotting showing legs 1 and 2 (numbering shown in Fig. 50) in stance (left), aerial (center), and then legs 0 and 3 in stance (right). Going from the left panel to the center panel, the active retraction of legs 1 and 2 (as described in Sec. 4.2.5) is also apparent. These snapshots are from the experiment in Fig. 59.

unexpected double stance (caused by unexpected ground contact on rough terrain) is handled gracefully, whereas it falls completely outside the logical jurisdiction of (Raibert et al., 1989, Fig. 6-6).

Pacing

We find that in the frontal plane, when the decoupled controller (3.5) is applied to the left and right virtual legs, Minitaur does not preflexively exhibit any coordination. This leads us to believe that it lies in the “chaotic” region on Fig. 30. The left column of Fig. 57 reveals typical preflexive behavior: a fall within a few steps.

However, when our phase controller (3.59) is applied (suggested by our analytical insight from De et al. (2016)), a stable anti-phase limit cycle emerges in the frontal plane. We reiterate here that since Minitaur does not have an ab/adduction joint, the virtual hips cannot be moved by using hip torques in the frontal plane. Thus, this stabilization is established only using the leg extension actuators, using the phase control ideas we have described in Sec. 3.5.1.

Trotting

In a trot, the virtual hips are located close to the center of mass [Raibert \(1986\)](#), effectively making d very small. Consequently, from (3.86), κ is very large, and as Fig. 30 shows, the in-phase limit cycle is preflexively stable.

This preflexive stability is very strong, and phase control (3.59) as in Sec. 4.2.3 is unable to produce a trot. The trot implementation in [Raibert et al. \(1989\)](#) used a sequenced state machine, logically forcing alternating virtual leg stances. We have employed a slightly less aggressive strategy (Fig. 49), where the virtual leg state machine is now updated to include 3 possible states: STANCE, FLIGHT, and RETRACT. For $i \in \mathcal{I}$, when virtual leg i goes through its liftoff event, it is placed in the RETRACT state where it is kinematically prevented from touching down. When leg $i + 1$ has lifted off, leg i is moved from RETRACT \rightarrow FLIGHT, where it can detect the touchdown event as usual.

The state machine above only allows a single leg to be in STANCE at any time instance, thus only allowing for trot gaits with an aerial phase. When implemented on Minitaur, we observe a stable trotting pattern as shown in Fig. 59.

The details of the attitude and speed control for the trot gait (both formally and empirically) deserve a more careful examination than is possible within the scope of this paper, such as a formal anchoring of the virtual leg to a monopodal template as was done for RHex in [Saranli and Koditschek \(2003\)](#); we defer this to future work.

CHAPTER 5 : Conclusion

This concluding chapter presents a variety of informal observations about the reported work and discusses some specific directions of future work that are either already or soon-to-be underway.

5.1 Hardware: Actuator Design using Dynamic Models

Motivation for future work While past literature has used Newton's laws to create useful models of manipulator dynamics, metrics for manipulability [Murray et al. \(1994\)](#), and their role in platform-level design [Asada and Youcef-Toumi \(1987\)](#), currently available models are still deficient in a number of ways.

- *Models of motor behavior are deficient, requiring post-fabrication empirical characterization (e.g. 2.1.2):* We aim to leverage existing dynamic models of motors [Maxon Motors \(2010\)](#), explicitly exposing their relation to the motor design parameters (Sec. 2.1), time-dependent characteristics, but in addition accounting for critical non-linear effects such as flux saturation, thermal dissipation, position-dependence of torque (ripple).
- *The thermo-electric performance of the driving electronics is currently treated as a “black box,” even though their dynamic characteristics are relevant for high-bandwidth actuation and sensing:* We aim to create dynamic models of the driving electronics, incorporating the effects of switching losses (PWM frequency selectable in software, trading off switching losses and control bandwidth), Joule losses, torque response (including characteristics of the control and communication software), as well as thermal dissipation;
- *Modeling of transmission bandwidth, and their relation to friction and compliance:* Recent studies have shed some light on the inner workings of gearboxes [Wang and Kim \(2015\)](#) and suggested a useful notion of bandwidth [Wensing et al. \(2017\)](#). We aim to leverage these studies to develop usable dynamic models of transmission bandwidth incorporating both continuous effects (springs, viscous, and static friction), as well as discrete effects (impacts) [Kenneally and Koditschek \(2017\)](#).

Desired outcome: model-driven design Leveraging usable models of these components should allow for principled design and selection for precisely defined criteria such as

- static performance (including stalled as well as constant-speed performance), typically studied under conventional motor selection, but now coupling the design space of the motor with the electronics;
- platform actuation bandwidth including dynamics of all the components (as suggested above), as well as knowledge of time-discretization in various control loops;
- platform sensing bandwidth including the role of both continuous dynamics as well as impact dynamics in the transmission rates of information and its tradeoff with power expenditure [Kenneally and Koditschek \(2017\)](#); and
- dynamic robot performance utilizing some of our analytical conclusions about the approximate dynamic behavior of the composed robot bodies (Chapter 3), or simplifications thereof, as a dynamic task specification.

5.2 Hybrid Averaging

Our applications of the Fig. 40 procedure in Sec. 3.7 are the first of many potential hybrid averaging stability results obtained using Thm. 4. As we have stated before, work currently in progress suggests straightforward applicability to (a) planar tail-energized hopping with the 3 DOF tailed SLIP system; and (b) planar bounding with the 3 DOF sagittal plane biped system; both listed in Fig. 1. We wish to also apply this result in the near future to:

- horizontal-plane locomotion on the 3 DOF lateral leg spring (LLS) model Schmitt and Holmes (2000);
- tail-energized hopping on the 4 DOF planar tailed monoped of Fig. 1, representative of our Jerboa results in Sec. 4.1;
- hip-energized hopping on the 4 DOF planar tailed monoped of Fig. 1, representative of our numerical results in Sec. 4.1.1;
- tail-energized spatial hopping on a spatial tailed monoped of Fig. 4 (right), suggesting control and design parameters for spatial hopping on the Jerboa;
- spatial bounding / pronking / trotting / pacing on the spatial quadruped of Fig. 27D, suggesting control parameters for Minitaur gaits;

etc. In addition, we anticipate applicability to even higher DOF models, potentially leveraging other symmetries than the two we have considered so far—virtual biped (Sec. 3.3) and time-reversal (Sec. 3.6)—for multilegged locomotion, as in Golubitsky et al. (1998).

5.2.1 Eliminating Inconclusive Applications of Hybrid Averaging

One drawback of the current version of our procedure for correct-by-design synthesis (Fig. 40) is that it can be inconclusive. So far, we don't have a formal result about the exact classes of systems for which the procedure will be guaranteed to be conclusive, but in our usage of Thm. 4, we have observed the following potential roadblocks, and speculate here on how they may be eliminated in future work:

Incompatible assignment of body states, actuators, and design parameters to templates'
In this thesis we have not explicitly considered design parameters or actuator configuration, instead modeling both templates (Sec. 3.1) and bodies (3.140) as closed-loop dynamical systems. In the next two discussion subsections, we detail our plans on extending our closed-loop theory in this regard, potentially enriching the procedure (Fig. 40) to either search for the correct assignment, or guarantee infeasibility.

Inadequate template library We discuss this topic in detail in Sec. 5.2.6.

Reset map linearization not $\mathcal{O}(\varepsilon)$ -Lipschitz The condition on S_0 in Thm. 4(ii) (inherited from Thm. 2(i)) has resulted in the neutral point stepping controller to be unaverageable in Sec. 3.7.2. Since we have used this controller with extensive empirical success (Chapter 4), there seems to be a discernible “logic gap” between the sufficient and necessary conditions pertaining to the reset Lipschitz condition. Further work is needed to ascertain if the neutral point controller is an “outlier” or if there are large classes of reset maps with appealing empirical behavior in robotics that similarly fail our current averageability criteria.

At present, an easy “fix” for this roadblock does not seem forthcoming, since the IFT usage in smooth dynamical averaging theory (Thm. 1) guarantees that a fixed point of the averaged

system, p_0 , is $\mathcal{O}(\varepsilon)$ away from a fixed point of the original system, $p_\varepsilon = p_0 + \mathcal{O}(\varepsilon)$, and if the reset linearization DR does not have an $\mathcal{O}(\varepsilon)$ Lipschitz constant, its contribution to return map stability (see proof of Thm. 2) may be drastically different in the original vs. averaged systems.

Nonetheless, since the neutral point controller is a specific instance of a deadbeat controller (as we show in Sec. 3.7.2), a promising direction of inquiry is to incorporate (partially) deadbeat resets as a special class of reset maps in our switching averaging theorem (Thm. 2) and attempt to leverage any analytical simplifications available therein.

5.2.2 Control Averageable Systems

The work presented here has assumed closed-loop templates, such that the available freedom at composition-time only allows for tuning of parameters. As an analogue of control Lyapunov functions (CLFs) Ames et al. (2014), we would like to explicitly incorporate the controller in the analytical procedure (Fig. 40). In order to do so, let us replace (3.140) ($\dot{\mathbf{y}} = F_{\mathbf{y}}(\mathbf{y})$) by

$$\dot{\mathbf{y}} = F_{\mathbf{y}}(\mathbf{y}, u), \quad (5.1)$$

i.e. the control input is listed as an explicit parameter.

With this modification, we expect that application of hybrid averaging to (5.1) will allow greater freedom in selection of control strategies for composition than the mere selection of constant parameters. Some potential benefits of allowing for this greater freedom include:

Analytical guarantees invariant to control strategy Instead of obtaining parametric limits on the control signal, we might obtain functional constraints. We expect constraints (or at least constraints that are sufficient if not necessary) will involve symmetry (Def. 2). This would allow us to prove, for instance, that the stability of some of our hopping compositions are independent of if Raibert’s “thrust at bottom” strategy Koditschek and Buehler (1991), Raibert (1986) is used or our “active damping” (Sec. 3.5).

Optimal controllers If the averaging conditions could suggest constraints for the control signal, the control synthesis problem might then be posed as an optimization problem on the averaged system. We would expect the simpler averaged system to allow for more efficient, and faster, search results.

5.2.3 Assignment Problem: Toward Morphological Reduction / Computation

Our work in Chapter 3 has not made any significant contributions in relation to the physical aspects of the template embedding in the composed body. As stated in Sec. 1.2.1, this includes (broadly) assignment / mapping of morphological parameters between the body and the template on one hand, and mapping control strategies from the template to the body on the other.

Specific instances of these morphological mappings include

Coordinate projection from body to template Suppose

$$\mathbf{y}_t = \pi_t(\mathbf{y}_b)$$

is a projection from body coordinates to template coordinates. We emphasize that π_t acts

before the subsequent coordinate changes to convert the physical template coordinates to oscillator coordinate (i.e. the template coordinate change from Sec. 3.1 is a property of the template itself, logically independent of π_t , a property of the body). In our work in this thesis, these projections have been nothing more than selections of some of the physical body coordinates, e.g. the z_1 coordinate of the slot hopper (Sec. 3.5) is mapped directly to the ζ vertical coordinate of the vertical hopper template (Sec. 3.1.1). We are intrigued by the possibility of a less rigid change of coordinates for π_t .

Parameter pullback A distinct *morphological reduction* map, Ξ maps parameters in the body to corresponding parameters in the template [Libby et al. \(2015\)](#), i.e.

$$p_t = \Xi_t(p_b).$$

A concrete example appears in our mapping of “mass” and “gravity” parameters in (3.91), such that the vertical hopper (template) control signals could be applied to the slot hopper (body). This map affords several exciting research prospects, such as an analytical study of allowable parameters (obstacles in parameter space) in the body from feasible parameter regions in the template. As an example, it may allow us to formalize questions such as *when is a “heavy toe” too heavy to allow Raibert’s decoupled stepping and pitch controllers (Raibert, 1986, Chapter 2) to work?*¹ Additionally, if we can establish a smooth dependence of stability criteria on parameters (for instance, in the analytical averaged return map obtained in Thm. 4) we may simply differentiate with respect to parameters to find their local optima (within the feasible region). More formally, instead of (5.1), we have

$$\dot{\mathbf{y}} = F_{\mathbf{y}}(\mathbf{y}, u, p). \quad (5.2)$$

Controller pushforward In the other direction, the controller (feedback) function must be mapped from template to body in a manner cognizant of the specific configuration of the actuator on the robot body. For instance, in our tail-energized hopping experiments (Sec. 4.1), the vertical hopper control input u_v (Sec. 3.1.1) is generated not by an actuator in the leg shank, but using the tail.

More formally, if $u_t(\mathbf{y}_t)$ is the template controller and π_t^* maps control signals from template to body, we may find the body actuator signal as

$$u_b(\mathbf{y}_b) = \pi_t^*(u_t(\mathbf{y}_t)) = \pi_t^* \circ u_t \circ \pi_t(\mathbf{y}_b). \quad (5.3)$$

5.2.4 Application to Return Map Approximation

One of the most exciting prospects for our averaging theory is the ability to get a good return map approximation with relative ease. As an example, in Sec. 3.7.2, we produced a superior return map approximation using averaging that far outperformed that of [Raibert \(1986\)](#) in selecting the neutral point, motivating a comparison of our general approximation technique to specific approximations of SLIP stance dynamics [Geyer et al. \(2005\)](#), [Sarang et al. \(2010\)](#). Future applications may include

¹Raibert placed a “balance beam” on his planar hopper in order to make the body inertia larger, effectively making the toe massless, in order to eliminate the “heavy toe” coupling toe swing dynamics (for fore-aft speed control) with body orientation.

reactive planning incorporating (iterations of) the controlled return map approximation, in order to plan footsteps while running.

5.2.5 Averaged Anchoring

We have not yet formalized a notion of averaged anchoring, but we observe (for instance) that the averaged SLIP energy dynamics (3.161) is a cross product of averaged isolated (decoupled) vertical hopper / compliant inverted pendulum dynamics, i.e. the *averaged* vector fields (and not their unaveraged versions, as posited in [Full and Koditschek \(1999\)](#)) are conjugate. This suggests a notion of averaged anchoring, as conjugacy of averaged vector fields.

The potential applications of averaged anchoring include finding reduced (averaged) CoM behavior of the spatial quadruped while executing its gaits (Sec. 4.2), in order to treat it as a horizontal plane agent for higher-level navigation.

5.2.6 Template Discovery

The templates are crucial in the sense that in our paradigm (Sec. 1.1.1), the behavior of the composed body must be approximated by a “product” of template behaviors. As a result, the template dynamics must express the requisite complexity to capture all elements of the body’s closed-loop dynamics. We anticipate that templates could be learned from data, in a way that is similar to the search for manipulation primitives / synergies from data [Todorov and Ghahramani \(2004\)](#). We expect that template plants / controllers can then be found by analyzing the reduced-dimensional template dynamics (as described in Sec. 5.2.2 above).

The benefits of data-driven template discovery would include a large library of known primitives, alleviating one source of inconclusive averaging results. In addition, a large “grammar” of known templates would accelerate the generation of previously unknown behaviors, found autonomously using our composition rules of Fig. 40 (or extensions thereof).

5.3 Design Paradigm

5.3.1 Feedforward vs. Feedback, Central vs. Distal

As described in the introduction, our control algorithms have had the characteristics of being highly

- feedback-driven—template control signals (Sec. 3.1) are exclusively feedback functions of the template state; and
- distal—by dint of being a composition of dynamical “modules,” the control is distributed among these modules rather than executed at a central location.

[Klavins et al. \(2002\)](#) articulates the orthogonal “axes” of feedforward vs. feedback, as well as central vs. distal.

We feel justified in our strong reliance on feedback strategies for simple tasks such as horizontal plane locomotion, since feedback strategies are typically resistant to catastrophic failure in the presence of perturbations [Kuo \(2002\)](#). In the animal world, [Sherrington \(1910\)](#) suggested that reflexes play large roles in the control of movement, but since then numerous studies of many invertebrate and vertebrate animals indicate central pattern generators (CPGs) can produce coordinated motor

patterns. However, when the nervous system interacts with the biomechanical system, regulation of relevant motor patterns requires additional feedback [Zehr and Duyens \(2004\)](#). A more recent study [Gazzola et al. \(2015\)](#) shows that inertial swimmers can use only proprioception (feedback) or a combination of proprioception and CPG signals for coordinated motion. Our argument (Sec. 1.1.2) is that since our engineered machines lack the evolution-refined low-level reflexes (feedback control systems) that animals possess, our control algorithms should compensate by including a preponderance of feedback elements in the control strategy. However, we acknowledge that feedback strategies are often “greedy,” and for more complex tasks, a combination of a deliberative feedforward signal and feedback may be more appropriate.

We are also intrigued by the central / distal question; while it seems unavoidable to have a distal-favored scheme as a result of our compositional paradigm, the informational coupling introduced between two vertical hoppers by our phase controller (Sec. 3.5.1) played a centralization role that deserves further study.

5.3.2 Application to Other Domains

Legged locomotion motivated our development of the paradigm in Sec. 1.1.1, as well as the accompanying analytical tools in Chapter 3. However, we believe that the paradigm applies to other domains as well, and many of our tools. The correspondence between locomotion and the “neighboring” field of manipulation has already been discussed in the literature [Johnson and Koditschek \(2013a\)](#), and we envision near-term future work could apply our phase-synchronization results (such as Sec. 3.5) to the juggling problem [Rizzi and Koditschek \(1994\)](#). Applications in dexterous manipulation / grasping would necessitate an extension of Thm. 3 to multiple “distinct” hybrid modes.

BIBLIOGRAPHY

- Ahmadi, M. and Buehler, M. (1999). The arl monopod ii running robot: Control and energetics. In *Robotics and Automation, 1999. Proceedings. 1999 IEEE International Conference on*, volume 3, pages 1689–1694. IEEE. [46](#)
- Altendorfer, R., Koditschek, D. E., and Holmes, P. (2004). Stability Analysis of Legged Locomotion Models by Symmetry-Factored Return Maps. *The International Journal of Robotics Research*, 23(10-11):979–999. [54](#), [63](#), [75](#), [120](#), [126](#), [130](#), [131](#), [139](#)
- Ames, A. D., Galloway, K., Sreenath, K., and Grizzle, J. W. (2014). Rapidly exponentially stabilizing control lyapunov functions and hybrid zero dynamics. *IEEE Transactions on Automatic Control*, 59(4):876–891. [139](#), [169](#)
- Arampatzis, A., Brgemann, G.-P., and Metzler, V. (1999). The effect of speed on leg stiffness and joint kinetics in human running. *Journal of biomechanics*, 32(12):1349–1353. [10](#)
- Arslan, O. and Saranli, U. (2012). Reactive planning and control of planar spring-mass running on rough terrain. *IEEE Transactions on Robotics*, 28(3):567–579. [138](#)
- Asada, H. and Slotine, J. (1986). *Robot Analysis and Control*. A Wiley-interscience publication. Wiley. [1](#)
- Asada, H. and Youcef-Toumi, K. (1987). *Direct-Drive Robots: Theory and Practice*. MIT Press. [12](#), [20](#), [21](#), [25](#), [27](#), [29](#), [39](#), [42](#), [167](#)
- Berkemeier, M. D. (1998). Modeling the dynamics of quadrupedal running. *The International Journal of Robotics Research*, 17(9):971–985. [15](#), [16](#), [90](#), [91](#), [92](#)
- Bernstein, N. (1967). *The co-ordination and regulation of movements*. Pergamon-Press. [4](#), [14](#)
- Bertsimas, D. and Sim, M. (2004). The price of robustness. *Operations research*, 52(1):35–53. [18](#)
- Biewener, A. (2003). *Animal Locomotion*. Animal Locomotion. OUP Oxford. [14](#)
- Blickhan, R. and Full, R. (1993). Similarity in multilegged locomotion: bouncing like a monopode. *Journal of Comparative Physiology A*, 173(5):509–517. [72](#)
- Brown, E., Moehlis, J., and Holmes, P. (2004). On the phase reduction and response dynamics of neural oscillator populations. *Neural computation*, 16(4):673–715. [138](#)
- Brown, I. E. and Loeb, G. E. (2000). *A reductionist approach to creating and using neuromusculoskeletal models*, page 148163. Springer. [4](#)
- Buehler, M., Battaglia, R., Cocosco, A., Hawker, G., Sarkis, J., and Yamazaki, K. (1998). SCOUT: A simple quadruped that walks, climbs, and runs. In *Robotics and Automation, 1998. Proceedings. 1998 IEEE International Conference on*, volume 2, pages 1707–1712. IEEE. [11](#)
- Buehler, M., Koditschek, D., and Kindlmann, P. (1989). *A simple juggling robot: Theory and experimentation*, volume 139 of *Lecture Lecture Notes in Control and Information Sciences*, pages 35–73. [11](#)
- Burden, S., Clark, J., Weingarten, J., Komsuoglu, H., and Koditschek, D. (2007). Heterogeneous leg stiffness and roll in dynamic running. In *Proceedings 2007 IEEE International Conference on Robotics and Automation*, pages 4645–4652. IEEE. [90](#), [92](#)
- Burden, S., Revzen, S., and Sastry, S. (2015). Model Reduction Near Periodic Orbits of Hybrid Dynamical Systems. *IEEE Transactions on Automatic Control*, 60(10):2626–2639. [62](#), [74](#), [75](#), [78](#)
- Burden, S., Sastry, S., Koditschek, D., and Revzen, S. (2016). Event-selected vector field discontinuities yield piecewise-differentiable flows. *SIAM Journal on Applied Dynamical Systems*, 15(2):12271267. [62](#), [76](#)
- Carlson, J. M. and Doyle, J. (2002). Complexity and robustness. *Proceedings of the national academy of sciences*, 99(suppl 1):2538–2545. [3](#)
- Clark, J., Goldman, D., Lin, P., Lynch, G., Chen, T., Komsuoglu, H., Full, R., and Koditschek, D. (2007). Design of a bio-inspired dynamical vertical climbing robot. In *Proceedings of Robotics: Science and Systems*, Atlanta, GA, USA. [10](#), [11](#), [34](#), [39](#)

- Clark, J. E. and Koditschek, D. E. (2006). A spring assisted one degree of freedom climbing model. *Lecture Notes on Control and Information Sciences*, pages 43–64. [34](#), [37](#)
- Csete, M. and Doyle, J. (2004). Bow ties, metabolism and disease. *Trends in Biotechnology*, 22(9):446–450. [2](#)
- Culha, U. and Saranli, U. (2011). Quadrupedal bounding with an actuated spinal joint. In *Robotics and Automation (ICRA), 2011 IEEE International Conference on*, pages 1392–1397. IEEE. [17](#)
- Davey, J., Kwok, N., and Yim, M. (2012). Emulating self-reconfigurable robots—design of the smores system. In *Intelligent Robots and Systems (IROS), 2012 IEEE/RSJ International Conference on*, pages 4464–4469. IEEE. [16](#)
- De, A. (2010). Neuromechanical control of paddle juggling. Master’s thesis, Johns Hopkins University. [138](#)
- De, A., Burden, S. A., and Koditschek, D. E. (2016). A hybrid dynamical extension of averaging and its application to the analysis of legged gait stability. *under review (author can provide preprint)*. [2](#), [78](#), [90](#), [91](#), [99](#), [100](#), [101](#), [104](#), [106](#), [114](#), [118](#), [120](#), [161](#), [164](#), [165](#)
- De, A. and Koditschek, D. E. (2013). Toward dynamical sensor management for reactive wall-following. In *Robotics and Automation (ICRA), 2013 IEEE International Conference on*, pages 2400–2406. IEEE. [164](#)
- De, A. and Koditschek, D. E. (2015a). Averaged anchoring of decoupled templates in a tail-energized monopod. In *International Symposium on Robotics Research*. preprint available: <http://kodlab.seas.upenn.edu/Avik/AveragingTSLIP>. [59](#), [62](#), [133](#), [135](#)
- De, A. and Koditschek, D. E. (2015b). Parallel composition of templates for tail-energized planar hopping. In *Robotics and Automation (ICRA), 2015 IEEE International Conference on*, pages 4562–4569. [57](#), [59](#), [78](#), [98](#), [104](#), [118](#), [124](#), [133](#), [140](#)
- De, A. and Koditschek, D. E. (2015c). The Penn Jerboa: A platform for exploring parallel composition of templates. Technical report, University of Pennsylvania. arXiv:1502.05347. [5](#), [47](#), [152](#)
- De, A. and Koditschek, D. E. (2016). Vertical hopper compositions for preflexive and feedback-stabilized quadrupedal bounding, pronking, pacing and trotting. *under review (author can provide preprint)*. [46](#), [58](#), [89](#), [118](#)
- De, A., Lynch, G., Johnson, A., and Koditschek, D. (2011). Motor sizing for legged robots using dynamic task specification. In *2011 IEEE Conference on Technologies for Practical Robot Applications (TePRA)*, pages 64–69. [28](#)
- DeWitt, D. and Incropera, F. (1996). *Fundamentals of heat and mass transfer*. Wiley New York. [23](#)
- Dickinson, M. H., Farley, C. T., Full, R. J., Koehl, M. A. n., Kram, R., and Lehman, S. (2000). How animals move: An integrative view. *Science*, 288(5463):100–106. [31](#)
- Duperret, J. M., Kenneally, G. D., Pusey, J. L., and Koditschek, D. E. (2014). Towards a comparative measure of legged agility. In *International Symposium on Experimental Robotics*. In press. [45](#), [48](#)
- Eriksson, E. (1971). Compartment models and reservoir theory. *Annual Review of Ecology and Systematics*, pages 67–84. [141](#)
- Fukuoka, Y. and Kimura, H. (2009). Dynamic locomotion of a biomimetic quadruped Tekken’ robot using various gaits: walk, trot, free-gait and bound. *Applied Bionics and Biomechanics*, 6(1):63–71. [17](#)
- Full, R. J. and Koditschek, D. E. (1999). Templates and anchors: neuromechanical hypotheses of legged locomotion on land. *Journal of Exp. Biology*, 202(23):3325–3332. [2](#), [3](#), [8](#), [9](#), [14](#), [17](#), [78](#), [110](#), [139](#), [146](#), [147](#), [171](#)
- Gabrielli, G. and von Karman, T. (1950). What price speed? In *Mechanical Engineering*, volume 72, pages 775–781. [46](#)
- Galloway, K., Haynes, G., Ilhan, B. D., Johnson, A., Knopf, R., Lynch, G., Plotnick, B., White, M., and Koditschek, D. (2010a). X-RHex: A Highly Mobile Hexapedal Robot for Sensorimotor Tasks. Technical report. [12](#), [50](#), [51](#)

- Galloway, K. C., Haynes, G. C., Ilhan, B. D., Johnson, A. M., Knopf, R., Lynch, G., Plotnick, B., White, M., and Koditschek, D. E. (2010b). X-rhex: A highly mobile hexapedal robot for sensorimotor tasks. Technical report, University of Pennsylvania. [5](#), [8](#), [10](#), [11](#), [21](#), [23](#), [31](#), [45](#)
- Gan, Z., Wiestner, T., Weishaupt, M. A., Waldern, N. M., and Remy, C. D. (2016). Passive dynamics explain quadrupedal walking, trotting, and tilting. *Journal of Computational and Nonlinear Dynamics*, 11(2):021008. [15](#)
- Gazzola, M., Argentina, M., and Mahadevan, L. (2015). Gait and speed selection in slender inertial swimmers. *Proceedings of the National Academy of Sciences*, 112(13):3874–3879. [13](#), [172](#)
- Gehring, C., Coros, S., Hutter, M., and Siegwart, R. (2015). An optimization approach to controlling jump maneuvers for a quadruped robot. In *Conference on Dynamic Walking*. [45](#)
- Geyer, H., Seyfarth, A., and Blickhan, R. (2005). Spring-mass running: simple approximate solution and application to gait stability. *Journal of theoretical biology*, 232(3):315–328. [15](#), [59](#), [122](#), [133](#), [142](#), [170](#)
- Ghigliazza, R. M., Altendorfer, R., Holmes, P., and Koditschek, D. (2005). A simply stabilized running model. *SIAM Review*, 47(3):519–549. [15](#), [133](#)
- Goldstein, H., Poole, C., and Safko, J. (2013). *Classical Mechanics*. Pearson Education International. [53](#)
- Golubitsky, M., Stewart, I., Buono, P.-L., and Collins, J. J. (1998). A modular network for legged locomotion. *Physica D: Nonlinear Phenomena*, 115(1):56–72. [15](#), [16](#), [52](#), [53](#), [125](#), [168](#)
- Gregorio, P., Ahmadi, M., and Buehler, M. (1997). Design, control, and energetics of an electrically actuated legged robot. *Systems, Man, and Cybernetics, Part B: Cybernetics, IEEE Transactions on*, 27(4):626–634. [11](#), [22](#)
- Grimes, J. and Hurst, J. (2012). The design of atrias 1.0 a unique monopod, hopping robot. *Adaptive Mobile Robotics - Proceedings of the 15th International Conference on Climbing and Walking Robots and the Support Technologies for Mobile Machines, CLAWAR 2012*, pages 548–554. [21](#), [45](#)
- Grizzle, J. W., Chevallereau, C., Sinnet, R. W., and Ames, A. D. (2014). Models, feedback control, and open problems of 3d bipedal robotic walking. *Automatica*, 50(8):1955–1988. [3](#)
- Guckenheimer, J., Hoffman, K., and Weckesser, W. (2003). The forced van der Pol equation I: The slow flow and its bifurcations. *SIAM Journal on Applied Dynamical Systems*, 2(1):1–35. [54](#)
- Guckenheimer, J. and Holmes, P. (1990). *Nonlinear Oscillations, Dynamical Systems, and Bifurcations of Vector Fields*. Applied Mathematical Sciences. Springer New York. [62](#), [63](#), [64](#), [65](#), [66](#), [123](#), [125](#), [126](#), [127](#)
- Guckenheimer, P. J. (1975). Isochrons and phaseless sets. *Journal of Mathematical Biology*, 1(3):259–273. [125](#)
- Haghverdi, E., Tabuada, P., and Pappas, G. J. (2005). Bisimulation relations for dynamical, control, and hybrid systems. *Theoretical Computer Science*, 342(2-3):229–261. [2](#)
- Hale, J. (2015). *Oscillations in Nonlinear Systems*. Dover Books on Mathematics. Dover Publications. [54](#)
- Hauser, J. and Chung, C. C. (1994). Converse Lyapunov functions for exponentially stable periodic orbits. *Systems & Control Letters*, 23(1):27–34. [123](#), [138](#)
- Haynes, G. C., Cohen, F. R., and Koditschek, D. E. (2011). Gait Transitions for Quasi-static Hexapedal Locomotion on Level Ground. In Pradalier, C., Siegwart, R., and Hirzinger, G., editors, *Robotics Research*, volume 70 of *Springer Tracts in Advanced Robotics*, pages 105–121. Springer Berlin Heidelberg. [158](#)
- Haynes, G. C., Rizzi, A. A., and Koditschek, D. E. (2012). Multistable phase regulation for robust steady and transitional legged gaits. *The International Journal of Robotics Research*. [53](#), [125](#)
- Heess, N., Wayne, G., Tassa, Y., Lillicrap, T., Riedmiller, M., and Silver, D. (2016). Learning and Transfer of Modulated Locomotor Controllers. *arXiv preprint arXiv:1610.05182*. [18](#)
- Hirsch, M., Devaney, R., and Smale, S. (1974). *Differential Equations, Dynamical Systems, and Linear Algebra*. Pure and Applied Mathematics. Elsevier Science. [64](#), [65](#), [71](#)

- Hogan, N. (1985). Impedance control: An approach to manipulation: part 1 - theory. *Journal of Dynamic Systems, Measurement and Control, Transactions of the ASME*, 107(1):1–7. [20](#)
- Holmes, P. (2005). Ninety plus thirty years of nonlinear dynamics: Less is more and more is different. *International Journal of Bifurcation and Chaos*, 15(09):2703–2716. [3](#), [7](#)
- Horn, R. and Johnson, C. (1990). *Matrix Analysis*. Cambridge University Press. [41](#)
- Hurst, J. W. (2008). *The Role and Implementation of Compliance in Legged Locomotion*. PhD thesis, Robotics Institute, Carnegie Mellon University, Pittsburgh, PA. [20](#)
- Hutter, M., Gehring, C., Bloesch, M., Hoepflinger, M., Remy, C., and Siegwart, R. (2012). Starleth: A compliant quadrupedal robot for fast, efficient, and versatile locomotion. *Adaptive Mobile Robotics - Proceedings of the 15th International Conference on Climbing and Walking Robots and the Support Technologies for Mobile Machines, CLAWAR 2012*, pages 483–490. [45](#)
- Hutter, M., Remy, C., Hoepflinger, M., and Siegwart, R. (2013). Efficient and versatile locomotion with highly compliant legs. *IEEE/ASME Transactions on Mechatronics*, 18(2):449–458. [21](#)
- Hutter, M., Sommer, H., Gehring, C., Hoepflinger, M., Bloesch, M., and Siegwart, R. (2014). Quadrupedal locomotion using hierarchical operational space control. *The International Journal of Robotics Research*, 33(8):1047–1062. [18](#)
- Johnson, A. M., Burden, S. A., and Koditschek, D. E. (2016). A hybrid systems model for simple manipulation and self-manipulation systems. *The International Journal of Robotics Research*, 35(11):1354–1392. [62](#), [78](#), [93](#), [94](#), [111](#), [112](#)
- Johnson, A. M., Chang-Siu, E., Libby, T., Tomizuka, M., Full, R. J., and Koditschek, D. E. (2012). Tail assisted dynamic self righting. In *Proc. Intl. Conf. on Climbing and Walking Robots*. [48](#), [59](#), [60](#), [144](#), [145](#), [148](#)
- Johnson, A. M. and Koditschek, D. E. (2013a). Legged self-manipulation. *IEEE Access*, 1:310–334. [5](#), [21](#), [44](#), [145](#), [172](#)
- Johnson, A. M. and Koditschek, D. E. (2013b). Toward a vocabulary of legged leaping. In *Proc. ICRA 2013*, pages 2553–2560. [5](#), [48](#)
- Kafader, U. (2006). *The Selection of High-Precision Microdrives*. Maxon Academy. [11](#), [23](#), [31](#)
- Kenneally, G., De, A., and Koditschek, D. E. (2016). Design Principles for a Family of Direct-Drive Legged Robots. *IEEE Robotics and Automation Letters*, 1(2):900–907. [5](#), [26](#), [44](#), [78](#), [151](#), [152](#), [153](#), [161](#)
- Kenneally, G. and Koditschek, D. E. (2014). Kinematic leg design in an electromechanical robot. Technical report, Workshop article presented at ICRA 2014, Hong Kong. [51](#)
- Kenneally, G. and Koditschek, D. E. (2017). Characterization of Robotic Transparency and Energetic Cost of Proprioceptive Information. In *in prep.* [4](#), [8](#), [10](#), [28](#), [153](#), [167](#)
- Klavins, E. and Koditschek, D. E. (2002). Phase regulation of decentralized cyclic robotic systems. *The International Journal of Robotics Research*, 21(3):257–275. [15](#), [16](#), [62](#)
- Klavins, E., Koditschek, D. E., and Ghrist, R. (2000). Toward the Regulation and Composition of Cyclic Behaviors. In Donald, B., Lynch, K., and Rus, D., editors, *Algorithmic and Computational Robotics: New Directions 2000 WAFR*, pages 205–220. Wellesley: A.K. Peters. [15](#), [58](#), [62](#), [79](#), [90](#)
- Klavins, E., Komsuoglu, H., Full, R. J., and Koditschek, D. E. (2002). The Role of Reflexes versus Central Pattern Generators in Dynamical Legged Locomotion. In *Neurotechnology for Biomimetic Robots*, pages 351–382. MIT Press, Cambridge, MA. [13](#), [14](#), [17](#), [171](#)
- Koditschek, D. E. (1987). Adaptive techniques for mechanical systems. In *Proc. 5th. Yale Workshop on Adaptive Systems*, pages 259–265. [60](#), [109](#)
- Koditschek, D. E. and Buehler, M. (1991). Analysis of a simplified hopping robot. *The International Journal of Robotics Research*, 10(6):587–605. [11](#), [15](#), [16](#), [20](#), [56](#), [62](#), [72](#), [107](#), [169](#)

- Kuindersma, S., Deits, R., Fallon, M., Valenzuela, A., Dai, H., Permenter, F., Koolen, T., Marion, P., and Tedrake, R. (2016). Optimization-based locomotion planning, estimation, and control design for the atlas humanoid robot. *Autonomous Robots*, 40(3):429–455. [18](#)
- Kuo, A. D. (2002). The relative roles of feedforward and feedback in the control of rhythmic movements. *MOTOR CONTROL-CHAMPAIGN-*, 6(2):129–145. [10](#), [14](#), [171](#)
- Lamb, J. S. and Roberts, J. A. (1998). Time-reversal symmetry in dynamical systems: a survey. *Physica D: Nonlinear Phenomena*, 112(1):1–39. [54](#)
- Levine, S., Pastor, P., Krizhevsky, A., Ibarz, J., and Quillen, D. (2016). Learning hand-eye coordination for robotic grasping with deep learning and large-scale data collection. *The International Journal of Robotics Research*, page 0278364917710318. [18](#)
- Libby, T., Johnson, A. M., Chang-Siu, E., Full, R. J., and Koditschek, D. E. (2015). Comparative design, scaling, and control of appendages for inertial reorientation. arXiv preprint arXiv:1511.05958 [cs.RO]. [59](#), [93](#), [170](#)
- Libby, T., Moore, T. Y., Chang-Siu, E., Li, D., Cohen, D. J., Jusufi, A., and Full, R. J. (2012). Tail-assisted pitch control in lizards, robots and dinosaurs. *Nature*, 481(7380):181–184. [44](#), [48](#)
- Lopes, G. A. D. and Koditschek, D. E. (2007). Visual Servoing for Nonholonomically Constrained Three Degree of Freedom Kinematic Systems. *The International Journal of Robotics Research*, 26(7):715–736. [164](#)
- Loughlin, C., Albu-Schäffer, A., Haddadin, S., Ott, C., Stemmer, A., Wimböck, T., and Hirzinger, G. (2007). The dlr lightweight robot: design and control concepts for robots in human environments. *Industrial Robot: an international journal*, 34(5):376–385. [20](#)
- Manchester, I. R., Mettin, U., Iida, F., and Tedrake, R. (2011). Stable dynamic walking over uneven terrain. *The International Journal of Robotics Research*, 30(3):265–279. [138](#)
- Maxon Motors (2010). Maxon Catalog, Key Information. [5](#), [20](#), [22](#), [23](#), [28](#), [29](#), [36](#), [38](#), [167](#)
- Minitaur (2016). Ghost robotics minitaur. <http://www.ghostrobotics.io/minitaur/>. [5](#), [7](#), [21](#), [78](#), [151](#)
- Murphy, K. N. and Raibert, M. H. (1985). Trotting and bounding in a planar two-legged model. In *Theory and Practice of Robots and Manipulators*, pages 411–420. Springer. [16](#), [92](#), [154](#), [159](#), [164](#)
- Murray, R. M., Li, Z., Sastry, S. S., and Sastry, S. S. (1994). *A mathematical introduction to robotic manipulation*. CRC press. [18](#), [42](#), [167](#)
- Neunert, M., Farshidian, F., Winkler, A. W., and Buchli, J. (2016). Trajectory Optimization Through Contacts and Automatic Gait Discovery for Quadrupeds. *arXiv preprint arXiv:1607.04537*. [18](#)
- Owaki, D., Kano, T., Nagasawa, K., Tero, A., and Ishiguro, A. (2013). Simple robot suggests physical interlimb communication is essential for quadruped walking. *Journal of The Royal Society Interface*, 10(78):20120669. [118](#)
- Park, H.-W., Sreenath, K., Hurst, J. W., and Grizzle, J. W. (2011). Identification of a bipedal robot with a compliant drivetrain. *IEEE Control Systems*, 31(2):63–88. [12](#)
- Piccoli, M. and Yim, M. (2014). Cogging Torque Ripple Minimization via Position Based Characterization. In *Proceedings of Robotics: Science and Systems*, Berkeley, USA. [51](#)
- Potkonjak, V. (1989). Thermal analysis and dynamic capabilities of DC motors in industrial robotic systems. *Robotics and Computer-Integrated Manufacturing*, 5(2-3):137 – 143. [11](#), [22](#), [37](#)
- Poulakakis, I. (2005). Modeling and Experiments of Untethered Quadrupedal Running with a Bounding Gait: The Scout II Robot. *The International Journal of Robotics Research*, 24(4):239–256. [15](#)
- Poulakakis, I. (2006). On the Stability of the Passive Dynamics of Quadrupedal Running with a Bounding Gait. *The International Journal of Robotics Research*, 25(7):669–687. [15](#), [63](#)
- Poulakakis, I., Smith, J. A., and Buehler, M. (2004). Experimentally validated bounding models for the scout ii quadrupedal robot. In *ICRA*, pages 2595–2600. [11](#)

- Pratt, G. A. and Williamson, M. M. (1995). Series elastic actuators. *IEEE International Conference on Intelligent Robots and Systems*, 1:399–406. [10](#), [20](#)
- Pratt, J., Carff, J., Drakunov, S., and Goswami, A. (2006). Capture point: A step toward humanoid push recovery. In *2006 6th IEEE International Conference on Humanoid Robots*, pages 200–207. [62](#)
- Proctor, J., Kukillaya, R. P., and Holmes, P. (2010). A phase-reduced neuro-mechanical model for insect locomotion: feed-forward stability and proprioceptive feedback. *Philosophical Transactions of the Royal Society A: Mathematical, Physical and Engineering Sciences*, 368(1930):5087–5104. [15](#), [52](#), [77](#), [118](#)
- Pusey, J. L., Duperret, J. M., Haynes, G. C., Knopf, R., and Koditschek, D. E. (2013). Free-standing leaping experiments with a power-autonomous elastic-spined quadruped. In *SPIE Defense, Security, and Sensing*, pages 87410W–87410W. International Society for Optics and Photonics. [17](#)
- Rad, H., Gregori, P., and Buehler, M. (1993). Design, modeling and control of a hopping robot. *International Conference on Intelligent Robots and Systems*, pages 1778–1785. [28](#), [43](#)
- Raibert, M. (1986). *Legged Robots that Balance*. Artificial Intelligence. MIT Press. [1](#), [11](#), [12](#), [13](#), [14](#), [16](#), [20](#), [47](#), [49](#), [53](#), [60](#), [72](#), [106](#), [120](#), [125](#), [131](#), [136](#), [137](#), [138](#), [140](#), [144](#), [149](#), [150](#), [153](#), [154](#), [155](#), [156](#), [158](#), [160](#), [166](#), [169](#), [170](#)
- Raibert, M. H. (1981). Dynamic stability and resonance in a one-legged hopping machine. In *4th Symp. Theory and Practice of Robots and Manipulators*. [39](#)
- Raibert, M. H., Brown Jr, H. B., Cheponis, M., Koechling, J., Hodgins, J. K., Dustman, D., Brennan, W. K., Barrett, D. S., Thompson, C. M., Hebert, J. D., and others (1989). Dynamically Stable Legged Locomotion (September 1985–September 1989). [9](#), [12](#), [16](#), [140](#), [152](#), [153](#), [154](#), [155](#), [163](#), [164](#), [165](#), [166](#)
- Razavi, H., Bloch, A. M., Chevallereau, C., and Grizzle, J. W. (2016). Symmetry in legged locomotion: a new method for designing stable periodic gaits. *Autonomous Robots*. [63](#), [129](#), [139](#)
- Revzen, S. (2009). *Neuromechanical control architectures of arthropod locomotion*. PhD thesis, University of California, Berkeley. [138](#)
- Revzen, S., Koditschek, D. E., and Full, R. J. (2009). Towards Testable Neuromechanical Control Architectures for Running. In Sternad, D., editor, *Progress in Motor Control*, volume 629 of *Advances in Experimental Medicine and Biology*, pages 25–55. Springer US. [12](#), [13](#)
- Richard, J.-P. (2003). Time-delay systems: an overview of some recent advances and open problems. *automatica*, 39(10):1667–1694. [10](#)
- Righetti, L. and Ijspeert, A. J. (2008). Pattern generators with sensory feedback for the control of quadruped locomotion. In *Robotics and Automation, 2008. ICRA 2008. IEEE International Conference on*, pages 819–824. [17](#), [118](#)
- Rizzi, A. and Koditschek, D. (1994). Further progress in robot juggling: solvable mirror laws. In *1994 IEEE International Conference on Robotics and Automation, 1994. Proceedings*, pages 2935–2940 vol.4. [11](#), [172](#)
- Sakagami, Y., Watanabe, R., Aoyama, C., Matsunaga, S., Higaki, N., and Fujimura, K. (2002). The intelligent asimo: System overview and integration. In *Intelligent Robots and Systems, 2002. IEEE/RSJ International Conference on*, volume 3, pages 2478–2483. IEEE. [44](#)
- Salisbury, J. K. and Roth, B. (1983). Kinematic and force analysis of articulated mechanical hands. *Journal of Mechanisms, Transmissions, and Automation in Design*, 105(1):35–41. [12](#)
- Saranli, U., Buehler, M., and Koditschek, D. E. (2001). RHex: a simple and highly mobile hexapod robot. *International Journal of Robotics Research*, 20:616631. [5](#), [48](#)
- Saranli, U. and Koditschek, D. E. (2003). Template based control of hexapedal running. In *Robotics and Automation, 2003. Proceedings. ICRA'03. IEEE International Conference on*, volume 1, pages 1374–1379. IEEE. [106](#), [156](#), [166](#)

- Saranli, U., Schwind, W. J., and Koditschek, D. E. (1998). Toward the control of a multi-jointed, monoped runner. In *1998 IEEE International Conference on Robotics and Automation*, volume 3, pages 2676–2682. [16](#), [62](#), [72](#)
- Saranli, U., Arslan, ., Ankaral, M. M., and Morgl, . (2010). Approximate analytic solutions to non-symmetric stance trajectories of the passive Spring-Loaded Inverted Pendulum with damping. *Nonlinear Dynamics*, 62(4):729–742. [170](#)
- Schmitt, J. and Holmes, P. (2000). Mechanical models for insect locomotion: dynamics and stability in the horizontal plane i. theory. *Biological cybernetics*, 83(6):501–515. [3](#), [15](#), [168](#)
- Schwind, W. J. and Koditschek, D. E. (1995). Control of forward velocity for a simplified planar hopping robot. In *1995 IEEE International Conference on Robotics and Automation*, volume 1, pages 691–696. [15](#), [59](#), [122](#), [133](#)
- Schwind, W. J. and Koditschek, D. E. (1997). Characterization of monoped equilibrium gaits. In *Robotics and Automation, 1997. Proceedings., 1997 IEEE International Conference on*, volume 3, pages 1986–1992. IEEE. [9](#)
- Seok, S., Wang, A., Chuah, M., Otten, D., Lang, J., and Kim, S. (2013). Design principles for highly efficient quadrupeds and implementation on the mit cheetah robot. *Proceedings - IEEE International Conference on Robotics and Automation*, pages 3307–3312. [27](#)
- Seok, S., Wang, A., Otten, D., and Kim, S. (2012). Actuator design for high force proprioceptive control in fast legged locomotion. In *2012 IEEE/RSJ International Conference on Intelligent Robots and Systems (IROS)*, pages 1970–1975. IEEE. [12](#), [20](#), [21](#), [26](#), [27](#), [50](#), [51](#)
- Seyfarth, A., Radkhah, K., and Von Stryk, O. (2015). Concepts of Softness for Legged Locomotion and Their Assessment. In *Soft Robotics*, pages 120–133. Springer. [17](#)
- Shahbazi, M. and Lopes, G. A. D. (2016). Coordination of Monopodal SLIP Models Towards Quadrupedal Running. In *2016 IEEE/RSJ International Conference on Intelligent Robots and Systems (IROS)*, Daejeon, Korea. [15](#), [63](#)
- Sherrington, C. (1910). *The integrative action of the nervous system*. CUP Archive. [171](#)
- Shkolnik, A., Levashov, M., Manchester, I. R., and Tedrake, R. (2011). Bounding on rough terrain with the LittleDog robot. *The International Journal of Robotics Research*, 30(2):192–215. [17](#)
- Slotine, J.-J. E. (2003). Modular stability tools for distributed computation and control. *International Journal of Adaptive Control and Signal Processing*, 17(6):397–416. [17](#)
- Spence, A. J., Revzen, S., Seipel, J., Mullens, C., and Full, R. J. (2010). Insects running on elastic surfaces. *The Journal of experimental biology*, 213(11):1907–1920. [20](#)
- Sprowitz, A., Tuleu, A., Vespignani, M., Ajallooeian, M., Badri, E., and Ijspeert, A. J. (2013a). Towards dynamic trot gait locomotion: Design, control, and experiments with Cheetah-cub, a compliant quadruped robot. *The International Journal of Robotics Research*, 32(8):932–950. [17](#), [161](#)
- Sprowitz, A., Tuleu, A., Vespignani, M., Ajallooeian, M., Badri, E., and Ijspeert, A. J. (2013b). Towards dynamic trot gait locomotion: Design, control, and experiments with Cheetah-cub, a compliant quadruped robot. *The International Journal of Robotics Research*, 32:932–950. [21](#), [45](#)
- Sung, C., Bern, J., Romanishin, J., and Rus, D. (2015). Reconfiguration planning for pivoting cube modular robots. In *Robotics and Automation (ICRA), 2015 IEEE International Conference on*, pages 1933–1940. IEEE. [16](#)
- Sutherland, I. E. and Carlson, F. H. (1983). *A walking robot*. Sutherland, Sproull & Ass. [14](#)
- Symon, K. (1971). *Mechanics*. Addison-Wesley World student series. Addison-Wesley Publishing Company. [95](#)
- Tabuada, P., Ames, A. D., Julius, A., and Pappas, G. J. (2008). Approximate reduction of dynamic systems. *Systems & Control Letters*, 57(7):538–545. [2](#)

- Tedrake, R. (2009). Underactuated robotics: Learning, planning, and control for efficient and agile machines course notes for MIT 6.832. Technical report. [17](#), [18](#)
- Todorov, E. (2009). Compositionality of optimal control laws. In *Advances in Neural Information Processing Systems*, pages 1856–1864. [18](#)
- Todorov, E. and Ghahramani, Z. (2004). Analysis of the synergies underlying complex hand manipulation. In *Engineering in Medicine and Biology Society, 2004. IEMBS'04. 26th Annual International Conference of the IEEE*, volume 2, pages 4637–4640. IEEE. [171](#)
- Topping, T. T., Vasilopoulos, V., De, A., and Koditschek, D. E. (2016). Towards bipedal behavior on a quadrupedal platform using optimal control. In Karlsen, R. E., Gage, D. W., Shoemaker, C. M., and Gerhart, G. R., editors, *SPIE 9837, Unmanned Systems Technology XVIII*, page 98370H. [18](#)
- Tosun, T., Jing, G., Kress-Gazit, H., and Yim, M. (2015). Computer-aided compositional design and verification for modular robots. In *IFRR International Symposium on Robotics Research*. [16](#), [17](#)
- Wang, A. and Kim, S. (2015). Directional efficiency in geared transmissions: Characterization of backdrivability towards improved proprioceptive control. In *Robotics and Automation (ICRA), 2015 IEEE International Conference on*, pages 1055–1062. [20](#), [28](#), [167](#)
- Weingarten, J. D., Groff, R. E., and Koditschek, D. E. (2004). A framework for the coordination of legged robot gaits. In *Robotics, Automation and Mechatronics, 2004 IEEE Conference on*, volume 2, pages 679–686. [161](#)
- Wenger, G., De, A., and Koditschek, D. E. (2016). Frontal plane stabilization and hopping with a 2dof tail. In *Intelligent Robots and Systems (IROS), 2016 IEEE/RSJ International Conference on*, pages 567–573. IEEE. [61](#)
- Wensing, P. M., Wang, A., Seok, S., Otten, D., Lang, J., and Kim, S. (2017). Proprioceptive Actuator Design in the MIT Cheetah: Impact Mitigation and High-Bandwidth Physical Interaction for Dynamic Legged Robots. *IEEE Transactions on Robotics*, pages 1–14. [12](#), [167](#)
- Westervelt, E. R., Grizzle, J. W., and Koditschek, D. E. (2003). Hybrid zero dynamics of planar biped walkers. *IEEE Transactions on Automatic Control*, 48(1):42–56. [139](#)
- Whitney, D. (1996). Why mechanical design cannot be like VLSI design. *Research in Engineering Design*, 8(3):125–138. [1](#), [17](#)
- Wieber, P.-B., Tedrake, R., and Kuindersma, S. (2016). Modeling and Control of Legged Robots. In Siciliano, B. and Khatib, O., editors, *Springer Handbook of Robotics*, pages 1203–1234. Springer International Publishing, Cham. [18](#)
- Wollherr, D., Hardt, M., Buss, M., and von Stryk, O. (2002). Actuator selection and hardware realization of a small and fast-moving autonomous humanoid robot. In *Proc. 2002 IEEE/RSJ Int. Conf. on Intelligent Robots and Systems (IROS)*. Citeseer. [37](#)
- Zehr, E. P. and Duysens, J. (2004). Regulation of arm and leg movement during human locomotion. *The Neuroscientist*, 10(4):347–361. [172](#)
- Zocholl, S. E. (2007). Optimizing Motor Thermal Models. In *Petroleum and Chemical Industry Conference, 2006. PCIC'06. Record of Conference Papers-IEEE Industry Applications Society 53rd Annual*, pages 1–9. IEEE. [31](#)